“Anisotropic fiber / hydrogel biomaterials of polysaccharides: Extrudability, spinnability and 3D printability for applications in biomedical engineering”

Von der Fakultät für Ingenieurwissenschaften
der Universität Bayreuth
zur Erlangung der Würde
Doktor-Ingenieur (Dr.-Ing.)
genehmigte Dissertation

von
M.Sc. Tuan Anh Tran
aus
Hanoi, Viet Nahm

Erstgutachter: Dr. Anayancy Osorio-Madrazo
Zweitgutachter: Prof. Dr.-Ing. Holger Ruckdäschel
Tag der mündlichen Prüfung: 06.07.2026

Lehrstuhl für Additive Verfahren für die Geweberekonstruktion (Organ Printing)
Universität Bayreuth
2026

Abstract

This thesis reports the development of functional chitosan-based biomaterials through microextrusion of viscous collodions and (bio)inks. Anisotropic fiber and hydrogel hybrid materials of enhanced mechanical performance and good biological properties were produced by respectively using gel spinning and extrusion-based 3D printing approaches to develop biomaterials with promising applications in tissue engineering and repair.

By precisely tailoring the molecular weight of chitosan and incorporating cellulose nanofibers, composite fibers with tunable mechanical properties, including enhanced stiffness, tensile strength, strain at break, and toughness were achieved by gel spinning. The synergistic interplay between low and high molecular weight chitosans provided an optimal balance of solubility, chain mobility, and structural integrity, while the cellulose nanofbers enhanced rheological behavior, extrusion fidelity, and contributed to promote preferential orientation and chitosan crystallization, to favor the formation of highly anisotropic and mechanically strong fibers for biomedical applications. Besides, extrusion-based 3D printing of cellulose nanofiber-filled chitosan viscous inks, allowed the preparation of anisotropic hydrogels whose process-related developed orientation could be quantified in situ using X-ray scattering at small (SAXS) and wide angles (WAXS) at the synchrotron beamline. The results revealed the controlled microstructural anisotropy and hierarchical organization, demonstrating that polymer and/or nanofiber filler orientation is strongly influenced by the shear stress-induced alignment during extrusion, the nanofiber morphology and aspect ratio, the chitosan concentration and the nanofiber content. These findings establish a platform for the processing of mechanically stable, bioinstructive 3D scaffolds based on natural biopolymers and physical hydrogels without chemical modification, promoting the use of sustainable and biocompatible functional materials in biomedical engineering. Further, in a proof of concept this thesis addressed the central challenge of achieving chitosan solubilization at around neutral pH compatible with cell survival for the development of cell-laden chitosan-based functional hydrogels by extrusion-based 3D bioprinting. Cell-laden bioinks composed of unmodified chitosan were successfully bioprinted, including cell-laden hybrid systems that incorporated cellulose nanofibers. Structurally stable 3D constructs were obtained which biological assessment showed good cell viability for even relatively long incubation period.

This work highlights the potential of biocompatible and bioactive unmodified chitosan/cellulose nanofiber bioinks for regenerative medicine, providing a versatile and tunable system for engineering complex, functional anisotropic tissues.

***Keywords**: Anisotropic hydrogels, chitosan, cellulose nanofibers, gel spinning, extrusion-based 3D (bio)printing, cell-laden chitosan-based hydrogels, functional biomaterials, tissue engineering*

Zusammenfassung

Diese Arbeit berichtet über die Entwicklung funktioneller Biomaterialien auf Chitosanbasis durch Mikroextrusion von viskosen Kollodionen und (Bio-)Tinten. Anisotrope Fasern und Hydrogel-Hybridmaterialien mit verbesserter mechanischer Leistung und guten biologischen Eigenschaften wurden durch Gelspinnen bzw. extrusionsbasierte 3D-Druckverfahren hergestellt, um Biomaterialien mit vielversprechenden Anwendungen in der Gewebezüchtung und -regeneration zu entwickeln.

Durch die präzise Anpassung des Molekulargewichts von Chitosan und die Einarbeitung von Zellulose-Nanofasern wurden durch Gelspinnen Verbundfasern mit einstellbaren mechanischen Eigenschaften – darunter verbesserte Steifigkeit, Zugfestigkeit, Bruchdehnung und Zähigkeit – erzielt. Das synergistische Zusammenspiel zwischen Chitosan mit niedrigem und hohem Molekulargewicht sorgte für ein optimales Gleichgewicht zwischen Löslichkeit, Beweglichkeit der Polymerketten und struktureller Integrität, während die Zellulose-Nanofasern das rheologische Verhalten und die Extrusionsgenauigkeit verbesserten und zur Förderung der bevorzugten Ausrichtung und Chitosan-Kristallisation beitrugen, um die Bildung hochgradig anisotroper und mechanisch starker Fasern für biomedizinische Anwendungen zu begünstigen. Außerdem ermöglichte der extrusionsbasierte 3D-Druck von mit Zellulose-Nanofasern gefüllten viskosen Chitosan-Tinten die Herstellung anisotroper Hydrogele, deren prozessbedingte Ausrichtung in situ mittels Röntgenstreuung bei kleinen (SAXS) und großen Winkeln (WAXS) an der Synchrotron-Beamline quantifiziert werden konnte. Die Ergebnisse zeigten die kontrollierte mikrostrukturelle Anisotropie und hierarchische Organisation und belegten, dass die Ausrichtung von Polymeren und/oder Nanofaserfüllstoffen stark von der durch die Scherspannung während der Extrusion induzierten Ausrichtung, der Nanofasermorphologie und dem Aspektverhältnis, der Chitosan-Konzentration und dem Nanofasergehalt beeinflusst wird. Diese Erkenntnisse bilden die Grundlage für die Herstellung mechanisch stabiler, bioinstruktiver 3D-Gerüste auf Basis natürlicher Biopolymere und physikalischer Hydrogele ohne chemische Modifikation und fördern den Einsatz nachhaltiger und biokompatibler Funktionsmaterialien in der Biomedizintechnik. Darüber hinaus befasste sich diese Arbeit in einem *Proof-of-Concept* mit der zentralen Herausforderung, eine Chitosan-Solubilisierung bei einem neutralen pH-Wert zu erreichen, der mit dem Überleben von Zellen einher geht, um zellbeladene, funktionelle Hydrogele auf Chitosan-Basis durch extrusionsbasiertes 3D-Bioprinting zu entwickeln. Es gelang, zellbeladene Bio-Tinten aus nichtmodifiziertem Chitosan zu bioprinten, darunter auch zellbeladene Hybridsysteme, die Zellulose-Nanofasern enthielten. Es wurden strukturell stabile 3D-Konstrukte erhalten, die bei der biologischen Bewertung auch nach relativ langer Inkubationszeit eine gute Zellviabilität zeigten.

Diese Arbeit unterstreicht das Potenzial von biokompatiblen und bioaktiven, nichtmodifizierten Bio-Tinten aus Chitosan/Zellulose-Nanofasern für die regenerative Medizin, und bietet ein

vielseitiges und anpassungsfähiges System für die Entwicklung komplexer, funktioneller anisotroper Gewebe.

Schlüsselwörter: *Anisotrope Hydrogele, Chitosan, Zellulose-Nanofasern, Nassspinnen, Extrusionsbasierte-3D-(Bio)Druck, Zellgeladene Chitosan-Hydrogele, Funktionsmaterialien, Tissue Engineering*

Parts of this work have already been published as article in peer reviewed journal:

Publications:

1) **Tran T.A.**, Doench I., Kamdem Tamo A., Jahangir, S., Marquez-Bravo, S, Molina, P., Helmstaedter, M., Morales-Helguera, A., Gorzelanny, C., Osorio-Madrazo A. “Biopolymer fibers of high strength and enhanced orientation by the synergy of high/low molecular weight chitosans in hybrid biomaterials processed by gel spinning”. *Journal of Functional Biomaterials* (2025),16(11):405. DOI:10.3390/jfb16110405

2) Morcos, A., **Tran, T.A.**, Sudre G., Osorio-Madrazo, A. Mai, V., Courtial, E.-J., Boulocher, C., Bruyere, P., David, L., Rieger, R. “Structural anisotropy characterization of fiber-reinforced hydrogels scaffolds during extrusion-based 3D printing for soft tissue repair”. *European Synchrotron Radiation Facility ESRF* (2024). DOI: 10.15151/ESRF-DC-2007535936

3) Kamdem, A., **Tran, T.A.,** Doench, I., Jahangir, S., Lall, A., David, L., Peniche-Covas, C., Walther, A., Osorio-Madrazo, A. “3D printing of cellulase-laden cellulose nanofiber/chitosan hydrogel composites: Towards tissue engineering functional biomaterials with enzyme-mediated biodegradation”. *Materials* (2022), 15, 6039. DOI: 10.3390/ma15176039

Conference Presentations:

1) **Tran, T.A.** et al, Osorio Madrazo, A. 16th International Conference on Chitin and Chitosan (16th ICCC), 14th Asian-Pacific Chitin and Chitosan Society Conference (APCCS 2025). August 2025, Taipei, Taiwan. “BioLab-on-chip and 3D cell/chitosan hydrogel bioprinting for tissue engineering”. Oral presentation

2) Shaghayegh J, **Tran, T.A** et al, Osorio Madrazo, A. 17th International Conference on Chitin and Chitosan (17th ICCC), 16th Ibero-American Chitin Society Conference (SIAQ 2025). October **2025**, Hermosillo, Mexico. "Engineering 3D cell microenvironment of biohybrid systems based on chitosan for the regenerative medicine". Oral presentation

3) **Tran T.A.** et al, Osorio-Madrazo, A. “Quantifying orientation of nanofibers in viscous ink biomaterials by X-ray synchrotron scattering during microextrusion”. 8th China-Europe Symposium on Biomaterials in Regenerative Medicine CESB. September 2024, Nuremberg, Germany. Poster

4) **Tran T.A.** et al, Osorio-Madrazo, A. “Orientation in chitosan-based inks extruded at the X-ray synchrotron beamline: Towards 3D printing of anisotropic hydrogels”. 15th International Conference on Chitin and Chitosan (15th ICCC), 14th European Chitin Society Conference (EUCHIS 2023). September 2023, Siglufjiordur, Iceland. Poster and Oral presentation.

5) Kamdem, A., **Tran T.A.** et al, Osorio-Madrazo, A. “Biofabrication of chitosan/cellulose nanofibers hydrogels by 3D printing: bioinspired, mechanically performant, biocompatible and biodegradable 3d tissue constructs”, 15th International Conference on Chitin and Chitosan (15th ICCC), 14th European Chitin Society Conference (EUCHIS 2023). September 2023, Siglufjiordur, Iceland. Oral presentation.

Acknowledgement

This work was carried out with the support and assistance of many individuals to whom I express my deepest gratitude.

I extend my sincere thanks to Dr. Anayancy Osorio Madrazo, my primary PhD supervisor, for welcoming me into the Chair of Organ Printing at the University of Bayreuth and for the scientific and human qualities she consistently demonstrated. Her valuable guidance, constant availability, and encouragement were instrumental throughout this study. Her commitment to clarity, rigor, and precision greatly enriched the quality of this work.

I also wish to express my gratitude to Dr. Ingo Dönch for his invaluable collaboration and unwavering availability, which were essential to the successful completion of this thesis. I offer him my respect and sincere appreciation for his continuous efforts and dedication.

My warm thanks go to my colleagues and members of Osorio Lab for their support and the stimulating work environment they provided. I am particularly grateful to Dr. Dulce Maria Gonzalez Mosquera, Dr. Per Arvid Löthman, Msc. Shaghayegh Jahangir, Dr. Isabel Fraile Gutierrez, and Dr. Arnaud Kamdem Tamo from the Chair of Organ Printing for their kind collaboration and their contributions to the results of this thesis. I also thank all the MSc students whose I had the privilege to co-supervise, their work significantly enriched this research.

I further acknowledge the Institute of Microsystems Engineering (IMTEK), the Freiburg Materials Research Center (FMF) and the Freiburg Center for Interactive Materials and Bioinspired Technologies (FIT) and Osorio Lab at the University of Freiburg as well as the Jena Center for Soft Matter (JCSM) and the Center for Energy and Environmental Chemistry Jena (CEEC) at University of Jena led by Prof. Ulrich S. Schubert , and the collegaues of those institutes for their support, fruitful scientific collaboration, and the welcoming atmosphere that allowed me to conduct my research under excellent conditions.

My gratitude also goes to Prof. Laurent David and Dr. Romain Rieger for hosting my research stay at the “Laboratoire Ingénierie des Matériaux Polymères (IMP)” at the University Claude Bernard Lyon 1 (France). I also thank PD Dr. Christian Gorzelanny for hosting my research stay at the Department of Dermatology and Venerology at the University Medical Center Hamburg-Eppendorf (UKE). Their advice and methodological guidance were invaluable to the successful advancement of this work.

I thank the members of the examination jury for the honor of receiving their evaluation of my thesis.

Finally, I warmly thank my family for their unwavering support and constant encouragement. To all those who, directly or indirectly, contributed to the realization of this work, I express my deepest gratitude and sincere thanks.

Content

Abbreviations and symbols

i. ADSCs: Human adipose-derived mesenchymal stem cells
ii. AFM: Atomic force microscopy
iii. AI: Artificial intelligence
iv. ALG: Alginate
v. BC: Bovine collagen
vi. BDNF: Overexpress brain-derived neurotrophic factor
vii. BM-MSCs: Bone marrow-derived mesenchymal stem cells
viii. BMP-2: Bone morphogenetic 2
ix. BSA: Bovine serum albumin
x. BTE: Bone tissue engineering
xi. BTE: Behind-the-ear
xii. CAD: Computer-aided design
xiii. CHI: Chitosan
xiv. CLSM: Confocal laser scanning microscopy
xv. CM: Cardiomyocyte
xvi. CMW: Critical molar mass
xvii. CNC: Cellulose whisker nanocrystals
xviii. CNF: Cellulose nanofibers (Nanofibrillated cellulose)
xix. CNS: Central nervous system
xx. CNT: Carbon nanotubes
xxi. CrI: Crystallinity index
xxii. CS: Chitosan
xxiii. CS–HA: Chitosan-hyaluronic acid
xxiv. Đ: Polydispersity index
xxv. D_2O: Deuterium oxide
xxvi. DA: Degree of acetylation
xxvii. DAPI: 4′,6-Diamidine-2′-phenylindole dihydrochloride
xxviii. DAT: Decellularized adipose tissue
xxix. DBB: Droplet-based bioprinting
xxx. DPBS: Dulbecco's phosphate buffered saline
xxxi. EBB: Extrusion-based (bio)printing
xxxii. ECM: Extracellular matrix
xxxiii. EDC: 1-Ethyl-3-(3-dimethylaminopropyl)carbodiimide

xxxiv. EDTA: Ethylenediaminetetraacetic acid
xxxv. f_H: Herman's orientation factor
xxxvi. FPT: Freeze–pump out–thawing
xxxvii. FTIR: Fourier-Transform Infrared
xxxviii. GAL: β-Galactosidase
xxxix. GelMA: Methacrylated gelatin
xl. GlcN: Glucosamine
xli. GlcNAc: N-Acetyl-glucosamine
xlii. hASCs: Human adipose-derived stem cells
xliii. HMW:High molecular weight
xliv. HPLC: High-performance liquid chromatography
xlv. IR: Infrared
xlvi. LAB: Light-assisted bioprinting
xlvii. LMW: Low molecular weight
xlviii. MALLS: Multi-angle laser light scattering
xlix. MSCs: Mesenchymal stem cells
l. MTT: 3-[4,5-Dimethylthiazol-2-yl]-2,5 diphenyl tetrazolium bromide
li. Mw: Molecular mass
lii. NHS: N-Hydroxysuccinimide
liii. NIH 3T3: Cells for sarcoma and leukemia virus
liv. NMR: Nuclear magnetic resonance
lv. NSCs: Neural stem cells
lvi. NT3: Neurotrophin-3
lvii. NTE: Nerve tissue engineering
lviii. PG: Polyglycerol sebacate
lix. PVA: Polyvinyl alcohol
lx. RT: Room temperature
lxi. SAXS: Small-Angle X-ray scattering
lxii. FBS: Fetal bovine serum
lxiii. SEC: Size exclusion chromatography
lxiv. SEM: Scanning electron microscopy
lxv. SR: Schopper-Riegler
lxvi. STE: Skin tissue engineering
lxvii. SWCNTs: Single-walled carbon nanotubes

lxviii. TE: Tissue engineering
lxix. TEM: Transmission electron microscopy
lxx. TGA: Thermogravimetric Analysis
lxxi. TPP: Sodium tripolyphosphate
lxxii. UV: Ultraviolet
lxxiii. VTE: Vascular tissue engineering
lxxiv. NTE: Nerve Tissue Engineering
lxxv. PEC: Polyelectrolyte complexation
lxxvi. XRD: X-ray diffraction

1. Introduction and Motivation

The ability to engineer biomaterials that recapitulate the architecture and functionality of native tissues represents one of the foremost challenges in regenerative medicine. Biological tissues exhibit an intricate interplay between structural hierarchy, dynamic mechanical properties, and tightly regulated biochemical signaling. In particular, the extracellular matrix (ECM) provides a compelling paradigm for such complexity: it is commonly a fiber-filled hydrogel, possesses hierarchical microstructure, viscoelastic behavior, molecular gradients and the capacity to transmit both mechanical and biochemical cues that regulate cell behavior. Despite significant advances, the field of engineering functional biomaterials and tissues still needs further progress in the design, processing and properties of materials that can integrate those tissue native features in a predictable and tunable manner, especially within hydrated three-dimensional (3D) mimicking environments relevant to tissue regeneration, in order to advance applications into the clinics. This unmet need to define a critical barrier to progress in fiber/hydrogel tissue engineering, where clinical translation increasingly requires biomaterials that are not only biocompatible but also structurally robust, adaptable across a range of tissue types, bio-mechanically functional and possibly bioactive.

Current ECM bioinspired strategies, including for example collagen-based hydrogels, glycosaminoglycan-based hydrogels, self-assembly of polypeptides, hybrid organic–inorganic composites, have advanced the state of the art but remain limited in one or more essential dimensions. Collagen systems, while biologically relevant, suffer from batch variability, poor mechanical strength, and limited control over fibrillar structure. Synthetic polymers offer tunability but often lack native bioactivity. Biomineralized composites, even if extensively used in bone tissue regeneration approaches, can improve stiffness but may compromise processability or cell compatibility. In many cases, softer hydrogels are required for target soft tissues like the neuronal.

Consequently, some research questions persist:

How can we design bioinspired fiber/hydrogel materials of modulated stiffness that simultaneously achieve structural fidelity, mechanical robustness for the target application, biochemical functionality, and manufacturability?

Addressing these challenges requires new strategies that unite controlled physicochemical behavior with reproducible processability and favorable mechanical, biological properties.

Within this context, chitosan offers unique advantages. As a naturally derived polysaccharide with structure resembling that of glycosaminoglycans, the chitosan forms ECM-like hydrogels, exhibits intrinsic biocompatibility, biodegradability and is bioactive, constituting a signaling

molecule that promotes cell adhesion and proliferation [1-4]. Chitosan biofunctionality has already motivated extensive research in wound healing, bone repair, cartilage regeneration, and controlled release systems [5-9]. Importantly, chitosan polycationic nature allows for electrostatic interactions with proteins, DNA, and other biomolecules, enabling promising tunability for therapeutic delivery and bioactive modulation. Despite these strengths, however, chitosan remains significantly constrained by several intrinsic limitations that prevent its widespread utility in structurally demanding or clinically oriented applications.

The primary limitation is its restricted solubility in neutral aqueous pH compatible with cells. Chitosan solubility is generally confined to a pH range between 3 and 6 [10-13]. It means, chitosan is mainly soluble in weakly acidic environments. It can limit chitosan processability into materials which processing primarily depends, on a first step, of solubilization into viscous polymer systems. This significantly complicates the blending with neutral-pH biomaterials and the incorporation of pH-sensitive bioactive agents. In many cases, the resulting systems exhibit non-uniform microstructure, poor dispersion of reinforcement components, and pH-dependent cytotoxicity. Furthermore, chitosan hydrogels lack sufficient mechanical strength, particularly in those highly hydrated conditions where swelling exacerbates structural instability. This compromises their suitability for load bearing or mechanically demanding tissues such as cartilage, tendon, intervertebral disc, bone. Additional challenges include batch-to-batch variability in chitosan molecular weight (Mw) and degree of acetylation (DA), which lead to unpredictable mechanical and biological outcomes, as well as uncontrolled degradation rates depending on Mw and DA that may not align with tissue remodeling timelines. These persistent barriers underscore a pressing need for strategies capable of improving chitosan physicochemical behavior while preserving or improving its biological properties.

Biological tissues often display directional anisotropy, which often determines their mechanical, structural, and functional performance [14-17]. For example, in tissues such as tendon and ligament, collagen fibers are highly aligned at the microscale, forming fascicles and bundles that provide exceptional tensile strength in the direction of physiological loading [18, 19]. The intricate organization, from nanoscale collagen fibrils to macroscale architecture, allows tissues to perform under complex physiological conditions while maintaining structural integrity. Replicating such anisotropy and complex functionality represents one of the major challenges in the field of tissue engineering. This thesis aims to develop hierarchically and anisotropic materials useful for tissue engineering and repair, focusing on the integration of structural design, processing of innovative materials and their characterization in real time during processing, as well as the assessment of mechanical and biological functionality.

A promising approach involves the reinforcement of chitosan hydrogels with cellulose nanofibers (CNFs) [20], which nanoreinforcement possess exceptional tensile strength, high crystallinity, and inherent biocompatibility [21]. Cellulose nanofibers have attracted growing

interest also due to their abundance, sustainability, and ability to form highly entangled, mechanically robust networks. Their nanoscale dimensions enable intimate interactions with chains of polymeric matrices, offering significant potential for enhancing mechanical properties, stabilizing hydrated structures like hydrogels, and contributing to hierarchical organization within composite materials [22]. Early studies have demonstrated that these nanofibers can reinforce a range of polysaccharides. However, fundamental questions remain regarding their interactions with chitosan, particularly in 3D architectures relevant to bioprinted constructs useful in tissue engineering. Specifically, the mechanisms by which cellulose nanofibers content and morphology, their alignment and distribution influence structure–function relationships within chitosan matrices are not well understood. This absence of mechanistic insight limits the rational design of optimized anisotropic fiber/hydrogel materials and restricts the translation into reproducible, clinically relevant constructs.

The thesis seeks to address these gaps by developing and systematically investigating chitosan–cellulose nanofiber composite systems of modulated macromolecular structure and composition across multiple length scales, using fabrication methods involving microextrusion, gel spinning and 3D (bio)printing. Our central premise is that cellulose nanofiber reinforcement, if properly understood and controlled, can overcome longstanding limitations associated with chitosan, most notably its inadequate mechanical stability and challenges in structural organization, while preserving its biological advantages. The overarching objective is therefore to define how cellulose nanoreinforcement modulates mechanical behavior, microstructural architecture, and biological performance in chitosan-based materials, and to leverage this knowledge to design improved ECM-bioinspired scaffolds.

To accomplish this goal, we propose an interconnected three-part experimental research strategy. Firstly, we will systematically evaluate the influence of cellulose nanofiber incorporation on the mechanical performance of chitosan-based fibers processed by gel spinning, using both low and high molecular weight chitosans. This comparative approach will allow us to elucidate the molecular weight dependent mechanical performance governing stiffness, strength, and strain at break of the composite fibers. Secondly, we will examine cellulose nanofiber and chitosan chains alignment, interaction, and distribution within chitosan-based inks in situ during 3D printed hydrogels by microextrusion. The understanding of how processing parameters such as shear stress, chitosan concentration, cellulose nanofiber morphology and content affect nanoscale and microscale organization is essential for controlling the hydrogel composite microstructure and properties. Finally, we will assess the biological performance of 3D-bioprinted chitosan-based hydrogel scaffolds containing encapsulated cells, providing insight into their spatio-resolution in 3D biomaterials, cytocompatibility, stability and suitability for tissue engineering applications.

Collectively, this work addresses a critical barrier to the advancement of bioinspired materials by establishing a mechanistic foundation for the design of cellulose nanofiber-reinforced chitosan scaffolds. The proposed research not only seeks to enhance the mechanical and structural performance of chitosan-based systems but also aims to generate broadly applicable principles for engineering ECM-mimetic materials with improved predictability and translational potential. By integrating materials science, multiscale characterization, and biofabrication, this research paves the way for advanced scaffold platforms consisting of bioactive, biocompatible, bio-based and anisotropic materials for tissue regeneration, to advance the transfer into the clinics.

2. State of the Art and Theoretical Background

This chapter discusses the state of the art in the field of bioinspired fibers, hydrogels and composite biomaterials in the context of fiber-reinforced and anisotropic biological materials and tissue engineering applications. It discusses recent advances in the design, processing and characterization of hydrogels, with particular emphasis on polysaccharides like chitosan and cellulose, and the use of nanofibers in the reinforcement of composites. The chapter discusses the existing challenges as well as theoretical background related to material processing, physical chemistry behavior, mechanical and biological properties, to identify the research questions in the development of functional biocompatible and bioactive materials for biomedical engineering.

2.1. Recreating Nature Architecture: Emerging Technologies for the Development of Hierarchical and Anisotropic Tissue Constructs

Native biological tissues display remarkable hierarchical organization and directional anisotropy, which together determine their mechanical, structural, and functional performance. In musculoskeletal tissues such as tendon and ligament, collagen fibers are highly aligned at the microscale, forming fascicles and bundles that provide exceptional tensile strength in the direction of physiological loading. In contrast, bone exhibits mineralized lamellae organized in a gradient fashion, creating a structure that is simultaneously strong and tough across multiple length scales. This intricate organization, from nanoscale collagen fibrils to macroscale architecture, allows tissues to perform under complex physiological conditions while maintaining structural integrity. Replicating such complexity represents one of the most formidable challenges in the field of tissue engineering. However, recent advances in materials science, biofabrication, and cellular mechanobiology have significantly advanced our ability to recapitulate these biological design principles. This review highlights emerging technologies that enable the fabrication of hierarchical and anisotropic tissue constructs, focusing on the integration of structural design, material innovation, and biological modulation.

The structural hierarchy of biological tissues encompasses multiple scales, from nanoscale extracellular matrix (ECM) fiber alignment and cellular organization to microscale vascular networks and macroscale morphology. Anisotropy in these tissues arises from the directional deposition of ECM components, cell alignment, and mechanical conditioning during development and growth (Figure 2.1). For example, tendons exhibit tensile strengths 200 to 500 times greater along the collagen fiber direction compared to the transverse direction, a phenomenon directly linked to their hierarchical architecture [23]. Similarly, the lamellar orientation in cortical bone, the fascicular organization of cardiac muscle, and the nerve fiber alignment in the spinal cord all demonstrate that function is intimately tied to multiscale

structure. Understanding these relationships provides the blueprint for engineering biomimetic constructs capable of replicating native tissue performance. Recent advances in multimodal imaging, such as second harmonic generation microscopy, micro-computed tomography, and confocal Raman spectroscopy, combined with computational modelling, now allow precise mapping of hierarchical features across scales [24]. Such quantitative insights into natural architectures guide the rational design of scaffolds and inform biofabrication parameters aimed at recapitulating native anisotropy.

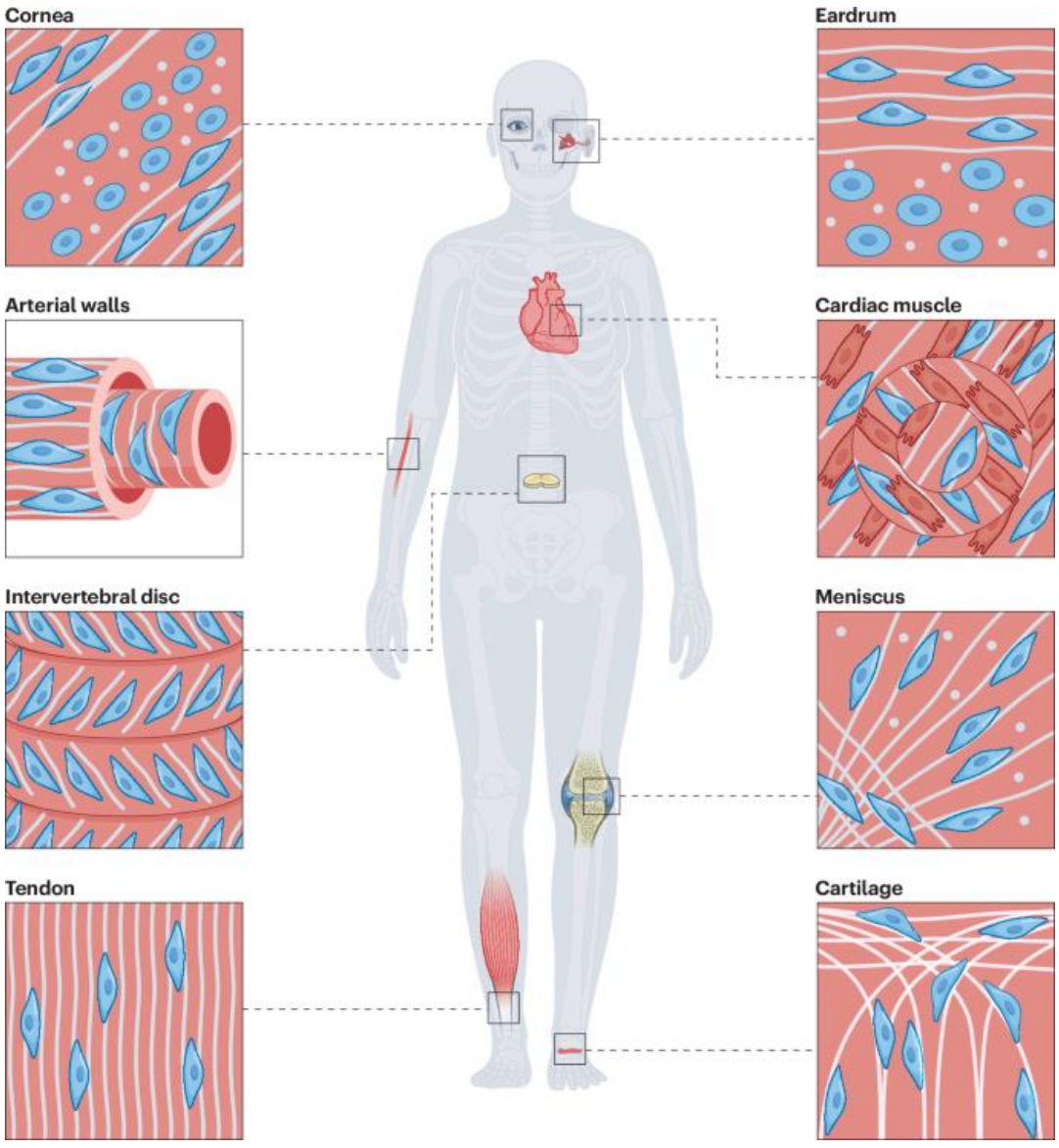

Figure 2.1. Schematic representation of cell and extracellular matrix structural organization at the microscopic scale in vivo. Reproduced with permission from De Mulde et. al., 2009 [24].

Material design is central to reproducing the hierarchical complexity of native tissues. Composite biomaterials that combine natural and synthetic polymers have been extensively investigated to achieve spatial control over stiffness, porosity, and degradation rates (Figure 2.2). These materials allow the creation of stiffness or compositional gradients that reflect those

present in heterogeneous tissues such as osteochondral or tendon-bone interfaces [25]. Aligned nanofibrous scaffolds fabricated via electrospinning or melt-electrowriting provide topographical cues that guide cellular alignment and promote anisotropic ECM deposition (Figure 2.3) [26]. Patterned hydrogels with micro-grooved surfaces or oriented pores have similarly been shown to enhance osteogenic differentiation by directing cytoskeletal organization.

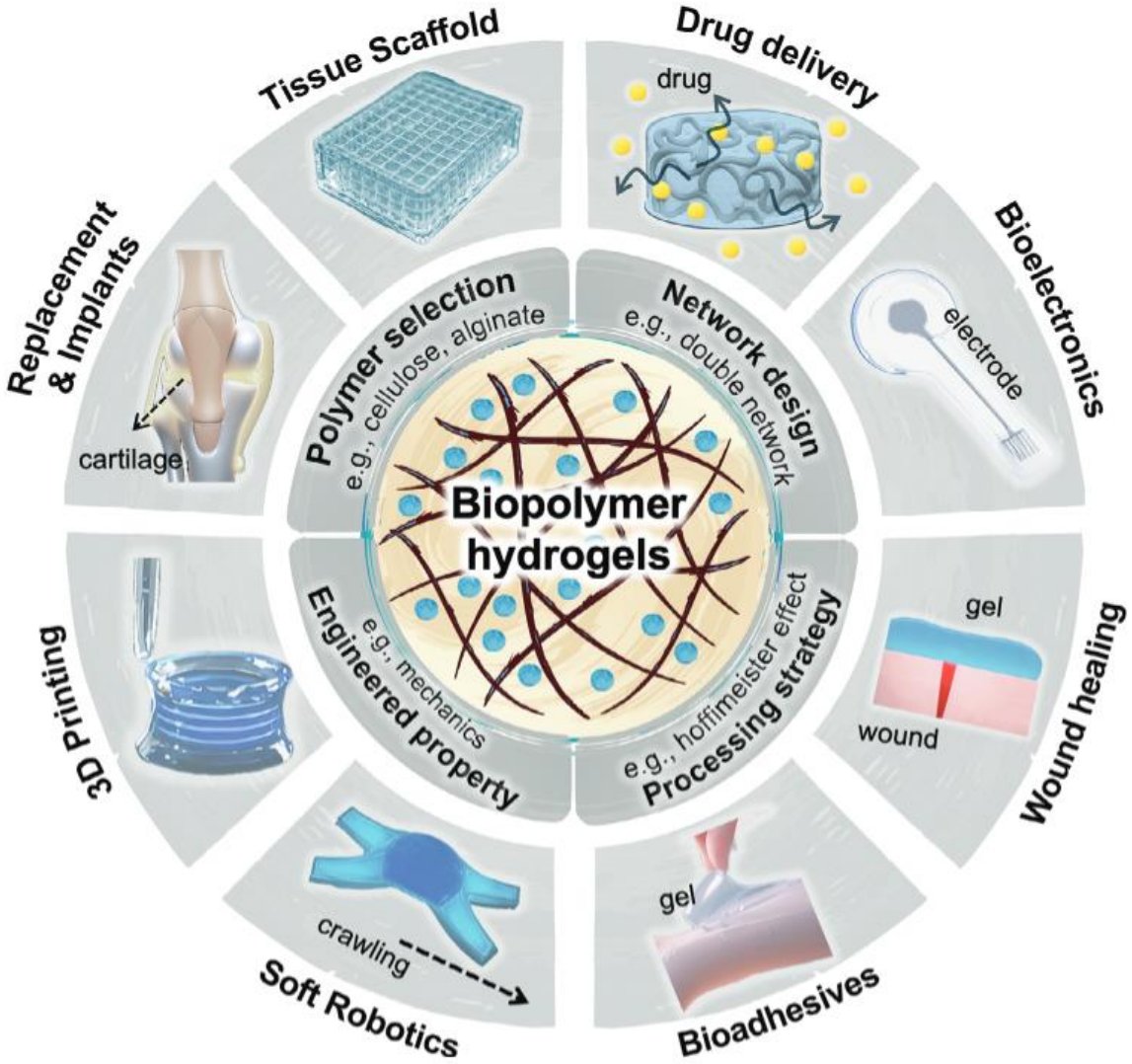

Figure 2.2. Schematic illustration of the biopolymer-based hydrogel design-to-application pipeline. Reproduced with permission from Mostert et. al., 2025 [25].

Beyond structural mimicry, new generations of dynamic and self-assembling biomaterials are enabling temporal evolution of hierarchical features. Self-assembling peptide hydrogels, for example, spontaneously organize into fibrillar networks that resemble native ECM architecture and can be tuned to evolve over time [27]. Magnetically responsive and light-triggered hydrogels offer further opportunities to induce or adjust anisotropy post-fabrication through non-contact stimuli [28]. Collectively, these advances demonstrate that achieving biomimetic

function requires materials that not only support cellular viability but also provide instructive, multiscale structural and mechanical cues that evolve dynamically as the tissue matures.

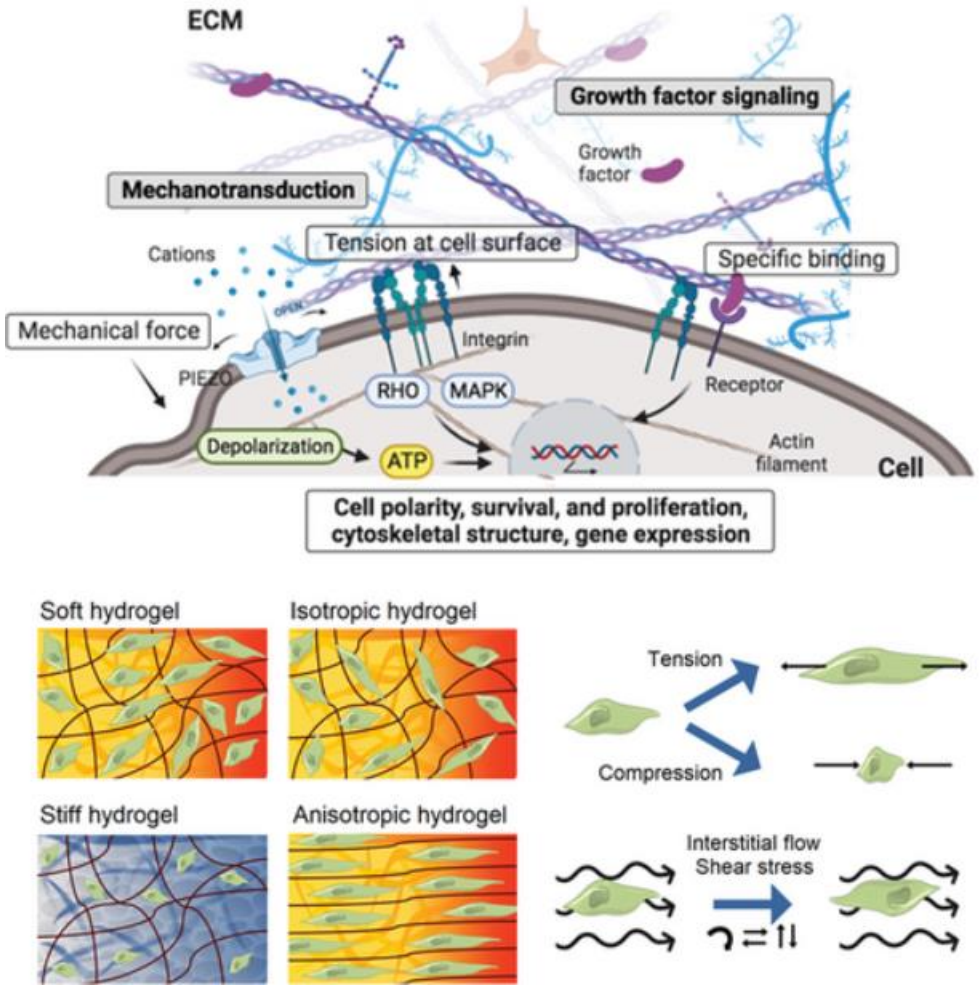

Figure 2.3. Representation of the most relevant mechanosignaling mechanisms involved in the interaction between fibrillar ECMs and resident cells. Reproduced with permission from Zhang et. al., 2020 [26].

The emergence of advanced biofabrication technologies has revolutionized our capacity to engineer tissues with defined hierarchies and anisotropies. Electrospinning and melt-electrowriting techniques generate aligned micro- and nanofibrous networks that replicate the anisotropic ECM architecture of connective tissues. These fibrous scaffolds have been shown to enhance alignment and contractility of induced pluripotent stem cell-derived cardiomyocytes, thereby improving their physiological function [26]. Three-dimensional (3D) and four-dimensional (4D) bioprinting further extend this control by allowing spatial deposition of multiple bioinks with gradient mechanical and biochemical properties across scales. Such approaches have successfully recreated tendon-like and cartilage-bone interfaces, in which anisotropy and hierarchical transitions are essential for mechanical integrity.

Microfluidic and soft lithography techniques enable patterning of biochemical gradients and microchannel networks that mimic the vascular hierarchies of native tissues [25, 27]. Meanwhile, non-contact assembly methods, such as acoustic, magnetic, and light-based

patterning, allow dynamic orientation of both cells and ECM components. Magnetically aligned hydrogels containing anisotropic nanocomposites have recently been used to direct cell alignment and tissue regeneration [28]. Integrating these fabrication strategies allows researchers to generate constructs with structural fidelity spanning multiple length scales, from nanofibrillar alignment to macroscopic tissue geometry, bringing engineered tissues closer to their native counterparts.

While structural design provides the foundation, the behavior of resident cells ultimately determines the success of hierarchical and anisotropic tissue engineering. Cells sense and respond to their microenvironment through mechano-transduction pathways that convert physical cues into biochemical signals. Substrate stiffness, topographical alignment, and mechanical strain are key regulators of cell polarity, migration, and ECM production. The phenomenon of contact guidance, in which cells align along micro- or nano-patterned substrates, is particularly important in generating anisotropy within engineered tissues. Dynamic bioreactors that apply cyclic strain or shear stress have been shown to further enhance cellular alignment and functional maturation.

Self-organizing systems such as organoids and cell-sheets add a biological dimension to structural design, enabling tissues to assemble hierarchically through collective cellular behavior. Combining these systems with external mechanical cues or anisotropic scaffolds leads to the emergence of highly organized, functional constructs. At tissue interfaces, such as tendon-to-bone junctions, hierarchical hydrogels with graded chemical and mechanical properties can direct spatially distinct differentiation of multiple cell types, recreating the complex transition zones observed in vivo [29]. Thus, the integration of biophysical and biochemical guidance is essential for achieving structurally and functionally anisotropic tissue regeneration.

The next frontier in hierarchical and anisotropic tissue engineering lies in the seamless integration of advanced biofabrication, smart materials, and biological self-organization. Computational design frameworks and artificial intelligence (AI)-assisted modelling are increasingly being employed to optimize scaffold architecture and predict cellular outcomes, bridging the gap between design parameters and biological performance. Dynamic, adaptive biomaterials that can remodel or respond to environmental stimuli represent a major step toward engineered tissues that behave like living systems. In parallel, scalable manufacturing technologies must be developed to reproduce complex architectures, consistently and cost-effectively, while meeting regulatory standards.

Another critical challenge remains the vascularization and innervation of large, anisotropic constructs. Hierarchically organized vascular networks are vital for nutrient delivery and metabolic function in thick tissues, while anisotropic neural integration is essential for musculoskeletal and cardiac function. Hybrid fabrication approaches that combine top-down

structuring (e.g., 3D printing) with bottom-up self-assembly (e.g., cell aggregation or ECM deposition) are likely to yield the most faithful replicas of native tissues. Emerging 4D fabrication methods that exploit shape-morphing or stimuli-responsive mechanisms further offer the ability to dynamically evolve tissue architecture post-implantation [30]. As these technologies mature, they will collectively enable the creation of living, adaptive tissues that truly recreate nature's blueprint.

2.2. From Anisotropic Tissues to Natural Architectures and Actuator Materials

In tissue engineering, the deliberate design of anisotropic scaffolds seeks to recapitulate the direction-dependent mechanical environment of native tissues (e.g., tendon, myocardium, nerve), because cells sense and respond to directional stiffness, porosity, and topography [31, 32]. Extending this design perspective beyond mammalian tissues to plants and other organisms reveals a broader set of structural strategies and actuation mechanisms that can enrich tissue-engineering approaches and inspire new actuator materials.

Plants and many non-mammalian organisms employ anisotropic micro- and nano-architectures to achieve multifunctionality. Plant cell walls, for example, rely on oriented cellulose microfibrils embedded in a matrix of hemicellulose and pectin; the angle of fibril deposition determines axial versus circumferential stiffness and controls growth anisotropy and movement (bending, twisting) in response to environmental cues (Figure 2.4) [33]. Seed pods, pinecones and some fungal structures exploit layered, bilayer, or gradient anisotropy to produce predictable hygroscopically driven shape changes: swelling or drying of discrete layers with different orientation or composition leads to bending and opening without metabolic energy. In animals, exoskeletons and integuments (e.g., insect cuticle, fish scales, cephalopod skin) frequently exhibit graded fiber orientations or laminate arrangements that balance flexibility, toughness, and directional strength. These natural motifs (aligned fibers, bilayers, gradients, and hierarchical orientation) provide blueprints for designing materials whose properties vary with direction and position.

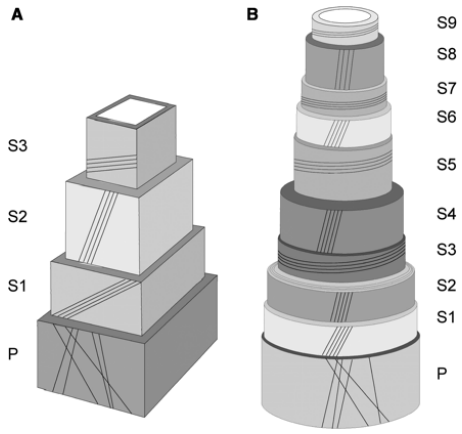

Figure 2.4. Schematic drawings of the organization of the cell wall in (**A**) wood fiber and (**B**) sclerenchymatic fiber of a monocotyledonous plant (bamboo) after Parameswaran and Liese. The orientation of cellulose microfibrils is indicated by black lines. Reproduced with permission from Cong et. al., 2024 [33].

Anisotropic architectures translate into specific mechanical signatures: directional stiffness (modulus variation with orientation), anisotropic strength and toughness (fracture paths guided by fiber orientation), controlled viscoelastic response (direction-dependent damping and relaxation), and spatially varying permeability or diffusivity [34]. At the microscale, fiber or fibril alignment concentrates load along preferred paths, improving tensile performance along the fiber axis while permitting compliance transverse to it; at the mesoscale, laminated or helicoidal stacking can deflect and dissipate cracks, increasing toughness. In hydrated, polymeric matrices (e.g., plant cell walls, hydrogels), anisotropic arrangement of reinforcing elements converts isotropic swelling into directional deformation, enabling large, predictable shape changes under modest stimuli.

Several biological actuation strategies explicitly exploit anisotropy. Hygroscopic actuation, which is ubiquitous in plants and some fungi, arises from anisotropic swelling: layers with orthogonal microfibril orientations swell differentially with moisture, producing bending or twisting motions (e.g., pinecone scales, seed dispersal mechanisms) [35]. Muscular-based actuation in animals similarly relies on anisotropic tissue architectures: aligned contractile fibers (muscle fascicles) produce force and directional shortening; connective-tissue anisotropy guides deformation and transmits force efficiently [36]. Other mechanisms include osmotic or turgor-driven movement in plants (direction set by cell-wall anisotropy) and the anisotropic propagation of strain waves in locomotory appendages. These natural actuators combine structural anisotropy with localized stimulus–response coupling to generate reliable, repeatable motion.

Materials scientists and soft-robotics researchers have translated these principles into engineered actuators by programming anisotropy at multiple scales. Examples include aligned-fiber hydrogels that bend or curl upon swelling; liquid crystal elastomers (LCEs) with

orientational order that contract or twist along the director when thermally or optically stimulated; and composite bilayers or gradient laminates where mismatch in anisotropic expansion produces curvature [37-39]. Fabrication methods such as directional electrospinning, extrusion 3D printing with controlled filament orientation, magnetic or electric field alignment of fillers, and layer-by-layer assembly enable deterministic control of anisotropy. Importantly, the same anisotropic strategies that enhance mechanical performance (load bearing along fibers, graded toughness) also create programmable, directional actuation when coupled with an appropriate stimulus.

Bridging tissue engineering and actuator design highlights two synergistic opportunities. First, tissue-engineered constructs can benefit from actuator-inspired anisotropy to create dynamic, mechanically active grafts or in vitro models that reproduce not only the static anisotropic stiffness but also stimulus-responsive deformation (e.g., scaffolds that change curvature under hydration or temperature to mimic morphogenetic forces). Second, tissue-informed anisotropic design principles, namely hierarchical orientation, graded mechanics, and multifunctional laminates, can improve artificial actuators by enhancing durability, energy efficiency, and complex motion profiles while maintaining biocompatibility for biomedical soft robotics or implantable devices. For example, incorporating helicoidal fiber arrangements or fracture-deflecting lamellae into soft actuators can increase fatigue life and prevent catastrophic failure under cyclic loading.

Key challenges remain in the precise, multiscale programming of anisotropy and in linking structure to cell-level mechanobiology under dynamic actuation. Fabrication techniques need to achieve simultaneous control of orientation, gradient, and local chemistry at tissue-relevant scales while preserving viability (for living constructs) or repeatability (for synthetic actuators). Quantitative models that couple anisotropic mechanics with stimulus–response kinetics are required to predict complex deformations and to design scaffolds that direct cell behavior under dynamic loading. Finally, integrating sensors and closed-loop control into anisotropic actuator–tissue hybrids will enable adaptive systems that can mimic biological feedback mechanisms.

2.3. Material Matters: How Bioinspiration is Redefining the Future of Tissue Engineering

While advances in fabrication and mechanobiological strategies have provided the structural and functional framework necessary to engineer hierarchical and anisotropic tissues, the true success of these constructs ultimately depends on the choice of material. Materials not only serve as passive scaffolds but actively dictate cellular behavior, matrix deposition, and long-term tissue integration. Nature itself provides an exceptional library of design principles, ranging from the viscoelastic resilience of cartilage and the mineral–collagen composite of bone to the fibrous anisotropy of tendon, that offer inspiration for synthetic and hybrid

biomaterial development. Translating these natural blueprints into engineered analogues requires a careful balance between biological recognition, mechanical competence, and controllable degradation. Therefore, the next critical step toward recreating nature's complexity lies in identifying and designing bioinspired materials that can both emulate native extracellular environments and interface harmoniously with advanced fabrication technologies.

Chitosan, a biopolymer generated from chitin, has progressed from a relatively unknown natural substance to a key participant in a variety of sectors. Chitosan, with its unique qualities such as biodegradability, biocompatibility, and non-toxicity, has found applications ranging from healthcare and food science to environmental sustainability. The increased interest in sustainable materials, combined with a greater emphasis on health and environmental protection, has accelerated research and development in chitosan-based applications. The most recent advances in chitosan research, revealing innovative aspects and trends, especially in tissue engineering, will be discussed in the next part of literature review.

2.4. Chitosan: Nature's Gift to Modern Biomaterials Science

Chitin and its deacetylated derivative, chitosan, are a family of linear polysaccharides comprised of β(1→4) linked residues of N-acetyl-2 amino-2-deoxy-D-glucose (glucosamine, GlcN) and 2-amino-2-deoxy-D-glucose (N-acetyl-glucosamine, GlcNAc) [1, 2, 40, 41]. Chitosan is soluble in aqueous acidic media through primary amine protonation. In contrast, chitin has a significant number of acetylated residues (higher degree of acetylation), which prevents the polymer from dissolving in aqueous acidic environments [42]. Despite their versatility and marketability globally, chitin and chitosan have only been industrially extracted from crustaceans and fungi [43]. Every year, over a thousand billion tons of chitin are reported in the biosphere [44]. Chitin and chitosan have been extensively studied due to their unique biological, chemical, and physical properties and applications [45-47]. For years, crab and shrimp shells have been the primary source of chitin and chitosan. However, isolating chitin and chitosan from fungi's cell walls resulted in reduced waste and allergenic chemicals, prompting further research. This also paved the way for numerous biotechnological uses [48, 49].

Chitin exists in nature in three distinct crystalline forms: α-chitin, β-chitin, and γ-chitin. According to Kaur et al., polysaccharide chains in chitin are organized in an antiparallel manner, allowing for maximal bonds [50]. Among these, α-chitin is the most prevalent, characterized by anti-parallel polymer chains, which contribute to its rigidity and structural strength, leading to high crystallinity chitin fibrils (80 percent) [51, 52]. This form is predominantly found in the exoskeletons of crustaceans like crabs and shrimp (Figure 2.5 and 2.6). In contrast, β-chitin consists of parallel polymer chains that form monoclinic crystals, stabilized by both intra- and intermolecular hydrogen bonding. This structure is typically found in natural materials such as squid pens, diatom spines, and pogonophoran tubes. Polymer chains are also linked together to form arrangement in β-chitin, and the crystallinity index of chitin fibrils is about 70%. This type is much more sensitive and dissolves in solvents due to the greater gap across neighboring polymer chains [53]. γ-chitin features a combination of both parallel and anti-parallel chains, blending characteristics of the α and β forms. It is generally found in sources such as fungi, yeast, and insect cocoons [54, 55]. Chitin derived from organisms with hard exoskeletons, such as crustaceans, invertebrates, and arthropods, is most often in the α-form due to its tightly packed structure, which results from strong hydrogen bonding between anti-parallel chains. The β-form, being composed of parallel chains, is mainly found in mollusks like squids [56]. γ-chitin, which has two parallel and one anti-parallel chain, is mostly associated with insect cocoons. While α-chitin can be converted into β-chitin under certain conditions, the reverse transformation is not possible. The crystallinity, purity, and

polymer chain structure of chitin can vary significantly depending on its biological source and the proportion of chitin present in the raw material.

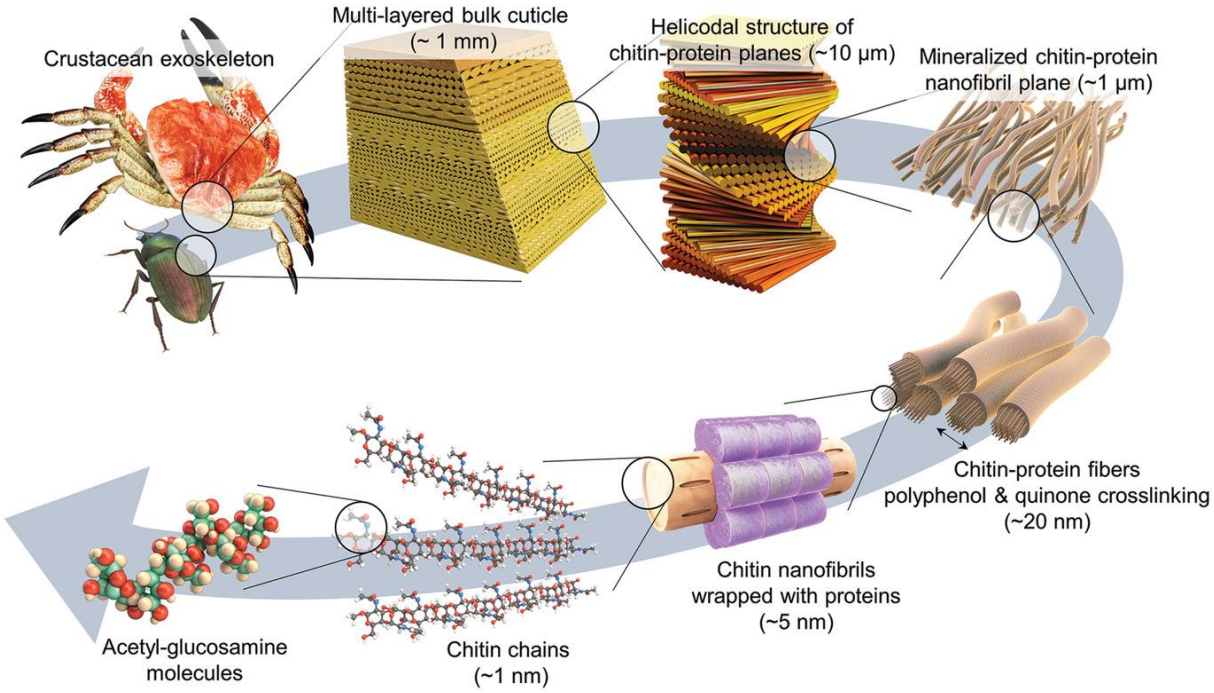

Figure 2.5. Physical structure of chitin in nature. Reproduced with permission from Lee et. al., 2022 [57].

In a prior study, chitin and its derivative chitosan were discovered to exhibit structural similarities to heparin, chondroitin sulfate, and hyaluronic acid - key mucopolysaccharides which are required for mammalian biology. These naturally occurring mucopolysaccharides are anionic due to the presence of carboxyl and sulfate groups. In contrast, chitosan is one of the few naturally occurring cationic polysaccharides. It is biocompatible, non-toxic, and biodegradable in humans, making it ideal for biomedical applications. However, its applicability in such applications is limited due to its low solubility in neutral or moderately aqueous environments. To overcome this limitation, chitosan can be chemically modified to enhance its solubility at physiological pH levels (around pH 7 and above). These modifications also enable the attachment of various functional groups, thereby allowing control over its ionic character (cationic or anionic) and hydrophobicity, which are critical for tailoring its biomedical functionality.

Studies on the physical and chemical structures of chitosan have revealed that it is a linear polysaccharide composed of alternating deacetylated and acetylated d-glucosamine units linked by (1, 4) glycosidic bonds. The process of deacetylating chitin involves the removal of the acetyl group, resulting in the formation of free $-NH_2$ group [2]. The degree of acetylation in chitosan is typically determined by the ratio of glucosamine to N-acetyl glucosamine. Chitin contains a higher proportion of N-acetyl glucosamine, while chitosan is characterized by a

greater proportion of glucosamine. The degree of acetylation (DA) significantly influences both the chemical and biological properties of chitosan. Chemically, it affects characteristics such as tensile strength, solubility, surface area, viscosity, conductivity, porosity, and flexibility. Biologically, it impacts properties like adsorption enhancement, biodegradability, antioxidant activity, bioavailability, and biocompatibility, depending on the specific conditions of the experiment.

Furthermore, chitin and chitosan have relatively high nitrogen levels, typically ranging from 2% to 8%, which makes them appealing for a variety of industrial applications. Due to its rigid crystalline structure and significant intra- and intermolecular hydrogen bonding, chitin is insoluble in water and most organic solvents. Chitosan, on the other hand, is readily soluble in weakly acidic aqueous media such as hydrochloric, citric, and acetic acids at pH values less than 6. Chitin's rigidity and poor solubility have limited its practical usage as compared to chitosan, which has more flexibility and better solubility properties.

The physicochemical properties of chitin and chitosan have a major influence on their applications. Because of its high number of acetyl group, chitin has limited uses, however it can be deacetylated to produce chitosan. The acetyl group in chitin is converted into amino group (-NH2) in chitosan throughout the deacetylation procedure. Modifying the reactive functional groups in chitosan allows for a variety of applications. Chitin has limited solubility and is insoluble in most solvents. In comparison to chitosan, chitin’s solubility challenge limits its application and uses in various fields.

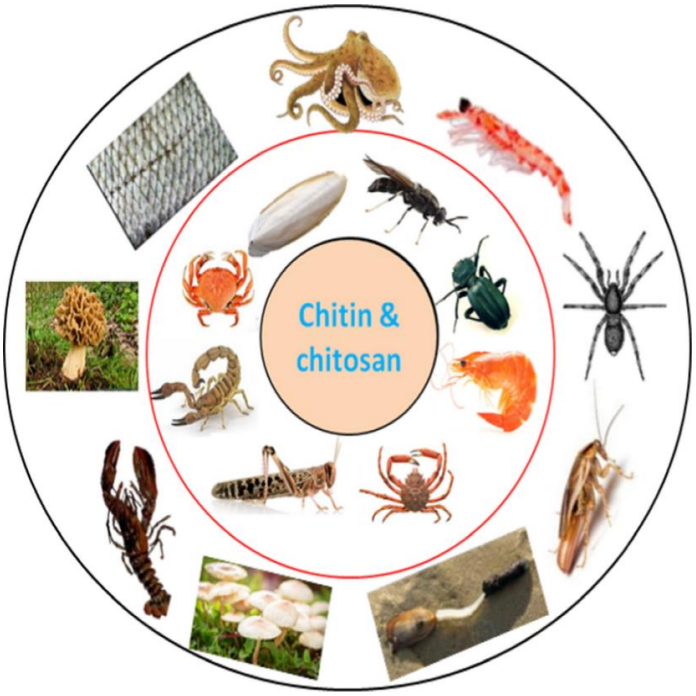

Figure 2.6. Natural sources of chitin and chitosan. Reproduced with permission from Hamdan et. al., 2022 [58].

Chitin and chitosan are highly efficient and promising biopolymers with varying physicochemical properties based on source and extraction procedure. There is no unique process for chitin manufacturing, hence numerous experiments have been undertaken to produce natural chitin without changing the physicochemical properties of the biopolymer. Chitin is commonly synthesized through established chemical or biotechnological processes that utilize fish waste as a low-cost and renewable feedstock. Additionally, the purification of chitin generates by-products rich in calcium carbonate or proteins, which can be further processed, thereby enhancing the overall economic viability of chitin production. In contrast, chitosan which is characterized by a lower molecular weight and degree of acetylation compared to chitin, is typically obtained via chemical deacetylation of chitin. The transformation process requires the application of a highly concentrated alkaline solution under elevated temperatures, rendering it environmentally unsustainable. To encourage a more sustainable approach to chitosan synthesis, chitin deacetylation under mild circumstances is advised. The possibility of a cost-effective production process reinforces the growing belief that chitosan holds more promise than chitin.. Chitosan has a greater range of applications than chitin, owing to its increased abundance of amine groups, lower intermolecular tensions, and solubility in acidic aqueous conditions. In contrast, chitin limited solubility, which reduces leaching and allows for repeated usage in a variety of settings, remains a unique feature.

The production of chitin and chitosan typically involves four fundamental processing steps: deproteinization, demineralization, decolorization, and deacetylation (Figure 2.7). Deproteinization is the removal of proteins using a strong alkaline solution, whereas demineralization is the elimination of calcium carbonate and calcium phosphate using a strong acid. Pigment removal and the conversion of chitin to chitosan are known as decolorization and deacetylation, respectively. Decolorization can be done with alcohols like ethanol, whereas deacetylation is usually done with a strong alkali, commonly sodium hydroxide (NaOH). Wang et al. [59] and Yang et al. [60] developed a method for deproteinizing crustacean chitin waste using microorganisms or proteolytic enzymes, providing a more cost-effective and ecologically friendly alternative to chitin and chitosan production. Despite this, the most used method for chitosan extraction is alkaline deacetylation of chitin with a strong alkaline solution. Prior to chemical processing, the raw material is often mechanically pretreated, which includes crushing, washing with water or detergent, and chopping. Given the variation in mineral content among exoskeleton sources, multiple evaluation methods may be required to optimize processing conditions. Regardless of the source, the deacetylation of chitin to produce chitosan remains a challenging process, primarily due to chitin’s limited solubility in most solvents. This limitation requires the use of high concentrations of sodium hydroxide and elevated temperatures. Moreover, deacetylation is often accompanied by polymer chain depolymerization, which diminishes the yield of high molecular weight chitosan

[61]. Furthermore, deacetylation under homogeneous conditions typically requires prolonged reaction times compared to heterogeneous methods, making it less suitable for industrial-scale applications [62]. In the more commonly employed heterogeneous process, chitin is treated with highly concentrated (30–50% w/v) aqueous sodium hydroxide at elevated temperatures (80–100 °C) for 1 to 2 hours. However, this moderate oxidative environment renders the glycosidic bonds highly susceptible to hydrolysis, resulting in significant polymer chain degradation. To produce highly deacetylated chitosan with high molecular weight, strategies such as conducting the reaction under an inert atmosphere (e.g., N_2 or Ar) or incorporating a reducing agent to scavenge oxygen have been proposed [63]. Additionally, repeating the deacetylation steps, with intermediate washing, isolation, and drying, has been shown to enhance deacetylation efficiency while significantly reducing the total reaction time compared to conventional methods [64]. Lamarque et al. introduced an innovative thermomechanical technique that enables the production of fully deacetylated chitosan with molecular weights around 450,000 g/mol [65]. This method incorporates vacuum freezing and thawing cycles, which improve GlcNAc site accessibility by disrupting crystalline structures and minimizing chain degradation through effective oxygen removal.

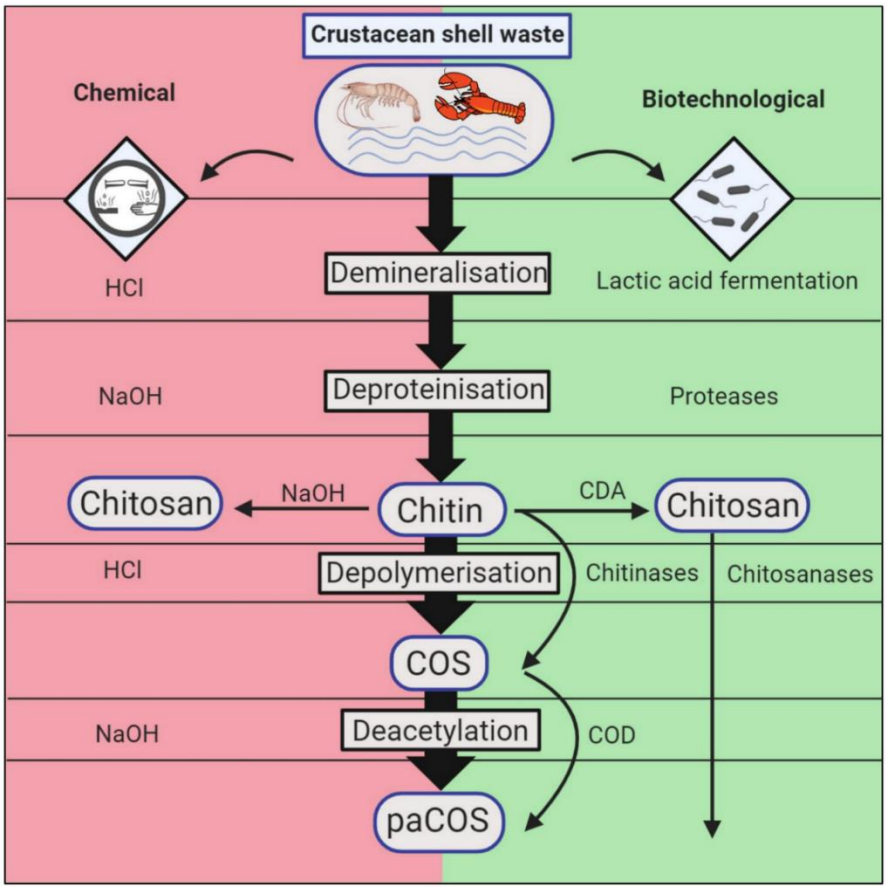

Figure 2.7. Chitin to chitosan conversion (COS: Chitooligosaccharides, CDA: Chitin Deacetylase, paCOS: pattern of acetylation). Reproduced with permission from Arnold et. al., 2020 [66].

2.5. Unveiling the Structural Fingerprint of Chitosan: Key Physicochemical Parameters and Characterization Methods

Knowledge of the distribution of repeat units, crystallinity, DA and molecular mass are very important parameters; many physico-chemical and biological properties of chitosan depend on it. We will briefly mention the techniques and methods most used to determine these characteristics in this section.

The degree of acetylation of chitosan (DA) is an important parameter that determines the physical, chemical and biological properties of chitosan. It affects the solubility, chain configuration, charge properties and biological properties of chitosan. A lower degree of deacetylation results in higher solubility in acidic media, which can be important for applications such as drugs and foods. Numerous analytical methods have been developed to determine the degree of acetylation of chitosan [67]. These include colloidal titration, potentiometry, conductometry, colorimetry, various spectroscopic techniques (such as ultraviolet (UV), infrared (IR), nuclear magnetic resonance (NMR), and mass spectrometry), chromatographic methods (including high-performance liquid chromatography (HPLC) and size exclusion chromatography (SEC), as well as thermal analysis. Among these, NMR stands out as the most widely employed technique, offering a direct, reliable, and accurate means of determining DA. Proton NMR is currently the most suitable and widely used technique for determining DA. It is still very easy to use, requires no calibration and allows precise results to be obtained using small amounts of product. Hirai et al. proposed to compare the resonance signal intensity of protons of methyl groups with that of ring protons (H2-H6'), located between 3 and 4 ppm (Figure 2.8) [68]. The degree of acetylation is then determined by the following relationship:

$$DA(\%) = \frac{\frac{1}{3} I\,CH_3}{\frac{1}{6} I\,(H_2 - H_6)} \times 100\% \qquad \text{(Eq. 2.1)}$$

The analysis is carried out at 70 °C to decrease the viscosity of the solution. The polymer is dissolved in a solution of deuterated hydrochloric acid at 0.5% (w/w) which can partially hydrolyze the acetamide function and lead to a slight doubling of the resonance peak of the methyl groups. It is then necessary to integrate the entire massif at around 2 ppm.

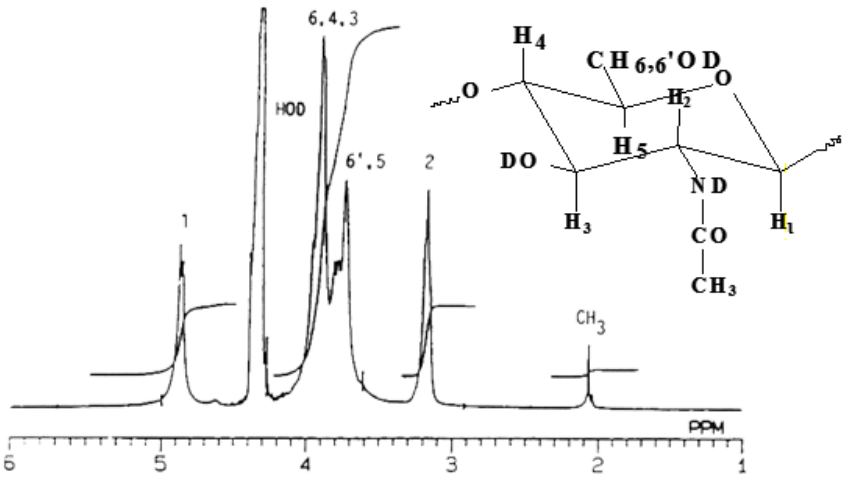

Figure 2.8. ^{1}H NMR spectra of chitosan with low DA. Reproduced with permission from Elizalde et. al., 2024 [68].

For DA > 60%, chitin solubilization can be difficult. To obtain better definition spectra, Vårum et al. propose to degrade chitins by nitrites to reduce viscosity [69]. The spectra are carried out in D2O, at pH between 3 and 4. To calculate the DA, they then use the resonance of the anomeric protons H1. As the peak area is small, the uncertainty in the final result may not be negligible. In addition, the sample preparation method is longer. The resonance of the H1 of the acetylated units is sensitive to the nature of the neighboring unit (acetylated or not), which causes the displacement of its peak and allows the determination of the distribution of the acetylated units along the chain (block or statistical), by calculating the frequency of appearance of diads.

Chitosan molecular weight significantly impacts its properties and applications. Higher molecular weight chitosan generally exhibits stronger antibacterial and bactericidal effects, better film-forming capabilities, and improved rheological properties, making it suitable for applications like food packaging and biomaterials. Lower molecular weight chitosan, on the other hand, is more soluble and may be preferable for certain biomedical applications. The advanced technique to characterize the polymer molecular weight is size exclusion chromatography coupled to light scattering. Static light scattering has emerged as the technique of choice for determining the molar mass of polymers in solution. It can be used alone or combined with size exclusion chromatography (SEC-MALLS coupling (multi-angle laser light scattering)). The mass average molecular mass (Mw) is calculated from the knowledge of the value of the refractive index increment (dn/dc). This parameter depends on the solvent used, the ionic strength of the solution and the DA. Unfortunately, the values of dn/dc differ greatly according to the authors (Table 2.1).

Table 2.1. Dependence of dn/dc on DA

Solvents	λ (nm)	DA (%)	dn/dc (mL/g)	References
AcOH 0.2M /AcONa 0.1M	436	0 9 26 31	0,208 0,194 0,189 0,175	Wang et al. [70]
AcOH 0.1M + NaCl 0.2M	632.8	5 15 28 42	0,201 0,191 0,183 0,180	Terbojevich et al. [71]
AcOH 0.3M /AcONa 0.2M	632.8	2-21 13-61	0,163 0,190	Rinaudo et al. [72]
AcOH 0.3M /AcONa 0.1M	632.8	0-24	0,181	Beri et al. [73]
AcOH 0.2M/ AcONa 0.15	632.8	1-71	Behavior law according to the DA	Schatz et al. [74]

The main difficulty in the light scattering technique concerns the clarification (removal of insoluble particles) from solutions. Chitosan can thus form intermolecular associations in solutions, which lead to a strong increase in the intensity diffused at small angles and to an uncertainty in the determination of Mw. The solutions are then centrifuged and / or filtered through membranes with a porosity less than or equal to 0.45 µm, while being careful not to modify the polymer concentration. Sorlier et al. [75] studied the evolution of dn / dc of chitosan over a wide range of DA ranging from 5 to 71%, then Schatz et al [76], from 1 to 71%, and that on homologous series, therefore at the study only the influence of the DA. The authors found on the one hand similar results and on the other hand showed that the variation of dn/dc followed a typical constitutive law as a function of the DA (Figure 2.9). For these two studies, the wavelength used was 632.8 nm and the solvent was an acetic acid/ammonium acetate buffer. These conditions were used during our thesis work to determine the mean molar masses of our products. This constitutive law is also in agreement with the work carried out by Lamarque et al. [77].

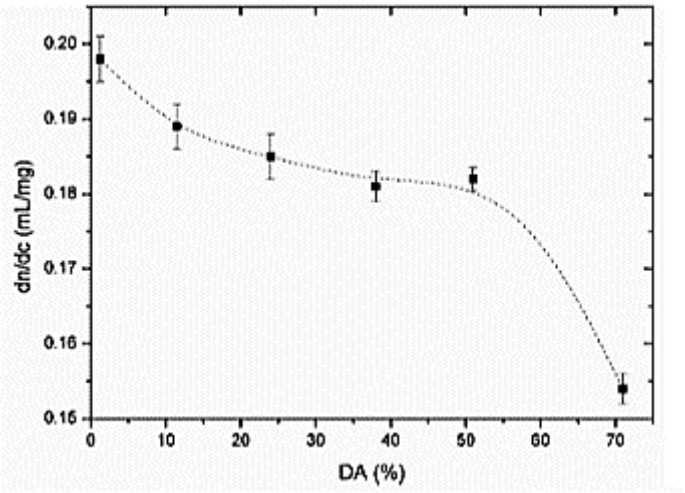

Figure 2.9. Variation of dn / dc as a function of the DA. Reproduced with permission from Sorlier et. al., 2001 and Schatz et. al., 2003 [75, 76].

The analysis of polyelectrolytes by SEC is delicate because of the numerous charge effects between the eluent, the solute and the stationary phase [78]. The choice of the eluent must make it possible to prevent the macromolecules from being eluted too early or too late, and therefore the molar mass from being incorrect. In the case of chitosan, the stationary phases are generally formed of polyacrylamide or cationic silica gels. The acetic acid / ammonium acetate buffer (pH = 4.5) used as eluent makes it possible to limit the possibilities of hydrogen bonds between the chitosan and the stationary phase, its ionic strength close to 0.15M makes it possible to screen the polymer fillers [79, 80]. SEC can be used alone, but more often it is coupled with light scattering for a more rigorous assessment of average molar masses.

To understand the influence of sample preparation (acetylation or deacetylation) on the distribution of residues (GlcNAc or GlcN), homogeneous acetylation provides a statistical distribution of acetyl units [81]. On the other hand, it is difficult to control this distribution during deacetylation, this process most often taking place under heterogeneous conditions with a material (chitin), initially insoluble in the reaction medium, which partially preserves its crystallinity. Kurita et al. observed that the heterogeneous deacetylation of chitin produces a block distribution of the two residues in that the sodium hydroxide acts first in the amorphous regions (up to a DA of 30%) then slowly penetrates the more crystalline regions [82]. By homogeneous deacetylation, a random distribution is observed [83]. Ottoy et al. by working in heterogeneous conditions put forward another explanation: part of the chitin attributed to the crystalline zones would not react during deacetylation [84]. Aiba homogeneously reacetylates, to a DA of 50-60%, two chitosans of DA 30 and 6% obtained by heterogeneous deacetylation of the same chitin [85]. Solubility and swelling are greater for the initial 6% DA, and the least deacetylated sample retained crystalline portions.

Despite these results, some authors obtain statistical distributions regardless of the mode of preparation [86, 87]. More recently, Chaussard et al. showed that the heterogeneous

deacetylation of β chitin leads to a block distribution (DA: 30-50%) [88]. Reacetylation of a completely deacetylated product, obtained by Lamarque et al, generates random copolymers. These authors compared the first three deacetylation kinetics of α and β chitins during multi-step heterogeneous deacetylation processes [89, 90]. The deacetylation of α chitin takes place in two stages: the amorphous domains are first deacetylated before the destruction of the crystal lattice allows its deacetylation, momentarily inducing a block arrangement of the copolymer. The deacetylation of β chitin, due to the low cohesive energy of its crystal lattice, assimilates to the reaction of a fully amorphous copolymer in homogeneous condition and leads to a random arrangement of residues.

Hence, it is important to know the behavior of chitosan in solutions and particularly its solubility in aqueous media. The solubility of chitosan depends on its structure (as a copolymer of GlcN and GlcNAc, linked β- (1 → 4)), as well as on its molecular mass and on the physico-chemical parameters of the medium in which it is introduced. These correspond to hydration, dielectric constant of the medium, pH, ionic strength and temperature [91]. The most used liquid medium for chitosan is water, which allows its solubilization under specific conditions. The DA, the distribution of acetyl groups along the chain, as well as the charge density are responsible for the physico-chemical interactions, more particularly electrostatic, and consequently, for the solubility of chitosan in the aqueous media. Chitosan, in its free amine form, is insoluble in pure water, by the presence of numerous hydrogen bonds involving the functions: hydroxyl, amine, acetamide and ether present on the repeating units. From a thermodynamic point of view, it is established that the solubility of a polymer chain is the consequence of a favorable balance between enthalpy and entropy of mixing, leading to a negative value of free energy. Dissolution is weakly favored for entropic reasons, the term of which depends essentially on the concentration and the molar mass of the polymer. Furthermore, the possibility for the enthalpy term to promote dissolution is determined by the balance between the polymer-polymer and polymer-solvent interactions [92]. The interaction parameter is thus sensitive to structural variables and again the physico-chemical environment.

Chitosan in an acidic aqueous medium, for example, HCl (aq) (the acid used in our study), becomes a polyelectrolyte by protonation of $–NH_2$ groups. The reactions which lead to the ionization of chitosan are as follows:

$$HCl + H_2O \longrightarrow H_3O^+ + Cl^-$$

$$\underset{(1-\alpha)C_p}{Chit\text{-}NH_2} + H_3O^+ \rightleftharpoons \underset{\alpha C_p}{Chit\text{-}NH_3^+} + H_2O$$

where Cp, is the total molar concentration of glucosamine residues, and α the degree of ionization of amino groups as displayed in the relationship:

$$\frac{[Chit-NH_3^+]}{[Chit-NH_2]} = \frac{\alpha \cdot C_p}{(1-\alpha)\cdot C_p} \qquad \text{(Eq. 2.2)}$$

This can be substituted in the expression of dissociation constant *Ka*:

$$K_a = \frac{[Chit-NH_2]\cdot[H^+]}{[Chit-NH_3^+]};\quad pK_a = pH + \log\frac{\left[Chit-NH_3^+\right]}{\left[Chit-NH_2\right]} = pH + \log\left(\alpha/(1-\alpha)\right) \qquad \text{(Eq. 2.3)}$$

where pKa is the apparent pK, which is approximately to the pH value when the degree of ionization α is equal to 0.5, this is, 50% of ionization (Equation 2.3).

The protonation of the amine function in a dilute acid solution provides sufficient electrostatic energy to destroy the network of hydrogen bonds mentioned above and to allow solvation of the chains. The main variable involved in the interactions of chitosan is the bulk charge density, i.e. the number of cationic charges per unit length along the chain axis, which depends on DA and environmental parameters such as pH, ionic strength, temperature and dielectric constant of the medium. Katchalsky's equation [92] illustrates the role of charge density:

$$pK_a = pH + \log\left(\alpha/(1-\alpha)\right) = pK_0 - \varepsilon\Delta\Psi(\alpha)/kT \qquad \text{(Eq. 2.4)}$$

where pK_0 is the intrinsic pK of a charge assumed to be isolated and not ionized. The last term to the right of the equation is a parameter of the difference in electrostatic potential between the surface of the polyion and a distance a from the axis of the chain, assumed to be linear and uniformly charged, which depends essentially on the charge density polymer. The solubility of chitosan is observed when the electrostatic repulsions are greater than the low energy attractive interactions represented by hydrogen bonds and hydrophobic interactions. This solubility is also favored by hydration, mainly of the charged sites [89]. Katchalsky's equation illustrates that the charge density depends on the pH, α and pK_0. The latter term also depends on structure, including chain length and DA.

The chain length is particularly important. Thus, for the first terms of the series of glucosamine oligomers, pK_0 varies between the values of the monomer in the region of 7.7 until rapidly reaching that of the completely deacetylated polymer in the region of 6.45 [93]. This value varies continuously with the DA. GlcN oligomers are soluble in water, whatever the pH, up to DP 7. In this case, both the charge density and the entropy parameter are important. The charge density, due to the higher pK_0 values, remains high over a wide pH range, and the entropy parameter low, compared to that of the polymer.

In the case of the polymer, the chain length does not play a major role. Considering completely deacetylated chitosans, insolubility generally occurs at pH> 6 when cationic charges become

insufficient to counteract attractive interactions. As DA increases, the pH range of solubility increases for two reasons. In the first place, by the increase of the steric discomfort linked to the increase in the number of acetyl groups which stiffen the polymer chains and promote their hydration, secondly, by the increase in the value of pK_0 as it has been shown by Domard et al. [90]. Sorlier et al. [94] have shown for the first time that, unlike previous work by Anthonsen and Strand [95, 96] and Rinaudo et al. [97] (pK_0 = 6 for DA = 12%), that the intrinsic pK of chitosan varies with the degree of acetylation (from 6.45 to 7.15 approximately) and this, for a wide range of DA (5-89%), in the case of homologous series of statistical distribution of the two types of residuals. The authors have shown that the hydrophobia provided by the acetylated units leads to an increase in the cationicity of the amine functions. Therefore, chitosans with DAs close to 50% are soluble in water whatever the pH. Vårum et al. have also shown that for DAs of between 50 and 70% approximately, chitosan is soluble in water regardless of the pH. In addition to pH, ionic strength is another external parameter affecting solubility, through its influence on electrostatic potential [98]. This effect is illustrated by the precipitation of chitosan in saline form, for pHs less than 2. The ionic force indeed produces a screening of the charges. The consequence is a decrease in the electrostatic potential favoring the folding of the chains, the exclusion of the solvent and consequently the interactions between chain segments, responsible for the precipitation. The same reason can explain the insolubility of chitosan (in the free amine form) in strong acids such as HCl for acid concentrations above 0.1 M. However, salt forms and this allows easy preparation of chitosan salts directly in the solid state. The degree of ionization of a chitosan solution (DA 12%, Mw = 2.95 x 10^5 g / mol) as a function of the HCl concentration, as well as the critical solubilization value were determined. It has been shown that in the presence of aqueous HCl, chitosan dissolves to a degree of ionization greater than 0.5. Under these conditions, the pH is equal to 4.5-5 for the polymer concentrations used [99].

2.6. Chitosan as a Versatile Biomaterial for Regenerative Therapies

As previously discussed, the emergence and advancement of tissue engineering in biomedicine are closely tied to the evolution and application of biomaterials. A central biological objective in this field is the development of functional constructs capable of providing structural and biological support for the restoration or regeneration of damaged tissues or organs. These engineered systems aim to facilitate repair, enhancement, or maintenance of tissue function through the integration of cells, bioactive agents, and biomaterials. Tissue engineering is inherently multidisciplinary and often tailored to the specific requirements of the target organ or tissue. Commonly employed biomaterials in this context include sponges, hydrogels, fibers, scaffolds, foams, and membranes, which are widely utilized in the repair of bone, vascular, neural, and skin tissue defects (Figure 2.10). Having previously described the remarkable properties of CS, these materials may offer unique opportunities for developing biomaterials for biomedical applications. The following sections will highlight the most recent advancements in the use of CS and its derivatives as biomaterials in tissue engineering, with particular emphasis on their applications in skin, bone, and nerve tissue regeneration.

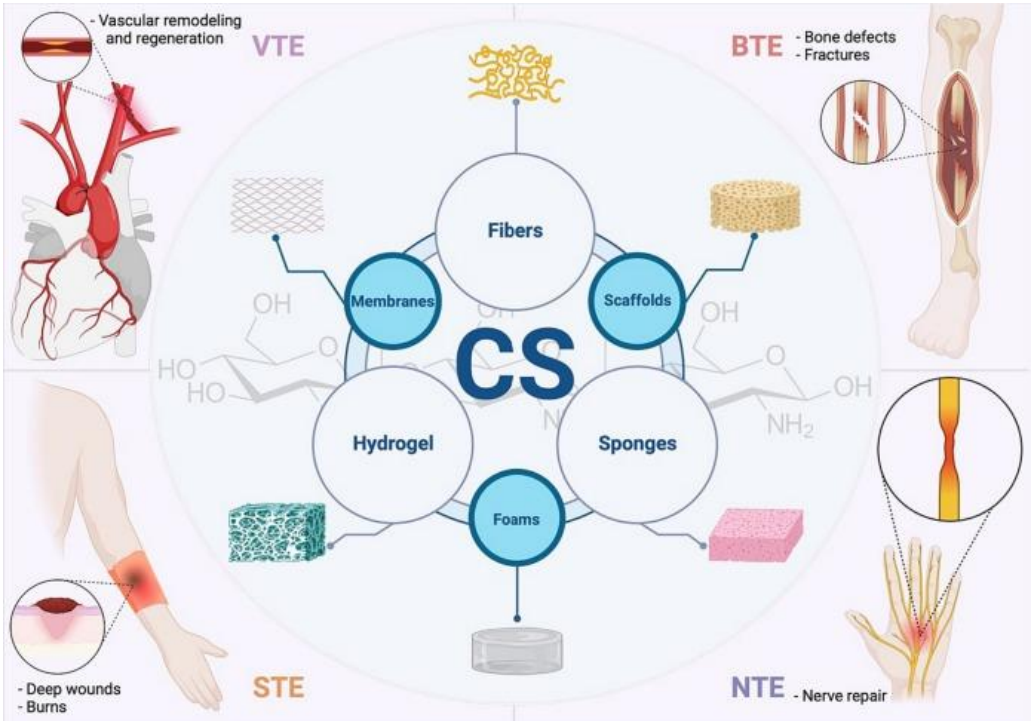

Figure 2.10. Main biomaterials obtained from CS and its derivatives and examples of their applications in tissue engineering. VTE = Vascular tissue engineering, BTE = Bone tissue engineering, STE = Skin tissue engineering, and NTE = Nerve tissue engineering. Reproduced with permission from Elizalde et. al., 2024 [100].

Chitosan in skin tissue engineering (STE)

Skin tissue engineering (STE) is a highly significant field in biomedicine, dedicated to restoring the normal anatomy and physiology of the skin. As the body's largest organ, the skin plays

critical protective, regulatory, sensory, and cosmetic roles that are essential for maintaining homeostasis [101]. It contributes to numerous physiological processes, including thermoregulation, fluid balance, and metabolic regulation, and serves as a vital barrier against pathogenic microorganisms and harmful environmental agents [102]. Structurally, the skin is a complex, multilayered organ composed of various cellular and extracellular components, including fibers, blood vessels, nerves, and appendages such as hair follicles [103].

When extensive structural damage occurs, the skin's innate regenerative capacity is often insufficient, leading to severe functional impairment and potential life-threatening complications. While autologous skin grafts remain the clinical gold standard for treating deep or extensive wounds, the availability and applicability of skin substitutes remain limited [104]. STE presents a promising alternative by aiming to produce functional skin tissue through the integration of cells, bioactive molecules (e.g., growth factors), and biomaterials that support cellular proliferation and tissue development [105].

Recent advances in biomaterial design have accelerated progress in wound healing and skin regeneration. Among these, chitosan (CS) and its derivatives have gained significant attention for their utility in constructing functional scaffolds. Their favorable properties, including high biocompatibility, intrinsic bioactivity, appropriate degradability, and tunable mechanical strength, making them ideal candidates. Additionally, CS can be engineered into multifunctional architectures that mimic the morphology and function of the natural extracellular matrix (ECM) [106].

The development of chitosan (CS)-based membranous scaffolds has garnered significant attention in recent years due to their promising applications in skin tissue engineering (STE). One notable study introduced an innovative agarose–CS membrane with characteristics suitable for regenerative medicine. With a pH of 5.98, closely matching that of human skin, the membrane demonstrated high exudate absorption capacity and elasticity. It also exhibited enzymatic sensitivity, facilitating biodegradation and enabling the controlled release of active compounds at the wound site to support the healing process. Fibroblasts adhered well to the membrane, retaining their characteristic morphology, thus confirming the material's cytocompatibility. These findings highlight the membrane's potential as a modulator of cell-mediated wound repair, further supported by CS's intrinsic antimicrobial properties, which enhance its suitability for STE applications [107].

More recently, a hybrid membrane composed of CS, collagen, and *Nigella sativa* was developed via electrospinning with polyvinyl acetate. This composite scaffold maintained a moist wound environment while allowing gas exchange—an essential factor for effective wound healing. It also supported cellular migration and proliferation and demonstrated sufficient tensile strength to withstand cell-induced traction forces. Additionally, the membrane

inhibited bacterial growth and achieved 100% cell viability, underscoring its potential for applications in tissue engineering for skin regeneration [108].

An emerging trend in membrane design focuses on developing multifunctional, or bimodal, scaffolds that not only support cellular activities and healing but also serve as delivery platforms for bioactive agents. For instance, Chen et al. reported the fabrication of a CS-based membrane for the localized delivery of solamargine, an alkaloid derived from eggplant. This membrane was engineered to establish a favorable microenvironment that modulates inflammation, immune activity, and tissue regeneration. The study demonstrated the membrane's ability to act as an extracellular matrix (ECM) analogue, effectively regulating macrophage behavior. Specifically, it suppressed macrophage-mediated inflammation and immune responses while promoting tissue repair, thereby providing compelling evidence for its utility in wound healing and STE [109].

Chitosan (CS)-based hydrogels have been widely explored for applications in skin tissue engineering (STE) due to their advantageous features, including high porosity, substantial water uptake and swelling capacity, biodegradability, biocompatibility, and suitable mechanical behavior. Furthermore, their morphology closely resembles that of native skin tissue. Nonetheless, pure CS hydrogels typically exhibit limited mechanical strength, prompting the development of composite hydrogels combining CS with other natural or synthetic polymers to enhance performance [110].

For instance, a recent study introduced a three-dimensional hydrogel composed of CS and alginate, loaded with crocetin to promote wound healing. This formulation demonstrated adequate porosity and biodegradability, along with a controlled release profile for crocetin. When loaded with 150 μM crocetin, the hydrogel facilitated the highest levels of wound closure, re-epithelialization, and gene expression. Notably, it significantly upregulated the mRNA levels of collagen types I and III, vascular endothelial growth factor (VEGF), and transforming growth factor-beta (TGF-β), identifying this system as a promising candidate for managing skin injuries in STE applications [110].

Similarly, Majidi et al. developed a CS–alginate hydrogel incorporating 4-methylcatechol for targeted skin regeneration. Following comprehensive physicochemical characterization, in vitro and in vivo assessments were conducted. The hydrogel exhibited pore sizes ranging from 24 to 62 μm. MTT assays and blood compatibility evaluations confirmed its non-toxic nature and its capacity to enhance cell proliferation. Moreover, in vivo results from a rat wound model demonstrated that the hydrogel containing 0.1% 4-methylcatechol significantly accelerated wound healing compared to conventional gauze treatments, supporting its potential utility in skin repair [111].

A current trend in STE hydrogel design involves the incorporation of extracellular matrix (ECM) components such as hyaluronic acid (HA), which is abundant in skin and connective tissues.

HA enhances tissue hydration, elasticity, and regeneration, while also contributing to hydrogel performance due to its high viscosity, polyelectrolyte nature, and gel-forming ability [112]. Drosdova et al. fabricated CS–HA hydrogels crosslinked with genipin or glutaraldehyde to improve mechanical stability and scaffold rigidity, thereby facilitating cell adhesion, migration, proliferation, and differentiation. The inclusion of low-molecular-weight HA further enhanced cellular responses, making these constructs particularly suitable for STE applications [113].

Building on these advancements, Zhang et al. utilized 3D printing and photopolymerization techniques to fabricate CS–HA hydrogels with superior structural integrity and defined architectures. These constructs exhibited a well-organized porous network with pore sizes ranging from 30 to 180 μm. The hydrogels were biodegradable under enzymatic conditions (e.g., lysozyme, hyaluronidase) and exhibited excellent cytocompatibility and adhesion to L929 fibroblast cells, emphasizing their viability for future clinical applications in STE [114].

As previously noted, the highly porous architecture of sponge-like biomaterials significantly enhances cellular adhesion, interaction, proliferation, and growth. This effect is attributed to their structural similarity to the extracellular matrix (ECM), making them particularly suitable for applications in skin tissue engineering (STE). For instance, a recent study described the fabrication of a highly biocompatible and porous chitosan (CS) sponge integrated with lithium chloride. This composite material notably accelerated wound healing, resulting in regenerated skin with a thickened epidermis, restored hair follicles, and normal morphological features. Furthermore, mRNA expression analyses confirmed that the CS sponge promoted sustained β-catenin expression—an essential regulator of dermal formation and wound repair [115].

In another recent investigation, a novel sponge composed of CS and hyaluronic acid (HA) was developed with enhanced hemostatic and antibacterial properties to mitigate wound infection. The composite formulation, which also included sodium bicarbonate and type I collagen, demonstrated excellent biocompatibility, antibacterial efficacy, and tissue healing capacity. Structurally, it exhibited superior porosity, increased water absorption, and a rougher external surface compared to sponges made solely from CS, thereby enhancing its functional effectiveness for wound management in STE [116].

Additionally, CS-based sponges have shown promise as carriers for therapeutic molecules that further support wound regeneration. Jiang et al. developed a multifunctional sponge comprising CS and sodium alginate, loaded with silver nanoparticles derived from sericin and curcumin. These agents endowed the sponge with potent antibacterial activity against *Pseudomonas aeruginosa* and *Staphylococcus aureus*, while also promoting epithelial regeneration and collagen deposition in infected wounds. These findings suggest that the sponge is an effective therapeutic platform for managing infectious skin injuries, offering a robust strategy for clinical applications [117].

Overall, the rapid advancements in the design and application of CS-based functional biomaterials highlight their vast potential in the treatment of wounds and the broader field of STE.

Chitosan in bone tissue engineering (BTE)

Bone tissue engineering (BTE) is a crucial area within regenerative medicine focused on developing strategies that include stem cells, advanced scaffolding systems, and bioactive molecules to promote consistent and functional bone regeneration. This field holds particular importance in improving the quality of life for aging populations and individuals affected by bone disorders [118]. Pathological conditions such as congenital malformations, cancers, trauma, rickets, osteomyelitis, osteoporosis, infections, and severe fractures can lead to significant bone loss and functional impairment. While bone is inherently capable of self-repair, this regenerative potential is limited to minor injuries, including small fractures and cracks [119]. Current clinical treatments for large bone defects typically rely on bone fixation using inert metal implants, autografts, and allografts, approaches that remain the gold standard. However, BTE seeks to overcome these limitations by engineering scaffold-based constructs that can be implanted into bone defects and guide the formation of new bone tissue [120]. Scaffolds serve as temporary ECM analogs, supporting cellular activities necessary for bone repair. Among the natural polymers employed for scaffold fabrication, chitosan (CS) has garnered considerable attention due to its biocompatibility, biodegradability, and support for cellular processes. However, the low mechanical strength of CS alone restricts its use in load-bearing applications. To address this limitation, CS is often combined with ceramics, synthetic or natural polymers, and other additives to enhance its structural and functional capabilities for BTE [121, 122].
A notable example is the work by Shaabani et al., who developed a CS-based scaffold by integrating a hydrophilic CS derivative with semiconductor properties into a shape-memory polyurethane-like matrix. This novel composite, based on CS-biguanidine and polyaniline, demonstrated exceptional shape fixation (>97%), shape recovery (>98%), and self-healing capability (>93%). Biological evaluations using human adipose-derived mesenchymal stem cells (ADSCs) confirmed the scaffold's ability to promote osteogenic differentiation, as evidenced by elevated expression of osteogenic markers including collagen type I, alkaline phosphatase, Runx2, and osteocalcin [123]
In another study, Imán et al. developed a CS derivative via grafting ε-caprolactone onto CS to enhance solubility and electrospinnability. This copolymer was blended with nanohydroxyapatite and electrospun into bone-mimetic scaffolds with improved mechanical integrity and osteoinductive properties. The resulting scaffolds exhibited superior bioactivity and biodegradability, representing a viable alternative to conventional bone grafts [124].

Further, Lu et al. engineered an electrospun nanofiber membrane incorporating CS modified with copper sulfide and fucoidan. This dual-functional biomaterial showed enhanced catalytic and antibacterial activity while promoting osteoblast differentiation, making it effective for both infection control and bone regeneration in BTE [125].

In an innovative approach to 3D bioprinting, Chang et al. synthesized a CS-based bioink containing ethylene glycol and methacrylate derivatives, crosslinked using riboflavin as a biocompatible photoinitiator. The printed scaffolds displayed high structural fidelity, cell viability, and osteogenic differentiation, marking a significant advancement in customizable scaffold development for bone repair [126]. Structural parameters, such as pore size, porosity, and morphology, are critical in scaffold design as they influence cellular adhesion, migration, nutrient diffusion, and ultimately osteogenesis. The ability of CS to form microporous structures conducive to cell attachment and mineralized matrix formation has made it a key material in scaffold-based BTE strategies.

Recent trends emphasize the integration of CS into bioinks for 3D-printed scaffolds. For example, Singh et al. developed scaffolds composed of CS and sodium alginate, utilizing polyelectrolyte complexation (PEC) to achieve interconnected porosity and optimal architecture for bone cell adhesion and proliferation [127]. In a similar application focused on craniofacial BTE, Yousefiasl et al. designed scaffolds through extrusion-based 3D printing using CS enriched with hydroxyapatite. These constructs demonstrated appropriate pore size, biocompatibility, and were non-toxic to rat bone marrow mesenchymal stem cells, suggesting their potential in complex craniofacial defect reconstruction [128].

Despite these promising developments, the mechanical properties of CS remain a limiting factor for broader application in BTE, particularly in load-bearing scenarios. Ongoing research must therefore prioritize enhancing the mechanical strength of CS-based scaffolds while preserving their bioactivity. Strategies that combine CS with structurally robust materials, while exploiting its ability to promote cellular responses and ECM mimicry, will be pivotal in extending its utility in bone tissue regeneration.

Chitosan in nerve tissue engineering (NTE)

Nerve Tissue Engineering (NTE) is a multidisciplinary field focused on the study, development, and application of materials for nerve repair. Successful nerve regeneration strategies must consider not only the type of scaffold or biomaterial used to establish a biocompatible and mechanically stable environment, but also the incorporation of stem cells and growth factors to promote cellular differentiation and tissue regeneration. These bioactive components play a critical role in the repair, regeneration, and replacement of damaged neural tissues. Nerve injuries and diseases caused by trauma, degenerative conditions, or genetic factors can result

in permanent disabilities, severely affecting patients' quality of life. Therefore, NTE aims to develop innovative, reproducible, and targeted approaches that accelerate nerve regeneration and restore sensory and motor functions, ultimately supporting a functional and healthy lifestyle [129].

One of the earliest breakthroughs in this field was the use of injectable hydrogels, which can fill damaged sites and support injured tissues without requiring invasive surgical procedures. However, pure chitosan (CS)-based hydrogels face limitations such as low solubility, poor processability, and insufficient mechanical strength. Recent advances have focused on addressing these challenges, including the development of self-healing hydrogels. For example, filling a spinal cord injury cavity with a self-healing material can bridge the damaged area, support axonal and myelin regeneration, and provide channels for electrical signal transmission in the central nervous system. These materials help create a regenerative microenvironment, promoting tissue repair [130].

Luo et al. developed a curcumin-releasing, self-healing, injectable CS-based hydrogel for spinal cord injury treatment. This hybrid hydrogel was synthesized using fluorenylmethoxycarbonyl (Fmoc) groups—one grafted onto CS at the N-terminus and another incorporated into a peptide—providing dynamic reversibility, self-healing, and injectability. The sustained release of curcumin over seven days significantly promoted neurite outgrowth from dorsal root ganglia neurons and enhanced Schwann cell migration, leading to myelinated segment development. These results underscore the hydrogel’s potential for promoting functional recovery in spinal cord injuries [131].

In another study, Liu et al. introduced a CS-based nerve-guiding conduit hydrogel fabricated via a one-step electrofabrication process that avoids toxic crosslinking agents. This conduit, designed for peripheral nerve repair, supported nerve cell adhesion and proliferation and guided axon regrowth across the lesion site, producing outcomes comparable to autologous transplantation [132].

Bhuiyan et al. optimized injectable thermosensitive CS/β-glycerophosphate hydrogels by varying the concentration of β-glycerophosphate to tailor their properties. Among the tested formulations, 0.5%:3% and 0.75%:3% CS/β-glycerophosphate hydrogels demonstrated rapid gelation, high porosity, and suitable swelling and degradation profiles. They also supported the in vitro proliferation of PC12 cells, a neuronal model, reinforcing their potential for NTE applications [133].

While self-healing hydrogels represent a promising direction, additional approaches—such as drug delivery systems, gene therapy, and growth factor-based materials—are also under exploration [134]. However, such strategies may still fall short in addressing complex lesions in the central nervous system (CNS). Therefore, NTE materials must exhibit not only mechanical and structural compatibility but also biological affinity to recruit, sustain, and guide

the differentiation of seed cells, which are integral for tissue repair [135-137]. Common seed cells used in NTE include bone marrow-derived mesenchymal stem cells (BM-MSCs), adipose-derived stem cells (ADSCs), endometrial stem cells, neural stem cells (NSCs), progenitor cells, neural crest stem cells, and induced pluripotent stem cells (iPSCs).

Recent efforts have focused on developing CS-based scaffolds that mimic the extracellular matrix (ECM), promoting the proliferation and directed differentiation of these seed cells. For instance, Chang et al. developed a 3D CS-based cell culture system that maintains pluripotency and supports lineage-specific differentiation of human iPSCs into NSCs, cardiomyocytes, and hepatocytes. Similarly, Ham et al. designed an interferon-γ-loaded CS-methacrylamide hydrogel tailored for NSC culture [138]. This scaffold, resembling spinal cord ECM architecture, facilitated NSC assembly into neurofilament clusters, promoting axon regeneration and spinal cord repair [138].

An emerging trend involves using genetically engineered seed cells in combination with biomaterials. For example, Ji et al. genetically modified ADSCs to overexpress brain-derived neurotrophic factor (BDNF) and neurotrophin-3 (NT3). These modified cells were cultured on CS–silk fibroin scaffolds, resulting in synergistic neuroprotective effects, including inflammation suppression, axonal regeneration, and improved motor function in a spinal cord injury rat model [139]. Despite encouraging results, nerve regeneration remains a complex and time-intensive process, requiring further refinement in biomaterial design. Although CS offers many benefits, alternative materials such as gelatin, collagen, polylactic acid, and decellularized ECMs often demonstrate superior biocompatibility and mechanical properties. Nonetheless, 3D bioprinting has emerged as a powerful strategy in NTE, enabling the precise spatial distribution of cells and construction of anatomically accurate, functional neural structures.

In this regard, Liu et al. developed a bioink composed of hydroxypropyl CS, thiolated hyaluronic acid, vinylsulfonated hyaluronic acid, and Matrigel [140]. This formulation supported 3D bioprinting of scaffolds for NSCs, maintaining cell viability and proliferation after 7 days, thereby preserving NSC stemness and highlighting its potential for spinal cord repair. Additionally, scanning electron microscopy (SEM) analysis revealed that, over a 7-day culture period, NSCs extended extensively, forming intercellular connections rich in filopodia, which are critical for cell communication and network formation [140]. Building on this, Cheng et al. recently developed dual-lattice composite bioinks composed of chitosan (CS) and polyurethane for 3D

bioprinting of scaffolds specifically designed for NTE applications. These printed constructs exhibited reduced stiffness, making them more mechanically compatible with soft neural tissues, while maintaining favorable self-healing and printability properties. Importantly, the scaffolds demonstrated excellent biocompatibility, supported robust NSC proliferation, and promoted their neuronal differentiation [141].

These findings highlight the growing role of 3D bioprinting as a powerful strategy for engineering cell-supportive materials that meet the minimum structural and functional requirements for NTE. A key factor in the success of these materials lies in their ability to closely mimic the extracellular matrix (ECM) of native neural tissue and provide enhanced neuronal support within a three-dimensional environment. This evolving trend may represent a pivotal advancement in the design of CS-based biomaterials, potentially leading to more effective therapies for a wide range of nerve tissue injuries.

2.7. Chitosan Fibers and Hydrogels for Biomedical Applications

Chitosan fibers and knitted fabrics

In many natural polymers, processing of fibers by melt spinning is not possible because in those biopolymers the glass transition temperature Tg is commonly higher than the degradation temperature. In the case of chitosan, cellulose and alginate, the wet spinning (also called solution spinning or gel spinning) is the commonly used method to spin fibers.

In the wet spinning process as illustrated in Figure 2.11, the biopolymer is dissolved at a concentration high enough to obtain a viscous, entangled solution, known as collodion. The collodion is extruded through a die directly into a coagulation bath. The appearance of intermolecular interactions allows the formation of a hydrogel filament. This latter is then drawn into a washing bath to remove traces of coagulant, then into a drying zone before being collected onto a reel. As in melt spinning processes, the filament may undergo stretching between each module. This stretching allows the molecular structure of the polymer to be oriented and may promote crystallization.

Several variants and derivatives of the wet spinning process have been developed. In the dry spinning process, the polymer is dissolved in a volatile solvent such as dichloromethane. The filament solidifies due to the evaporation of the solvent immediately after extrusion. In the dry-wet spinning process, the extruded filament travels a distance (a few centimetres) through the air before reaching the coagulation bath. Gravity causes the filament to stretch as it travels through the air. The incorporation of other agents into the collodion, the choice of a spinneret with a single hole (production of a monofilament) or several holes (production of multi-filaments), the choice of hole diameter, the temperatures of the different baths, the draw ratios

of the drying method and the addition of a polymer relaxation step are all parameters to be controlled, in order to optimise the spinning conditions according to the targeted application.

Specifically for chitosan, the polymer is dissolved in an acidic aqueous solution and then coagulated in a basic solution. Neutralising the protonated amine functions of chitosan removes the electrostatic repulsion between the chains, which promotes the interactions between the polymer chains. In the wet spinning of chitosan, the deprotonated and thereby coagulation is commonly performed by a base, for example, sodium hydroxide (Figure 2.11) [142]. In the pseudo-wet spinning, the chitosan can be coagulated using ammonia vapours. The production speed of wet spinning is slower (between 50 and 150 m/min than that of melt spinning (250-2000 m/min).

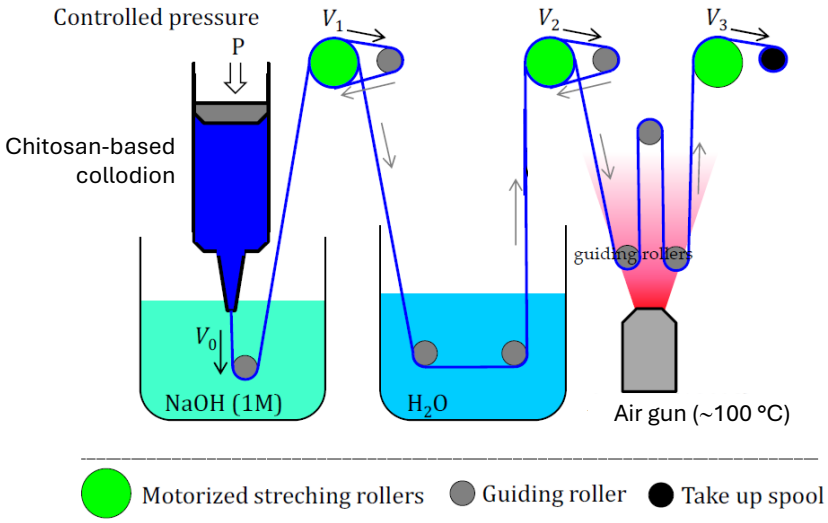

Figure 2.11. Wet/gel gel spinning set up used to spin chitosan fibers, consisting of a pressurized syringe with conic needle, a coagulation bath (NaOH 1M), three motorized stretching rollers (in green), which rotate at an adjustable speed (V_1, V_2 or V_3) to control the stretching rates, eight guiding rollers (grey circles) which guide the fiber into washing and drying zones, and a final take-up spool (black circle) where the spun fiber is collected and stored. Reproduced with permission from Bentley et. al., 2022 [142].

Some researches have been dedicated to optimizing the various parameters of the spinning process, whether in terms of the composition of the collodion, the coagulation bath or optimization of the physical parameters of the spinning process. In some procedures, it has been considered the reinforcement of chitosan matrix with fillers like nanoparticles, blending with other polymer, use a copolymer, or by crosslinking the chitosan [143].

Monofilaments, multi-filaments or fiber yarns of chitosan with varied mechanical properties have been processed for textile applications including the biomedical. Since the increase in tenacity [142] is generally concomitant with the decrease in strain at break, it is interesting to locate the processed yarns in a graph representing tenacity as a function of strain at break. The mechanical properties of some selected chitosan threads can be compared with mechanical properties of other yarns listed in the literature. The mechanical properties of the

chitosan threads can also be compared with those of commercially available resorbable yarns like:

- PolyGlycolic Acid (PGA) is the main component of Dexon® brand yarns which degrade in about 15 d and have mechanical properties comparable to polyester (Te = 5.5 cN/dtex, εb = 23%) [144].
- Polyglactin 910, better known as Vicryl® (consisting of a mixture of polyacid lactic and polyacideglycolic) resolves in 35-40 days. Mechanical properties Vicryl® yarns similar to those of polyester (Te = 5,7 cN/dtex, εb = 18%) can often be used to produce resorbable knits [145].
- Poliglecaprone 25 (consisting of 25% ε -caprolactone and 75% PGA) is available under the brand name Monocryl ® and is often knitted in combination with polypropylene for forming partially resorbable knits [146]. The tenacity of monofilaments Monocryl ® is approximately 5.9 cN/dtex with a strain at break of approximately 12 %.

Even after many attempts to optimize fiber spinning, the mechanical properties of the achieved chitosan threads are generally below than those of the resorbable yarns available on the market. However, the mechanical performance approaches that of cotton, which yarns are used in knitted fabrics.

The structure and composition of the chitosan collodion, i.e. the macromolecular characteristics like chitosan average molecular weight (Mw), degree of acetylation (DA) and polymer concentration Cp influence the mechanical properties of spun chitosan fibers. These effects are highlight in some previous works. Desorme et al. [147] produced chitosan fibers of high and medium molecular weight (Mw = 410 kg/mol and Mw = 195 kg/mol, respectively). Collodions of two polymer concentrations were compared (Cp = 2.4% and Cp = 1.8%, for high molecular weight chitosan). As expected, using longer polymer chains promoted self-assembly, increasing the degree of crystallinity of spun fibers. However, neither the change in polymer concentration Cp nor the decrease in polymer molecular weight increased the crystallinity index under those used conditions. The use of a chitosan collodion of lower molecular mass was not possible because the hydrogel would be too fragile and would break during spinning.

The mechanical properties of spun fibers are generally evaluated in uniaxial tensile tests. A fiber of cross sections S is held between two grips, one of which moves at a constant speed, thus imposing a force F on the fiber sample. The stress is considered homogeneous along the sample and expressed as $\sigma = F/S$. The strain (ε) is the quotient obtained by dividing, the achieved deformation of the fiber under stretching, between the original length of the tested (clamped) fiber section. The tensile strength is defined as the highest stress achieved obtained

in the stress-strain diagrams. The sample is deformed until it breaks. The break occurs at the called stress at break σ_b, which corresponds to the highest achieved deformation represented by the strain at break ε_b.

Numerous efforts have been made to improve the mechanical properties of the fibers of chitosan to make use of its excellent biological properties in biomedical applications. The addition of alcohol to collodion to promote the crystallisation of chitosan has allowed improving the mechanical properties. The addition of cross-linking agents has led to fibers with better mechanical properties. However, the processes involved (immersing the fibres for several hours in special baths to allow cross-linking) are difficult to adapt to an industrial process. Post-spinning pseudo-crosslinking of chitosan by forming intermolecular coordination complexes with Cu^{2+} and Zn^{2+} has led to a significant increase in the strength of chitosan yarns, accompanied by an increase in strain at break. Indeed, some works have reported on the influence of complexation on the mechanical properties of chitosan [148]. The use of ionic liquids to change the macromolecular conformation has been reported to increase strength of chitosan fibers.

Previous works brought us to think that the incorporation of chitosan of low molecular mass within a collodion of high molar weight would increase the crystallinity index in spun chitosan fibers. Nevertheless, recent works of our group demonstrated that the only addition of low into high molecular chitosan did not allow significantly increasing crystallinity and only a minor increase of orientation was observed [142]. Those findings motivated us to propose the combination of low and high molecular weight chitosan in hybrid systems [143] also containing cellulose nanofibers as filler to possibly promote the crystallization of chitosan in relation to its interaction with the nanofibers, to achieve the processing of chitosan-based fibers of higher orientation, crystallinity and strength by gel spinning.

Chitosan fiber knitted fabrics

The efforts to optimise the production of chitosan yarns with good mechanical properties have led to the processing of a few knitted fabrics from chitosan multifilaments (or spun fibres). The formation of chitosan into mono or multifilament yarns had allowed some tries to produce some knitted fabrics. Such textile materials would have many applications, in biomedicine (dressings, implants, parietal reinforcements, wound healing, etc.). However, the mechanical properties of chitosan fibers are not yet good enough to allow them to be easily knitted.

Numerous studies have therefore been carried out with the aim of improving the mechanical properties of chitosan fibers to make them knittable. The yarns that make up the knits can be separated into different classes. When each yarn is made up of a single strand, it is called a monofilament. If it consists of several continuous and twisted strands, it is called multifilament.

Finally, if it is consists of several discontinuous fibres held together by twisting, it is simply called a fiber yarn. The characteristics used to describe the properties of materials are sometimes difficult to apply to yarns. The "textile industry" has therefore used specific therminologies. The titre Ti is equivalent to the diameter. The concept of diameter or section of the yarns is often difficult to determine precisely, particularly in the case of multifilaments or fibre yarns. It is easier to characterise a yarn by its linear mass (equal to the solid cross-section of the yarn multiplied by the density f the material). The titre or yarn count is a unit of measurement comparable to the linear mass. Several units have been used to quantify the titre of a thread. The "*tex"* corresponds to the mass in g of 1000 m of yarn. *Decitex* is more often used than *tex* (1 dtex = 1 g/10000 m of yarn). In the case of yarns, the notion of cross-section has been replaced by the notion of tenacity. It has been therefore necessary to define an equivalent to the notion of stress. A specific stress has been defined as the ratio between F and Ti. The specific tensile strength is generally called textile tenacity Te = Fr/Ti. Thus, textile tenacity is equivalent to tensile strength and Te is often expressed in cN/dtex. This is a notion quite different from the tenacity in fracture mechanics, quantified by the critical stress intensity factor Kc (MPa/m1/2) or the critical energy release rate Gc (kJ/m2) to characterize the fracture of materials.

The characterisation of yarns in uniaxial tensile tests also allows the evaluation of the elastic modulus of the yarns, the stress at the plasticity threshold, the hardening of the yarn in the plastic domain and the tenacity. However, the uniaxial tensile characterization does not reflect the stresses involved in the knitting process. Indeed, the yarn undergoes a complex combination of stresses in bending, torsion, tension and compression.

Although the mechanical properties of chitosan fibres make knitting difficult, some studies have reported the knitting of chitosan (Figure 2.12) [148].

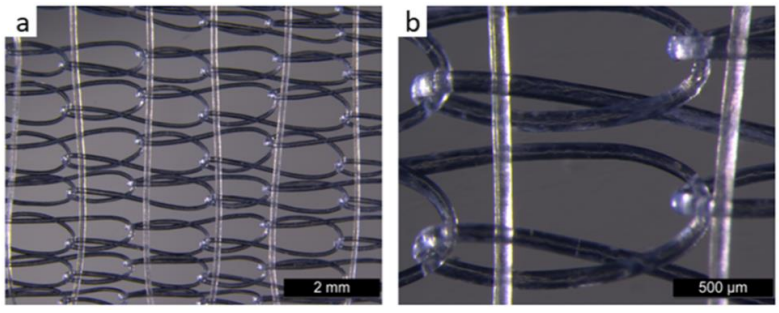

Figure 2.12. Chitosan fabrics knitted with eight monofilaments of wet-spun Cu^{2+} complexed chitosan fibers. Reproduced with permission from Passieux et. al., 2022 [148].

The manufacture of knitted fabrics from chitosan multifilaments with tenacities ranging from 0.99 to 2.49 cN/dtex, with strain at break of less than 6% was reported by and the Institute of Textile Machinery in Dresden in collaboration with the company Heppe Medical Chitosan (HMC+). Balea et al. reported the knitting of multifilaments (or fibre yarns) [149]. Filaments of

an average length of 38 mm were produced using a chitosan with a degree of deacetylation of 86%. A count of 160 dtex, a tensile strength at break of 2 cN/dtex and a strain at break of 18% were obtained.

Other study focused on the manufacture of chitosan multifilament knitted fabrics containing gold, silver or copper nanoparticles. The strands have tenacities of around 1 to 1.4 cN/dtex with 10% strain at break. The strain at break of the twisted multifilament drops to less than 4%. Although knitted fabrics could be obtained, the authors acknowledge that the knitting was not regular and homogeneous, as the multi-filaments did not have enough strain at break. To our knowledge, no production of knitted fabrics mainly consisting of chitosan fibers has been reported in the market, even if some knitting trials on laboratory-scale knitting machine have been reported.

The knitting of chitosan fibers is an important goal to produce biomedical textile fibers for several applications in biomedicine like suture threads, implants, wound healing, etc. due to the excellent biological properties of chitosan, being biocompatible, bacteriostatic, fungistatic and in addition bioactive in tissue engineering and cell growth applications. Therefore, there is the demand and challenge to improve the mechanical properties of chitosan fibers, by optimizing the monofilament spinning process. The mechanical properties of chitosan fibers are determined by the macromolecular structure of chitosan, its concentration as well as the spinning processing parameters.

Chitosan physical hydrogels

Several works have highlighted the biocompatibility, antibacterial activities, biodegradability, non-toxicity of chitosan physical hydrogels useful in tissue engineering applications [150-153]. Montembault et al. [154] developed physical CHI-based hydrogels and defined optimal conditions for a favorable biological response for cartilage regeneration. Gel-cell interactions were studied by putting physical hydrogels grounded pieces (around 20-50 µm in diameter, DA~45%) into contact with human and rabbit chondrocytes in vitro. Chondrocytes retained their phenotype and produced a significant amount of cartilaginous ECM. The presence of hydrogel particles promoted cell adhesion and induced the production of agrecans, with the gel particles “encapsulating” the cells. Chondrocytes showed a great affinity for CHI hydrogel, which constituted a physical and chemical "decoy" material [154]. Boucard et al. performed studies about multi-layered CHI physical hydrogels of chitosan for in vivo reconstruction of skin tissue following a third-degree burn [155]. They implemented a three-layer physical hydrogel bioinspired from skin microstructure. After resection and implantation, the flexible layer of the

material ensured perfect continuity between hydrogel material and tissue. A more rigid hydrogel layer on the outer surface of the implant provided good mechanical strength and maintained good hydration of the wound while protecting it from contamination during healing. A kinetics study showed that this material allows perfect tissue reconstruction at the different skin sub-layers: hypodermis, dermis, epidermis and dermo-epidermal junction. Ladet et al. prepared an onion-like multi-membrane hydrogel architecture of pure chitosan [156]. This biomaterial is also very interesting for the engineering of complex tissues showing a multi-layered structure like cornea, blood vessels, intervertebral discs, skin. The three-dimensional architecture, thanks to its independent inter-membrane spaces, allowed separate co-culture of cells in a closed “bioreactor”. The authors studied the behavior of chondrocytes introduced into inter-membrane spaces or cavities [156]. The chondrocytes preserved their phenotype and produced a significant amount of cartilaginous ECM, which completely filled the inter-membrane spaces. The multimembrane structure allowed cellular communication across membranes by diffusion of their paracrine secretome [156, 157].

Besides, CHI has been combined with other natural polymers in order to enhance biological properties and microstructural features of the resulting 3D biomaterial models. Gelatin-chitosan hydrogel was formulated and optimized for 3D bioprinting in skin tissue engineering. Chitosan was first modified through the oppositely charged functional groups of gelatin to form a polyelectrolyte complex. The biocompatibility of the contructs used in the culture of dermal fibroblasts revealed good cell viability and proliferation on prepared scaffolds. Good printability was achieved at room temperature, with high shape fidelity of the 3D printed constructs [157].

2.8. Cellulose Nanofibers and their Use as Reinforcement in Composites

The cellulose nanofibers are promising nanoreinforcements for the development of tissue engineering biomaterials and composites for the most varied applications. This material has interesting intrinsic and extrinsic properties, which give it a strong potential for use in biomedicine. The properties of cellulose nanofibers include biodegradability, biocompatibility, low density and non-toxicity, self-assembly in aqueous dispersion media, and specially high mechanical and thermal stability due to their high crystallinity and aspect ratio (L/d: length/width), yielding a green-nanoreinforcement with extremely high stiffness. Cellulose is a linear homopolymer of β(1→4)-linked units of D-glucose found in terrestrial and aquatic plants, animals, bacteria, and some amoebas. In Nature, the polymer is arranged into microfibrils as result of the biosynthesis mechanism. Cellulose chains arrange in a parallel fashion, and their interactions lead to the formation of a highly crystalline material [158]. However, native cellulose contains both crystalline regions (in general 40-70%) and amorphous phase. Especially, algal native cellulose can present a very high crystallinity of around 70%. Cellulose crystals of DP as high as 23 000 are produced by certain algae [158]. In the crystalline structure

of native cellulose, linear chains are stiffened by intramolecular H-bonds. The chains interact to each other to form a regular crystalline structure of cellulose I allomorph. Cellulose microfibril lengths can reach tens of microns. In the sea animal *Halocynthia roretzi,* called tunicin, cellulose microfibrils are highly crystalline and have a specific orientation, revealing a liquid crystal arrangement. The *Acetobacter* cellulose also has different levels of organization. In general, each microfibril has a diameter of 3.0-3.5 nm and approximately 50-80 microfibrils form ribbons of 40-60 nm in diameter [159].

The microfibrils of native cellulose can present two crystal forms, Iα and Iβ. The cell walls of some algae and bacteria are rich in cellulose Iα, whereas cotton, ramie fibers, wood and most terrestrial plants are predominantly composed of cellulose Iβ. Using X-ray and neutron crystallographic techniques, Nishiyama et al. determined the crystal structures and H-bond arrangements in both allomorphs Iα and Iβ at atomic resolution (1 Å). Cellulose Iα corresponds to a triclinic P_1 unit cell with one chain that has two adjacent glucose residues related by pseudo two-fold screw-axis symmetry. Cellulose Iβ has a monoclinic $P2_1$ unit cell containing two conformationally distinct chains, which are referred to as the corner and center chains. Each cellulose Iβ chain has a two-fold screw axis that requires the adjacent glucosyl residues in that chain to be identical. The cellulose chains in both allomorphs are arranged parallel up and edge-to-edge, making flat sheets that are held together by H-bonds. The major difference between celluloses Iα and Iβ is the shift pattern of these sheets in the wrap direction [160].

The origin of the cellulose nanofibers has a large impact on their dimensions and properties. One generally defines two major families of polysaccharide nanofibers based on how native polysaccharide microfibrils are processed. Slender rod-like cellulose nanocrystals, also coined nanowhiskers (CNW) represent one of these families, which are mainly obtained by hydrolysis of the polysaccharide substrate. Alternatively, nanofibrillated cellulose, especially micro (MFC) or nano-fibrillated cellulose (NFC), results from the shearing of native cellulose microfibrils into an entangled network of nanofibers with a broad range of sizes and displaying a hairy morphology. The delamination of the microfibril bundles through shearing is commonly performed with mechanical devices such as high pressure homogenizer or microfluidizers although alternative methods such as cryo-crushing, refining and ultrasonication have also been reported. Next to these families, as mentioned above, nanofibers of cellulose can also be biosynthesized in the form of continuous ribbons by bacteria and are generally termed bacterial cellulose or microbial cellulose.

The knowledge of the dimensions and morphology of cellulose nanofibers plays a key role in their applications, as these features directly impact the properties of the final products. Nanocrystals prepared by sulfuric acid hydrolysis of cellulose substrates are rigid, acicular-shaped and highly crystalline nanoparticles [161]. The morphology of polysaccharide nanocrystals can be accurately determined by microscopic methods like transmission electron

microscopy (TEM), cryo-TEM, atomic force microscopy (AFM), field emission gun scanning electron microscopy (FEG-SEM), or by light scattering techniques and small- and wide-angle neutron or X-ray scattering (SANS, WANS, SAXS and WAXS, respectively).

Electron microscopy enables the direct observation of the dimensions (*i.e.,* length and width) at the individual particle resolution and AFM provides information on morphology, surface topography and dimensions in environment conditions. A combination of imaging and scattering data was used by Elazzouzi-Hafraoui et al. [161] to precisely describe the morphology of cellulose nanocrystals obtained from different sources.

The aspect ratio L/d of polysaccharide whiskers varies from 1 to 120 depending on the substrate origin [162] (Table 2.2). The cellulose nanowhiskers (CNWs) have a length typically ranging from 50 to 1000 nm and a width varying from 2 to 50 nm (Table 2.2). CNWs have high length-to-width aspect ratios (10-100). Their morphology depends on the cellulose source and the processing parameters (type and concentration of acid, acid-to-cellulose (liquid/solid) ratio, hydrolysis time and temperature (Table 2). For cellulose whiskers obtained from cotton, the length and width dimensions (e.g. L = 100-300 nm et d = 8–10 nm) are much lower than those observed for tunicin cellulose whiskers with L = 0.5-2 μm, d~10 nm, L/d~70 and for *Cladophora sp.* algae whiskers with L = 0.2-4 μm and d = 30 ± 12 nm.

Table 2.2. Size distribution of cellulose nanowhiskers from some different sources. Reproduced with permission from Vestena et. al., 2016 [162].

Cellulose crystal nanowhiskers and source	Length (nm)	Width	Aspect ratio
Sisal	100-200	3-7	~ 30
Ramie	50-250	5-10	~ 15
Rice	50-300	10-15	~ 12
Cotton	50-300	5-10	~ 20
Microcrystalline cellulose (MCC) from wood	50-500	5-50	~ 10
Tunicate	100-3000	10-50	~ 100
Algae *Cladophora*	200-4000	15-40	~ 150
Algae *Microdictyon tennius*	1000-10000	25-35	~ 200
Bacteria	200-3000	10-75	~ 100

The morphology of the nanofibrillated cellulose is determined by their aspect ratio typically in the range of L/d = 100 to 200 for MFC towards L/d = 200 to 400 for NFC. The morphology of the fibers may be described qualitatively or quantitatively by the fiber diameter, surface

roughness, size distribution or degree of fibrillation. The latter increases the surface area and influences the absorption properties, softness of the fiber, rheological properties and interactions with a polymer matrix in composites. The morphology gradually changes with the processing sequence in the microfluidizer and corresponding diameter of the interaction chamber and/or number of passes. The increase in number of passes per chamber reduces the fiber diameter and yield more homogeneous dimensions [163].

The mechanical properties of single CNWs are very difficult to determine and be uniquely assigned. After cellulose amorphous phases removal by acid hydrolysis, the remaining nanowhiskers should theoretically have a modulus close to a defect-free cellulose crystal. According to experimental AFM bending stiffness measurements on single cellulose nanofibrils from tunicate with cross-sectional diameters of 8 to 20 nm, the elastic moduli of the single fibrils prepared by TEMPO-oxidation and by acid hydrolysis were 145.2 ± 31.3 and 150.7 ± 28.8 GPa, respectively. The result showed that the experimentally determined modulus agreed with the elastic modulus of native cellulose crystals. Other measurements by Raman spectroscopy provided similar values with stiffness of about 143 GPa [164].

However, it is doubtful that the mechanical properties and stiffness of nanofibers extracted from biomass will approach the modulus of crystalline cellulose, since only the internal structure of nanofibrils/fibers, nanocrystals/whiskers will have these properties, while the experimental values for the nanofibers may be variable. The latter can only be assessed by good understanding of the arrangements and interactions of the sub-nanofibril fiber structure. The nanofibril moduli in the MFC sheets were approximately 29-36 GPa based on Raman spectroscopy and are within the same range of moduli for intact plant fibers.

In relation to the intrinsic properties of polysaccharide nanofibers like high surface area, high aspect ratio, high crystallinity and mechanical performances, the polysaccharide nanowhiskers and nanofibrils give rise to outstanding mechanical and barrier properties when added into polymer matrices in so called polysaccharide nanofiber-filled nanocomposites. This is generally due to the formation of a percolating network in the case of the nanowhiskers, and to an inherent entangled network morphology in the case of the nanofibrils.

2.9. Guiding Architecture: Orientation of Reinforcements in Bioinspired Scaffolds

The hierarchical organization and alignment of structural components in bioinspired scaffolds are crucial determinants of both mechanical performance and cellular behavior in tissue engineering applications. Native tissues such as tendon, muscle, nerve, and cartilage exhibit pronounced anisotropy, where the directional alignment of extracellular matrix (ECM) fibers governs tissue mechanics and provides guidance cues for cell proliferation, migration, and differentiation [165]. Replicating these anisotropic features in synthetic scaffolds is therefore a key challenge in the design of high-performance biomaterials. Chitosan (CHI)–cellulose composites have emerged as promising candidates for bioinspired scaffolds, combining the biocompatibility, biodegradability, and bioactivity of chitosan with the outstanding mechanical properties and tunable morphology of cellulose nanofibers (CNFs) [166, 167]. CNFs can reinforce chitosan hydrogels or fibers, significantly improving stiffness, tensile strength, and toughness while maintaining a hydrated environment suitable for cell survival.

Importantly, the orientation of CNFs within the chitosan matrix directly affects the macroscopic mechanical anisotropy and the microenvironmental cues experienced by cells [168]. Aligned CNFs enhance load transfer along the fiber direction, mimicking the mechanical anisotropy observed in native tissues, and can also influence cell alignment, elongation, and differentiation, particularly for musculoskeletal and neural applications [169]. Several strategies have been developed to control CNF orientation in chitosan-based scaffolds. Wet spinning is commonly used to produce aligned composite fibers, where shear forces during extrusion induce partial alignment of CNFs along the flow direction [170]. Parameters such as polymer concentration, molecular weight, and CNF content can be adjusted to optimize fiber morphology and mechanical properties. Electrospinning has also been employed for nanofiber mats composed of chitosan–cellulose blends. By modifying collector design (e.g., rotating mandrels or parallel electrodes) and controlling the electric field, fibers can be deposited with uniaxial alignment, improving tensile strength along the alignment axis and promoting directional cell growth [171, 172]. Shear-induced alignment during extrusion-based 3D bioprinting represents another effective approach. Here, the flow of chitosan–CNF inks through narrow nozzles aligns CNFs along the printing direction, resulting in scaffolds with anisotropic mechanical behavior and topographical cues for cells [173]. Complementary post-processing techniques, such as mechanical stretching or freeze-casting, can further enhance CNF alignment and create hierarchically organized porous structures [174]. Magnetic alignment has also been explored by incorporating magnetically responsive CNFs or nanoparticles, enabling contactless orientation control in 3D hydrogel matrices while preserving biocompatibility [175, 176].

Accurate characterization of fiber orientation is critical for correlating scaffold structure with function. Techniques such as scanning electron microscopy (SEM), transmission electron microscopy (TEM), and confocal laser scanning microscopy (CLSM) provide high-resolution imaging of fiber alignment, while small-angle X-ray scattering (SAXS), X-ray diffraction (XRD), and polarized light microscopy offer quantitative information on nanoscale orientation [175, 176]. Image analysis tools, including orientation distribution functions, Fourier transform analysis, and alignment indices, allow precise evaluation of alignment and its effect on mechanical anisotropy and cell behavior. The impact of CNF orientation on scaffold performance has been extensively demonstrated. Uniaxially aligned CNFs in chitosan matrices enhance tensile modulus and strength along the alignment direction compared to randomly oriented composites [170]. In addition, aligned scaffolds guide cell elongation and alignment, promote cytoskeletal organization, and influence differentiation pathways in musculoskeletal and neural tissue models [177]. Conversely, poor alignment or heterogeneous orientation can reduce mechanical reinforcement and result in isotropic or mechanically weak constructs, highlighting the importance of controlled orientation for both material and biological performance.

Despite these advances, challenges remain in achieving multi-scale hierarchical alignment in hydrated, bioactive hydrogels while maintaining processability and biocompatibility. Most current methods provide alignment at either the micro- or nanoscale, whereas native tissues often require anisotropy across multiple length scales. Additionally, high CNF loadings required for mechanical reinforcement can increase viscosity and complicate extrusion or printing processes. Addressing these challenges will require the integration of advanced fabrication techniques, responsive materials, and real-time characterization tools to create reproducible, anisotropic scaffolds that faithfully mimic the structure and function of native tissues.

2.9.1. Engineering Complexity: Top-Down vs. Bottom-Up Approaches to Tissue Regeneration

Tissue engineering (TE) relies on a fundamental triad comprising cells, signaling cues, and scaffolds [178-181]. Among these core elements, living cells play a central role in generating new tissue and facilitating its integration with host tissue. Signaling cues such as growth factors, cytokines, or physical stimuli like mechanical or electrical signals, are used to modulate various cellular behaviors. Scaffolds serve as structural frameworks that support cellular organization and tissue formation, functionally mimicking the extracellular matrix (ECM) found in vivo [182]. Given the ECM's complex roles in native tissue, scaffolds must do more than provide mechanical stability; they also regulate cell adhesion, proliferation, migration, and differentiation [182, 183]. Thus, both scaffolds and signaling factors are essential for establishing a conducive environment for tissue regeneration. To effectively replicate the structural and functional characteristics of target tissues, and to minimize immune rejection in clinical applications, the selection of appropriate cell types and scaffold materials is critical [183]. Fundamental biological interactions, including cell–cell and cell–scaffold interactions, must be thoroughly characterized to inform the design of engineered tissues [184-186]. However, these interactions are often oversimplified or overlooked in the conventional top–down TE approach, which typically involves the one-step seeding and culturing of a limited number of cell types within 3D scaffolds that mimic the gross anatomy of the target tissue, rather than emulating the intricate processes of natural tissue development.

Although the TE challenges for clinical applications have already been recognized by scientists for many years, they are yet to be overcome [187, 188]. This is mostly owing to the intrinsic, intractable limits of the top-down strategy, which differs significantly from natural tissue formation. Hence, an alternative bottom-up technique has been proposed to mimic and utilize in vivo tissue development, structure, and function, which is strongly related to systems biology and developmental biology. The bottom–up strategy differs markedly from the conventional top–down approach in several way. Firstly, bottom-up utilizes a broader spectrum of essential cell types rather than focusing solely on a few dominant ones for tissue reconstruction. Secondly, instead of employing a single large scaffold that replicates the target tissue's dimensions and morphology, bottom-up involves the fabrication of numerous modular scaffolds of smaller sizes and varied geometries tailored to different cell types. Thirdly, tissue formation in bottom-up approach is achieved through precisely orchestrated temporal and spatial processes, contrasting with the simplified one-step cell seeding and culture characteristic of the top–down approach [188].

The use of smaller scaffold units and the progressive incorporation of vascular networks in bottom-up facilitates improved nutrient delivery and waste removal via both convective and

diffusive mechanisms. As a result, mass transport within the developing tissue is not a significantly limiting factor. Mimicking the natural processes of tissue development more closely, the in vivo-like nature of the bottom–up approach offers superior physiological relevance compared to the top–down method. Moreover, the staged nature of the bottom–up strategy enhances both observability and controllability, allowing for deliberate adjustments to temporal and spatial parameters. This is in stark contrast to the empirical or trial-and-error modifications typical of top–down processes. The increased reproducibility afforded by this approach supports the development of standardized tissue manufacturing protocols, representing a significant advantage of bottom-up strategy and contributing to its greater overall efficiency [189].

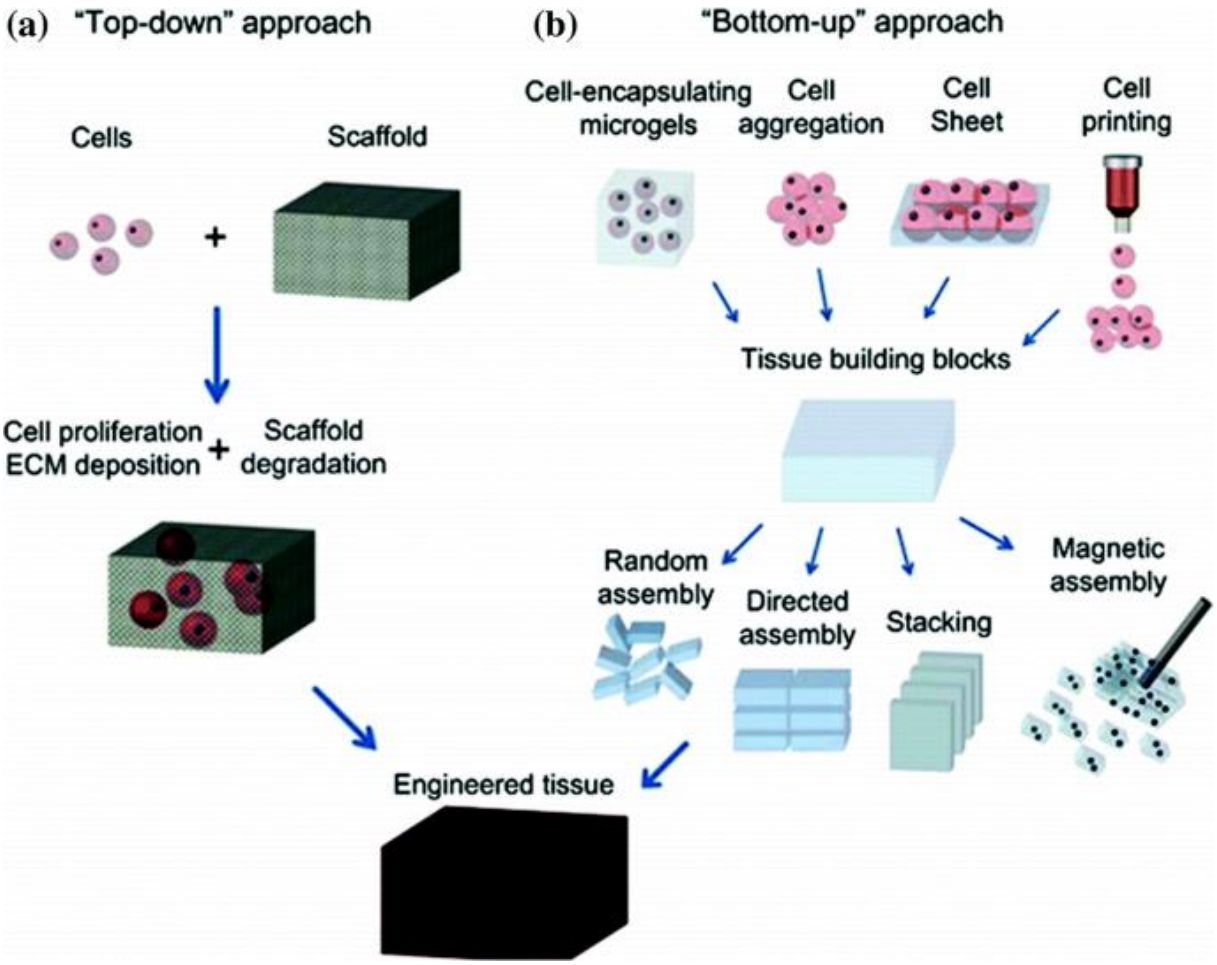

Figure 2.13. Top-down vs. Bottom-up in tissue engineering. Reproduced with permission from Kang et. al., 2016 [189].

2.9.2. Navigating 3D Bioprinting: Core Parameters and Emerging Technologies

Bioink can either be printed layer-wise [190], continuously plotted [191] or dispensed drop by drop [192]. In the process, the most important technical characteristics to consider are the printing resolution (45-1000 mm) [193], viscosity range of printable fluids (1-8000 mPa) [193],

post-printing cell viability (69-99%) [194]. The technique is evaluated on the ability to generate both large, free-standing objects and high-resolution/micropatterned structures.

To better control the physical guidance provided by the microarchitecture and the heterogeneous distribution of functional biomolecules, such as growth factors, peptide ligands and so on, resolution needs to be improved to the subcellular or molecular level (nanometer scale) for most of the existing bioprinters. And to provide the essential physical, chemical and biological cues to the printed cells, the biocompatibility of the bioprinter to a variety of biomaterials needs to be extended, since the biomaterials act as the direct interface with the cells. Consequently, identifying the most suitable printing technique, aspects related to materials (e.g. viscosity range), cells (e.g. post-printing viability) and application (e.g. planar or free-standing structure) should be taken into consideration.

Essential characteristics of bioink include low viscosity, suitable biodegradability and biocompatibility, enhanced cell adhesive properties, bioprintability and high mechanical strength. However, such characteristics limit the range of exploitable biomaterials. Therefore, a limited range of hydrogels are available as bioink for the chosen bioprinting technique. Although extensive research, the current technologies implemented in bioprinting are mostly incapable of printing functional solid organs. Researches have approached this issue by developing templates that could be used in vivo to support the development of vascularized solid organs such as bones. 3D bioprinting of vasculature network is particularly its foremost significance in maintaining tissue viability and promoting functional maturation.

Based on the smallest printable entity, the 3D bioprinting techniques can be divided into different classes. The main current 3D bioprinting techniques include (i) inkjet-based (drop-by-drop), (ii) extrusion-based, (iii) laser assisted, and (iv) stereolithography. The comparison of these 3D bioprinting techniques is shown in Figure 2.14.

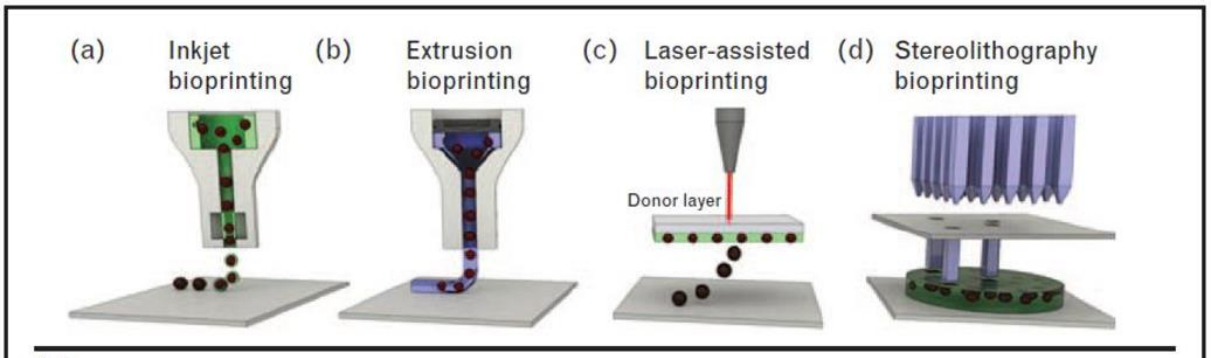

(e) Comparison of 3D bioprinting modalities

	Inkjet	Extrusion	Laser assisted	Stereolithography
Ink viscosity	3.5–12 mPa/s	Up to 6 x 10^7 mPa/s	1–300 mPa/s	No limitation
Cell density	Low, <10^6 cells/ml	No limitation	Medium, <10^8 cells/ml	No limitation
Resolution	High	Moderate	High	High
Print speed	Fast	Slow	Medium	Fast
Cost	Low	Medium	High	Low

Figure 2.14. Basic principles of 3D bioprinting technologies. Reproduced with permission from Chahal et. al., 2012 [195].

Starting with inkjet bioprinting, also known as drop on demand printing, is a noncontact printing process that precisely droplets of bioink onto a surface simultaneously in a control manner. This technology is cost-effective and allows high resolution of the printed constructs while maintaining a fast-printing speed. Inkjet bioprinting physically manipulates a bioink solution to generate droplets. It leverages gravity, atmospheric pressure and the fluid mechanics of the bioink solution to eject droplets onto a receiving substrate (which also can be a hydrogel). Bioinks with viscosities lower than 10 mPa.s have been reported printable via inkjet. Droplet-based bioprinting (DBB) offers many advantages due to its simplicity and agility with controlled volumes of bioink deposition, at predefined locations, of biologics including cells, growth factors, genes, drugs and biomaterials [196]. Due to its immense versatility, DBB technology has been adopted by various application areas, including but not limited to, TE and regenerative medicine, transplantation and clinics, pharmaceutics and high-throughput screening, and cancer research. Despite the great benefits, the technology currently faces several challenges such as a narrow range of available bioink materials, bioprinting-induced cell damage at substantial levels, limited mechanical and structural integrity of bioprinted constructs, and restrictions on the size of constructs due to lack of vascularization and porosity. Inkjet printing methods could be classified into three categories: continuous-inkjet, electro-

hydrodynamic jet, and drop-on demand inkjet bioprinting. In continuous-inkjet (CIJ) bioprinting, the bioink solution is forced under pressure through a nozzle, which subsequently breaks up into a stream of droplets owing to Rayleigh-Plateau instability. The third category happens to be the largest and most used one consisting of thermal, piezoelectric, and electrostatic inkjet bioprinting. The thermal inkjet printers are widely available at relatively low cost, but low droplet directionality, nozzle clogging and the risk of exposing cells to thermal and mechanical stress pose considerable concerns to the use of these printers in 3D bioprinting. Thus, it is not commonly used in TE due to activity loss resulting from very high temperatures which may reach above 200 °C. For instance, Setti et al. reported 15% activity loss while printing β-galactosidase (GAL) [197]. However, some studies employ piezoelectric inkjet bioprinting. For example, a piezoelectric inkjet printing system was utilized to print breast cancer cell suspensions [198]. Although the technology currently enables fabrication of heterocellular tissue constructs in a high-throughput and reproducible manner [199], DBB currently faces the limited translation of the technology into clinics. Integration of DBB with microfluidics and microwell technology is relatively new. Despite all limitations, novel breakthroughs such as angiogenesis and in-situ bioprinting, which leverage nature-driven mechanisms, make the eventual clinical translation of DBB technology inevitable. Finally, inkjet printing within 3D bioprinting technologies has been limited compared to extrusion-based studies, with the main reason being the inherent inability of printing head to provide a continuous flow which limits its bioprinting application. Besides, inkjet printing offers fast fabrication speed but low cell densities.

In extruded-based bioprinting, mostly referred to as microextrusion, as the technique utilizes extruding devices to print a thin and continuous line of the biomaterial onto a substrate of thin lines of bioink are deposited onto a substrate (line by line bioprinting) [200]. The versatility of microextrusion-based bioprinting, which combines both microscopic resolution and the ability to generate macroscopic hydrogel structures, plus its broad range of dispensable materials make it a frequently used technique suitable for a vast range of applications. Depending on the bioink and the plotting device, lines with a width ranging from 45 mm to 1200 mm can be printed with high precision. Microextrusion is suitable for a broad range of materials and inexpensive setups can be used [201]. Liquids with either low or very high viscosity (1 to $1x10^7$ mPa s) are reported to be printable via extrusion printing [202, 203]. Microextrusion has been chosen for the generation of both large, freestanding objects and planar microstructures. The versatility of microextrusion-based bioprinting which combines microscopic resolution and the ability to generate macroscopic hydrogel structures, plus its broad range of dispensable materials, make it a technique suitable for a vast range of applications. In fact, in comparison with inkjet bioprinting, extrusion-based bioprinting offers lower speed and resolution but higher cell densities [204]. Thus, extrusion-based bioprinting is extensively developed to produce cell-

laden bioconstructs. Its methods are categorized into pneumatic, piston-driven, and screw-driven dispensing. In pneumatic dispensing, air pressure provides the required driving force, while in piston and screw-driven dispensing, vertical and rotational mechanical forces initiate printing, respectively. There are three main factors to consider toward bioprintability via extrusion: 1) adjustability of the viscosity, 2) bioink phase prior to extrusion, 3) material-specific biofabrication window [205]. Viscosity can be a function of temperature or shear thinning and therefore, needs to be adjusted. The bioink needs to be in liquid phase to avoid nozzle clogging. Not all biomaterials are printable and those which are printable may not be printable in a wide range of processing parameters.

In the past, microextrusion was mainly applied for the printing of filaments comprising only one bulk material. However, recent modifications enable the extrusion of lines with multiple materials and core-shell structures. Thus, a core-shell nozzle system has emerged as a new extrusion-based method (Figure 2.15). Controlling the flow rate of differently loaded, microfluidic channels connected to one nozzle allows the generation of single filaments with material properties displaying spatio-temporal variation [206]. Moreover, feeding different materials into the center and the annulus of a coaxial nozzle enables the printing of lines with a core-shell structure [207] and tubular filaments [208]. For example, a crosslinking agent can be supplied while the bioink is being dispensed from the core of the nozzle. Core-shell printing was employed for rapid printing and gelation of cell-laden alginate 3D constructs [209]. The printed mesh structures showed cell viabilities higher than 90% for preosteoblasts and hASCs. Cell-laden bioink based on alginate and collagen were also printed by this method [210]. Cell encapsulating collagen bioink was loaded in the core barrel and alginate in the shell to improve cell viability during printing and crosslinking, while enhancing overall printing fidelity. 3D constructs prepared using core-shell method, showed noticeable higher cell viability compared to regular alginate-based bioinks. Overall, it is worth noticing that inkjet and extrusion bioprinters have unique advantages in terms of simplicity, flexibility and low cost. However, these two methods have limitations as well. Firstly, cell damage and death as well as cell sedimentation and aggregation exist in both methods due to the shear stress and the small orifice diameter of the nozzles used to deliver the bioink. Secondly, the printing resolution is limited by the physical confinement of the nozzles, usually above 50 mm. Moreover, the structural integrity of the printed structures is another obstacle, especially at the interfaces of droplets (in the case of inkjet printing) and lines (in the case of extrusion printing).

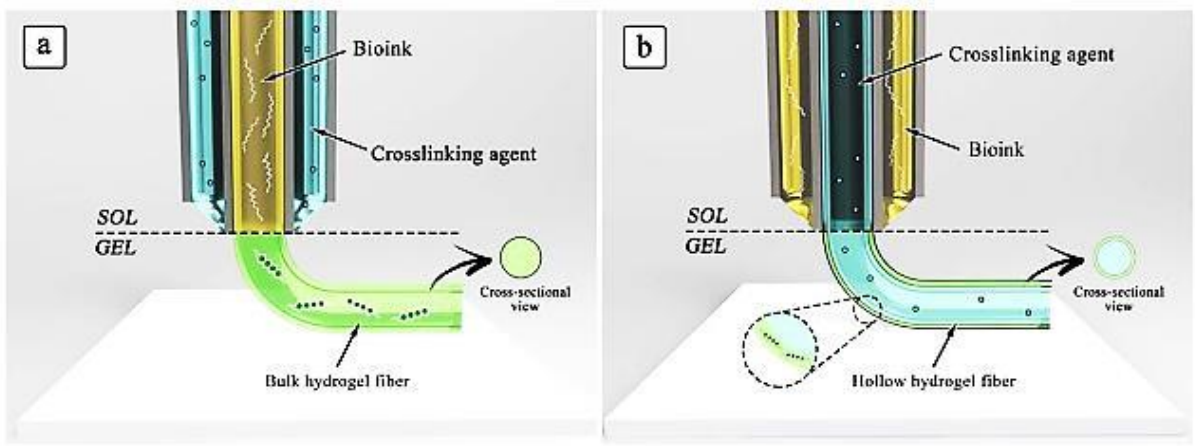

Figure 2.15. Schematic representation of a co-axial extruder. Reproduced with permission from Tondnevis et. al., 2020 [211].

Lastly, light-assisted bioprinting (LAB) and stereolithography uses photochemical cross-linkable polymer to form 3D objects, and patterns. It utilizes digital light projection control to polymerize light-sensitive materials to fabricate structures from curable acrylics and epoxy. In comparison with other methods, stereolithography is a technique with high printing quality, speed, and cell viability. However, drawbacks have been reported resulting from using this method. For instance, UV light source, which is the common polymerization method, has been reported to be harmful for DNA cells and even cause skin cancer [191].

Mombini et al. [212] fabricated electrospun nanofiber scaffolds composed of polyvinyl alcohol (PVA), chitosan (CHI), and varying concentrations of carbon nanotubes (CNTs) to mimic the native cardiac extracellular matrix. The optimized PVA–CHI–CNT scaffold containing 1 wt% CNT exhibited superior physicochemical and biological properties, including an elastic modulus of 130 ± 3.6 MPa**,** electrical conductivity of 3.4×10^{-6} S cm^{-1}, high water uptake, strong cell adhesion, and over 80% cell viability. Furthermore, the differentiation of rat mesenchymal stem cells (MSCs) into cardiomyocytes on this scaffold, under electrical stimulation, markedly enhanced the expression of cardiac-specific markers [129].

Gerasimenko et al. [213] developed a laser-based fabrication approach to produce multilayered composite structures from lyophilized bovine serum albumin (BSA), bovine collagen (BC), and chitosan succinate (CS) incorporated with single-walled carbon nanotubes (SWCNTs) for cardiovascular and tissue engineering (TE) applications. Scanning electron microscopy revealed that the composite layers exhibited smooth surfaces prior to irradiation, whereas laser exposure at controlled energy thresholds induced increased surface roughness and porosity. Notably, a bimodal pore size distribution, large pores (100–200 μm) and small pores (1–5 μm), was achieved in BSA/BC/CS + SWCNT composites at specific E_th values, facilitating cell adhesion, proliferation, vascularization, and innervation. The laser-fabricated composites demonstrated enhanced electrical conductivity, hardness, and endothelial cell

viability compared to thermostated counterparts. Fluorescence microscopy further confirmed their cytocompatibility, underscoring their promise for implantable tissue-regenerative constructs [213].

In another study, polyurethane nanofibers were physico-chemically and biologically modified with gelatin (Gel) and SWCNTs, followed by electrospinning to generate functional nanofibrous scaffolds [131]. The resulting Gel/SWCNT nanofibers exhibited mean diameters ranging from 210 nm to 140 nm, influencing initial cell adhesion and proliferation. Incorporation of gelatin enhanced scaffold biodegradability and imparted biomimetic mechanical properties comparable to native vascular tissue. The inclusion of SWCNTs significantly increased the Young's modulus (16.47 ± 0.5 MPa) and ultimate tensile strength (23.73 ± 0.5 MPa), while gelatin improved extensibility. SWCNT addition also enhanced electrical conductivity, and biological assessments revealed dense cellular coverage after 7 days, confirming the scaffold's suitability for cardiovascular tissue engineering [214, 215].

Similarly, Kharaziha et al. engineered hybrid electrospun nanofibrous scaffolds by embedding CNTs within aligned poly(glycerol sebacate) (PG): gelatin matrices to replicate the anisotropic structure of the myocardium. Gelatin crosslinking was achieved using 1-ethyl-3-(3-dimethylaminopropyl) carbodiimide and N-hydroxysuccinimide [132]. Increasing CNT concentrations within the PG-based scaffolds enhanced fiber alignment, electrical conductivity, and mechanical toughness, while maintaining cardiomyocyte (CM) viability, organization, and contractile function. CNT–PG scaffolds exhibited lower excitation thresholds, stronger synchronous contractions, and higher capture rates than CNT-free PG scaffolds. Immunofluorescence staining confirmed well-developed sarcomeric organization and elevated connexin-43 (Cx43) expression, indicating improved intercellular coupling and electrical functionality. Overall, the aligned CNT–PG scaffolds demonstrated superior mechanical performance and bioelectrical integration, highlighting their potential for the fabrication of organized, mature cardiac tissue constructs [132].

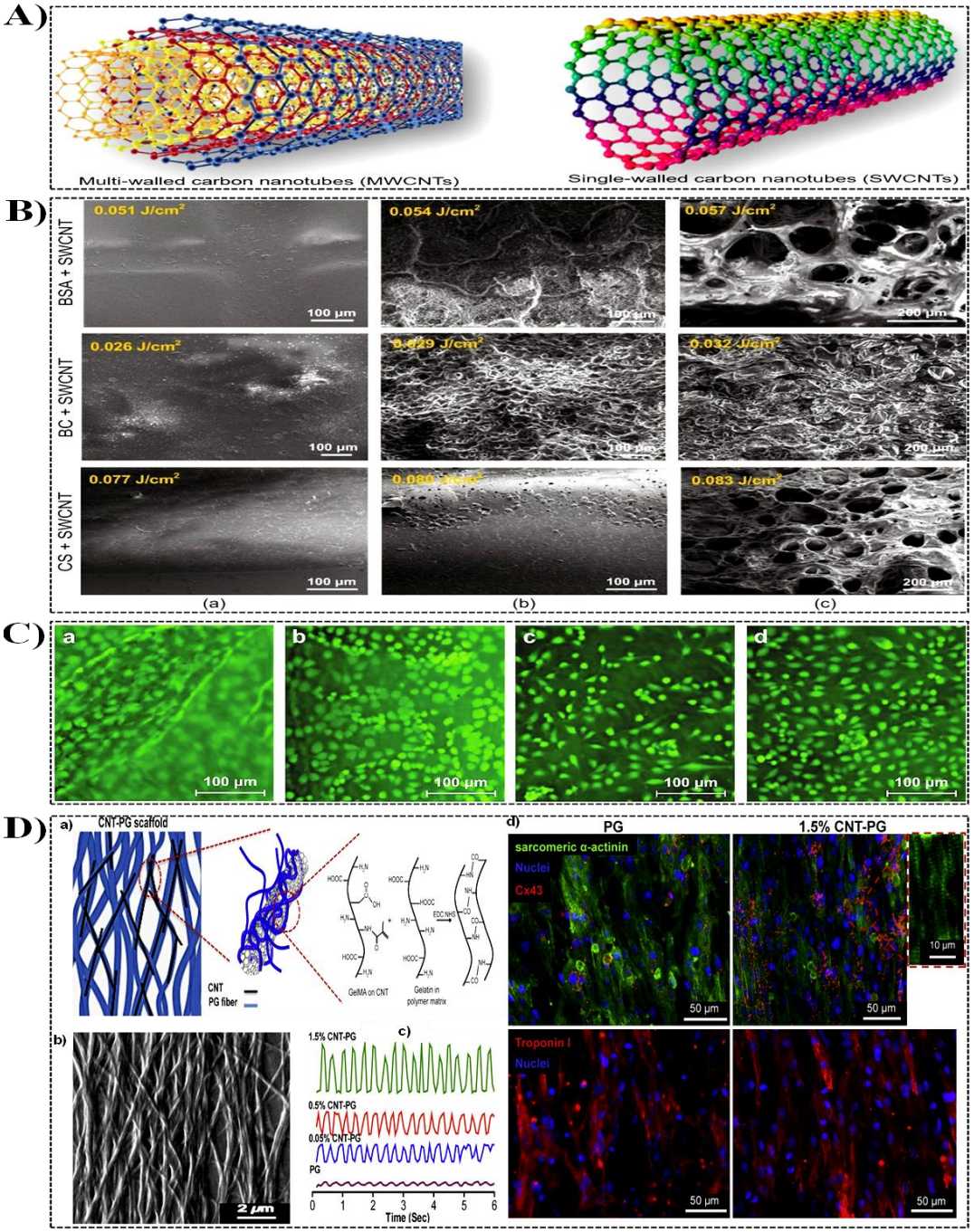

Figure 2.16. (A) Nanostructures of multi-wall carbon nanotubes (MWCNTs) (left) and single-wall carbon nanotubes (SWCNTs). (B) SEM images of developed composites. (C) Fluorescence microscopy images capture endothelial cells within the structure of composite layers from BSA (a), BC (b), CS (c) with SWCNT (0.01 wt%), and a control sample (d). (D) (a) Schematic representation illustrates CNT interactions with PG scaffold upon cross-linking with EDC/NHS, (b) SEM images display cross-linked 1.5% CNT-PG scaffold, (c) Contraction patterns of electrically stimulated CMs on PG scaffold versus CNT-PG scaffold after 7 days of culture, (d) Immunofluorescence staining for sarcomeric a-actinin (green), Cx43 (red), and DAPI (blue), as well as Troponin I (red) and DAPI (blue) after 7 days of culture, revealing organized sarcomeres with higher Cx43 expression on 1.5% CNT-PG than PG scaffold. A high-magnification image (inset in Figure 2.16 D(d) shows interconnected sarcomeric structures perpendicular to the direction of the nanofibers. Reproduced with permission from Lee et. al., 2012 [216].

2.9.3. From Polymers to Bioinks: Biomaterial Compounds in 3D Bioprinting

The biomaterials chosen for the bioink development play a major role. Researchers prefer to use biomaterials previously proven to be compatible with cells in commercial or non-commercial products/ devices. Thus, the variables are decreased, and the outcome is more likely to be predicted [217]. Alginate (Alg) has been widely used as a bioink material due to its biocompatibility, ease of gelation, and mechanical properties. It forms a gel via ionic crosslinking in the presence of divalent ions such as calcium. Hence, alginate and its composites with other biomaterials have been widely used for 3D printing of various cells, such as osteoblasts, chondrocytes, fibroblasts, stem cells [218]. The properties of alginate gel can be further modulated depending on its molecular weight, glucuronic acid unit composition, concentration, and ion crosslinker concentrations [219].

M13 phages were shown to provide good blending properties with alginate. Pati et al. devised a new method to print cell-encapsulating decellularized adipose tissue (DAT) bioink [218]. Porous dome-shaped structures were prepared and tested in vitro and in vivo for cell viability and differentiation of human adipose-derived stem cells (hASCs). The DAT 3D printed constructs were found to express more adipogenic lineages than that of non-printed DAT gel. Effects of alginate compositions on printability and NIH 3T3 fibroblast cell viability were studied [220]. Depending on compositions, alginate bioinks exhibit different viscosity and mechanical properties. The distribution of viable cells within the printed scaffolds has been also investigated as an additional essential factor for cell printing and scaffold applications. The shapes and uniformity of the bioinks upon extrusion at the nozzle depended on the bioink composition [221]. In one hand, higher proportions of low molecular weight Alg resulted in lower viscosity and inhibited printability. On the other hand, high molecular weight Alg and polymer compositions yielded high viscosity bioink and formed relatively rigid scaffolds; which negatively affected fibroblast cell growth. Besides, bioinks incorporating low-Mw Alg may enable better mass transfer, cell migration, and growth within softer environments. Nevertheless, when low-Mw Alg portions were high in the scaffolds, their features were not well defined and heterogeneous with bigger strand sizes. Bioinks which balanced physicochemical properties required for fine printing and cell growth are the best to support cell proliferation. Bioinks prepared with 3 wt% alginate, containing High and low-Mw Alg at a 2:1 ratio, showed the best performance, including good printability, distinct porous structures and a suitable environment for cell growth, proliferation and distribution [221].

Although alginate has substantial advantages as a bioink for cell printing, there are still several obstacles to the use of alginate bioinks in the fabrication of effective 3D printed scaffolds. The alginate bioink must have sufficient viscoelasticity to achieve good printability and to maintain the overall shape of the fabricated scaffold during and after 3D printing. Thus, this

processability can be partly promoted by blending alginate with various materials (e.g., bio-ceramics and other polymers) or simply controlling concentration. Alginate does not have cell binding moieties and often leads to improper cellular interactions. Several studies have attempted to control the printing conditions by incorporating bioactive molecules or by chemically modifying the alginate [222].

PCL/alginate struts were coated with alginate based bioink to reinforce the structure [223]. The ratio of alginate crosslinking agents was also varied to find the optimum conditions for cell-coating. A highly concentrated bioink consisting of alginate and polyvinyl alcohol (PVA) was developed and studied for co-printing with bovine serum albumin (BSA) and bone morphogenetic 2 (BMP-2) [224]. It was shown that the release profiles of BSA and BMP-2 were strongly dependent on the micropores in the scaffolds which was related to the PVA sol contribution. A bioink consisting of alginate and bone formation peptide-1 was proposed, to enhance bone regeneration [225]. In vitro and in vivo studies showed that the developed bioink provided a stable environment for cell proliferation. While alginate is a common biomaterial employed as bioink, most studies are based on native alginates with limited degradation.

Gelatin, due to its physical gelation properties is commonly used in proof-of-concept bioprinting experiments. Collagen and gelatin have been also studied as bioink. Biomaterial hydrogels of collagen, gelatin and alginate were used for cell-laden 3D printed tissue constructs, to control the degradation rate of the hydrogel by changing the mole ratio of sodium citrate present in the medium to the sodium alginate present in the hydrogel. High cell proliferation rate indicated the possibility to improve the alginate bioink. Oxidized alginate hydrogels were studied as bioinks with controlled degradation [226]. Alginate and gellan were used along with BioCartilage (clinical product) to prepare a new-fashioned bioink for printing cartilage grafts proved to support chondrocytes proliferation. Furthermore, a cation-loaded polymer was used to stabilize overhanging structures in this strong but ductile bioink. A porous 3D constructs was printied with a bioink consisting of collagen/ECM and alginate [227]. Developed bioink displayed decent cell viability and higher osteogenic activity compared to conventional bioinks based on alginate. Zhao et al. studied the effect of composition, concentration, temperature and holding time on printability and cell survival after gelatin extrusion printing [222]. Cell survival rate was found to decrease when viscoelasticity of the gelatin-based bioinks were increased. Bioprinted collagen type I, agarose, and chitosan blends were employed to study human mesenchymal stromal cells differentiation. Among the studied blends, osteogenesis was shown to be more likely in anisotropic soft collagen-rich substrates while adipogenesis was more likely in isotropic stiff agarose-rich matrices. Different ratios of collagen type I and agarose blend were concluded to suit wide range of mesenchyme-based applications.

Besides the afore mentioned biomaterials, chitosan has been viewed as a desirable material in tissue engineering and regenerative medicine, owning to its biocompatibility, biological

activity, biodegradability and none-toxicity. Several attempts have been made to fabricate 3D-printed chitosan hydrogels; however, most of these printed structures exhibit poor mechanical strength, significantly limiting their applicability in tissue engineering. For instance, Ang et al. reported the 3D printing of chitosan–hydroxyapatite scaffolds by extruding a chitosan pre-gel solution into a sodium hydroxide (NaOH) coagulation bath [228]. Building on this approach, Geng et al. introduced a dual-nozzle system that simultaneously extruded chitosan and NaOH solutions, enabling in-situ crosslinking during the printing process [229]. In contrast to these in-situ crosslinking strategies, Wu et al. printed chitosan pre-solution directly in air and relied on solvent evaporation to preserve the printed structure [230]. However, scaffolds printed in this manner were dry and uncross-linked, necessitating an additional NaOH coagulation bath, which may cause some shrink-induced shape distortion, reducing the intrinsic biocompatibility of chitosan. In addition, the printing and crosslinking processes are separated, resulting in a lengthy production time.

3. Objectives and Scope of the Thesis

Bioinspired materials field encompasses both biological and engineering materials whose structures, properties or functions emulate those of biological tissues, organs or other biological materials. Typically composed of polymer chains organized into three-dimensional (3D) interconnected networks that retain a large amount of water, these materials form hydrogels with structural and mechanical characteristics analogous to those of natural soft tissues. In the human body, biological tissues such as skin, muscle, cartilage, tendons, are composed of 3D assemblies of macromolecules reinforced by fibers constituting the extracellular matrix, within which cells are embedded and actively interact. The entanglement and spatial organization of these macromolecular chains impart biological functionality and define the distinct mechanical and biochemical properties of the specific tissue.
Inspired by these natural systems, in this work we propose the development of bioinspired hydrogels by using chitosan as macromolecular matrix reinforced by nanofibers of cellulose which should reproduce the hydration, viscoelasticity, and bioactivity of native extracellular matrices. Such materials are being increasingly explored for the fabrication of high-performance biomedical implants and tissue engineered 3D constructs. Furthermore, the advent of advanced biofabrication technologies, including 3D bioprinting and fiber/gel spinning, has enabled the design of structurally complex and multifunctional hybrid hydrogel systems capable of mimicking the hierarchical organization and dynamic behavior of living tissues.

The following **hypotheses** are proposed in this thesis:

Hypothesis 1:
Viscous gellable suspensions of chitosan of modulated macromolecular mass filled with cellulose nanofibers are well suited as collodions and inks, respectively, for gel spinning and extrusion-based 3D printing of functional biomaterials for applications in biomedical engineering.

Hypothesis 2:
Cellulose nanofiber-filled chitosan hydrogels are well suited for the design of anisotropic biomaterials and cell-laden hydrogels useful for applications in tissue repair/engineering.

The main aim underpinning this thesis stems from the gaps identified in the development of functional chitosan-based hydrogels. The **general objective** of this work is to develop functional chitosan-based biomaterials through the microextrusion of viscous collodions, which should lead to fiber and hydrogel materials of enhanced mechanical performance and good

biological properties for applications in tissue engineering and repair. A central challenge addressed in this thesis is the issues of chitosan at around neutral pH and the mechanical limitations of pure chitosan hydrogels, coupled with the lack of reliable approaches for inducing and modulating anisotropy in printed constructs. The scope and **specific objectives** of the investigations essentially consist of the following parts:

The first specific objective is to investigate the incorporation of cellulose nanofibers into matrices of chitosan of modulated polymer molecular weight, to elucidate how cellulose nanofiber (CNF) reinforcement, combined with controlled blending of low and high molecular weight chitosans, influences the structural, rheological properties of collodions and finally mechanical properties of spun hybrid materials processed by gel spinning. This involves studying how low molecular weight chitosan reduces viscosity, and improves chain mobility to promote orientation, while high molecular weight chitosan contributes to favor entanglement, network strengthening and structural integrity. By combining low/high molecular weight chitosan with optimal content of cellulose nanofibers serving as nucleation sites for crystallization, this objective seeks to identify formulations that achieve a balanced combination of good extrudability, mechanical robustness of gels and spinnability, as well as biological compatibility provided by the polysaccharides. A key aspect of this study is to evaluate how nanofiber morphology, concentration, and nanofiber-matrix interfacial interactions contribute to homogeneity and development of anisotropy and crystallization for the achievement of spun bio-nanocomposites of high strength.

The second specific objective is to investigate the formation and evolution of anisotropic microstructural organization in chitosan/cellulose nanofiber hydrogels during extrusion-based printing, through in situ monitoring of orientation by synchrotron X-ray scattering at small (SAXS) and wide angles (WAXS). Because under extrusion printing the material is subjected to significant shear stress, it can induce alignment of nanofibers and chains of polymer matrix. However, the extent and stability of this alignment in chitosan/cellulose nanofiber systems remain insufficiently understood. This objective focuses on quantifying alignment across multiple length scales with complementary SAXS and WAXS analyses, relating structural anisotropy to printing conditions such as extrusion pressure, nozzle geometry, ink formulation, morphology and aspect ratio of nanofiber filler. X-ray scattering is used to capture structural rearrangements during hydrogel filament formation, generating insights into how molecular and nanoscale interactions dictate anisotropic architecture. Understanding this relationship is essential for designing scaffolds that mimic organized biological tissues such as muscle, tendon, nerve.

The third specific objective is to develop a robust, unmodified chitosan-based bioink that overcomes chitosan solubility challenges and enables reproducible control over anisotropy during 3D printing. Instead of relying on chemical modification, which can alter biological activity and reduce clinical relevance, this objective emphasizes
physical blending strategies, molecular weight tuning, and nanofiber incorporation. The goal is to engineer a bioink with optimal viscosity, shear-thinning behavior, and post-extrusion stability, while maintaining biological compatibility. This objective also covers evaluating cellular responses, construct stability under physiological conditions, and the ability of the printed structures to support cell adhesion, growth, and alignment. By integrating knowledge from the first two objectives, the final goal is to establish a versatile and translational bioink platform capable of producing mechanically reinforced, directionally organized, and biologically functional scaffolds.

In the following **chapter 4**, the materials, synthesis and processing methods used throughout the experimental work are discussed. It details the preparation of chitosan and cellulose nanofibers as well as of their anisotropic spun fibers and hydrogel composites, the fabrication techniques employed for gel spinning of functional fibers, hydrogels and 3D bioprinted cell-laden scaffolds by extrusion methodologies. The analytical characterization methods used to evaluate the chemical structure, physico-chemical behavior, mechanical and biological properties are also presented in chapter 4.
In **chapter 5**, the experimental results are presented in detail and discussed. The specific goals related to the design and optimization of formulations for the development of anisotropic cellulose nanofiber-filled chitosan spun fibers and extrusion-based printed hydrogels and the strategies employed to improve orientation and mechano-functional properties, are addressed. The anisotropy and induced crystallization as well as mechanical properties in relation to design, processing strategies and obtained microstructure were systematically characterized. The influence of cellulose nanofiber incorporation on the mechanical behavior, structural organization, and biocompatibility of the composite hydrogels is investigated. The physico-chemical properties of chitosans of varying degrees of acetylation (DA) in solution is analyzed for the achievement of cell-laden chitosan-based printed bioconstructs. Particular attention is given to the correlation between material composition, processing parameters, and functional performance relevant to tissue engineering and repair.
Chapter 6 summarizes the main findings and conclusions drawn from the research in this thesis. It also discusses the broader implications of the results and proposes future perspectives for the development of advanced bioinspired anisotropic hydrogel systems based on bioactive polymer chitosan and their potential applications in regenerative medicine and related biomedical fields.

4. Materials and Methods

4.1. Materials

4.1.1. Starting High Molecular Weight Chitosan

High Molecular Weight Chitosan: Mahtani Chitosan (Veraval, Gujarat, India) provided chitosan (Type: CHITOSAN 144, Batch No. 20120926) derived from squid pen chitin.

4.1.2. Cellulose Nanofiber

4.1.2.1. Nanofibrillated Cellullose (CNFs)

Gel-like suspensions of nanofibrillated cellulose (CNF) were created at the Centre Technique du Papier (CTP, Grenoble, France) from bleached pine sulfite dissolving pulp using a mechano-enzymatic process developed from Pääkkö et al. [228]. The pulp was refined at 4.5% consistency for 25 min with a 12″ single disk refiner before 1 h incubation at 50°C with a solution of endoglucanase FiberCare R® (Novozymes Biologicals, Paris, France) at pH 5.0. The digested samples were processed further to generate a pulp solution with an SR (Schopper-Riegler) value more than 80 and a mean fiber length less than 300 μm. An Ariete homogenizer was used to process 2% (w/w) fiber suspensions, with one step at 1000 bar followed by three steps at 1500 bar. The surface charge density of the obtained CNFs was 40–80 mmol/kg. In other words, they had carboxylate moieties that were weakly charged. As previously reported by Sofia et al. [143], atomic force microscopy (AFM) was used to characterize the cellulose nanofiber morphology, which revealed an entangled network of linked nanofibrils with an average width of 35.2 ± 8.1 nm and bundles up to 100 nm wide.

4.1.2.2. Cellulose Whisker Nanocrystals (CNCs)

The cellulose whisker nanocrystals (CNCs) were prepared by heterogeneously acid-hydrolysis of bleached pine pulp to remove the amorphous regions of native cellulose fiber bundles. To extract the cellulose nanocrystals, the bleached pulp suspension was mixed with concentrated sulfuric acid at 60% (w/v) at a solid/liquid ratio 1:20 and heated at 60°C while mechanically stirring. After 1 h, the reaction was stopped by neutralizing and cooling in an ice bath. The suspensions were then washed with deionized water using repeated centrifuge cycles of (10 min at 12,000 rpm). A last wash was conducted using dialysis with deionized water until constant pH and conductivity. The samples were then sonicated (SONOPULS Ultrasonic,

Bandelin electronic GmbH, Berlin, Germany) twice for 5 min in an ice-bath to avoid overheating. Finally, colloidal systems of suspended cellulose nanocrystals were obtained and preserved as colloids in water.

4.1.3. Alginate

Sodium alginate (ALG) was purchased from Sigma Aldrich (Steinheim, Germany). Weight- and number-average molecular weights of ALG were determined by size exclusion chromatography (SEC) as described below.

4.1.4. Gelatin

Type A porcine-skin gelatin (gel strength ≈300 g Bloom, ≥99% purity), catalogue number G2500 (Sigma-Aldrich, St. Louis, MO, USA). Gelatin from porcine skin (Sigma-Aldrich, G2500) The material was supplied as a dry powder and was stored at room temperature in a desiccated environment until use. All solutions were prepared immediately before experiments by dissolving the gelatin in deionized water under gentle heating (40–50 °C) and stirring until fully dissolved.

4.2. Methods

4.2.1. Characterization of Polymer Molecular Weight by Size Exclusion Chromatography (SEC)

Chitosan

Size exclusion chromatography linked to multi-angle laser light scattering (SEC-MALLS) was used to determine the chitosan molar masses, as previously described [226]. Briefly, a chitosan solution at 0.1% (w/v) was prepared in an acetic acid/ammonium acetate buffer pH = 4.5, which was used as eluent. Then, the solution was filtered through 0.45 µm pore size membranes (Millipore, Merck KGaA, Darmstadt, Germany). The chromatographic equipment was connected to a Protein Pack 200 SW (Waters GmbH, Eschborn, Germany) column and a TSK gel G6000 PWXL. A multiangle laser light scattering detector DAWNDSP (Wyatt Technology Europe GmbH, Dernbach, Germany), operating at 632.8 nm, was coupled online to a WATERS 410 differential refractometer. The number (M_n) and weight-average molar masses (M_w) of the above-mentioned starting high molecular weight chitosan as determined by SEC-MALLS were

4.10 × 10^5 g/mol (± 6.4%) and 6.11 × 10^5 g/mol (±9.6%), respectively, which yield a polydispersity index $Đ = M_w/M_n$ = 1.49 (±11.6%).

Alginate

Alginate aqueous solutions at 0.1% (w/v) were prepared in 0.1 M $NaNO_3$ adjusted to pH 7, which was also used as eluent. Then, they were filtered through 0.45 µm pore size membrane (CME, Merck-Millipore, Burlington, MA, USA). The chromatographic equipment was composed of an IsoChrom LC pump (Spectra-Physics, Andover, MA, USA) connected to PL aquagel-OH MIXED-M and PL aquagel-OH MIXED-H columns (Agilent Technologies, Santa Clara, CA, USA). A multiangle laser light scattering (MALLS) detector DAWN DSP (Wyatt Technology, Toulouse, France) operating at 664.0 nm, was coupled on line to a WATERS 410 differential refractometer. The refractive index increment dn/dc was 0.134 mL/g. The size exclusion chromatography (SEC) coupled to MALLS allowed determining a weight (Mw) and a number-average molecular weight (Mn) of alginate of 9.62 × 10^4 (±0.66%) and 4.55 × 10^4 (±2.21%) g/mol, respectively; with a polydispersity index (Mw/Mn) of 2.11 (±2.30%), showing a relatively narrow molecular weight distribution.

4.2.2. Characterization of Chitosan Degree of Acetylation (DA)

The chitosan degree of acetylation (DA) was determined using ^{1}H NMR spectroscopy, as described by Hirai et al [51]. Chitosan (10 mg) was dissolved in 1mL of D_2O that had been acidified with 5 µL of HCl 12 M. The experiment was carried out using a Bruker ALS 300 spectrometer (300 MHz) at 298 K (Bruker GmbH, Ettlingen, Germany). The DA was calculated from the ratio of the integrated area of the methyl proton signal (around 2ppm) of the N-acetylated units (–CH_3) to the total integrated area corresponding to the H2–H6 protons (from around 3.1 to 3.8 ppm for H2, H3, H4, H5 and H6) of both glucosamine and N-acetylglucosamine residues (Figure 4.1), as expressed in Equation 4.1, where I CH_3 represents the integral of the methyl proton signal, while I (H2–H6) denotes the sum of the integrals for protons H2 to H6. The determined degree of acetylation (DA) of the starting high molecular weight chitosan was 2.5%. Same procedure was used to determine the DA of the other chitosans obtained in this work.

$$DA(\%) = \frac{\frac{1}{3} I\ CH_3}{\frac{1}{6} I\ (H_2 - H_6)} \times 100\% \qquad \text{(Eq. 4.1)}$$

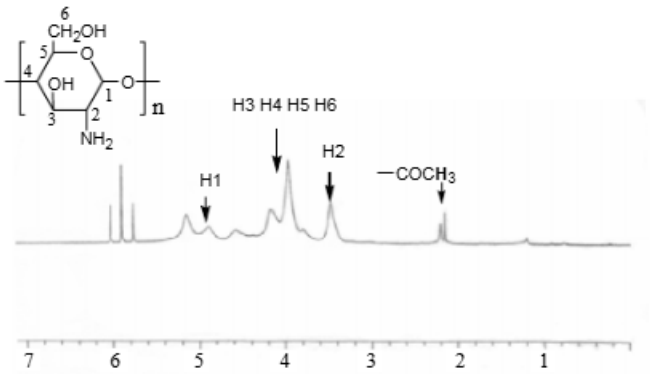

Figure 4.1. Proton assignation and ¹H NMR spectrum of chitosan. Reproduced with permission from Hirai et. al., 1991 [51].

4.2.3. Fourier-Transform Infrared (FTIR)

The chitosan/cellulose nanofiber spun fibers were characterized by FTIR in attenuated total reflection (ATR) mode using an FTIR-ATR 65 spectrometer (PerkinElmer). Spectra in the range of 400–4000 cm^{-1}were recorded. Reference spectra of the used chitosan powder and of the nanofibrillated cellulose (CNF) were also recorded.

Reacetylated chitosan samples of expected higher DA (samples with R 0.4, and R 0.5) were characterized by FTIR in attenuated total reflectance (ATR) mode using a FTIR-ATR Spectrum 65 spectrometer (PerkinElmer, Baesweiler, Germany). Infra-red spectra in the range from 400 to 4000 cm^{-1} were recorded. The DA is analyzed using the ratio of A_{1320}/A_{1420} (Equation 4.2) as suggested by Brugnerotto et al. [55].

$$DA = \left(\frac{A_{1320}}{A_{1420}} - 0.03822\right)/0.03133 \qquad \text{(Eq. 4.2)}$$

4.2.4. Thermogravimetric Analysis (TGA)

Thermogravimetric analysis of the CHI/CNF spun fibers was performed on a STA449 F5 NETZSCH thermal gravimetric analyzer. Approximatively 10mg of cut fibers were weighed in a platinum pan and heated from room temperature (~25°C) up to 650°C with a heating rate of 10°C /min, under nitrogen atmosphere with a flow rate of 100 mL/min.

4.2.5. Scanning Electron Microscopy (SEM)

The fracture and the lateral surfaces of the chitosan/cellulose nanofiber spun fibers were observed using a FEI Scios DualBeam FIB/SEM microscope at an accelerated voltage of 5 kV after sputter-coating an ultrathin Au layer.

4.2.6. Transmission Electron Microscopy (TEM)

Morphology and dimensions of the cellulose nanofibers were investigated by transmission electron microscopy (TEM). Drops of a 0.001% (w/v) nanofiber suspension were deposited on carbon coated copper grids (CF400-CU Carbon Film, 400 Mesh Copper grids), which were previously cleaned with plasma to get rid of surface contamination and make the grid more adhesive towards the sample. The samples were negatively stained with 2% (w/v) uranyl acetate in suspension. Then, samples were allowed to dry and were observed in the TEM microscope, model Zeiss LEO 912 Omega (Carl Zeiss Microscopy GmbH, Jena, Germany), and operated at 80 kV.

Ultrathin section TEM analysis

Polysaccharide fiber samples were fixed in 10% formalin, 2% glutaraldehyde in Dulbecco's phosphate buffered saline (DPBS) overnight at 4°C. The sample was then incubated in 1% uranyl acetate in 70% ethyl alcohol overnight at 4°C and further dehydrated in increasing concentrations of ethyl alcohol and finally acetone. After embedding in Durcupan resin, ultrathin sections of the fiber under analysis were cut either parallel to the fiber axis (lateral view), or perpendicular (cross-section view) by using a UC7 Ultramicrotome (Leica, Wetzlar, Germany), and collected on Formvar-coated copper grids. Post staining was done for 1 min with 3% lead citrate followed by imaging using a Zeiss Leo 912 (ZEISS, Oberkochen, Germany) transmission electron microscope operating at 80 kV.

4.2.7. X-Ray Scattering

4.2.7.1. X-Ray Diffraction with Laboratory Source

Chitosan nanofibers in dried state were analyzed by X-ray diffraction. Wide-angle X-ray scattering (WAXS) patterns of the cellulose nanofibers (both nanocrystals (CNC) and nanofibrillated (CNF)) were recorded in reflection mode with a Bruker D8 Advance diffractometer, operating at 35 kV and 30 mA with the Cu Kα radiation (λ=1.5406 Å). The

diffraction angle 2θ varied between 4° and 70° by steps of 0.03°. It is worth to notice that the aqueous suspension of 2% (w/w) cellulose nanocrystals (CNC) was also analyzed by synchrotron X-ray scattering as shown below.

4.2.7.2. X-Ray Scattering with Synchrotron Radiation (SAXS and WAXS)

X-ray synchrotron scattering analyses were performed at the beamline BM02/D2AM at the European Synchrotron Radiation Facility ESRF (Grenoble, France), which setup allowed simultaneously measuring wide (WAXS) and small-angle X-ray scattering (SAXS) using two-dimensional ImXpad WOS and D5 detectors. Data was collected at wavelength λ of 0.79078 Å with a synchrotron X-ray beam width of approximately 56 μm, which passed through the middle of CHI/cellulose nanofiber printed hydrogel filament placed in a holder with Kapton foil windows, or through different relative positions along the cross-section of extruded viscous filaments immediately at the exit from extrusion needle, this latter setup allowing for in situ WAXS/SAXS analysis during microextrusion. Lanthanum hexaboride and silver behenate were used as standard to calibrate the scattering vector q-range for WAXS and SAXS patterns. Data treatment included transmission corrections and background subtraction. The sample-detector distances were set at 20 cm for WAXS and 1.5 m for SAXS.

The ink rheological behavior study allowed identifying an appropriate flow pressure to be applied in the in situ analyses at the X-ray synchrotron beamline. That pressure was applied in the Nordson fluid dispenser, to ensure consistent flow during ink extrusion and *in situ* scanning at the beamline. A calibration step aligned the center of the incident beam precisely with the center of the extruded ink filament (x = 0 mm), located directly under the printing nozzle (z ≈ 0 mm). The synchrotron beam scanned the extruded filament immediately after ejection from the nozzle (z = 0 mm) along the extrudate cross-section. This scan recorded WAXS and SAXS images along the x-axis from -0.7 mm to 0.7 mm across 16 distinct horizontal positions, each with an X-ray beam exposure time of 10 s. A similar scan was also conducted at a different height along the extruded filament, precisely at the vertical position z = 4 mm. To ensure comparison of results for different sample formulations and nozzle sizes, scanning positions were standardized, by expressing them as a ratio of x/R, where x denotes the beam's horizontal position relative to the nozzle center, and R represents the radius of the printing nozzle. This methodology was consistently applied for each extruded ink formulation.

4.2.8. Preparation of Low Molecular Weight Chitosan by Nitrous Deamination

Chitosan of low molecular weight (LMW) was obtained by depolymerization of the above HMW chitosan. The depolymerization was carried out by nitrous deamination with sodium nitrite

($NaNO_2$), as described in previous works [231]. Chitosan at concentration of 4% (w/v) was dissolved in a stoichiometric amount of acetic acid to protonate the chitosan amine groups. Then, $NaNO_2$ was added to obtain a given molar ratio r of glucosamine (GlcN) to $NaNO_2$ as follows (Equation 4.3):

$$r = \frac{n_{GlcN}}{n_{\mathrm{NaNO2}}} \qquad \text{(Eq. 4.3)}$$

The base solution of $NaNO_2$ was added dropwise to each of the chitosan sample solutions while being stirred vigorously for 24 h at room temperature (RT), allowing the $NaNO_2$ to react with the glucosamine units and depolymerize the chitosan chains at a given extension depending on the specifically used molar ratio r. Then, the chitosan was precipitated, centrifuged, washed and lyophilized. First, the precipitation of chitosan was carried out with sodium hydroxide (NaOH) at pH 9. Second, the centrifugation was realized at 1000 rpm for 10 min at 20°C. While the supernatant was carefully poured into a beaker to avoid loss of coagulated chitosan, deionized water was added to the centrifugation vessels to wash the precipitated chitosan. The pH of the discarded liquid was measured to confirm that the CHI was completely washed. Finally, the freeze-drying of the depolymerized sample was performed.

4.2.9. Preparation of Fully De-acetylated Chitosan

Highly deacetylated low molecular weight chitosan was prepared following the protocol described by Lamarque et al. [48] with minor modifications. Briefly, 30g of low molecular weight chitosan (DA ≈ 2.5%) was weighed and mixed with 50% (w/w) sodium hydroxide solution at a solid-to-liquid ratio of 1:25 (w/v) in a Schlenk flask. The mixture was first frozen using liquid nitrogen and subsequently subjected to vacuum pumping for approximately 2 min to remove oxygen, thereby minimizing chitosan degradation under alkaline conditions. The flask was then thawed at room temperature until complete liquefaction of the chitosan solution was achieved. This freeze–pump out–thaw (FPT) cycle was repeated 8 times. After completing the 8 FPT cycles, the Schlenk flask containing the chitosan–NaOH mixture was immersed in a preheated silicon oil bath at 120°C for 1.5 hours to promote deacetylation. The reaction was terminated by rapidly cooling the flask using liquid nitrogen combined with acetone. The resulting mixture was neutralized with concentrated hydrochloric acid (37%) until pH 7.0 was reached. To remove salts and by-products, the suspension was repeatedly washed and centrifuged (Hettich ROTINA 420, 4500 rpm, 15 min per cycle). Finally, the chitosan product was lyophilized to obtain a highly deacetylated chitosan powder suitable for subsequent experimental use.

4.2.10. Synthesis of Chitosan of Different Degrees of Acetylation (DA) by Re-acetylation of the Fully De-acetylated Chitosan

The N-acetylation of chitosan was performed according to the following procedure. Chitosan (3.5g) was accurately weighed and dissolved in an aqueous acetic acid solution to obtain a 1% (w/v) chitosan solution. The mixture was stirred continuously until complete dissolution of the polymer was achieved. To prepare a 0.5% (w/v) chitosan solution in a 1,2-propanediol/aqueous acetic acid medium, 350mL of 1,2-propanediol was added to the previously obtained 1% (w/v) chitosan solution under constant stirring to ensure a homogeneous dispersion. Subsequently, N-acetylation was carried out by the addition of acetic anhydride dissolved in a 1,2-propanediol–water mixture. The reaction was maintained under continuous stirring at ambient temperature for 24 h. The quantity of acetic anhydride added was calculated based on the desired molar ratio (R) between acetic anhydride and the glucosamine units of chitosan (Equation 4.4).

$$R = \frac{n_{anhydride}}{n_{Glu}} \qquad \text{(Eq. 4.4)}$$

Variation in R allowed the preparation of chitosan samples with different degrees of acetylation (DA), particularly in the low-DA range. Re-acetylated chitosan samples with ratio R equals 0.1; 0.2; 0.3; 0.4; and 0.5 were prepared. After 24 h of continuous stirring, the reaction mixture was neutralized to precipitate the acetylated chitosan. Precipitation was achieved by the gradual addition of 2 M sodium hydroxide (NaOH) solution dropwise, under constant stirring, until the pH reached approximately 8.5. The pH was continuously monitored using a pH indicator to ensure accurate control throughout the neutralization process. Following precipitation, the polymer was collected and subjected to repeated washing and dialysis against deionized water until the pH of the solution returned to near-neutral conditions (pH ≈ 6). The resulting acetylated chitosan was subsequently lyophilized to obtain a dry, purified product suitable for further characterization.

4.2.11. Gel Spinning of Cellulose Nanofiber/Chitosan Composite Anisotropic Fibers

For the processing of the fibers, a gel spinning setup was used which consisted of a 30mL syringe. The syringe contained the chitosan/cellulose nanofibers viscous formulation, which was connected to a controlled air-pressure clip of a Performus I Nordson EFD dispenser linked to a compressed air source [231, 232]. The syringe was attached to a conic needle with a tip diameter of 0.58 mm (gauge 20, pink, Nordson EDF). Briefly, the biopolymer viscous extrudate

was directed into a coagulation bath containing 3M NaOH. The coagulated hydrogel macrofilament was pulled with aid of a first direct current electrical motor (DC motor). Afterward, the hydrogel macrofiber passed through a washing bath of deionized water, stretched and pulled by means of a second spinning DC motor. The third and fourth spinning DC motors were implemented to further stretch the fibers, while allowing them to dry. Finally, the spun fibers were collected onto a bobbin. Composite fibers of chitosan/cellulose nanofibers were processed using viscous formulations with a total chitosan concentration (LMW plus HMW) of 4 wt%, and CNF contents of 0.3, 0.4, and 0.5 wt%, respectively.

4.2.11.1. Preparation of Viscous Collodions Containing Low- (LMW) and High-Molecular Weight (HMW) Chitosans with Cellulose Nanofibrils

To spin fibers, viscous formulations with low and high molecular weight chitosans (LMW and HMW) and with dispersed cellulose nanofibers of the type nanofibrillated cellulose (CNF) as described above, were prepared to obtain compositions as displayed in Table 4.1. A fine powder of high molecular weight (HMW) chitosan was mixed with different percentages of low molecular weight (LMW) chitosan (produced for molar ratio *r* of glucosamine (GlcN) to $NaNO_2$ of 20 and 50) to yield mixed chitosan acetate solutions (hereafter named collodions or dopes) containing a total chitosan concentration of 4% (*w*/*w*) (Table 4.1). The aqueous dispersions were sonicated with a SONOPULS ultrasonic homogenizer (Bandelin electronic GmbH, Berlin, Germany) with a Bandelin titanium alloy ultrasonic probe Booster Horn SH 213G of 13 mm diameter, for 5 min at 40% amplitude. The acetic acid was added in stoichiometric amounts to protonate the amine moieties of chitosan (DA = 2.5%) to solubilize the chitosan. Finally, the mixture was kept under mechanical stirring overnight.

Table 4.1. Summary of composition of formulations of low (LMW) and high molecular weight (HMW) chitosan filled with cellulose nanofibers (CNF), which were used in the fiber spinning. Reproduced with permission from Tran et. al., 2025 [238].

Formulation		HMW	LMW		CNF
		% (*w*/*v*)	% (*w*/*v*)		% (*w*/*w*)
			r20	r50	
(F1)	CHI/r20	3.4	0.6	0	0
(F2)	CHI/r20/CNF0.3	3.4	0.6	0	0.3
(F3)	CHI/r20/CNF0.4	3.4	0.6	0	0.4
(F4)	CHI/r20/CNF0.5	3.4	0.6	0	0.5
(F5)	CHI/r50	3.4	0	0.6	0
(F6)	CHI/r50/CNF0.3	3.4	0	0.6	0.3
(F7)	CHI/r50/CNF0.4	3.4	0	0.6	0.4
(F8)	CHI/r50/CNF0.5	3.4	0	0.6	0.5
(F9)	CHI	4	0	0	0
(F10)	CHI/CNF0.3	4	0	0	0.3
(F11)	CHI/CNF0.4	4	0	0	0.4
(F12)	CHI/CNF0.5	4	0	0	0.5

4.2.12. Rheological Characterization

An AR2000 rheometer (TA Instruments Ltd., New Castle, DE, USA) with a cone-plate geometry (diameter: 25 mm; angle: 4°) was used to assess the rheological properties of various chitosan-based viscous formulations at 25°C. The gap size was 0.116 mm, and a solvent trap was employed to prevent drying or evaporation. The cone-plate design ensures a consistent shear rate throughout the sample. The analysis was conducted in triplicate, operating in continuous mode within a shear rate range of 0.01 to 500 s^{-1}. Flow curves, which are plots of steady-state shear viscosity against shear rate for the viscous collodions, were generated to determine the Newtonian viscosity in the low shear rate range plateau.

4.2.13. Microtensile Testing

Microtensile tests of the chitosan/cellulose nanofiber spun fibers were performed using a DEBEN mini-tester equipped with a 20 N load cell. All tests were carried out at room temperature, and a constant strain rate of 0.5 mm/min. Fiber segments were fixed to the tester allowing a span length of 3 mm between the clamps, corresponding to the initial length (L0) before straining of the fiber. The nominal stress σ was calculated as the ratio of the applied force F to the initial cross-sectional area A of the fiber ($\sigma = F/A$), whose dimension was determined using a light optical microscope (Olympus BX Series, Hamburg, Germany). The nominal strain (ε) was expressed as the ratio between the extension of the fiber with respect to its initial length L0 ($\varepsilon = \Delta L/L0 = (L - L0)/L0$). The Young's modulus (E), yield stress (σy) and

strain (εy), ultimate stress (σb), and strain at break (εb) were determined from the obtained stress–strain curves, considering at least ten replicates (n = 10) for each spun fiber formulation.

4.2.14. Extrusion-Based Printed Hydrogels of Cellulose Nanofiber/Chitosan

4.2.14.1. Crystalline Cellulose Nanofiber-Filled Chitosan Viscous Inks Preparation

Chitosan (CHI) viscous solutions: A stoichiometric amount of acetic acid was added to chitosan powder dispersed in MilliQ water, as to protonate the free amine groups present in the glucosamine units of chitosan (accounting for a chitosan degree of acetylation (DA) value of 2.5%) and thereby allow the CHI complete solubilization. The mixture was left under mechanical stirring overnight. Chitosan aqueous solutions at 1.5%, 1.7%, 2%, and 3% (w/v) were prepared, named as CHI1.5, CHI1.7, CHI2, and CHI3 formulations, respectively. Cellulose nanofiber-filled CHI viscous suspensions: The CHI powder was firstly mixed with the cellulose nanofibers aqueous suspension (of whisker nanocrystals (CNC) or of nanofibrillated cellulose (CNF)) in MilliQ water, and the dispersions were sonicated with a SONOPULS Ultrasonic homogenizer (Bandelin electronic GmbH, Berlin, Germany) twice for 3 min at 40% amplitude. Then, a stoichiometric amount of acetic acid was added to completely solubilize the CHI contained in the mixture. The obtained suspensions were mechanically stirred overnight to ensure a good dispersion of the nanofibers within the CHI solution. Viscous ink formulations, with the above-mentioned CHI concentrations and cellulose nanofibers (either CNC or CNF) at contents of 0.4%, 0.6%, 0.8 or 0.9% (w/w) were obtained (see details below in Table 4.2). For further use of the viscous formulations in extrusion-based printing procedure, the viscous suspensions were collected in 50 mL syringes and the systems were centrifuged at 100 rpm for 3 min, to remove all bubbles insides the viscous inks.

Table 4.2. Summary of composition of formulations of high molecular weight chitosan filled with cellulose nanofibers (CNF), which were used in the extrusion printing. Reproduced with permission from Tran et. al., 2025 [238]

Sample	**Chitosan CHI** % (w/v)	**Cellulose nanocrystals CNC** % (w/w)	**Nanofibrillated cellulose CNF** % (w/w)
CHI 1.5/CNC 2	1.5	2	-
CHI 1.5/CNC 3	1.5	3	-
CHI 1.5/CNF 0.8	1.5	-	0.8
CHI 1.5/CNF 0.9	1.5	-	0.9
CHI 1.5	1.5	-	-
CHI 1.7/CNC 2	1.7	2	-
CHI 1.7/CNC 3	1.7	3	-
CHI 1.7/CNF 0.8	1.7	-	0.8
CHI 1.7/CNF 0.9	1.7	-	0.9
CHI 1.7	1.7	-	-

CHI2/ CNC0.4	2	0.4	-
CHI2/ CNC0.6	2	0.6	-
CHI2/ CNF0.4	2	-	0.4
CHI2/ CNF0.6	2	-	0.6
CHI 2	2	-	-
CHI3/ CNF0.4	3	-	0.4
CHI3/ CNF0.6	3	-	0.6
CHI 3	3	-	-

The obtained formulations of cellulose nanofiber-filled chitosan viscous inks were initially extruded using a printing dosing conic needle of an inner diameter (ID) of 250 μm (Nordson EFD, Westlake, USA, Catalog No. 7018373) connected to an Optimum transparent clear cartridge of 10 or 30mL transparent cartridge (Nordson EFD, Westlake, USA), to obtain printed hydrogel filaments which were afterwards analyzed by synchrotron X-ray scattering SAXS and WAXS.

4.2.14.2. In Situ Characterization at the Synchrotron Beamline

In a more sophisticated setup adapted to in situ synchrotron X-ray analysis, the viscous ink formulations were extrusion-based printed at the beamline and characterized in real time during printing. The setup comprised the use of a 10 mL transparent cartridge, Optimum clear syringe barrel (Nordson EFD, Westlake, USA, Catalog No. 7366040), which was filled with the ink and operated by a high-precision motorized arm. For this research, the printing dosing needle had an inner diameter (ID) of 410 μm and length of 12.7 mm (0.50”) (Nordson EFD, Westlake, USA, Catalog No. 7018272), which was used for the ink microextrusion. This was a straight needle of stainless steel with PP SafetyLok™ connection for secure connection to the cartridge. The extrusion was carried out using an Ultimus I fluid dispenser (Nordson EFD, Westlake, USA, Catalog No. 7012584), linked to a compressed air source facilitating the movement of the piston in the syringe by applying a given pressure depending on formulation, which should enable the microextrusion of the ink through the nozzle. The fluid dispenser was attached to the syringe barrel pressure adapter (Nordson EFD, Westlake, USA, Catalog No. 7012057). Throughout the entire process, the printing temperature was maintained at room temperature ~22°C.

4.2.15. 3D Bioprinting of Cell-Laden Viscous Chitosan Solutions

4.2.15.1. Preparation of Buffers at Varying pH and Study of Chitosan Solutions

Buffer solutions comprising ammonium acetate (NH_4Ac) and acetic acid (HAc) were prepared at various pH values ranging from 4.5 to 7.0. Initially, a 0.2 $mol \cdot L^{-1}$ HAc solution (1L total

volume) was prepared, to which NH_4Ac was added to reach a final concentration of 0.15 $mol \cdot L^{-1}$. This composition resulted in a buffer with a pH of approximately 4.5–4.8, representing the lowest pH condition used in this study. To obtain buffers at higher pH values (5.0, 5.3, 5.8, 6.1, 6.5, and 7.0), a 2 $mol \cdot L^{-1}$ HAc solution was titrated with a concentrated NH_4Ac solution (10 $mol \cdot L^{-1}$) until the target pH was reached. All buffers were sequentially filtered through 0.2 and 0.45 µm syringe membranes to ensure clarity and sterility. Chitosan samples were subsequently dissolved in the prepared NH_4Ac/HAc buffers at a concentration of 2 $mg \cdot mL^{-1}$ (0.2% w/v), by dispersing 60mg of chitosan in 30mL of the respective buffer. The chitosans used included fully deacetylated chitosan (DA 0), partially acetylated chitosan (DA 2.5%, serving as the parent polymer), and a series of reacetylated derivatives with degrees of reacetylation (R) of 0.1, 0.2, 0.3, 0.4, and 0.5. The dispersions were stirred mechanically at room temperature for 24 h to promote complete dissolution. Following incubation, solutions were transferred to sterile 50mL centrifuge tubes for further processing.

4.2.15.2. Potentiometric Titration

Chitosan solutions were prepared to obtain a final concentration of 0.01 mol L^{-1} with respect to amino groups. The required amount of each chitosan sample was calculated based on the moles of glucosamine units, corresponding to the amino group content. A stoichiometric amount of acetic acid (0.05 mol L^{-1}) was subsequently added to the polymer to ensure complete protonation of the amino groups and to facilitate dissolution. The mixture was stirred continuously at room temperature until a homogeneous solution was obtained. Thereafter, distilled water was added to adjust the total volume to 15mL for each chitosan sample. Potentiometric titration was conducted to determine the acid–base behavior of the chitosan solutions. The titrations were performed using a TitroLine® 7800 automatic titrator (SI Analytics, WA, Germany) equipped with a 20mL titration vessel and a combined glass electrode. The titration procedure involved gradual addition of standardized titrant under constant stirring, while continuously recording the pH variation. All experiments were carried out at ambient temperature (25 ± 1°C), and each measurement was repeated in triplicate to ensure reproducibility and accuracy.

4.2.15.3. UV/Visible Spectroscopy

The solubility of chitosan with varying degrees of acetylation (DA) was determined under different pH conditions using a UV–visible spectrophotometer (Lambda series, PerkinElmer, Baesweiler, Germany). Chitosan powders were dispersed in ammonium acetate/acetic acid (NH_4Ac/HAc) buffer solutions adjusted to the desired pH values. Each sample was prepared

to a final concentration of 2% (w/v) by gradual addition of chitosan under continuous magnetic stirring at room temperature until complete dispersion was achieved. The resulting mixtures were incubated for 24 h to ensure equilibrium dissolution. The apparent solubility was quantified by measuring the absorbance of each sample at 600 nm using the UV–vis spectrophotometer, with the respective buffer solution (without chitosan) serving as the blank reference. The absorbance values were used as indicators of turbidity, which inversely correlated with the solubility of chitosan in each pH condition. All measurements were performed in triplicate, and the results were reported as mean ± standard deviation.

4.2.15.4. 3D Bioprinting of Cell-Laden Chitosan/Cellulose Nanofiber Hydrogels

Cell-laden chitosan bioinks were prepared by incorporating NIH 3T3 fibroblast cells (murine fibroblast, strain: NIH/Swiss) into chitosan viscous solutions with varying degrees of acetylation (DA). Chitosan solutions were first prepared in NH_4Ac/HAc buffer solutions prior to cell encapsulation. Murine fibroblast cells (NIH 3T3) were cultured and expanded under standard cell culture conditions. Cells were maintained in T-25 cell culture flasks (25 cm^2; Sarstedt, Nümbrecht, Germany) containing Dulbecco's Modified Eagle Medium (DMEM; Gibco, Thermo Fisher Scientific, Leicestershire, UK) supplemented with 10% (v/v) fetal bovine serum (FBS) and 2 mM L-glutamine. Cultures were incubated at 37°C in a humidified atmosphere containing 5% CO_2. Cells were subcultured every 3–4 days and used for bioink preparation once they reached approximately 90% confluence. For passage, the culture medium was aspirated, and cells were rinsed twice with phosphate-buffered saline (PBS; Gibco, Thermo Fisher Scientific, UK) to remove residual serum proteins. Cells were detached using a 0.25% trypsin–ethylenediaminetetraacetic acid (EDTA) solution and incubated for 5 min at 37°C. The enzymatic reaction was neutralized by adding an equal volume of complete DMEM medium. The cell suspension was then centrifuged at 1500 rpm for 5 min. The supernatant was discarded, and the resulting cell pellet was resuspended in fresh culture medium to achieve the desired concentration for bioink preparation.

The cell suspension was gently mixed with the chitosan solutions to achieve a final cell density of 1.0×10^4 cells mL^{-1}. The resulting mixtures were homogenized carefully to ensure uniform cell distribution without inducing shear-induced cell damage. The prepared bioinks were subsequently transferred into sterile printing cartridges (Nordson EFD, Feldkirchen, Germany) and immediately centrifuged at 1500 rpm for 2 min to remove entrapped air bubbles and facilitate even cell distribution throughout the cartridges. Three-dimensional (3D) printing of cell-laden chitosan bioinks was performed using a 3D-Discovery Evolution bioprinter (RegenHU, Villaz-St-Pierre, Switzerland). The instrument is equipped with an x–y–z-axis positioning system integrated with a multi-tool charger, enabling the use of multiple printhead

stations, and a temperature-controlled building platform. The 3D printing process was designed and controlled via proprietary computer-aided design (CAD) software (BioCAD, RegenHU), which guided the motion of the extrusion tip along the defined trajectories. In this study, both extrusion-based and coaxial bioprinting techniques were employed to evaluate the cell compatibility of chitosan viscous solutions with varying physicochemical properties.

Extrusion-based printing of the cell-laden chitosan was performed after the sterile printing cartridges containing the prepared bioinks were mounted onto the bioprinter's extrusion head. The constructs were printed directly into 12-well culture plates prefilled with a coagulation bath composed of 5% (w/v) sodium tripolyphosphate (TPP) dissolved in phosphate-buffered saline (PBS, pH 7.4). Printing was carried out using precision conic dispensing tips with an inner diameter of 580 µm (Nordson EFD, Feldkirchen, Germany). One-layered square scaffolds (2 × 2 cm^2) were printed with a filament spacing of 0.85 mm, a printing speed of 20 mm s^{-1}, and an extrusion pressure ranging from 0.1 to 0.5 bar. The printed constructs were allowed to crosslink in the TPP/PBS coagulation bath for 3 min to ensure sufficient gelation. Subsequently, the coagulation medium was carefully removed, and the scaffolds were rinsed with sterile PBS for 3 min to eliminate residual TPP. The resulting CHI-based hydrogel scaffolds were immediately transferred to fresh culture medium for subsequent analyses.

For the coaxial bioprinting of cell-laden chitosan (CHI) viscous inks, a coaxial extrusion nozzle (RegenHU, Villaz-St-Pierre, Switzerland) for contact dispersing was used. The inner (core) channel was loaded with the NIH 3T3 cell-laden chitosan bioink prepared, while the outer (shell) channel was filled with either an alginate–gelatin blend (3% w/v alginate and 4% w/v gelatin) or alginate solution alone (4–5% w/v). The coaxial nozzle assembly consisted of an inner needle with an internal diameter of 0.3 mm and an outer needle with an internal diameter of 0.45 mm. Printing was carried out at a controlled temperature of 25°C under sterile conditions. The extrusion pressure was maintained between 0.4 and 0.7 bar, and the printing speed was set to 15 mm s^{-1} to ensure smooth filament deposition and stable coaxial flow. The printed constructs were collected directly in sterile culture plates containing a 4% (w/v) calcium chloride ($CaCl_2$) solution, which served as a crosslinking bath for the alginate-based shell. Crosslinking was allowed to proceed for 3 min to ensure adequate gelation and mechanical stabilization of the printed structures. Following crosslinking, the $CaCl_2$ solution was carefully removed, and the scaffolds were rinsed three times with phosphate-buffered saline (PBS) for 3 min each to eliminate excess calcium ions and unreacted materials. The resulting coaxially printed hydrogel scaffolds were then transferred to sterile Petri dishes containing complete cell culture medium and incubated under standard conditions (37°C, 5% CO_2) for subsequent cell viability and morphological analyses.

For extrusion-based 3D printing of cell-laden re-acetylated chitosan with cellulose nanofibers, the bioink was formulated by mixing a solution of a highly re-acetylated chitosan sample at 2%

(w/w) (R: 0.4) with a small portion of nanofibrillated cellulose (0.4% w/w), and NIH3T3 cells (10000 cells/mL). The mixture was directly printed into small cell-adherent Petri dishes that had been prefilled with a coagulation bath consisting of 0.5% (w/v) sodium tripolyphosphate (TPP) in phosphate-buffered saline (PBS). Printing was performed using precision conic dispensing tips with an inner diameter of 580 µm (Nordson EFD, Feldkirchen, Germany). Single-line fibers were printed at a speed of 20 mm s^{-1} under an extrusion pressure of 0.1–0.5 bar. The printed structures were then crosslinked in the TPP/PBS coagulation bath for 3 min to ensure proper gelation. Afterward, the coagulation solution was gently removed, and the scaffolds were rinsed with sterile PBS for 3 min to remove any residual TPP. The resulting chitosan-based hydrogel scaffolds were immediately transferred into fresh culture medium for further analysis.

4.2.15.5. Live/Dead Cell Viability Assay

Cell viability within the chitosan (CHI)-based bioinks was evaluated to assess the survival and proliferation of NIH 3T3 fibroblasts encapsulated in the printed hydrogel scaffolds. Viability was determined using a fluorescent live/dead assay (LIVE/DEAD™ Viability/Cytotoxicity Kit, Thermo Fisher Scientific, Leicestershire, UK), based on calcein acetoxymethyl ester (calcein AM) and ethidium homodimer-1 (EthD-1) staining. After 1, 3, 5, 7, 10, and 13 days of culture, the cell-laden 3D scaffolds were gently washed with Hank's Balanced Salt Solution (HBSS; Gibco, Thermo Fisher Scientific, UK) to remove residual culture medium. Subsequently, the scaffolds were incubated with the LIVE/DEAD™ staining solution prepared according to the manufacturer's protocol and incubated for 15 min at room temperature in the dark. Following incubation, the samples were rinsed once with HBSS to remove excess dye. Fluorescence imaging was performed using a Leica laser scanning confocal microscope (Leica Microsystems, Wetzlar, Germany). Live cells were visualized as green-fluorescence due to the enzymatic conversion of calcein AM within the cytoplasm, whereas dead cells were identified by red nuclear fluorescence resulting from EthD-1 binding to DNA of membrane-compromised cells. Acquired confocal images were used for qualitative assessment of cell distribution and viability throughout the 3D constructs.

5. Results and Discussions

5.1. Biopolymer Fibers of High Strength and Enhanced Orientation by the Synergy of High/Low Molecular Weight Chitosans in Hybrid Biomaterials Processed by Gel Spinning

In the field of biomaterials, there is an increasing interest in using bio-based materials, especially biopolymers with relevant biological properties, for the most varied applications in biomedicine. Chitosan (CHI) is a linear polysaccharide composed of a copolymeric structure, consisting of (1→4) linked units of 2-acetamido-2-deoxy-β- D-glucopyranose and 2-amino-2-deoxy-β-D-glucopyranose. It is primarily derived through the deacetylation of chitin. CHI is regarded as the second most abundant natural polysaccharide, following cellulose, and it is mainly extracted from crustacean shells and cephalopod endoskeletons. Recent interest in chitosan has surged within the fields of bioengineering, biofabrication, and biomedicine, owing to its favorable biological characteristics, including bioactivity, biocompatibility, biodegradability, low toxicity, and hemostatic properties. The mechanical properties of chitosan are largely influenced by its macromolecular structure and the degree of deacetylation (DA), because both characteristics govern the polymer chains interactions and network formation. Higher molecular weight and longer chains increase entanglement and tensile strength, while a higher DA introduces more free amine groups, enhancing possibility for hydrogen bonding and intermolecular interactions. Together, these structural features determine the stiffness, flexibility, and overall mechanical performance of chitosan-based materials. Additionally, its solubility in acidic aqueous environments makes CHI suitable for various processing techniques, including wet spinning. Wet-spun chitosan fibers have been previously produced using either multifilament spinning, which involves washing the fibers in organic solvents to prevent them from adhering to each other in the yarn, or monofilament spinning, which eliminates this issue. In previous studies, yarns made from multifilament spun fibers have been washed with solvents such as acetone or methanol. Additionally, chitosan solutions for wet spinning have been formulated with organic cosolvents, including methanol, isopropyl alcohol, and propane-1,2-diol. Cellulose nanofibrils (CNFs), known for their exceptional mechanical properties due to their high crystallinity and aspect ratio, are considered promising green nano-reinforcement agents, also due to their ability to form both intramolecular and intermolecular networks through hydrogen bonding. These properties, coupled with their biocompatibility, possible biodegradation, and the fact that CNFs constitute sustainable materials that originate from plant sources highly abundant in Earth, make CNFs a promising bio-based reinforcement material for composites in biomaterials for biomedical applications. The reinforcement of polysaccharide hydrogels and fibers with nanocellulose has been previously reported [143], as

well as in film materials produced through a straightforward casting-evaporation technique. In the case of wet spinning, it necessitates precise management of solution viscosity and efficient material flow through spinneret orifices to prevent clogging. Furthermore, during the wet-spinning process, uniaxial alignment of both chitosan polymer chains and nanoparticles is anticipated to occur during extrusion, drawing, and drying stages. Low molecular weight chitosan (LMW) might be another potential reinforcing mate- rial in biomedical chitosan fibers. Low-molecular-weight (LMW) chitosan demonstrates higher solubility and lower viscosity, which enhances its bioavailability and facilitates its incorporation into biological systems. The reduced size of LMW chitosan allows for more efficient cellular uptake and interaction with biomolecules, conferring superior antimicrobial, antioxidant, anti-inflammatory, and immunomodulatory properties in comparison to its high-molecular-weight counterpart. This makes LMW chitosan particularly advantageous for applications driven by biological activity, including drug delivery, wound healing, and nutraceutical formulations. Polymeric chitosan and chitosan oligomers have been demonstrated to promote the formation of phytoalexins or antimicrobial chemicals, which help restrict disease transmission, owing to chitosan's strong antibacterial capabilities. Rufino et al. described the chemical synthesis of various sizes of chitosan oligomers, which resulted in particular biological activity [229]. Lower molecular weight chitosan variations exhibit higher crystallinity, which is a key element in chitosan crystallization during optimization of wet spinning process. Moreover, the biological activity of chitosan is strongly regulated by its molecular weight, degree of deacetylation (DA), solution pH, and other variables, as well as the target organism. In biomedical settings, LMW chitosan is notably efficient for anticancer activity, oral insulin administration, treatment of gastric ulcers, liver protection, blood cholesterol reduction, diabetic control, and antioxidant benefits [233, 234]. In previous studies, chitosan-based fibers were shown to be cytocompatible and demonstrated antibacterial activity [232]. In vivo studies also reported low inflammatory response and slow degradation rate after subcutaneous implantation in rats. More specifically, our wet spun chitosan fibers are formulated with low molecular weight chitosan (LMW) of low degree of acetylation (DA = 2.5%), which might bring additional biological activities. The impact of molecular weight (Mw) on the antibacterial activity was recently reviewed and modeled [235]. The intrinsic impact of weight-average Mw can be described as a linear relationship with the antibacterial activity (evaluated as Log(1/MIC), where MIC is the minimum inhibitory concentration when Mw is below a critical molar mass concentration (CMW), with a plateau activity achieved when Mw > CMW [235]. Thus, LMW chitosan, as proposed in the present work, should contribute to a maximum bacterial inhibition effect, combined with improved bioavailability, due to better solubility and faster release of shorter chains from processed fibers. Such bioavailability of LMW chitosan also could improve their antioxidant properties and increase cellular intake [234]. Finally, the association of low and high molecular chitosan in

wet-spun fibers could combine the structural and mechanical properties associated with the high molar mass of the polymer, and the bioactivity-driven applications promoted by the low molecular mass. Wet spinning of chitosan represents an important research area, addressing the limitations of chitosan-based materials, particularly in enhancing their mechanical properties. These properties are often diminished in the wet state due to the highly hydrophilic nature of chitosan. The objective of this study is to combine high molecular weight (HMW) chitosan solutions with low contents of CNFs and low molecular weight chitosan (LMW, "oligomers"), to develop chitosan-based spun composite fibers of high strength, by modulating the microstructure and properties of fibers in a wet-spinning process. These fibers have promising applications in biomedicine, for example, as biomedical textile fibers. The approach used in this work aims to enhance the performance of chitosan-based bioactive materials, with potential biomedical applications like in tissue engineering, suture threads, knitted fabrics, wound healing, and repairing and regeneration of mechanically demanding tissues.

In this section 5.1, the development of chitosan-based composite fibers is presented, focusing on the combination of high molecular weight (HMW) chitosan with small amounts of cellulose nanofibers (CNFs) and low molecular weight (LMW) chitosan oligomers. The influence of these components and the controlled wet-spinning parameters on the fibers' microstructure and mechanical performance was investigated to enhance their suitability for tissue engineering applications.

5.1.1. Rheological Behavior of Mixture Solutions of Low (LMW) and High-Molecular Weight (HMW) Chitosan Viscous Formulations Filled with Cellulose Nanofibers (CNF)

Figure 5.1.1 presents the flow diagrams of the different formulations. These include chitosan/cellulose nanofiber mixtures prepared with low molecular weight chitosan, which were synthesized at molar ratios (r) of glucosamine to $NaNO_2$ equal to 20 and 50. As expected, adding low molecular weight to the system, initially consisting of high molecular weight, reduced the Newtonian viscosity of the collodions. The HMW chitosan will have a reduced polymer mobility, leading to a higher viscosity compared to LMW chitosan. Thus, chitosan concentration and average molecular weight of the mixture allow for control over viscosity. Then, the incorporation of CNF into the mixture of high and low molecular weight chitosan re-increased the zero-shear viscosity. This effect was enhanced when adding the chitosan of intermediate low molecular weight. This is specially enhanced when adding "higher" low molecular weight (Mw) as for r50 to the systems having the highest contents of CNF (0.4 and 0.5% (w/w)). This might be explained due to strong interactions between CNF and chitosan macromolecules in those suspensions of higher concentrations of CNF and higher average molecular weight of chitosan [143]. Figure 5.1.1 illustrates the relationship between viscosity

(η) and shear rate (γ.) for suspensions containing high (HMW) and low molecular weight chitosan (LMW for molar ratios r20 and r50), reinforced with varying CNF contents (0, 0.3, 0.4, and 0.5 (w/w)). Each dispersion exhibits a nonlinear, non-Newtonian shear-thinning behavior typical of CHI solutions, where η decreases as γ. increases due to the disentanglement of polymer chains and the disruption of the initial polymer solution structure, which enhances chain orientation [236, 237]. Further comparisons were made for the systems of CHI/r20/CNF and CHI/r50/CNF at different CNF contents (Figure 5.1.1b, c). The use of low molecular weight produced for r50 introduces longer chains than those produced for r20. Together with CNFs, they formed intermolecular aggregates that limited polymer chain movement and disentanglement, resulting in a more rigid structure [238], also increasing shearing effects.

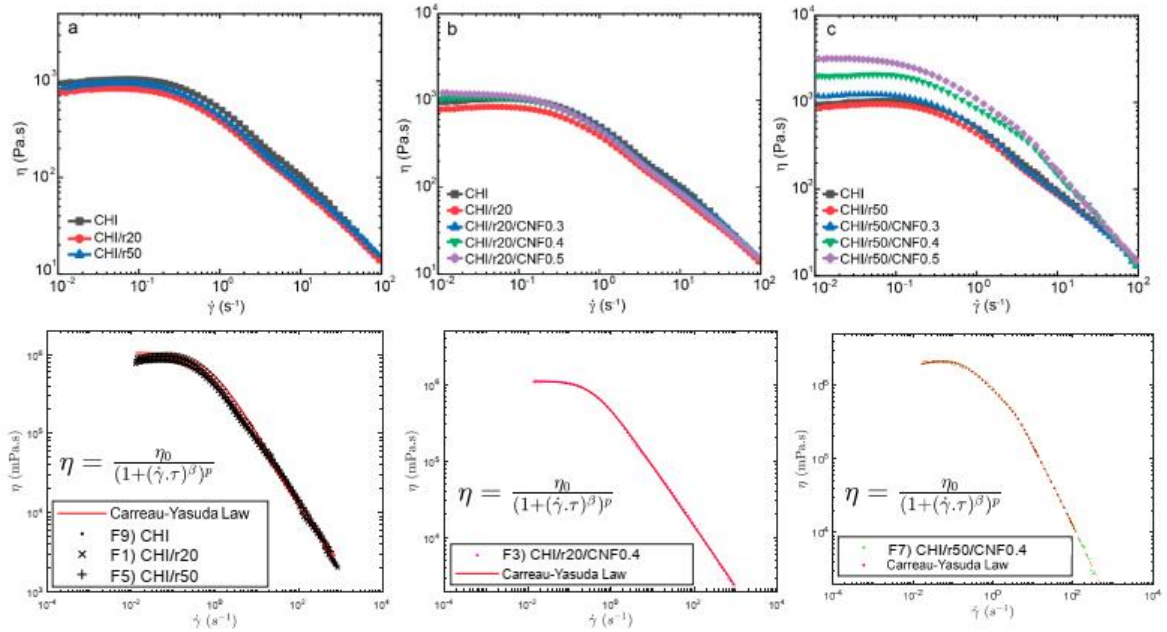

Figure 5.1.1. Flow diagrams showing the evolution of the viscosity (*η*) vs. shear rate (*γ*.) of: (**a**) HMW chitosan with LMW chitosan ("oligomers") produced for ratio r = 20 or r = 50 (formulations: F1 or F5; Table 5.1.1, and CHI (HMW) reference solution (formulation: F9; Table 5.1.1), (**b**) CNF-filled CHI/LMWr20 suspensions (formulations: F2, F3, F4; Table 5.1.1) and CHI reference solution, and (**c**) CNF-filled CHI/LMWr50 suspensions (formulations: F6, F7, F8; Table 5.1.1) and CHI reference solution. (***Bottom***) Examples of modeling of the flow diagrams with Carreau-Yasuda law (Equation (5.1.1)). Reproduced with permission from Tran et. al., 2025 [238].

Table 5.1.1. Flow parameters determined from the fitting of the viscosity vs. shear rate curves of different chitosan/cellulose nanofiber collodions also containing low molecular weight chitosan of used molar ratios r20 or r50 in the depolymerization reaction, by using the Carreau-Yasuda (Equation (5.1.1), Figure 5.1.1). Reproduced with permission from Tran et. al., 2025 [238].

	Formulation	Log_{10} (η_0/mPa·s)	τ (s)	*P*	*β*
(F1)	CHI/r20	5.9448	1.8582	0.7408	1.1043
(F2)	CHI/r20/0.3CNF	6.0558	2.3068	0.6299	1.2686
(F3)	CHI/r20/0.4CNF	6.0459	2.5849	0.5926	1.3280
(F4)	CHI/r20/0.5CNF	6.0878	2.9427	0.6281	1.2493
(F5)	CHI/r50	5.9867	2.0874	0.6140	1.2932
(F6)	CHI/r50/0.3CNF	6.0926	2.7594	0.4994	1.6075
(F7)	CHI/r50/0.4CNF	6.3558	0.8584	1.4199	0.8217

(F8)	CHI/r50/0.5CNF	6.5297	1.5515	1.2003	0.8862
(F9)	CHI	6.0229	1.4948	0.7200	1.1963

At higher shear rates, the typical non-Newtonian shear thinning behavior of chitosan solutions was observed, with a Power law decrease of viscosity with increasing shear rates. The flow behavior is related to the disentanglement of the chitosan chains, also inducing chain orientation. Overall, flow-induced orientation tends to form an anisotropic structure under the action of a shear field [236, 237]. In the highest shear range, the viscosity similarly decreased in the "pure" chitosan solutions and in the chitosan/cellulose nanofiber viscous suspensions, revealing that the shear-thinning behavior in the latter is governed by the disentanglement of chitosan chains and practically not affected by the presence of the nanofibers, which should become oriented in the flow direction [239]. This is advantageous to achieve the extrusion of nanofiber reinforced viscous chitosan systems without compromising the extrudability of chitosan systems themselves as in fiber spinning processes. This should be the first premise to achieve the processing of nanofiber-filled chitosan fibers by wet spinning to develop fibers of improved mechanical performance, as envisaged in this work. A Carreau-Yasuda law (Equation (5.1.1)) was used to model the flow diagrams (η vs. shear rate) of the chitosan solutions and the chitosan/cellulose nanofiber viscous suspensions that also contained low molecular weight chitosan as illustrated in Figure 5.1.1 (Bottom) as the following:

$$\eta = \frac{\eta_0}{(1 + (\gamma . \tau)^{\beta})^{p}} \qquad \text{(Eq. 5.1.1)}$$

where η0 is the Newtonian or zero-shear viscosity, τ is the transition time, β is the exponent that accounts for the width of the transition region between the zero-shear viscosity and the Power law region, and p = (1 − β)/β is the viscous exponent. The parameters obtained for the different formulations after modelling with the Carreau-Yasuda law are displayed in Table 5.1.1. For the CNF 0.4 and 0.5% (w/w), having low molecular weight chitosan from used ratio r50, a second fast flow mode was introduced to obtain a good fit with the model. This could be explained to a representative interaction between the CNF and the low molecular weight chitosan of intermediate Mw (for r50) specially being significant at those high contents of cellulose nanofibers (0.4 and 0.5% (w/w)).

5.1.2. Structure of Spun Fibers. Composite Fibers and Relation to Macromolecular Structure of Chitosan Determined by SEC-MALLS

Figure 5.1.2a displays the size-exclusion chromatograms (SEC) of the starting chitosan of high molecular weight (HMW) as well as of the low molecular weight chitosan (LMW) produced by nitrous deamination depolymerization of the HMW sample. Figure 5.1.2 confirmed the

decreasing of chitosan molecular weight by varying the molar ratio r of glucosamine to NaNO2 (for example: r20 and r50). Figure 5.1.2 also shows the chromatograms of the chitosan contained in the different fiber formulations. For this analysis, the spun fibers were redissolved in buffer pH 4.5 (AcOH (0.2 M)/AcONH4 (0.15 M) for solubilization of chitosan and the obtained system was subsequently filtered through 0.22 µm pore size membranes (Millipore). The SEC analysis allowed verifying the obtaining of bimodal distribution of molecular weights, containing chitosan of high and low molecular weight after the fiber spinning process, with elution volumes corresponding to that of the HMW and LMW chitosan used in viscous collodion. Due to the non-solubility of CNF in buffer pH 4.5, it was possible to reconstruct the chitosan weight distribution within the fiber composite. Figure 5.1.2b shows, for each formulation, two Gaussian curves representing the distribution of components of HMW and LMW chitosan, respectively. It confirmed that despite the high mobility of the low molecular weight chains, they were not removed during coagulation in base or water washing baths and remain present in the final fibers (Figure 5.1.2b). Table 5.1.2 summarizes the obtained molecular weight and polydispersity index (Đ) of chitosan in the different samples.

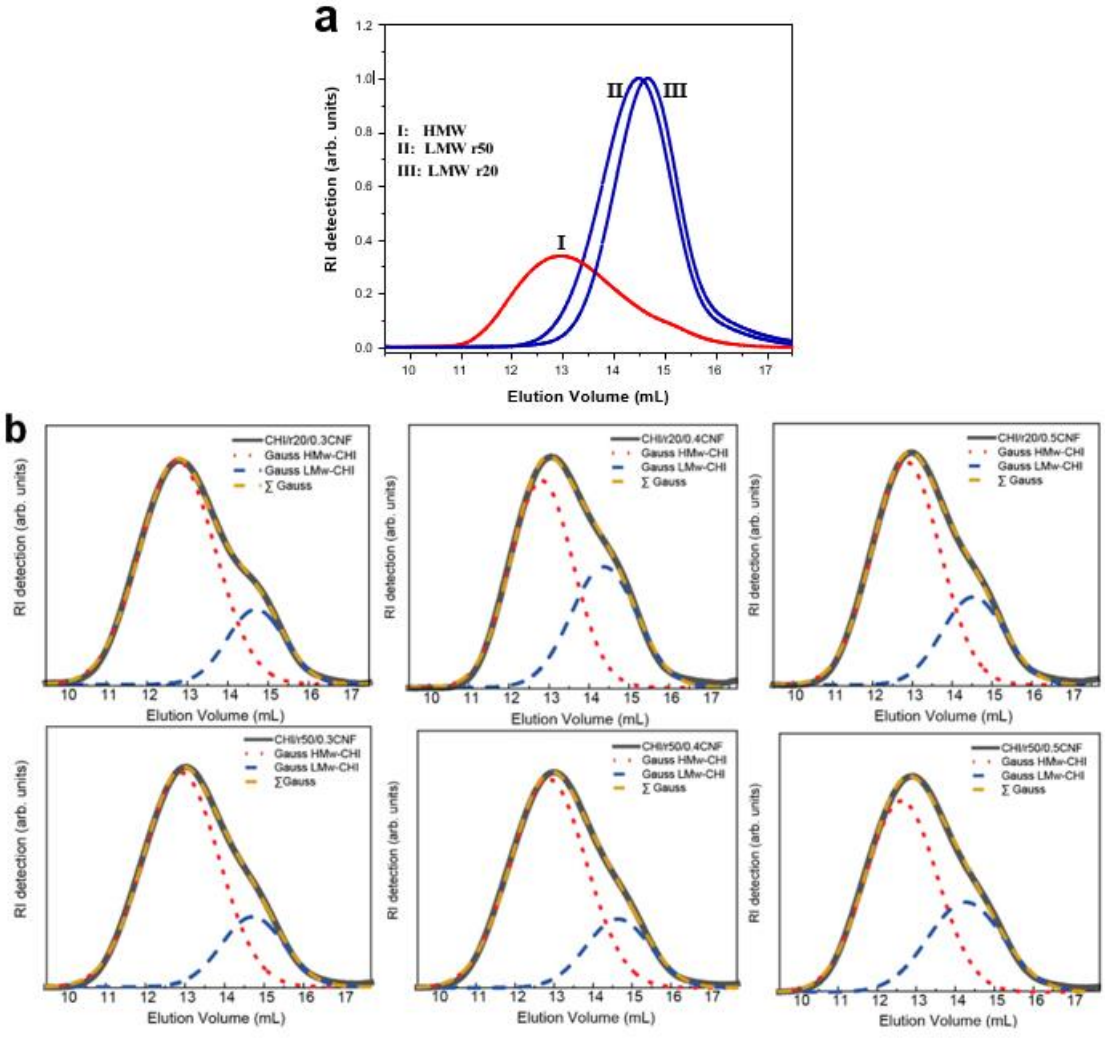

Figure 5.1.2. The SEC-MALLS analysis of the colloidal dispersions for: (**a**) low (LMW, blue) and high molecular weight (HMW, red) chitosan weight distribution, and (**b**) chitosan molecular weight distribution

in the processed spun fibers containing low (LMW) and high molecular weight (HMW) chitosan. The curves in (**b**) are deconvoluted using the two Gaussian (Gauss HMW-CHI for HMW chitosan (red), and Gauss LMW-CHI for LMW chitosan (blue)), with a sum (ΣGauss) that coincides with the experimental curve of the SEC chromatogram. Reproduced with permission from Tran et. al., 2025 [238].

Table 5.1.2. Molecular weight and polydispersity index of CHI formulations. Reproduced with permission from Tran et. al., 2025 [238].

	Formulation	Chitosan Mw (g/mol)	Chitosan Polydispersity Index Đ
(F1)	CHIr20	29340 (±0.63%)	1.3 (±1.33%)
(F2)	CHI/r20/0.3CNF	378100 (±0.91%)	2.8 (±1.35%)
(F3)	CHI/r20/0.4CNF	243600 (±0.62%)	2.3 (±1.02%)
(F4)	CHI/r20/0.5CNF	284100 (±0.69%)	2.4 (±0.91%)
(F5)	CHIr50	43840 (±0.49%)	1.5 (±0.89%)
(F6)	CHI/r50/0.3CNF	365500 (±0.98%)	2.8 (±1.37%)
(F7)	CHI/r50/0.4CNF	427100 (±1.03%)	2.7 (±1.65%)
(F8)	CHI/r50/0.5CNF	434600 (±1.04%)	2.7 (±1.79%)
(F9)	CHI	554000 (±1.06%)	1.6 (±1.59%)

Table 5.1.2 shows the molecular weight and polydispersity index (Đ) of the different chitosan samples. The samples containing pure chitosan of high molecular weight HMW (CHI) or of low molecular weight LMW (produced for ratios r20 and r50) exhibits a relatively low Đ (≤1.6), indicating a narrow polymer molecular weight distribution. It is important to note that the degree of acetylation (DA) in CHI remains unchanged after the depolymerization reactions by nitrous deamination, suggesting that the acetylation process is not affected by the changes in molecular weight during this reaction.

5.1.3. Fourier-Transform Infrared Spectroscopy (FTIR) of the spun fibers

The bonding mechanism between chitosan and CNF in the composite fibers was investigated using the Fourier transform infrared spectroscopy (Figure 5.1.3). Both chitosan alone and chitosan/CNF composite fibers exhibit a broad absorption band between 3350–3150 cm^{-1}, corresponding to O-H and N-H stretching vibrations. This indicates the formation of inter-molecular hydrogen bonds between CNFs and CHI molecules. The peaks at 2934 and 2852 cm^{-1} are attributed to the asymmetric and symmetric stretching vibrations of the C-H group, respectively. The carbonyl band, which is usually observed at ~1670 cm^{-1} for chitosan in its free amine form, slightly shifted to a lower wavenumber when acetic acid was added to chitosan to form a chitosan-acetate salt complex as it can persist in our fiber processing. Indeed, for some spun fibers the presence of remaining sodium acetate was still revealed after washed as observed in the X ray diffraction patterns (see below). A characteristic absorption related to the amide I group in CHI was observed as a shoulder at 1671 cm^{-1}, corresponding to C=O stretching. Additionally, the amide II group presents a peak at 1574 cm^{-1}, which corresponds to both N-H bending vibration and NH3+ symmetric deformation. An increase in

CNF content leads to a rise in the intensity of the latter peak, indicating favorable interactions (electrostatic and hydrogen bonding) between the COO- group of cellulose and the amine group of CHI. In summary, the band region 1630–1540 cm^{-1} is normally assigned to the amide group, which suggests the interaction of amino groups of chitosan with carboxyl groups as expected in fibers of chitosan-acetate interacting with partially carboxylated cellulose nanofibers. Furthermore, the methyl distortion is observed approximately at 1380 cm^{-1}, and the stretching of the C–O groups from primary and secondary hydroxyl groups shows characteristic bands at 1044 and 1013 cm^{-1}, respectively. Finally, CHI and other polysaccharides exhibit a fingerprint region with peaks around 800–1000 cm^{-1}.

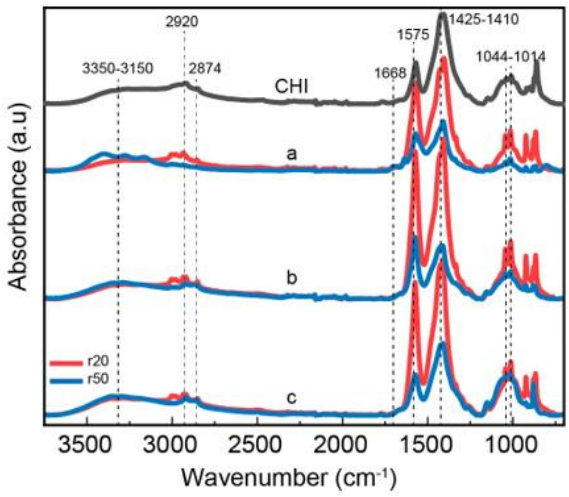

Figure 5.1.3. ATR-FTIR spectra of spun composite fibers consisting of high molecular weight chitosan (HMW), low molecular weight chitosan (LMW) as obtained using different molar ratios of glucosamine to NaNO2 (r20: red; r50: blue), and cellulose nanofibers (CNF) at different contents: (a) 0.3; (b) 0.4 and (c) 0.5%; as well as CHI) the reference spectrum of the pure high molecular weight chitosan fibers (HMW). Reproduced with permission from Tran et. al., 2025 [238].

5.1.4. Morphology and Microstructure of Fiber Yarns

The lateral and cross-sectional surface morphology of the spun fibers was analyzed using scanning electron microscopy (SEM), and transmission electron microscopy of ultrathin sections, which analyses were performed transversally (cross-section) or along the axial direction of fibers. The SEM micrographs in Figure 5.1.4 reveal the good compatibility of cellulose nanofibers with chitosan matrix in composites, due to the similar structure of the polysaccharides chitosan and cellulose as well as the possibility of electrostatic interaction between matrix and nanofibers, especially at the surface of the cellulose nanofibers. The spun fibers display a relatively homogeneous inner microstructure, which confirms strong compatibility between nanofiber filler and matrix and thereby an effective formation of composite, with the presence of also low molecular weight chitosan into the matrix, and low

contents of CNF [143]. For the higher CNF contents (0.4, and 0.5% (w/w)), the outer surface of fibers is characterized by a fibrillar topography for formulations containing any of the synthesized low molecular weight chitosan (for r20 and for r50), which effect should result from the spinning and stretching process and especially enhanced for higher nanofiber contents in composites. The orientation of that outer fibrillar microstructure observed by SEM aligns parallel to the stretching direction. In the cross-sectional microstructure, an internal homogeneity is also observed for all spun fibers with CNF contents 0.3 and 0.4% (w/w) as well as for the fibers with CNF content of 0.5% with the low molecular weight chitosan of lower Mw (for r20). In contrast, for spun fibers with that higher CNF content of 0.5% incorporating low molecular weight chitosan of higher Mw (for r50) it seems that the homogeneous microstructure starts to be disrupted, due to the higher concentration of nanofibers and increase of average molecular mass of chitosan chains [143]. Figure 5.1.4k shows that the average diameter of the spun fibers ranged from 60 to 98 μm, with the presence of r50 “oligomers” and highest CNF content (0.5% (w/w)) contributing to an increase in diameter.

Microscopy observations at higher resolution, which were performed by transmission electron microscopy (TEM) of ultrathin fiber sections, allowed better characterizing the inner microstructure of the fibers. In the micrographs of Figure 5.1.5, a pattern of parallel arrangements with a period width of 50–100 nm is observed when looking at sections cut along the spun fiber axis (Figure 5.1.5 *Middle*). This observed period in the patterns is in the range of the average width of the nanofibrils constituting the nanofibrillated cellulose filler CNF, which nanofibrils have an average width of 35.2 ± 8.1 nm with bundles up to 100 nm. The TEM results might reveal the good dispersion of the cellulose nanofibers in the chitosan matrix, even at the resolution of single nanofibril bundles as present in the starting cellulose nanofiber material (CNF suspension), which was added to the chitosan-based viscous collodion to be spun into hybrid fibers. A preferential orientation in the direction of the fiber axis was observed in the patterns, which might coincide with the orientation of cellulose nanofibers inside the composite, and/or the orientation of the semicrystalline chitosan produced after stretching and drying while spinning [143]. The cross-sectional ultrathin section of the spun fibers in the TEM micrographs (Figure 5.1.5 *Bottom*) shows homogeneously distributed bright and dark regions, which might correspond to regions containing cellulose nanofiber and chitosan, respectively, matching with the patterns observed when looking at orientation along fiber direction as described above (Figure 5.1.5 *Middle*).

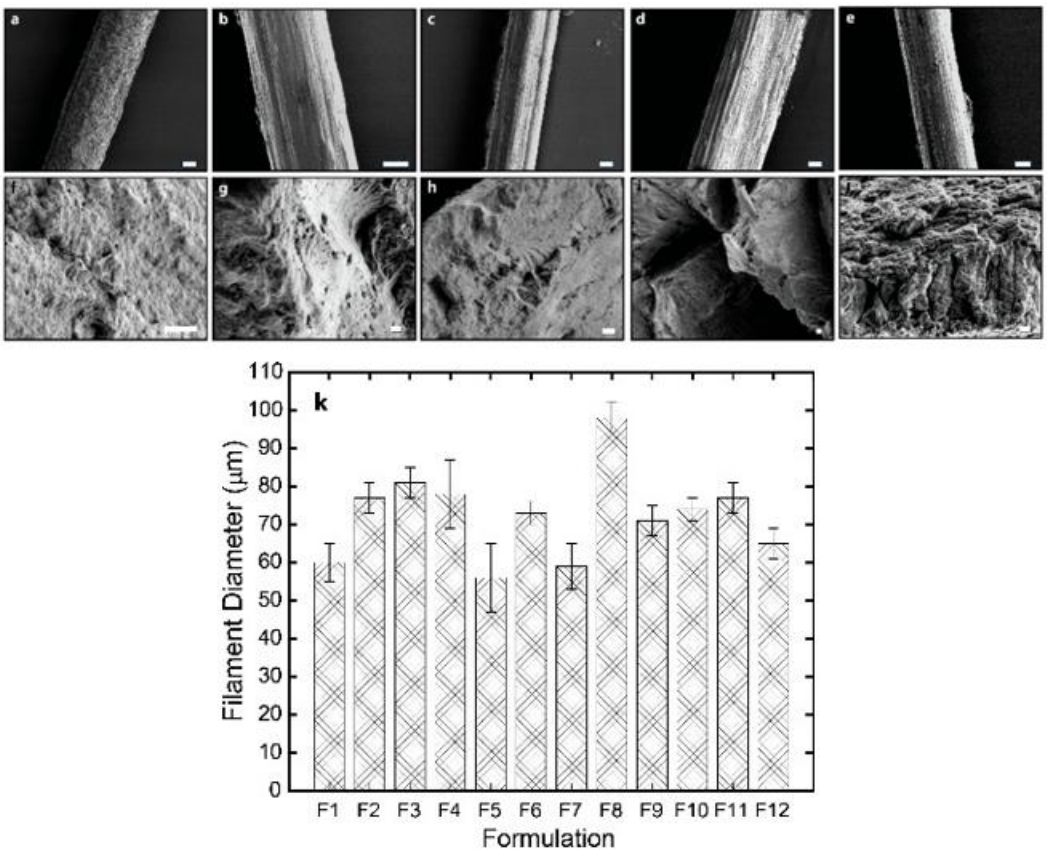

Figure 5.1.4. The SEM micrographs of the lateral (*top*) and fracture cross-section (*bottom*) surface of the spun HMW/LMW/CNF composite fibers of (**a,f**) CHI/r20/CNF0.3; (**b,g**) CHI/r20/CNF0.4; (**c,h**) CHI/r50/CNF0.4; (**d,i**) CHI/r20/CNF0.5; and (**e,j**) CHI/r50/CNF0.5. The scale bars for the lateral surface are 20 μm, and the scale bars for the fracture cross-section surface are 2 μm. (**k**) The histogram showing the mean fiber diameter obtained with the different HMW/LMW/CNF collodion formulations (F1–F12). Reproduced with permission from Tran et. al., 2025 [238].

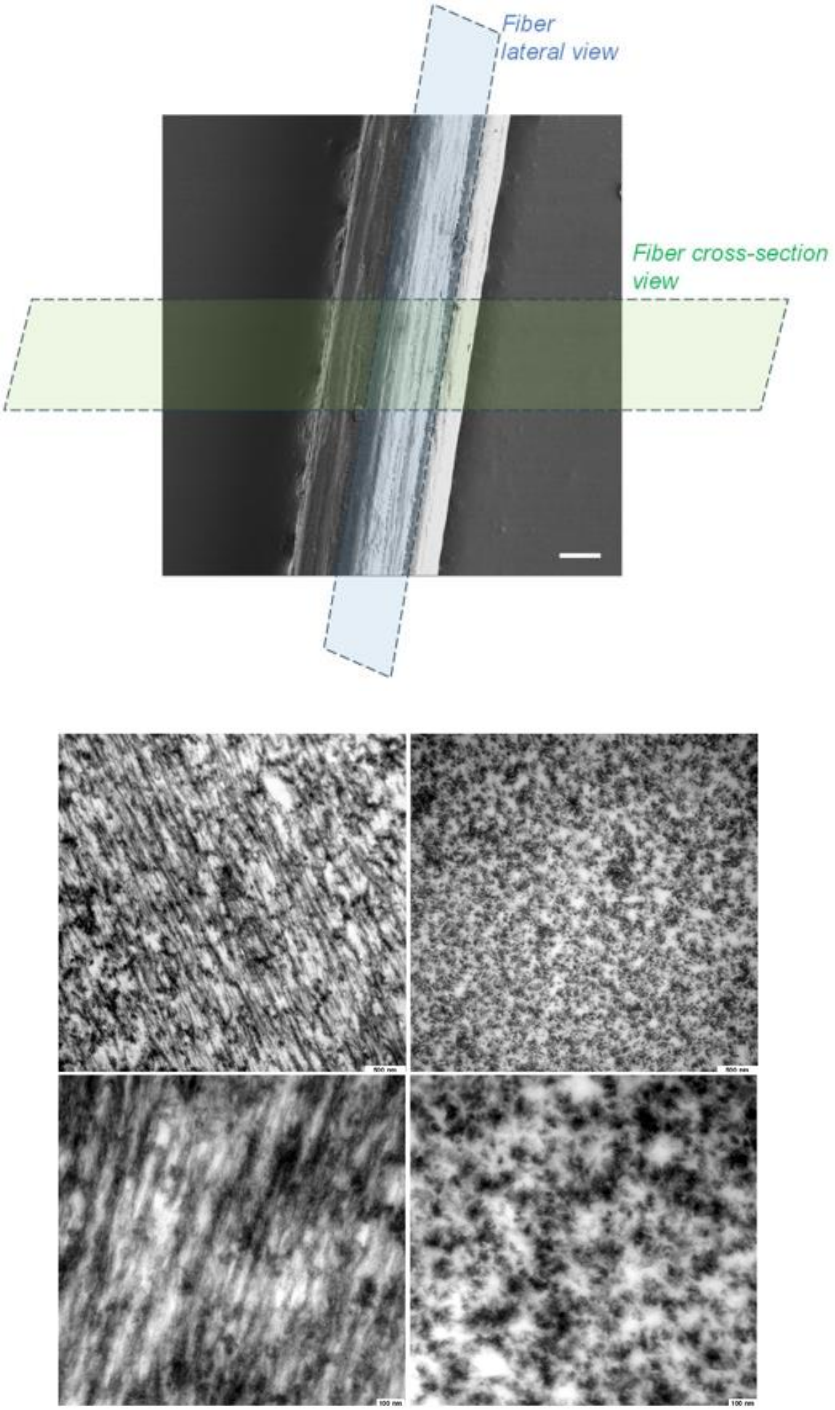

Figure 5.1.5. Micrographs of ultrathin section of spun hybrid fiber produced from formulation F7 (CHI/r50/CNF0.4), which consists of low molecular weight chitosan (for r50) at 0.6% (w/w), cellulose nanofiber content 0.4% (w/w), and high molecular weight chitosan at 3.4% (w/w). (*Top*) The SEM micrograph of fiber overview, with the scale bar of 20 µm. (*Middle-left*) The TEM micrograph of fiber cut parallel to the fiber axis (Lateral view). (*Middle-right*) The TEM of fiber cut perpendicular to the fiber axis (Cross-section view). (*Bottom-left*) Higher magnification photo of fiber cut parallel to the fiber axis (Lateral view). (*Bottom-right*) Higher magnification photo of fiber cut perpendicular to the fiber axis (Cross-section view). Reproduced with permission from Tran et. al., 2025 [238].

5.1.5. Crystalline Microstructure of Spun Fibers at Wide-Angle X-Ray Scattering (WAXS)

The hybrid chitosan/cellulose nanofiber spun fiber composites were examined using X-ray diffraction, which shows appropriate anisotropic behavior along the direction of fiber stretching (Figure 5.1.6), with preferential orientation of the hydrated chitosan allomorph as displayed in the 2D diffraction images by the arc signal of the corresponding crystallo- graphic planes. Figure 5.1.6e displays the X-ray scattering radial average profile curves with the main crystallographic peaks of the biopolymers. These peaks were observed at 2θ = 10.61° for the $(020)_h$ planes of the hydrated crystalline polymorph of chitosan, and at 19.85° and 20.38° for the reflections of the $(200)_h$ and $(220)_h$ planes of the hydrated polymorph. The overall spectra are characteristic of hydrated CHI. In some samples, the washing with water did not effectively remove the salt sodium acetate produced as byproduct during neutralization, and crystallographic signal of that salt was observed in the WAXS pattern of some fiber samples. For quantitative analyses of WAXS data, the sharp peak signals of salt were removed in the WAXS radial profile, to better investigate the crystalline aspects related to chitosan and cellulose.

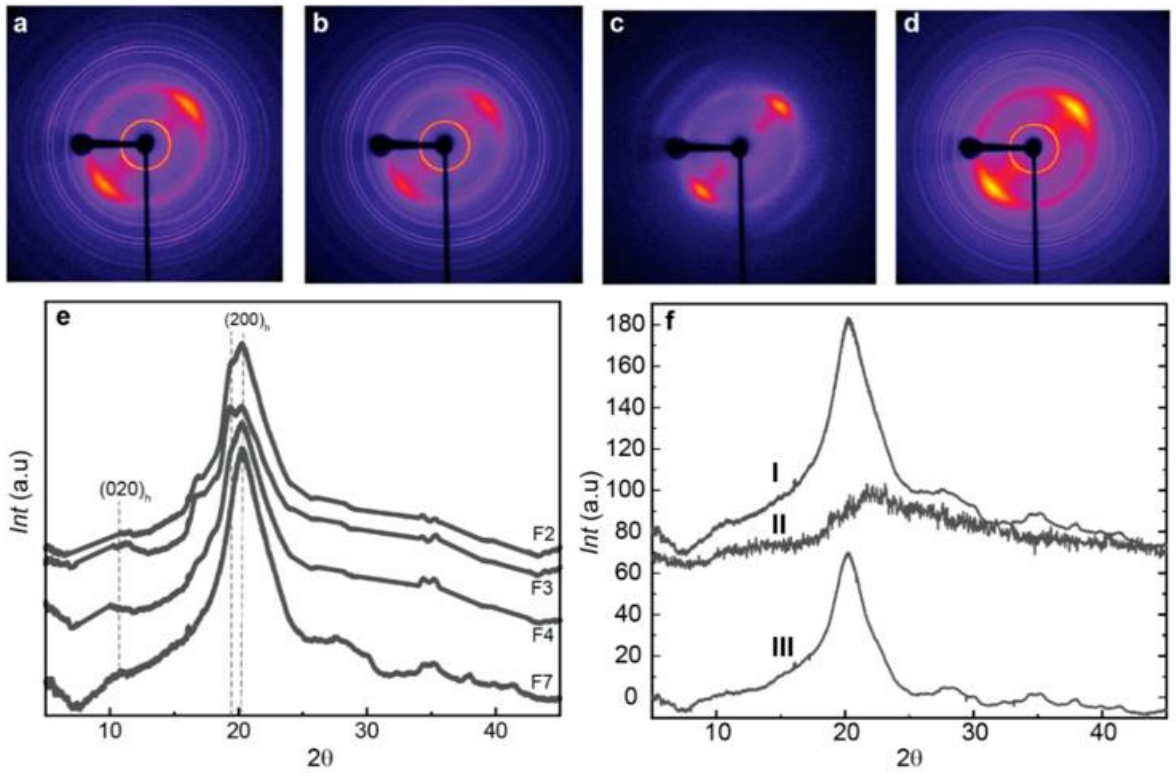

Figure 5.1.6. (*Top*) Two-dimensional wide-angle X-ray scattering (2D-WAXS) images of the spun CHI/OLIG/CNF fibers of (a) CHI/r20/CNF0.3, (b) CHI/r20/CNF0.4, (c) CHI/r50/CNF0.4, and (d) CHI/r20/CNF0.5 with fiber axis tilted by −45◦ from the vertical position. (*Bottom*) (e) Radial average over the 360◦ azimuth of the above 2D-WAXS images of spun fibers of varied CHI/OLIG/CNF formulations. (f) Procedures for the calculation of crystallinity indexes from WAXS diffraction patterns of the fibers. (fI) Diffraction diagram of the original CHI/r50/CNF0.4 fiber. (fII) Diffraction diagram of the amorphous

chitosan sample. (fIII) Estimated crystalline contribution of CHI/r50/CNF0.4 fiber after subtraction of the area of the amorphous diffractogram II. Reproduced with permission from Tran et. al., 2025 [238].

Chitosan is a semicrystalline polymer, composed of both amorphous and crystalline phases. The crystallinity index (CrI) gives insight into the percentage of crystalline regions with respect to the sum of amorphous and crystalline phases. Moreover, higher crystallinity typically leads to increased rigidity and thereby stiffness and strength of the material. To calculate the crystallinity index (CrI), we used the diffractogram of an experimentally obtained amorphous chitosan. The amorphous diffractogram was adjusted by a coefficient, to match the amorphous background in the diffractograms obtained for the spun fibers (Figure 5.1.6f). The CrI was determined by comparing the amorphous contribution with the total area of the diffractogram. Figure 5.1.7 presents the CrI values obtained for spun fibers of different formulations. It can be observed that the combined addition of LMW chitosan and CNF to HMW chitosan contributes to increasing the crystallinity in the fibers, with a higher contribution being observed when adding low molecular weight produced for r50 than for r20. This is a higher average molecular mass of chitosan will contribute to obtaining fibers of higher crystallinity. The observed increase in CrI is primarily associated with the presence of CNF, as chitosan polymer chains adsorb to the CNF surface during the coagulation and stretching processes, acting the nanofiber as nucleating points to promote the growth of chitosan crystals [143].

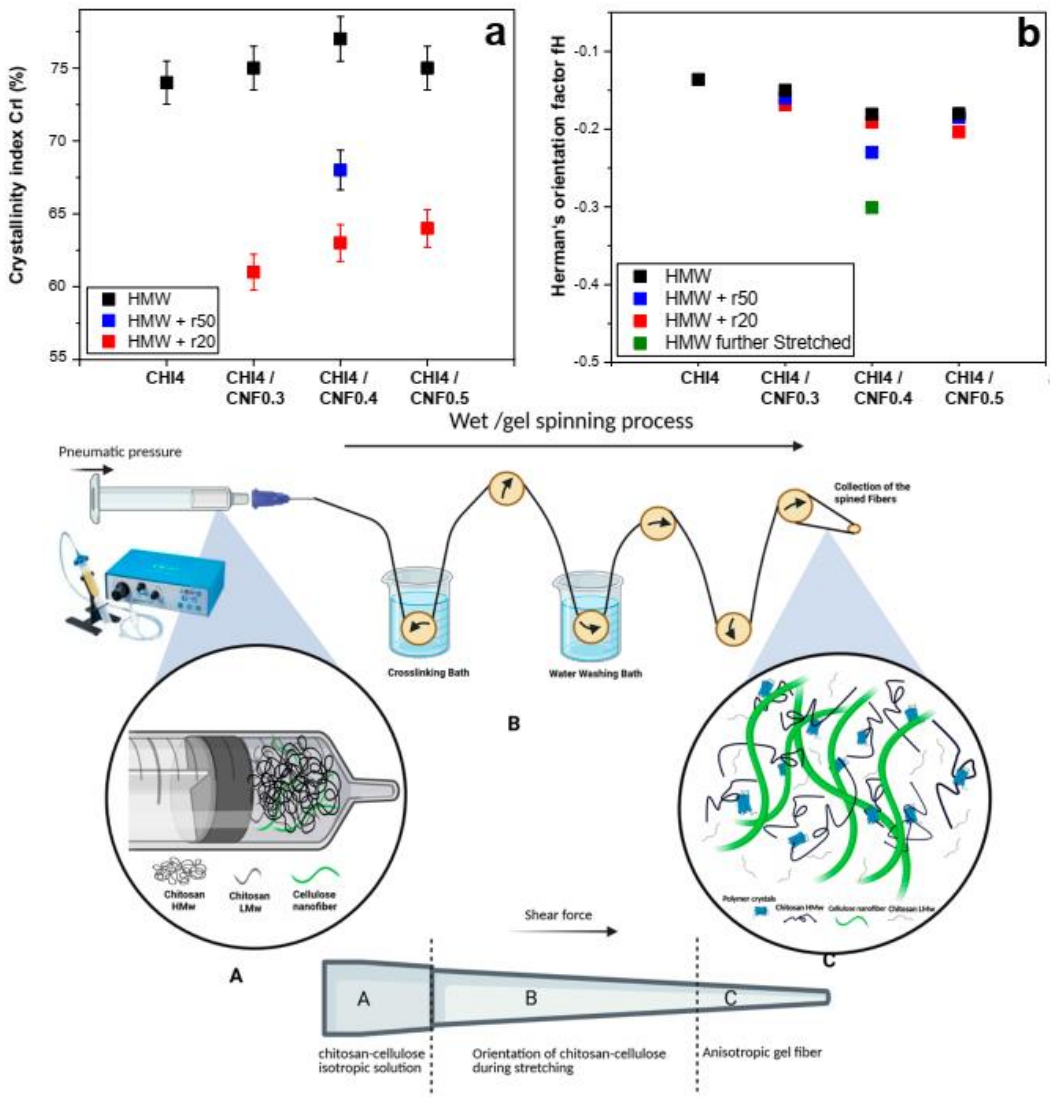

Figure 5.1.7. (a) The crystallinity index (CrI) and (b) the Herman's orientation factor (fH) values of spun fibers obtained for different formulations containing high (HMW) and low molecular chitosan (LMW, with used molar ratio of glucosamine to NaNO2 of: r20 or r50), and cellulose nanofibers (CNF). (*Bottom*) Schematics summarizing the transition from isotropic collodions to anisotropic spun fibers, involving formation and orientation of crystalline materials due to shearing and molecular mobility during extrusion, stretching and drying in spinning of chitosan/cellulose nanofiber hybrid fibers. Reproduced with permission from Tran et. al., 2025 [238].

The Herman orientation factor (f_H) can be calculated from the 2D WAXS images. The Herman equation (Equation 5.1.2) defines and relates the orientation factor in relation to the crystallites within the fibers. To this end, the 2D wide angle X-ray scattering (WAXS) images were azimuthally sectorized, and the intensity peak around the (*h*,*k*,*l*) crystallographic peak was deconvoluted for each sector centered at the azimuthal angle $\varphi_{h,k,l}$. For the calculation of the Herman orientation factor (f_H), the average of the cosine squared of azimuthal angle $\varphi_{h,k,l}$ is determined by integrating the measured peak intensity at each angle and dividing by the total integrated intensity as the following (Equation 5.1.2):

$$f_{h,k,l} = \frac{1}{2}3cos^2 \varphi_{h,k,l} - \frac{1}{2} \qquad \text{(Eq. 5.1.2)}$$

The Herman's factor values closer to −0.50 indicate a higher orientation of the crystals within the fibers, while values closer to 0 signify isotropic behavior. Interestingly, the addition of both chitosan "oligomers" and cellulose nanofibers contribute to enhance orientation (Figure 5.1.7). The Herman's orientation factor values around −0.20 were achieved, with further enhanced orientation values of −0.23 for the formulation F7 (CHI/r50/CNF0.4), consisting of low molecular weight chitosan of intermediate Mw, of cellulose nanofiber content 0.4% (*w*/*w*), and of high molecular weight chitosan. Then, a further stretching of this fiber led to further increase alignment within the fibers and Herman's orientation factor of −0.3 was achieved (Figure 5.1.7). To summarize, the schematics in Figure 5.1.7 illustrate how the contribution of cellulose nanofibers, serving as nano-reinforcement and surface for nucleation of chitosan crystallites, contributes to the increase crystallinity and orientation. This effect combined with the shearing during extrusion, the stretching and drying during spinning, yields fiber composites of enhanced crystallite orientation. This is specially enhanced when incorporating into the CHI/CNF formulation a chitosan of intermediate low molecular weight chitosan like Mw: 4.4×10^4 g/mol produced for r50. The intermediate polymer chain lengths were produced through the depolymerization (by nitrous deamination) by using a molar ratio *r* of glucosamine to $NaNO_2$ of r50, which yielded an intermediate molecular weight of chitosan of Mw of 4.4×10^4 g/mol. This Mw was higher (i.e., intermediate) than the low molecular weight of Mw of 2.9×10^4 g/mol obtained by using a molar ratio *r* of glucosamine to $NaNO_2$ of r20. Thus, the effect of enhanced crystallinity and orientation could be attributed to the presence of shorter chains, but not as short as for r20 (Mw: 2.9×10^4 g/mol), which ensures higher molecular mobility of shorter chains, but still allowing for some entanglement of the intermediate Mw chains (Mw: 4.4×10^4 g/mol) to sense shearing and contribute to orientation (Figure 5.1.7). These interpretations could serve as the basis for the analysis of the spun fiber composite properties like thermal and mechanical in the following sections.

5.1.6. Thermal Properties

The thermal stability and decomposition patterns of the composite fibers (CHI/LMW/CNF) were evaluated using thermogravimetric analysis (TGA). Figure 5.1.8 demonstrates how the presence of chitosan "oligomers" and nanometric CNF influences the thermal behavior of the CHI matrix. The use of CNF fibers is known to enhance the thermal stability of composite fibers [143]. Most of the samples exhibit similar decomposition patterns, with an initial mass reduction

observed at around 100˚C, which corresponds to water desorption associated with the hydrogen bonding in the polysaccharide/water structure. The next phase, visible at 260˚C, corresponds to the decomposition of the polysaccharide macromolecules of both CHI and CNFs. Finally, at approximately 400˚C, the degradation of any residual sodium acetate from the neutralization step occurs, which was not entirely removed during the washing steps with water when spinning the composite fibers [143, 231].

Interestingly, the CHI/r20/CNF0.4 formulation shows a different behavior compared to the other samples, with three distinct degradation steps after water evaporation (around 100˚C). The first degradation step, at 189˚C, is likely related to the breakdown of the “weak link” of CHI chains and added oligomers. The subsequent degradation steps around 260˚C and 400˚C correspond to the decomposition of the macromolecules and the residual sodium acetate, respectively.

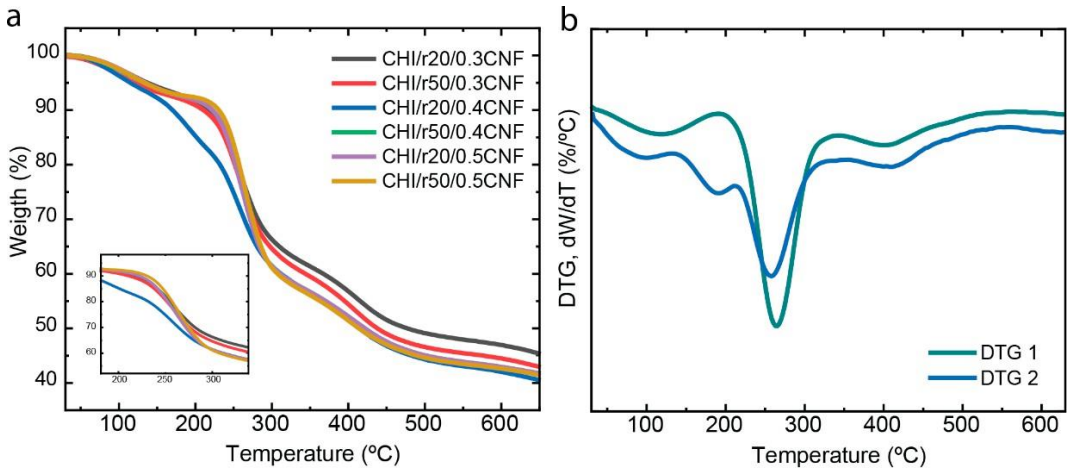

Figure 5.1.8. (a) The thermogravimetric analysis (TGA) and (b) derivative thermogravimetry (DTG). Reproduced with permission from Tran et. al., 2025 [238].

5.1.7. Micromechanical Properties

The incorporation of CNFs up to 0.4 wt% into the CHI matrix leads to a significant enhancement in the overall mechanical performance of the composite fibers. The addition of CNFs improves the nanocomposite’s mechanical properties, attributed to the high aspect ratio of the nanofiber reinforcement, which promotes efficient stress transfer between the matrix and the fibers []. This study focuses on examining the influence of “oligomers” on the mechanical behavior of the composite fibers, specifically evaluating parameters such as the Young’s modulus (E), yield point (σy and εy), stress-at-break (σb), elongation-at-break (εb), and toughness (Ut). Figure 5.1.9 illustrates the stress-strain curves for all formulations. When comparing composite fibers with different oligomers, r50 (F5–F8) demonstrates superior properties, like increased Young’s modulus E, yield stress σy and stress-at-break σb, compared to those with r20 (F1–F4). Previous studies have shown that an optimal CNF content of 0.4 wt% yields the best results,

which is why this condition was also selected for combination with the “oligomers” in this study. The oligomers significantly influence the stiffness (E) of the samples, with r50 samples reaching an average Young’s modulus value of 19 GPa, while with r20 a value of 9 GPa was reached, in both cases for a cellulose nanofiber content of 0.4 wt%. Furthermore, the yield and tensile strength (σy and σb) of the composite fibers with r50 were as high as 101% and 151%, respectively. Specifically, for the toughness value Ut, some variability was observed with higher standard error observed in the sample formulation F5 with r50 low molecular weight chitosan, and without containing cellulose nanofibers. For the yield stress and stress at break, a large fluctuation of the values was also obtained for some composite fibers. The increase in the crystallinity index in fibers with LMW chitosan for r50 contributes to the highest stiffness of composites, whereas the shorter chains produced for r20 allowed for higher molecular mobility, leading to a reduction in overall mechanical performance.

To achieve the highest stiffness (E modulus) and strength (σy) of spun fibers, in terms of chitosan molecular, the optimum composition seems to be that containing high molecular chitosan combined with a low molecular weight chitosan of not too short chains, this is, of intermediate Mw. The low molecular weight chitosan should have a Mw between that for r50 (Mw: 4.4×10^4 g/mol) and that of HMW (Mw: 5.5×10^5 g/mol). The results showed that both the low molecular weight chitosan and CNFs positively influence Young’s modulus and yield stress of spun hybrid fibers. However, only the chitosan molecular weight seems to have significant influence on fiber toughness. Thus, the highest Young’s modulus, yield stress and toughness are achieved at adding a low molecular weight chitosan of intermediate Mw value (e.g., for r50 sample) and cellulose nanofibers to the high molecular weight chitosan collodion, with the remark that the variation of CNF content in the considered CNF contents (0.3–0.5% (w/w)) is not significantly affecting toughness. To conclude, the best mechanical properties were achieved at combining low molecular weight from r50 with CNF at content 0.4% (w/w) with high molecular weight chitosan, when using collodions containing a total chitosan percentage of 4% (w/w). This composition also corresponds to the highest achieved values of crystallinity index (CrI) and the highest orientation within the fiber (see evolution Herman’s orientation factor f_H)) as illustrated in Figure 5.1.7. It can be concluded that the crystallization, molecular mobility and shearing associated with the addition of low molecular weight chitosan of intermediate Mw, leads to an improvement of the fiber mechanical properties. It demonstrates the major role of introducing low molecular weight chitosan of intermediate Mw and cellulose nanofibers into chitosan collodions, to combine enhancement of crystallization and crystallites orientation in spinning process for the development of high strength fibers.

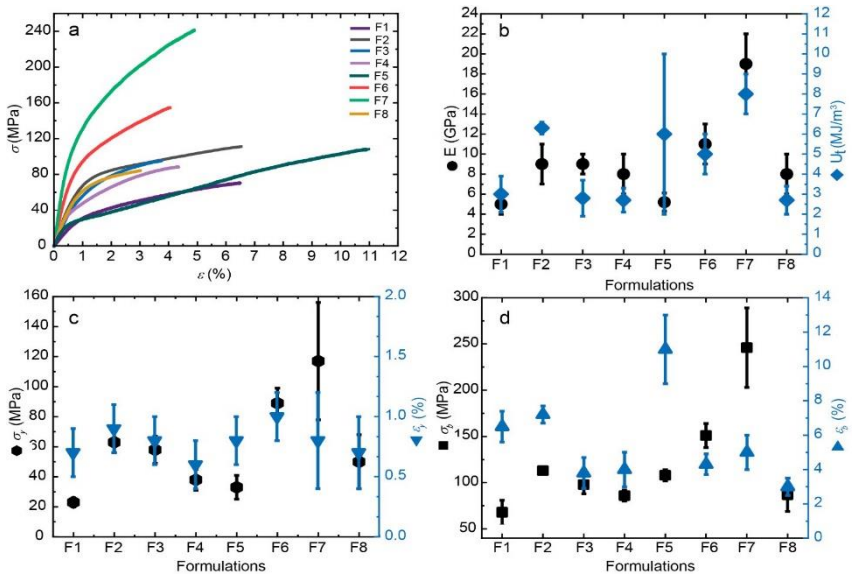

Figure 5.1.9. Tensile mechanical properties of spun CHI/LMW/CNF fibers obtained for different formulations. (a)The nominal stress–strain curves. Evolution of (b) Young's modulus E and toughness Ut, (c) the stress (σy) and strain (εy) values at the yield point, and (d) the stress-at-break (σb) and strain-at-break (εb), with the increase of CNF content in spun fibers. Reproduced with permission from Tran et. al., 2025 [238].

Tuning the molecular weight in chitosan formulations allows optimizing both the physico-chemical behavior and the physical properties for fiber processability and mechanical performance, as well as the biological properties through the incorporation of low molecular weight chitosan into high molecular weight-based systems, to advance biomedical and textile applications. The molecular weight of chitosan definitely should govern the physicochemical and biological properties as follows: (i) high molecular weight chitosan (HMW) contributes to increase viscosity in collodions, to lower the solubility into coagulation by approaching neutral pH, and it is better for structural applications like to produce films, hydrogels, fibers; and (ii) low molecular weight chitosan (LMW) contributes to higher chain mobility and solubility, to lower viscosity, and to better biological activity due to improved bioavailability. Especially shorter polymer chains, i.e., LMW chitosan, promote cellular uptake and interaction with biomolecules, conferring enhanced antimicrobial, antioxidant, anti-inflammatory, and immunomodulatory properties compared to HMW chitosan. Summarizing, a combination of HMW and LMW chitosans has a dual application domain. The HMW chitosan improves the engineering of high mechanical performance structural fibers, while the LMW chitosan promotes bioactivity-driven applications. This synergy of chitosan molecular weight combination, together to the incorporation of high strength cellulose nanofibers in spun composites, advances the achievement of functional materials for biomedical applications, as the development of biocompatible and biologically functional fibers of high mechanical performance.

5.2. 3D Printing of Nanofiber/Polymer Inks by Extrusion In situ at the Synchrotron X-Ray Scattering Beamline to Develop Anisotropic Hydrogel Biomaterials

Research in hydrogel biomaterials is an interesting area which is increasingly focused on the development of three-dimensional **(**3D) biomaterials to regenerate/repair tissues and organs affected by diseases or injuries [1-4]. 3D printing of hydrogels has emerged as a powerful tool for tissue engineering, which applies additive manufacturing to biofabricate tissue-resembling objects with a high degree of spatial organization. A layer-by-layer deposition of hydrogel precursor materials, called (bio)inks, is performed in specifically designed 3D shapes. It could impact patient care through biofabrication of tissue substitutes for implantation in individualized medicine, or for drug and toxicity screening [10-15]. These technologies typically involve the incorporation of pharmaceutical or biological molecules (e.g., growth factors) and the use of natural polymers such as proteins (e.g., collagen, silk fibroin) or polysaccharides, and composites. Those with the special and uncommon property of bioactivity, such as chitosan, hyaluronic acid, collagen [20-25], are envisioned to produce innovative materials, either entirely natural or partially synthetic, that closely mimic the structure and function of tissues. Engineering of hydrogel biomaterials with controlled microstructure approaching tissue architecture and functionalities, while serving as model to grow cells and investigate their behavior in 3D mimicking environments, is challenging. Especially, the development of fiber-filled viscous inks, with good printability and bioactive properties, for the achievement of bioinspired hydrogels showing preferential orientation in their microstructure, to control cellular fate and cell orientation still needs to be improved. Soft tissues like the skin, intervertebral disc, cartilage, meniscus, are commonly complex fiber-reinforced hydrogel composites with many of them being anisotropic. In 3D printing strategies, viscous ink characteristics should include appropriate viscosity, printability, biocompatibility, enhanced cell adhesion, mechanical performance, and if desired, also biodegradability. Hydrogels of collagen, gelatin modified or not with methacrylate moieties, agarose, chitosan and derivatives, polycaprolactone (PCL), silk fibroin, hyaluronic acid (HA), have been 3D (bio)printed. Specially, extrusion-based (bio)printing (EBB) can be performed with a broad range of viscosity of the dispensed materials [20]. Depending on ink and plotting device, hydrogel lines with a wide range of resolution (e.g. 45 to 1200 ***μ***m) can be printed by EBB. Specially, the ink should be in “liquid” phase prior to extrusion to avoid nozzle clogging, and must gel very fast after extrusion, to become a stable 3D free-standing object. In this work, EBB methodology was chosen to print fiber-filled hydrogels with preferential alignment in their microstructure, to advance the development of bioinspired 3D gel materials of good biological and mechanical properties for tissue engineering. There is an increasing interest in using natural sources like biopolymers for the development of functional materials [1-6]. Among the selection of natural polymers, chitosan

(CHI) is increasingly attracting the attention in researches about gels for regenerative medicine and its 3D constructs, due to its biocompatibility, bioresorbability, and bioactivity, as well as its hemostatic, bacteriostatic, and fungistatic qualities [23]. CHI is a linear polysaccharide composed of a copolymer structure with connected (1-4) units of 2-acetamido-2-deoxy- β-D-glucopyranose and 2-amino-2-deoxy- β-D-glucopyranose, which is mostly derived from chitin through deacetylation [1-4], and can be extracted from fungi cell walls. Furthermore, chitin can be derived from crustacean shells and squid endoskeleton, making it the second most abundant natural polysaccharide after cellulose. Regarding gels, films and fibers prepared from CHI aqueous solutions, the presence of just β (1-4) type glycosidic linkages along the polymer backbone (as in cellulose) may provide oriented self-assembly and even crystallization of chitosan into chitosan-based products of good mechanical properties [235-237]. Thus, chitosan biomaterials can be used in a variety of physical forms, including hydrogels to mimic 3D microenvironments for cells, dressings to limit fungal and bacterial proliferation and promote tissue regeneration, knitted textile implants to improve biocompatibility and stimulate healing mechanisms, bioresorbable surgical materials, composites [10]. A traditional method for improving mechanical properties of chitosan biomaterials is to combine chitosan with other polymers. Researchers have been able to create materials with acceptable mechanical qualities using chitosan combined with synthetic polymers such as poly(vinyl alcohol) (PVA), though they may not be totally bioresorbable, biocompatible, or bioactive as natural polymers. Other investigations concentrated on the development of entirely bio-based and resorbable materials. Chitosan and cellulose have been combined in biomaterials, making advantage of the good interaction between these two polysaccharides [62]. Chitosan was also employed as a coating on premade alginate fibers to link chitosan's bacteriostatic properties with alginates' mechanical performance [143, 231].

The use of polysaccharide nanofillers (such as cellulose nanofibrils (CNFs) and cellulose nanocrystals (CNCs)) has also been investigated to improve the mechanical properties of chitosan materials, owning to the nanometric size, high aspect ratio, high crystallinity and ability to form intra and intermolecular network structures through hydrogen bond interactions in cellulose nanofibers. In this work, we aim to develop bioinspired anisotropic gel materials of chitosan filled with cellulose nanofibers (CNFs or CNCs) through extrusion-based 3D printing, to achieve hydrogels with preferential orientation that show superior mechanical properties and can mimic cell microenvironments to provide better support for cell growth and differentiation in anisotropic supports. However, there have been few studies exploring the effect of the local and global distribution of orientation within 3D printed chitosan-based hydrogels. In this work, the orientation and microstructure of the chitosan-based hydrogels will be characterized by the interaction of the chitosan/cellulose viscous ink’s rheological behavior, extrusion-induced

shearing, printing settings, and the *in situ* orientation of both the embedded fibers and assembled chitosan in hydrogel matrix, during the printing of hydrogel composites.

In section 5.1, the X-ray diffraction results clearly indicate a preferential orientation of the nanofibers in spun chitosan fibers after gel spinning, suggesting a high degree of alignment within the material (Figure 5.1.7). While this observation provides valuable insight into the structural characteristics at the nanoscale, it does not directly reveal the origin of this orientation. Specifically, it remains unclear whether the alignment arises primarily from the gel-spinning process itself or if it is significantly influenced by the subsequent organization and distribution of the nanofibers within the cartridge during extrusion. To address this ambiguity, a more targeted investigation is required which is more capable of distinguishing between process-induced alignment and orientation resulting from the spatial arrangement of nanofibers during material handling.

In this section 5.2, we aimed to develop a technique for dynamic monitoring of the real-time orientation in polymer inks during 3D printing of viscous formulations containing chitosan solutions filled with nanofibrillated cellulose (CNF) or cellulose whisker nanocrystals (CNC). This method aims to assess the self-assembly of macromolecules from the ink components at both nano and microscales within the extruded material at the nozzle exit. Bioink formulations will be optimized by testing a variety of CNF, CNC and chitosan concentrations. The orientation and microstructure of the 3D printed gel filaments were assessed in situ by synchrotron X-ray scattering analysis during extrusion. These results provide an original toolbox for the development of bioinks and their bioprinting into anisotropic 3D hydrogel scaffolds for guided 3D cell growth and tissue engineering.

5.2.1. Microstructure of Cellulose Nanofibers

Figure 5.2.1 shows TEM micrographs and X-ray diffraction patterns of both cellulose whisker nanocrystals (CNC) and nanofibrillated cellulose (CNF) samples, used to produce the cellulose nanofiber-filled chitosan inks and printed hydrogels. The CNC represents very long needle-like single crystals with a high aspect ratio, as displayed in Fig. 5.2.1. They have an average width of 6 ± 1.2 nm and a length ranging from 80 nm to 1 µm. An X-ray diffraction pattern of a pellet of cellulose nanocrystals was recorded and the diffraction pattern showed diffraction peaks indexed as the $(1\bar{1}0)$, (110), (012), (200), and (004) reflections of native cellulose I allomorph [234-237]. The CNF consisted of an entangled network of interconnected nanofibrils with very high aspect ratio (length/width), with an average width of elementary fibers also around 6 nm, but mainly appearing attached into bundles of fibrils of 35.2 ± 8.1 nm with bundles achieving up to around 50 nm width (Fig. 5.2.1). The relatively high value of this latter could be related to the drying during TEM sample preparation, which might induce partial fibril aggregation. The

mechanoenzymatic hydrolysis used to produce the nanofibers yields long nanofibrils preserving the native cellulose I crystalline allomorph structure, as also displayed in the X-ray diffraction pattern of CNF (Fig. 5.2.1), with partly amorphous regions, which can inherently entangle and form a fibril network with hairy branches [143]. As expected, the observed X-ray diffraction patterns demonstrated that the CNC showed quite higher crystallinity than that of CNF. The preserved native cellulose I allomorph with intra and intermolecular hydrogen-bond interactions present in the crystalline cellulose nanofibers contribute to efficient nanoreinforcement effect in “composite” inks including those hybrid systems of chitosan-based viscous formulations and hydrogel composites.

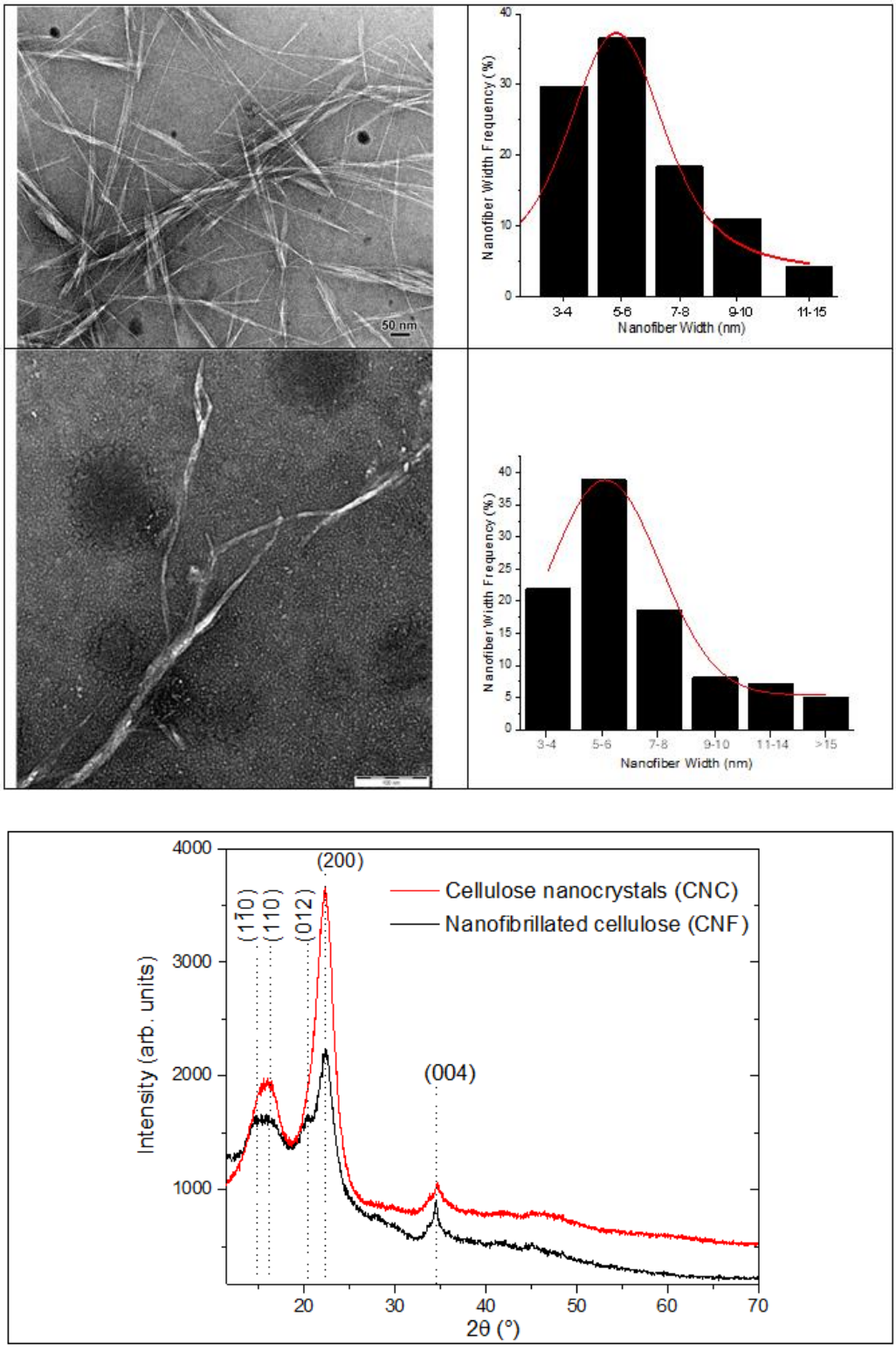

Figure 5.2.1. *(Top)* TEM images of cellulose whisker nanocrystals (CNC) and of nanofibrillated cellulose (CNF), with histogram of distribution of nanofiber widths (*Top-Right*). (*Bottom*) Wide angle X-ray diffraction pattern of the above different cellulose nanofiber types: CNC (red), and CNFs (black), with the indexation of the crystallographic planes of native cellulose I allomorph.

5.2.2. Rheological Behavior of Chitosan-Based Viscous Inks Containing Cellulose Nanocrystals (CNC) and Nanofibrillated Cellulose (CNF)

Figure 5.2.2 shows the flow diagrams of the cellulose nanofiber-filled chitosan suspensions and the corresponding references of chitosan solutions. A steady plateau, corresponding to the Newtonian viscosity, was distinctly observed for the chitosan solutions and for the chitosan-based suspension containing cellulose nanocrystals (CNC) at lower content (0.4 % (w/w)). At higher shear rates, shear-thinning behavior is observed, with a decrease of viscosity as the shear rate increases for all characterized samples.

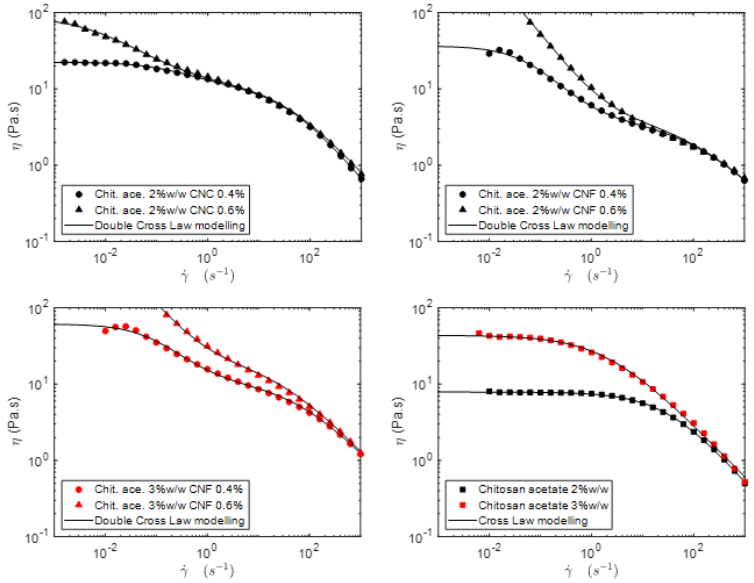

Figure 5.2.2. Rheology of CHI/CNC inks, and CHI/CNF inks with different compositions. (*Top-Left*) CHI2 and CNC0.4/0.6, (*Top-Right*) CHI2 and CNF0.4/0.6, (*Bottom-Left*) CHI3 and CNF 0.4/0.6, and (*Bottom-Right*) CHI2 and CHI3 as reference.

The flow diagrams (η vs. shear rate ($d\gamma/dt$)) of the pure chitosan acetate solutions (Figure 5.2.2) could be modelled with the three-parameter Cross law [62] (Equation (5.2.1)):

$$\eta = \frac{\eta_{0,CHI}}{1 + (\dot{\gamma}\tau_{CHI})^{1-n_{CHI}}} \qquad \text{(Eq. 5.2.1)}$$

The Cross equation yields the Newtonian or zero-shear viscosity η_0, the flow behavior index n_{CHI} with $p_{CHI}=1-n_{CHI}$, and the relaxation time of chitosan polymer chains τ, as displayed in Table 5.2.1. As expected, the steady-state shear viscosity of the pure CHI inks increased with increasing CHI concentration from 2 to 3 % (w/w), resulting from an increase of polymer chain interactions and entanglements increased with the polymer concentration, restricting the chain relaxation. The CHI/cellulose nanofiber viscous suspensions exhibited more complex flow diagrams, with higher viscosities measured in the low shear rate range (< 1 s^{-1}) and shear

thinning occurring in two different regimes, which was more evident for using CNF or CNC at higher contents (Figure 5.2.2). Thus, these two-step flow diagrams of the CHI/cellulose nanofiber suspensions could be modelled with a double Cross law (Equation 5.2.2):

$$\eta = s\frac{\eta_{0,CHI}}{1+(\dot{\gamma}\tau_{CHI})^{p_{CHI}}} + \frac{\eta_{0,CNF}}{1+(\dot{\gamma}\tau_{CNF})^{p_{CNF}}} \qquad \text{(Eq. 5.2.2)}$$

where $\eta_{0,CNF}$, τ_{CNF}, and $p_{CNF} = 1 - n_{CNF}$ are the flow parameters of the chitosan interacting with the CNF network, possibly influenced by the interactions between chitosan and cellulose nanofibers (CNFs), with chitosan chains bridging the cellulose nanofibers resulting in a slower flow behavior. Rheological model fitting used a Levenberg–Marquardt nonlinear regression algorithm in the GNU Octave programming environment. Table 5.2.1 shows the flow parameters obtained for the CHI/cellulose nanofiber suspensions and the Newtonian viscosity $\eta_{0,\,CHI}$, the relaxation time τ_{CHI}, and the exponent $p_{CHI} = 1 - n_{CHI}$ for "pure" CHI solutions. For a given CHI concentration, the presence of nanofibers induced an increase of the Newtonian viscosity measured at low shear rates. With the increase of the shear rate, the viscosity of both the pure CHI viscous solutions and the CHI/nanofiber inks similarly decreased. Thus, in the CHI/nanofiber formulations two different chain relaxation phenomena might occur. In the "pure" CHI inks, the main chain relaxation, being dominating at high shear rate and corresponding to the disentanglement of the polymer chains transient network, shows relaxation time of 0.03 s in inks with 2% (*w/v*) CHI, and around 0.05 s in inks with 3% (*w/v*) CHI (Table 5.2.1). The similar shear-thinning behaviors of CHI solutions and CHI/nanofiber suspensions with similar flow exponents at high shear rates, could be explained due to the CHI polymer chain relaxation (disentanglements) impacted by the CHI concentration. The cellulose nanofibers surface is weakly negatively charged with carboxylate (for CNF) or sulfated (for CNC) moieties [62]. Weak electrostatic interactions could establish between the CHI polycation and the nanofibers polyanionic surface, allowing for stress transfer from the CHI solution matrix to the nanofibers. According to the results, in the CHI/nanofiber inks the establishment of a rigid cellulose network with permanent nanofiber–nanofiber interactions would not occur, as a gel-like flow behavior with $\eta \sim 1/\text{shear rate}$ would be instead observed [66]. CHI chains could absorb on the cellulose nanofibers surface and play a role in the bridging of nanofibers [229], resulting in entanglements formation between the chains adsorbed of the nanofiber surface and the other CHI chains in the solution. Addition of the nanofibers, even at low concentrations like used in the study (≤0.6 % w/w), is likely to impact the dynamics of CHI chains since the surface area of the nanofibers is very large [229].

Table 5.2.1. Flow parameters determined from the viscosity vs. shear rate curves (Figure 5.2.2) of different CHI/cellulose nanofiber compositions, by using the Cross model for naked CHI solution inks and double Cross model for CHI/cellulose nanofiber suspension inks.

Formulation	$\eta_{0,\,CHI}$ (Pa.s)	τ_{CHI} (s)	p_{CHI}	s	$\eta_{0,\,CNF}$ (Pa.s)	τ_{CNF} (s)	p_{CNF}
CHI2	7.9	0.030	0.780	-	-	-	-
CHI2/CNC0.4	10.8	0.030	0.806	1.22	11.6	3.65	0.864
CHI2/CNF0.4	3.8	0.012	0.645	1.56	32.7	14.1	0.969
CHI2/CNC0.6	11.4	0.033	0.746	1.75	78.7	102.2	0.681
CHI2/CNF0.6	5.3	0.043	0.502	1.75	589	117.9	0.982
CHI3	43.6	0.050	0.690	-	-	-	-
CHI3/CNF0.4	10.3	0.017	0.7133	1.11	50.9	9.3	0.958
CHI3/CNF0.6	18.5	0.039	0.708	1.88	870	94.8	0.925

Thus, the relaxation time τ for chitosan is hypothesized to be influenced by the incorporation of CNF. When adding the CNFs, the observed relaxation time τ_{CNF} can increase due to both the increase of CNF content and of CHI concentration (Table 5.2.1). Such relaxation time is tentatively related to the rupture of CNF/CHI network (CNF strands bridged by chitosan chains), which effect seems to be more important after reaching a threshold of CHI concentration beyond 2 % (*w/v*). Increasing the CNF content should result in a denser CNF network. Then, higher CHI concentration also should contribute to the establishment of the CNF/CHI network, since adsorbed CHI chain would act as fibril binders. It also will imply a denser network with longer relaxation times, associated with larger scale reorientation and interfibrillar bridge rupture with applied strains. A study of the flow diagrams in an extended shear rate range, for example by capillary rheometry with use of the Weissenberg–Rabinowitsch correction as we previously investigated [143], would be necessary to determine the exponent parameter p with even better precision.

Thus, the CHI/CNF inks flow at high shear rates is dominated by the CHI chains disentanglement and is less affected by the presence of the CNFs. However, at low shear rates the presence of cellulose fillers brings higher viscosity. This is advantageous for printability by extrusion of this system, as CNFs contribute to increase the zero-shear viscosity and improve the mechanical properties, while practically not affecting the extrudability and thereby printablity of CHI-based systems (higher shear rates).

5.2.3. WAXS and SAXS Analyses of Cellulose Nanofiber/Chitosan Inks and Extrusion-Based Printed Hydrogels. Evaluation of Orientation

5.2.3.1. Hydrogels Obtained by Extrusion-Based Printing of Cellulose Nanofiber/Chitosan Inks

Table 5.2.2 shows the adjusted pressure to achieve the extrusion-based printing of the used formulations of cellulose nanofiber/chitosan inks, through a precision conic dispense needle with inner diameter of 250 μm (Nordson EFD, Westlake, USA, Catalog No. 7018373) and by using a printing speed of 40 $mm.s^{-1}$. The extruded filaments were printed into a coagulation bath of 2M NaOH, for chitosan neutralization to achieve gelation. As expected from the obtained viscosities in above flow diagrams (Figure 5.2.2), the higher the cellulose nanofiber content the higher the pressure applied for extrusion of the ink. Then, at comparing CNC and CNF-based systems, higher extrusion pressure was needed for inks containing nanofibrillated cellulose (CNF) compared to whisker nanocrystals (CNC). Finally, a higher CHI concentration also required higher pressure, with 0.085 MPa being the highest pressure, which was needed for inks of chitosan 3 % (w/w) and CNF 0.6 % (w/w).

Table 5.2.2. Extrusion pressure of CHI 2 or 3 with different cellulose nanofibers compositions.

Sample	Chitosan CHI % (w/v)	Cellulose nanocrystals CNC % (w/w)	Nanofibrillated cellulose CNF % (w/w)	Extrusion Pressure (kPa)
CHI2/ CNC0.4	2	0.4	-	30
CHI2/ CNC0.6	2	0.6	-	40
CHI2/ CNF0.4	2	-	0.4	35
CHI2/ CNF0.6	2	-	0.6	45
CHI3/ CNF0.4	3	-	0.4	77
CHI3/ CNF0.6	3	-	0.6	85

Figure 5.2.3 shows the synchrotron SAXS and WAXS analyses of the printed hydrogel filaments with different concentrations of chitosan (CHI) and cellulose nanofibers, these latter being either cellulose nanocrystals (CNC) or nanofibrillated cellulose (CNF).

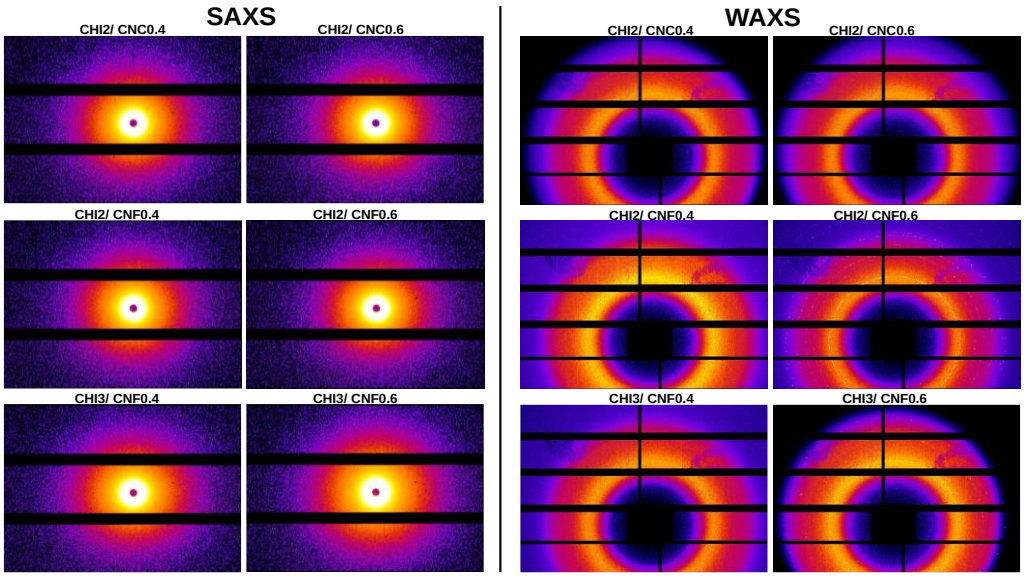

Figure 5.2.3. SAXS and WAXS of printed cellulose nanofiber/chitosan hydrogels, with formulations containing 2 or 3 % (w/w) of chitosan (CHI), and 0.4 or 0.6 % (w/w) of cellulose nanofibers, these latter being cellulose nanocrystals (CNC) or nanofibrillated cellulose (CNF).

Figure 5.2.4 shows the radial-average WAXS scattering curves of the printed cellulose nanofiber/chitosan hydrogels for the different formulations of Table 5.2.1 (incident X-ray beam located in the middle of the sample). In the WAXS images, the signals of crystallographic planes (120) and (121) of chitosan anhydrous allomorph, and of (012) and (200) of cellulose I allomorph were detected, with the peak (200) of cellulose I being identified, amidst the strong WAXS signal of water (Figure 5.2.4).

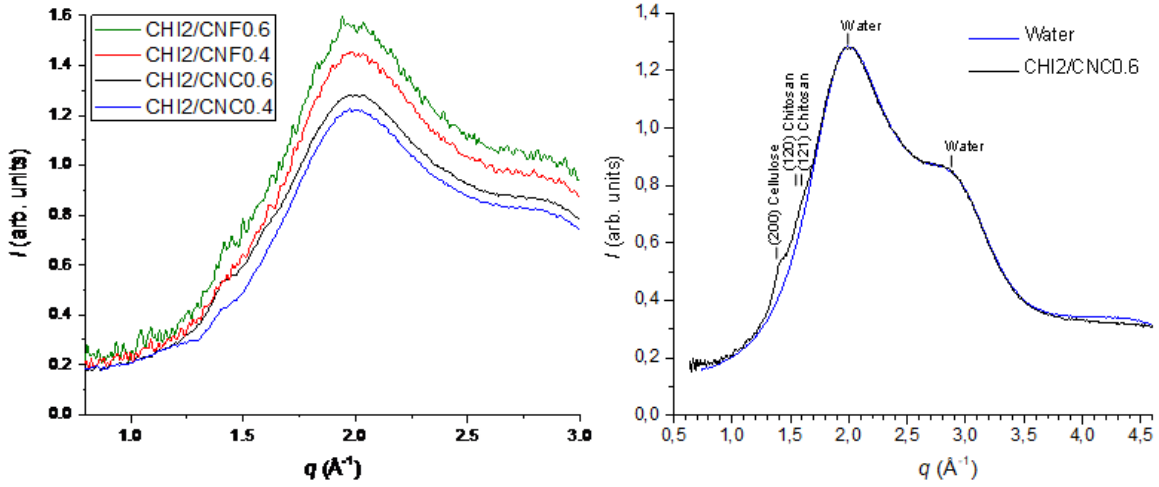

Figure 5.2.4. Radial average scattering curves obtained from the synchrotron 2D-WAXS analysis of printed cellulose nanofiber/chitosan hydrogels (CHI/CNC or CHI/CNF), with different concentrations of chitosan (CHI) and cellulose nanofibers (CNC or CNF).

Nevertheless, the used concentrations of cellulose nanofibers, being relatively low of 0.4% and 0.6% (w/w), the intensity difference between the (200) signal of cellulose crystallites and that of water signal are relatively weak and do not allow a proper determination of the Herman's orientation factor f_H of cellulose crystallites to precisely characterize their alignment in the

printed hydrogels for those concentrations. In addition, a possible loss of orientation could be related to the coagulation step to produce hydrogel self-assembly, which resulted in observed isotropic WAXS patterns at that low nanofiber concentration. To allow quantitative evaluation of orientation by using the cellulose nanofibers signal after extrusion printing, the concentration of nanofibers in the inks increased and the *in situ* synchrotron X-ray scattering analysis of ink filaments was performed immediately at the exit of the extrusion needle (see scheme of Figure 5.2.5) with 30 μm horizontal spatial resolution.

5.2.3.2. Extruded Cellulose Nanofiber/Chitosan Viscous Inks

Table 5.2.3 shows the different formulations of chitosan/cellulose nanofiber viscous inks, which were extruded through a precision conic dispense needle of 420 μm, which procedure was performed in situ at the synchrotron beamline, to allow simultaneous WAXS and SAXS analyses of extruded inks directly at the exit of extrusion needle (see scheme of Fig. 5.2.5). It's worth noticing that chitosan reference solutions of 1.5 and 1.7% (w/w) were also prepared and analyzed.

Table 5.2.3. Composition and extrusion pressure needed in the 3D printing of different chitosan/cellulose nanofibers formulations with chitosan concentrations of 1.5% and 1.7% (w/w).

Sample	Chitosan CHI % (w/w)	Cellulose nanocrystals CNC (w/v)	Nanofibrillated cellulose CNF % (w/w)	Extrusion Pressure (kPa)
CHI 1.5/ CNC2	1.5	2	-	14
CHI 1.5/ CNC3	1.5	3	-	19
CHI 1.7/ CNC2	1.7	2	-	26
CHI 1.7/ CNC3	1.7	3	-	40
CHI1.5/ CNF0.8	1.5	-	0.8	15
CHI1.5/ CNF0.9	1.5	-	0.9	21
CHI 1.7/ CNF0.8	1.7	-	0.8	27
CHI 1.7/ CNF0.9	1.7	-	0.9	32

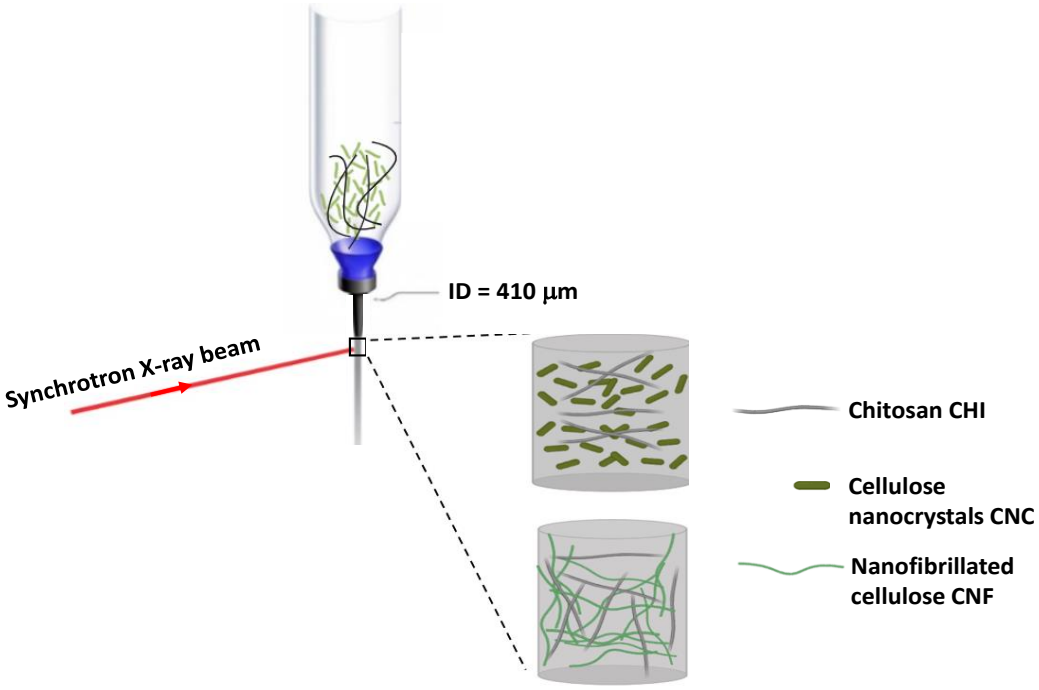

Figure 5.2.5. Scheme showing the design for *in situ* measurement of synchrotron WAXS and SAXS scattering during microextrusion of chitosan viscous inks with either nanofibrillated cellulose or whisker cellulose nanocrystals.

In situ WAXS analysis

Figure 5.2.6 shows 2D wide angle X-ray scattering image and radial-average WAXS scattering curves of extruded chitosan/cellulose nanofiber viscous ink formulations of different compositions (Table 5.2.3), with the WAXS analysis performed at the center of the extruded filament (x/R =0, with x being the position along the cross-section of the printed filament, and R the radius of the extrusion needle).

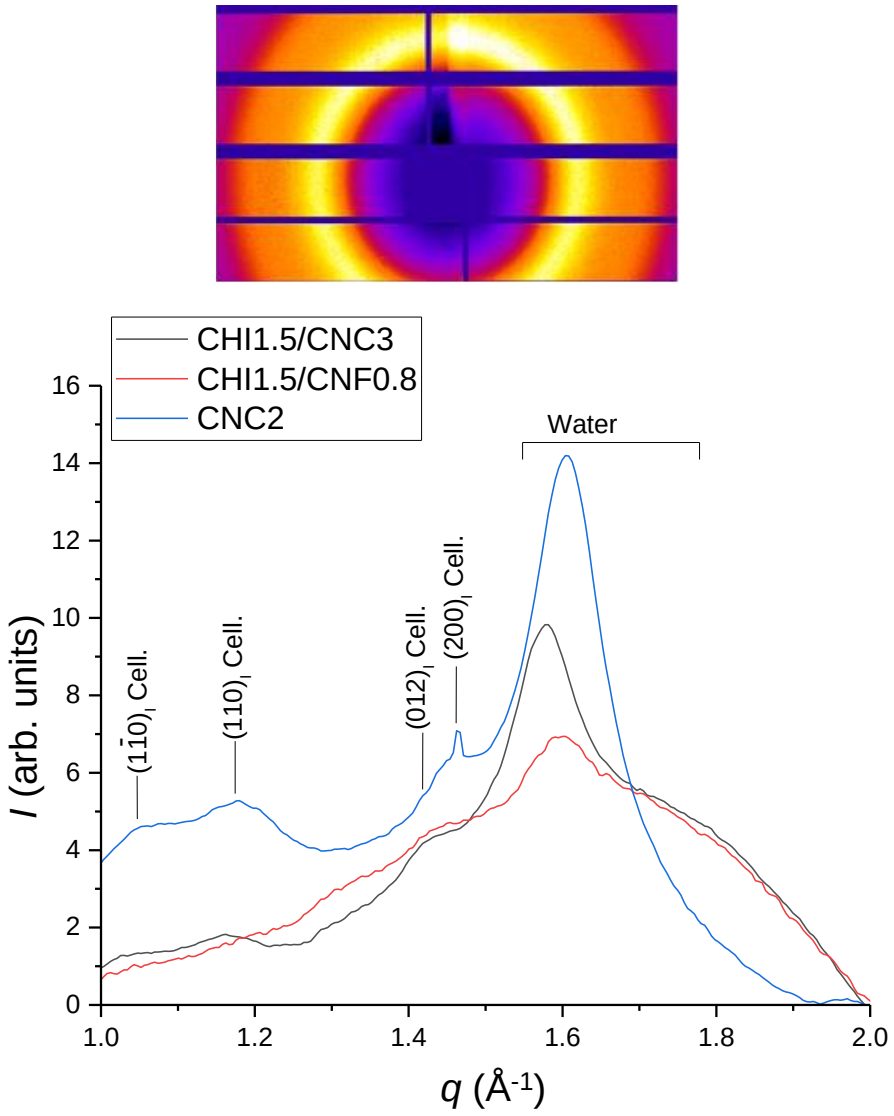

Figure 5.2.6. (*Top*) 2D synchrotron wide angle X-ray scattering (WAXS) image obtained at the center of the extruded gel-like filament of formulation CHI1.5/CNC3, obtained at the exit of the extrusion needle. (*Bottom*) Radial-average WAXS scattering curve of the extruded filaments for different CHI/cellulose nanofiber formulations with the cellulose nanofibers being cellulose nanocrystals (CNC) or nanofibrillated cellulose (CNF). The presented WAXS analysis was performed at the center of the extruded filament (x/R = 0). As comparison, the WAXS scattering curve of the colloidal suspension of cellulose nanocrystals (2% CNC) is displayed as reference.

To characterize the orientation of the crystalline cellulose nanofibers within the extruded filament, the analysis of the 2D-WAXS patterns was performed at different points within the extrudate and by dividing each image into 48 azimuthal sectors, with each sector spanning an azimuthal angle range of $\Delta\Phi$=7.5°. The intensity difference between the (200) signal of cellulose crystallites and that of water signal at q = 1.4 Å^{-1} (see also Fig. 5.2.4) was used to calculate of the Herman's orientation factor f_H, to quantitatively assess the alignment of the cellulose crystallites embedded in the cellulose nanofibers, with these latter also constituting the extruded cellulose nanofiber/chitosan filament (Figure 5.2.5). Due to the inherent symmetry in X-ray scattering, the scattering intensities concerning azimuthal angles are consolidated

within a range of Φ=0° to Φ=90°. From the $I_{200,\,k}$ sectorization, the Herman's orientation factor for the (200) reflection of cellulose I was obtained as follows (Equation 5.2.3):

$$f_H = \frac{3\cos^2<\Phi> - 1}{2} \qquad \text{(Eq. 5.2.3)}$$

where Φ represents the azimuthal angle corresponding to the center of each azimuthal sector with $\Delta\Phi$=7.5°, and $<\cos^2\Phi>$ is determined by the Equation 5.2.4:

$$<\cos^2\Phi> = \frac{\int_0^{\frac{\pi}{2}} I\cos^2\Phi\sin\Phi d\Phi}{\int_0^{\pi/2} I\,\sin\Phi d\Phi} = \frac{\sum_{k\,sector} I_{(200),k}\cdot\cos^2(\Phi_k)\sin(\Phi_k)\Delta\Phi}{\sum_{k\,sector} I_{(200),k}\cdot\sin(\Phi_k)\Delta\Phi} \qquad \text{(Eq. 5.2.4)}$$

The calculation of the Herman's orientation factor f_H was performed for the different extruded formulations of Table 5.2.3. Figure 5.2.7 shows Herman's factor (f_H) values obtained by using the (200) crystal signal of cellulose I, to estimate possible orientation of cellulose crystallites in the extruded inks, which was analyzed along the cross-section of the extruded filament at relative positions *x*/*R* (Fig. 5.2.7).

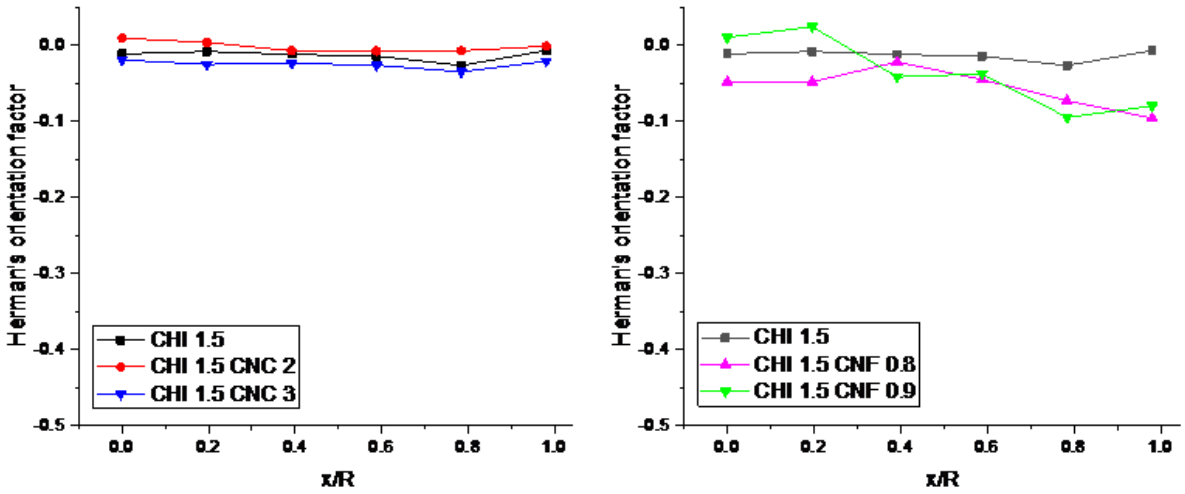

Figure 5.2.7. Herman's orientation factor (f_H) values for the (200) reflection of cellulose I obtained from WAXS analysis of extrusion printed cellulose nanofiber/chitosan inks using different types of cellulose nanofibers: (*Left*) cellulose nanocrystals (CNC) at different concentrations, (*Right*) nanofibrillated cellulose (CNF) at different concentrations, which printed filaments were analyzed at different relative positions x/R along the cross-section of the extruded filament (see scheme of Fig. 5.2.5).

According to the WAXS analysis results (Fig. 5.2.7), the Herman's orientation factor f_H for chitosan-based inks containing 2 or 3% (w/w) of CNC remains approximately constant, around f_H = 0, across all observed x/R relative positions from x/R = 0 to x/R = 1.0 (needle center to needle wall, respectively). This indicates that there is no significant CNC nanocrystal alignment within the bioink extrudate during extrusion, and the variation of the CNC concentration did not

noticeably influence the orientation of the crystalline nanofibers within the printed ink composite. It is worth mentioning that similar behavior was observed regardless of chitosan concentration changing from 1.5% to 1.7%. A factor $f_H = 0$ indicates no orientation in the ink components, while values between $-0.5 < f_H < 0$ would indicate a preferential orientation of crystallites of CNC or CNF in the direction of extrusion flow, after calculation f_H related to the (200) crystallographic planes of cellulose I (Equations (5.2.3) and (5.2.4)). From the WAXS analyses, the obtained f_H values around zero, for all relative position x/R and for the different formulations containing either CNC or CNF as cellulose nanofiber type, means that the crystallites of cellulose constituting the nanofibers practically did not orient during extrusion for the constituent concentrations as used in this work. Practically, either the crystalline parts constituting the nanofibrils network of nanofibrillated cellulose (CNF) nor those of the cellulose whisker nanocrystals (CNC) in the chitosan-based composites were oriented. In the case of the CNF, a minor variation of the f_H values was observed, which could mean a minor orientation of the networked fibrils in CNF at approaching the extrusion needle wall ($x/R \sim 1$), characterized for a higher shear stress regime respect to the needle center ($x/R = 0$).

In situ SAXS analysis

Figure 5.2.8 shows 2D small angle X-ray scattering (SAXS) image and radial-average SAXS scattering curves of the filaments extruded from chitosan/cellulose nanofiber viscous inks of different concentrations.

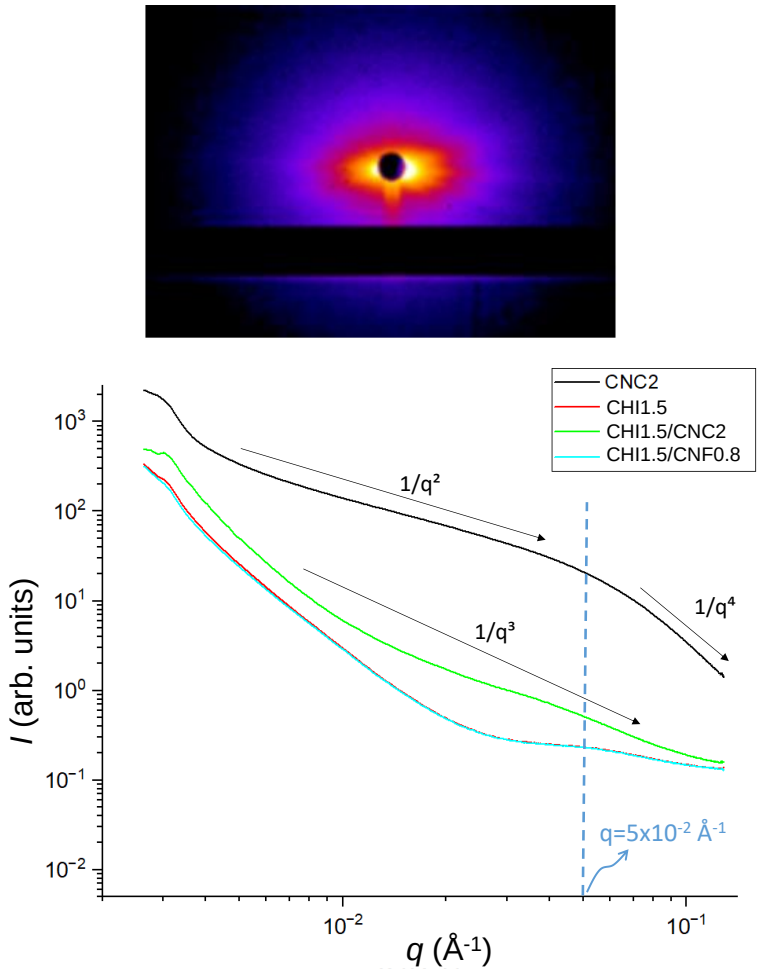

Figure 5.2.8. (*Top*) 2D synchrotron small angle X-ray scattering (SAXS) image obtained at the normalized position x/R = 1.0 of the extruded gel-like filaments of formulation CHI1.5/CNC2, obtained at the exit of the extrusion needle. (*Bottom*) Radial-average SAXS scattering curve of the extruded filaments of cellulose nanofiber/chitosan for different formulations, in which the used cellulose nanofibers were either cellulose nanocrystals (CNC) or nanofibrillated cellulose (CNF) (Fig. 5.2.5). These radial averages specifically shows the analysis performed at the center of the extruded filament (x/R = 0), highlighting in the X-axis the scattering vector *q* value of 5 x 10^{-2} $Å^{-1}$, for which the intensity at the different azimuthal average over the 360° was estimated in the 2D SAXS pattern (e.g. in *Top* image), to apply the Equation (5.2.3) for the calculation of Herman's orientation factor f_H related to SAXS signal. As comparison, the scattering curves of the colloidal suspension of cellulose nanocrystals (CNC) at 2% (w/w), and of the CHI solution at 1.5 % (w/w) are also displayed.

In the SAXS *q*-range (where $qR_0 << 1$, with R_0 denoting the radius of the nanofibrillar objects), the scattering intensity followed a power-law decay between $1/q^2$ and $1/q^4$. For the cellulose nanocrystal (CNC) suspension, the scattering tends toward a $1/q^2$ dependence at the lowest *q*-values and approached $1/q^4$ at higher *q*-values. In contrast, "pure" chitosan solutions and those containing a low concentration of nanofibrillated cellulose (CNF) exhibited a behavior more consistent with a $1/q^4$ to $1/q^2$ transition. Mixtures of chitosan with dispersed CNCs showed an intermediate scattering profile, falling between the $1/q^4$ and $1/q^2$ regimes. These scattering behaviors could be attributed to a large distribution of cross-section radii R_0 of fibril-like features constituting a fibrillar network hydrogel microstructure in pure CHI hydrogels, as previously observed for chitosan hydrogels, and also due to the morphology of rod-like particles as the

cellulose nanofibers with broad cross-sectional size distribution (Fig. 5.2.1). The *q*-values Guinier region was revealed till q_{max} around 0.05 Å^{-1}, from which value the final Porod region appeared (Fig. 5.2.8). In the *q*-range for $q > 0.05$ Å^{-1}, the Porod's law ($I(q) = C/q^4$) is clearly evidenced, especially for the cellulose nanocrystals, confirming the sharp electron density variation within the microstructure (Fig. 5.2.1 and 5.2.8).

Due to the inherent symmetry in X-ray scattering, also in the SAXS analysis the used azimuthal angles were those within a range of 0° to 90°, for the calculation of the Herman's orientation factor f_H. Figure 5.2.9 shows the Herman's orientation factor values (f_H) obtained by using the SAXS signal at q = 5 x 10^{-2} Å^{-1}, which was evaluated along the cross-section of the extruded filament at given relative positions x/R (Fig. 5.2.5).

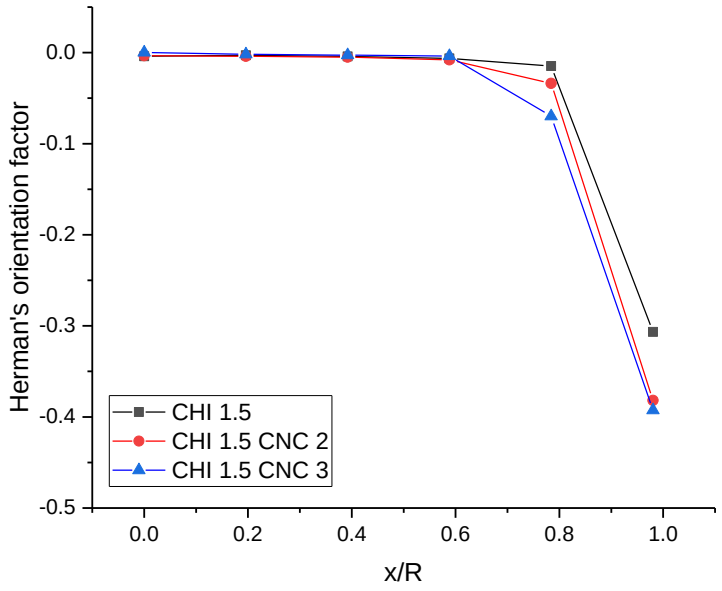

Figure. 5.2.9. Herman's orientation factor (f_H) values obtained from SAXS analysis of extruded cellulose nanofiber/chitosan inks with different concentrations cellulose nanocrystals CNC, for different relative positions x/R along the cross-section of extruded filament (see scheme of Fig. 5.2.5).

The f_H values obtained from SAXS analysis should showcase the orientation of the system as a whole at the nanoscale, including both the orientation of cellulose nanofibers and of self-assembled chitosan chain aggregates. The SAXS analysis of extruded inks containing cellulose whisker nanocrystals (CNC) in Figure 5.2.9 shows that the apparent orientation factor f_H remains constant around zero when moving horizontally from the center of the extruded hydrogel filaments (x/R = 0) to halfway across their cross-section (around x/R = 0.6). Then, the f_H decreases to negative values when moving further to approach extrudate edge (x/R = 1.0), indicating a partial alignment in the direction of the extrusion flow. As mentioned above, f_H values between -0.5 and 0 indicate partial orientation of the system. Importantly, $f_H = -0.5$ would indicate perfect alignment in the extrusion flow direction. One possibility of induced orientation is due to the shear stress imposed by the extrusion pressure, which leads to a shearing on the entangled chitosan chains into elongated aggregates with embedded cellulose nanofibers.

This effect is more pronounced in the outer layer (the extruded filament edge) where the shear stress is higher than in the filament center (x/R = 0), indeed in this latter region no orientation was observed (x/R = 0).

Regarding the effect of cellulose nanocrystals on the orientation in the printed CHI/CNC gels, it was observed that the increase of the CNC content in the inks induced a slight decrease of the Herman's orientation factor f_H into the negative values, especially when going from the cross-sectional relative position x/R = 0.6 to x/R = 0.8. The CHI/CNC composite system containing the highest percentage of CNC, for example, CHI1.5%/CNC3%, goes from an isotropic behavior at position x/R = 0.6 into an anisotropic orientation observed at position around the filament edge (x/R = 1.0) where the determined f_H value dropped to -0.4. For the mixture containing 2% CNC the f_H decreases to -0.3 at edge position x/R = 1.0. These results indicate that chitosan-based inks with relatively high contents of cellulose nanocrystals (>2%) have an anisotropic distribution within the extrusion-printed hydrogel filament.

The variation in chitosan concentration from 1.5% to 1.7% did not have a significant impact, displaying a similar trend when transitioning from x/R = 0 to x/R = 1.0. However, there is a slight difference in the Herman's orientation factor at the edge of the extrudate: f_H= -0.3 for the formulation with 1.5% chitosan, and f_H= -0.4 for the formulation with 1.7% chitosan. However, these findings do not completely negate the influence of chitosan concentration on determining the alignment of the cellulose crystals in the formulation. This is expected because chitosan chains remain the primary contributor to the final viscosity of the ink, as demonstrated in the rheology analysis. In the SAXS analysis, an enhanced alignment of the self-assembled macromolecular chains near the edge in extruded filament is observed, indicating partial alignment of aggregates at the nano/microscale. These chitosan aggregates should have embedded the cellulose nanofibers due to the good interaction between chitosan and cellulose nanofibers through hydrogen bonds and electrostatic interactions at the surface of the nanofibers. In the case of CNF, the nanofibers are slightly negatively charged with carboxylate moieties (surface charge density of 40–80 mmol/kg), and in the case on CNC, the nanofibers are also negatively charged at the surface due to sulfonate moieties. The chitosan behaving as polycation in weakly acidic aqueous solution, this is, positively charged, it will electrostatically interact with the negatively charged cellulose at the surface of the nanofibers.

Regarding the other type of cellulose nanofibers and the orientation observed in the extruded inks, this is, the effect of nanofbrillated cellulose (CNF), the results showed that the f_H value also exhibited a gradual decrease in CHI/CNF formulations containing CNF 0.8% and 0.9% (w/w). The f_H ranges from around zero at position x/R = 0 (extrudate center) to approximately f_H = -0.1 at x/R = 1.0 (extrudate edge) (Figure 5.2.10). It is worth noticing that even if for that variation of the CNF concentration a significant change in the value of the orientation factor f_H was not observed at screening the positions from x/R equal 0 (center) to 1.0 (edge), when

comparing the effects between CNF and CNC on the Hermann's orientation factor in formulations with the same chitosan concentration (e.g. 1.5%), we observed that in CHI/CNF formulations, the decrease of orientation factor already started at an inner position like x/R = 0.4 and this factor kept slowly and steadily decreasing from f_H = 0 to f_H = -0.1, for example when moving from position x/R = 0.2 to x/R = 1.0. In contrast, for CHI/CNC formulations, the f_H zero value remains unchanged till position x/R = 0.6, before a sudden drop of f_H value into -0.3 was observed. This could be explained due to the restricted mobility of a network of longer and entangled hairy nanofibrils as in the CNF, which in addition electrostatically interact with the chitosan macromolecular chains, with these latter likely serving as coating of the CNF nanofibrils as suggested by the rheological results.

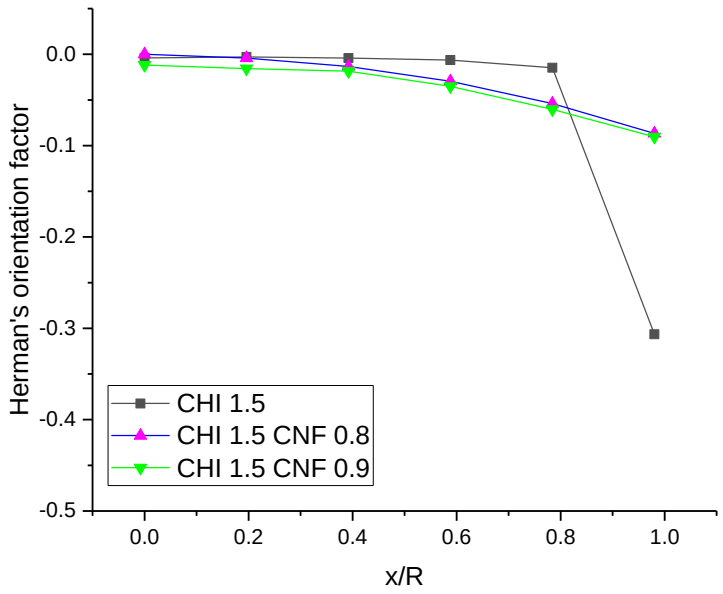

Figure 5.2.10. Herman's orientation factor f_H obtained by SAXS analysis of CHI/CNF printed formulations containing different concentrations of CNF in chitosan-based ink formulations, which were analyzed at different relative positions x/R across the cross-section of extruded gel filament.

The steric hindrance of CNF might slow the formation of elongated chitosan aggregates produced by self-assembly which will orient themselves in the direction of flow under shearing constraints. Nevertheless, the good interaction between CHI chains and CNF nanofibrils should favor a slow but steady orientation of CHI aggregates embedded with nanofibers. In contrast, the slender and rigid rod-like nanocrystals as constituting the CNC nanofibers should have a faster mobility to go together with the chitosan macromolecular chains in the direction of flow under shearing. The nanocrystals CNC should not restrict the CHI self-assembly into elongated and orientable aggregates as it would do a network of nanofibrils (CNF). This should contribute to more orientation of CHI/CNF system in the flow direction, especially at regions of high shear stress like the wall of extrusion needle, translated as a significant reduction of the factor f_H at the edge of extrudate. In this highly hydrated system, when shorter nanoparticles

like the CNC are far from the extrudate edge and subjected to only a mild shearing, it seems the CNC could relocate and easily loss orientation of nanocrystals even when staying within a CHI macromolecular aggregate. Then, for the significant shear stress at the extrudate edge the CHI aggregates will orient and the suspended nanocrystals do not seem to compromise the orientation of the CHI/nanofiber, as similar high orientations with f_H values between –0.3 and –0.4 were obtained in extrusion printed gels both of "pure" chitosan and of CHI/CNC. This is not contradictory with the no orientation observed for cellulose crystallites by WAXS analysis. The CHI/cellulose nanofiber printed systems as a whole achieve orientation, but the cellulose crystallites are practically randomly oriented within the assembled chitosan-based material in the extruded filament. The scheme of Figure 5.2.11 summarizes how the extrusion printing of nanofiber-filled polymer inks could contribute to the development of anisotropic hydrogels by orienting the system in the direction of the nozzle axis, due to the shear stress specially important at the wall of the extrusion needle, which orientation could be quantify in real time by using simultaneously X-ray scattering analyses SAXS and WAXS.

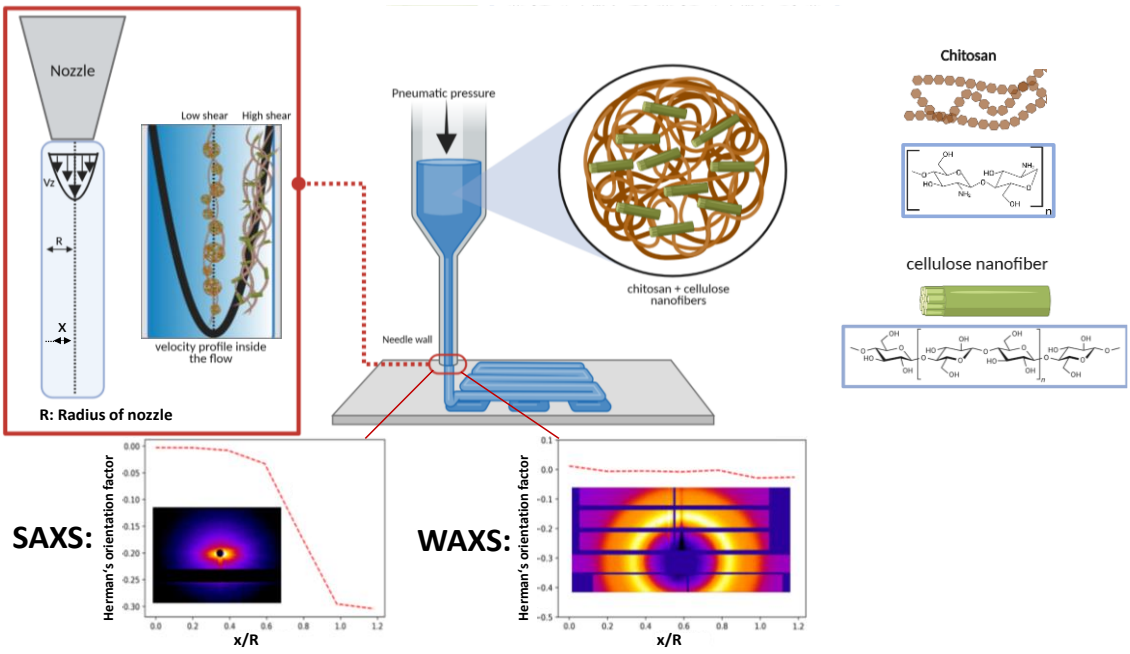

Figure 5.2.11. Schematics of extrusion of cellulose nanofiber-filled chitosan viscous ink, showing the transition from isotropic ink to extruded anisotropic hydrogel-precursor filament.

The orientation in the extruded material was quantified *in situ*, by synchrotron X-ray scattering analyses SAXS and WAXS, simultaneously, on the extruded filament at the exit of the extrusion needle. The SAXS analysis revealed the orientation of elongated self-assembled chitosan polymer with embedded cellulose nanofibers, with the effect being enhanced at higher x/R cross-sectional positions approaching the wall of the nozzle (edge), where higher shear stresses occur. At the lowest length scale, the WAXS analysis mainly revealed isotropic behavior with practically no specific alignment of the cellulose crystallites of the nanofibers

along the nozzle length direction, for the investigated cellulose nanofiber contents and chitosan matrix concentration.

5.3. 3D Bioprinting Strategies for Cell-Laden Chitosan Based Bioinks. Guiding Anisotropy in Bioactive Engineered Tissues

Tissue engineering (TE) has evolved considerably in recent years, driven by the need to develop functional biomaterial–cell architectures that recapitulate native tissue micro-environments. Among the diverse fabrication strategies explored, three-dimensional (3D) bioprinting of cell-laden hydrogels has emerged as a transformative technology in regenerative medicine [1-5]. This additive manufacturing process enables the precise spatial deposition of bioinks containing living cells and biomaterials, allowing the creation of complex, patient-specific constructs with interconnected porous architectures. Such 3D configurations provide a physiologically relevant milieu that promotes cell–cell and cell–matrix interactions, thereby enhancing tissue-specific functionality.

The major advantage of 3D bioprinting lies in its capacity to generate cellularised constructs with well-defined spatial organisation and compositional fidelity. Nevertheless, the fabrication of functional tissue analogues remains technically challenging, with limitations primarily related to biomaterial selection, cell viability, and the integration of vascular networks [7-9]. In this context, bioinks, hydrogel formulations embedding cells and biologically active components such as growth factors, nucleic acids, or therapeutic agents, play a pivotal role. Effective bioinks must exhibit controlled rheological properties, high biocompatibility, biodegradability, printability, and mechanical integrity, while providing micro-environments conducive to cell adhesion, proliferation and differentiation [11, 12].

Among available bioink materials, alginate (ALG) and its derivatives are widely employed due to their gentle gelation mechanisms and cytocompatibility. ALG-based systems have supported fibroblast, stem cell and chondrocyte viability, and have facilitated osteogenic and neurogenic differentiation [15]. Nevertheless, the absence of intrinsic cell-adhesive motifs and the rapid degradation of alginate often result in limited cell–matrix interactions. Other hydrogels such as gelatin, methacrylated gelatin (GelMA), collagen, agarose, chitosan (CHI), polycaprolactone (PCL), silk fibroin, and hyaluronic acid (HA) have also been evaluated. Yet, many of these systems were not originally engineered for TE, and in numerous cases, cells were incorporated post-gelation, limiting spatial uniformity and construct fidelity.

Chitosan-based hydrogels have shown promise in cartilage and skin regeneration, where bioinspired multilayer configurations emulate native tissue architecture and support cellular integration [20, 21]. However, these systems typically involve post-gelation cell seeding, resulting in non-homogeneous cell distribution and limited spatial precision, constraints that can be overcome through 3D bioprinting. The key challenge lies in formulating unmodified chitosan bioinks that maintain physicochemical conditions compatible with cell viability while retaining suitable viscosity and gelation behavior for extrusion or inkjet printing [11].

Although the acidic solubilisation and gelation characteristics of chitosan have hindered its direct application as a cell-laden bioink, its cationic nature, tunable viscosity, and high molecular weight render it a promising candidate for the fabrication of stable, bioresorbable scaffolds [21]. Overcoming current physicochemical limitations would enable the development of unmodified chitosan-based bioinks capable of supporting viable cells during printing. Such systems could facilitate the fabrication of biocompatible, bioactive, and bioresorbable 3D constructs for applications in tissue engineering, regenerative medicine, and in vitro tissue modelling, ultimately advancing the clinical translation of bioprinted tissues [12].

Following the quantitative analysis of cellulose nanofiber orientation within chitosan-based viscous bioinks in section 5.2, the acquired knowledge will be leveraged in the 3D bioprinting of the same bioinks integrated with living cells. The incorporation of cells into these structurally characterized bioinks will enable the fabrication of cell-laden constructs in which the predetermined nanofiber alignment may serve as biophysical guidance cues. It is anticipated that the oriented nanofibers will promote anisotropic cellular organization and alignment, thereby contributing to the development of engineered tissues with enhanced structural integrity and functional performance. Due to the inherently acidic nature of chitosan solutions, which is not conducive to maintaining cell viability during the preparation of cell-laden bioinks, a chemical modification approach was employed to improve its biocompatibility. Specifically, the reacetylation of the starting chitosan was carried out to increase its degree of acetylation, thereby enhancing its solubility under near-neutral pH conditions (approximately pH 7.4). This modification allows the formulation of chitosan-based bioinks in a more physiologically relevant environment, minimizing cytotoxic effects associated with acidic media and facilitating the encapsulation and printing of viable cells within the bioink matrix.

5.3.1. Full Deacetylation of Chitosan and its Reacetylation into Random Chitosan Copolymers

5.3.1.1. Determination of the Chitosan Degree of Acetylation (DA)

After successfully synthesizing randomly distributed chitosan samples with varying DA, it was essential to accurately determine their DA values to guide subsequent experiments. As outlined above, DA was evaluated using ^{1}H NMR spectroscopy and ATR-FTIR spectroscopy. Among these, ^{1}H NMR, as proposed by Hirai et al. [51], is considered one of the most reliable methods due to its straightforward spectral interpretation and reproducibility. Figure 5.3.1 top shows the proton assignments of chitosan used for ^{1}H NMR analysis. Protons H2–H6 are present in both glucosamine (GlcN) and N-acetylglucosamine (GlcNAc) residues, whereas GlcNAc contains an additional three protons from the methyl group (H7). Accordingly, DA can

be calculated from the ratio of the integrated area of the methyl protons of GlcNAc to that of the H2–H6 protons of both GlcN and GlcNAc units.

Representative ^{1}H NMR spectra of chitosan with different DAs are shown on bottom of Figure 5.3.1. As the R value increases, the intensity of the methyl proton signal at ~2 ppm also increases, reflecting the higher GlcNAc content in the polymer chain. This trend is consistent from DA = 0 up to R = 0.3. However, at higher DAs, ^{1}H NMR shows limitations: the methyl proton signal in the R = 0.4 sample appears stronger than in the R = 0.5 sample. A likely explanation is that excess acetic anhydride, tightly associated with the polymer during re-acetylation, is difficult to remove and produces overlapping signals near the methyl resonance.

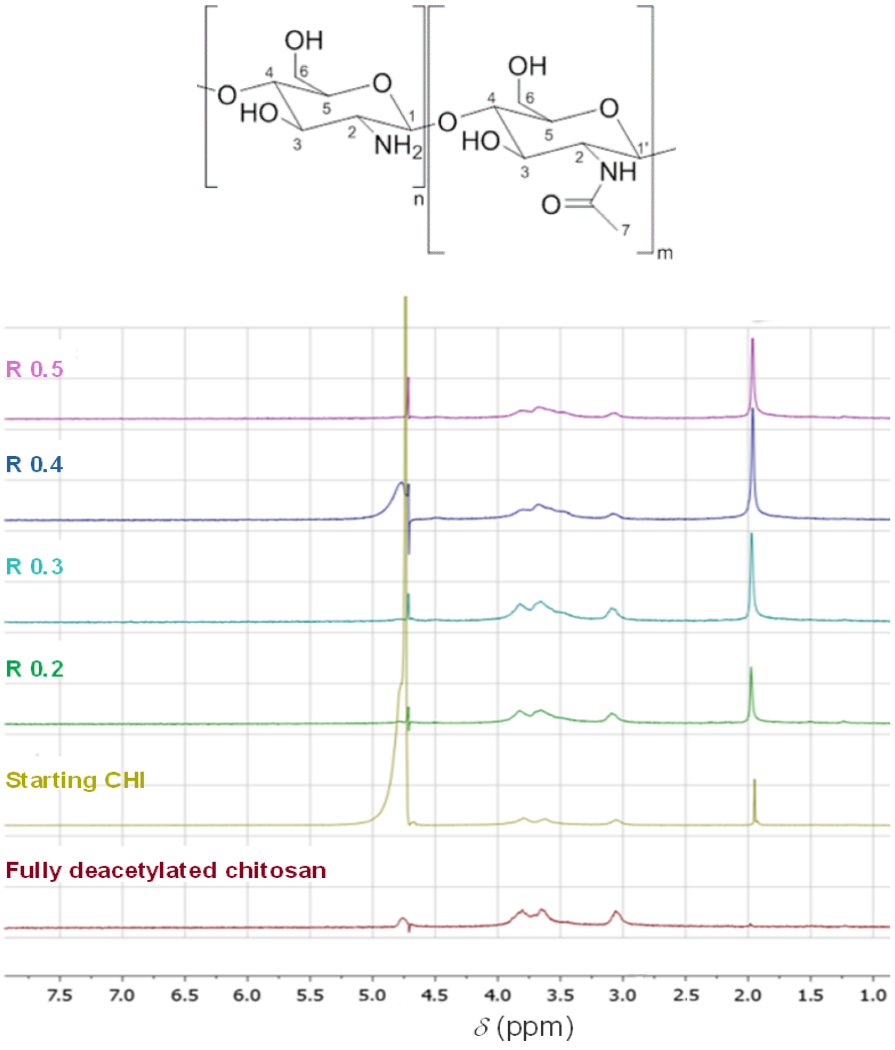

Figure 5.3.1. *(Top)* Proton assignments for ^{1}H NMR analysis. *(Bottom)* ^{1}H NMR spectra of chitosan samples.

To address this limitation, FTIR spectroscopy was employed for samples with R = 0.4 and 0.5. As demonstrated by Brugnerotto et al. [55], FTIR is a robust complementary method capable of reliably determining DA across the full range of acetylation. In FTIR spectroscopy, several methods have been proposed for calculating the DA of chitosan, all of which rely on the absorbance ratios of characteristic spectral bands. However, the calculated DA values may

vary depending on the chosen expression. In this study, we adopted the method recommended by Brugnerotto et al. [55], shown in section 4.2.3, where DA is determined from the absorbance ratio A1320/A1420. This approach provides results that are consistent with those obtained from other techniques, including ^{1}H and ^{13}C NMR spectroscopy. Moreover, the bands at 1320 cm^{-1} and 1420 cm^{-1} are stable under different humidity conditions, thereby minimizing reproducibility issues often associated with FTIR measurements.

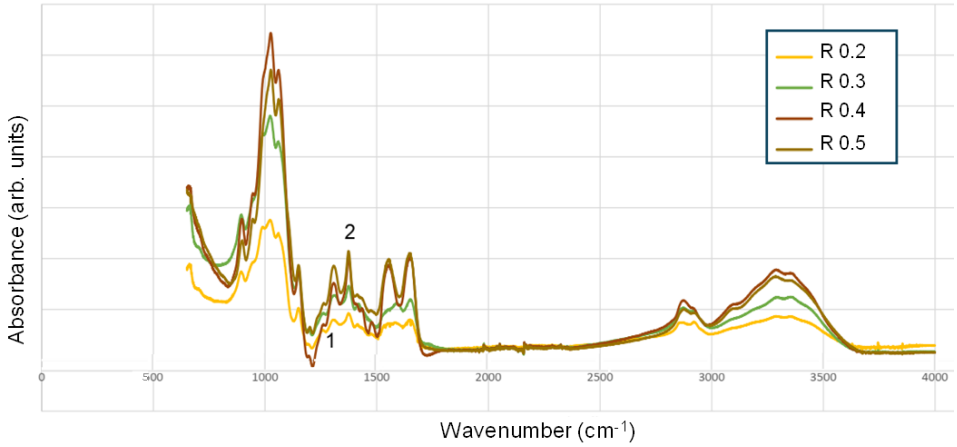

Figure 5.3.2. FTIR spectra of chitosan samples (R = 0.2, 0.3, 0.4, and 0.5). Key absorbance peaks are indicated: (1) 1320 cm^{-1} and (2) 1420 cm^{-1}.

Representative FTIR spectra of re-acetylated chitosan samples are shown in Figure 5.3.2. With increasing N-acetylglucosamine content (corresponding to higher R values), the absorbance of the 1320 cm^{-1} band, attributed to $–CH_3$ groups, increases progressively, confirming higher degrees of acetylation. Using both ^{1}H NMR and FTIR methods, chitosan DA values were determined and are summarized in Table 5.3.1.

5.3.2. Size Exclusion Chromatography coupled to Multiangle Laser Light Scattering (SEC-MALLS)

Figure 5.3.3 shows the obtained SEC-MALLS chromatograms for some chitosan samples like those obtained after full deacetylation of the starting chitosan of DA 2.5%, to produce fully deacetylated chitosan of DA = 0, and after the re-acetylation of this latter to produce a random copolymer chitosan, for example of DA 39.6% (R0.4).

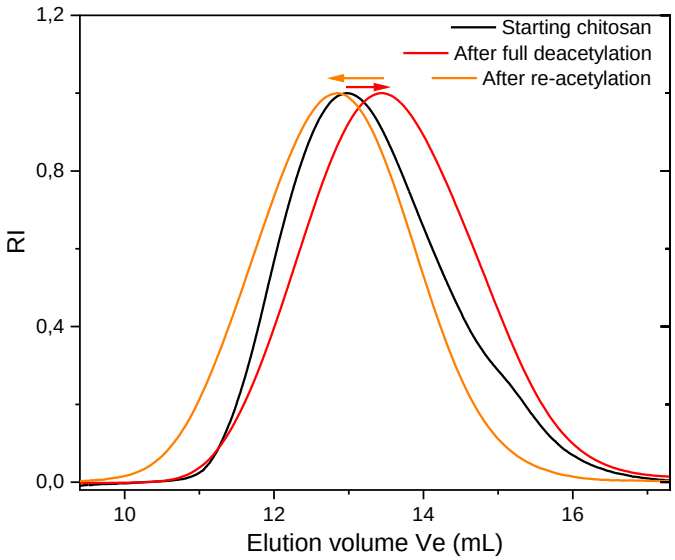

Figure 5.3.3. SEC-MALLS chromatograms for the chitosan samples after full deacetylation of the starting chitosan of DA 2.5%, to produce fully deacetylated chitosan of DA = 0, and after the re-acetylation of this latter to produce a random copolymer chitosan, for example of DA 39.6%.

Table 5.3.1 shows the achieved number and weight-average molecular masses (Mn and Mw, respectively) and polydispersity index Đ obtained for the fully deacetylated chitosan (R0, DA = 0), and of the re-acetylated random copolymer chitosans obtained after using different molar ratio of acetic anhydride to glucosamine (R0.1 to R0.5), to produce chitosans of different DA values. The results show that the chitosan polymer chain length was practically not affected after the processes, so that the expected high viscosity of chitosan solutions as for bioinks would not be compromised.

Table 5.3.1. Degree of acetylation (DA), number and weight-average molecular masses (Mn and Mw, respectively), and polydispersity index Đ of fully deacetylated chitosan (R0), and of re-acetylated random copolymer chitosans obtained after using different molar ratio of acetic anhydride to glucosamine (R0.1 to R0.5).

Chitosan samples	**Degree of acetylation** (%)	**Polymer molecular mass** Mn (g/mol)	Mw (g/mol)	Mw/Mn
Starting chitosan	2.5 ± 0.5	3.447×10^5 (±1.183%)	5.540×10^5 (±1.061%)	1.607 (±1.590%)
R 0	0	2.572×10^5 (±0.639%)	3.059×10^5 (±0.574%)	1.619 (±1.042%)
R 0.1	12.0 ± 0.8	2.999×10^5 (±0.712%)	4.857×10^5 (±0.760%)	1.619 (±1.042%)

R 0.2	28.5 ± 0.7	3.131×10^5 (±0.706%)	4.702×10^5 (±0.730%)	1.502 (±1.016%)
R 0.3	32.5 ± 0.8	3.244×10^5 (±0.634%)	4.930×10^5 (±0.807%)	1.520 (±1.027%)
R 0.4	39.6± 0.5	3.221×10^5 (±0.776%)	5.444×10^5 (±0.895%)	1.690 (±1.185%)
R 0.5	44.8 ± 0.7	3.838×10^5 (±1.311%)	7.622×10^5 (±1.225%)	1.986 (±1.794%)

5.3.3. Potentiometric Titration and Solubility Evaluation of Chitosans of Varying Degree of Acetylation (DA)

The solubility of chitosan depends on both its DA and the pH of the surrounding solution. To determine the specific pH conditions required to dissolve chitosan samples of different DAs, potentiometric titration was employed to evaluate their degree of dissociation (α). For this analysis, chitosan samples were dissolved in acetic acid to ensure stoichiometric protonation of the amine groups on the glucosamine residues. The resulting protonated chitosan solutions were subsequently titrated with sodium hydroxide. The variation of pH as a function of α was then examined for samples with different DAs. Because chitosan in its ammonium form behaves as a weak acid, the self-dissociation of the $–NH_3^+$ groups in solution must be taken into account when calculating α. Following the method described by Sorlier et al. [75], the degree of dissociation of chitosan was determined using the expression presented below.

$$\alpha = \alpha' + [H^+]/C \qquad \text{(Eq. 5.3.1)}$$

Here, $[H^+]$ denotes the concentration of free protons, which can be deduced from the pH values; C represents the concentration of glucosamine units; and α′ is the degree of neutralization, directly inferred from the amount of NaOH added during titration.

Figure 5.3.3 presents the potentiometric titration curves of chitosan samples with different DAs, where pH variation is plotted as a function of α, starting from the initial pH of the protonated chitosan solution up to pH 10. For a given DA, all samples contain the same concentration of glucosamine units, but exhibit different degrees of dissociation. At low α values, the titration curves of all samples overlap closely. A slight increase in pH is observed in samples with higher DA at low α, which may be attributed to the formation of aggregates, a phenomenon strongly influenced by DA. Chitosan with a low degree of acetylation tends to exhibit greater chain stiffness due to extensive intermolecular hydrogen bonding.

As α increases, the titration curves of samples with DA values above 30% deviate more significantly. The sharper increase in pH at higher DA is likely associated with enhanced hydrophobic interactions, which become more prominent as acetyl content rises. To further assess the influence of DA on dissociation, the apparent pK_a values of the $–NH_3^+$ groups were determined from the titration curves. We calculated the pKa of the $–NH_3^+$groups to determine the effect of DA on the degree of dissociation of chitosan and thereby on its pH of solubilisation. The dissociation constant Ka, and the pKa = -logKa is calculated as follows:

$$pKa = pH + \log \frac{[Glc-NH_3^+]}{[Glc-NH_2]} \quad \text{or} \quad pKa = pH + \log \frac{(1-\alpha)}{\alpha} \qquad \text{(Eq. 5.3.2)}$$

Such relation indicates that pH = pKa when [Glc-NH_2] = [Glc-NH_3^+], i.e. when the acid dissociation factor α is equal to 0.5. The titration curves of Fig. 5.3.3 show the starting pH of a series of chitosan solutions containing 0.01 M of glucosamine units, which chitosans were dissolved in stoichiometric amount of acetic acid and then brought to a 15mL volume by water addition, and finally titrated with NaOH 0.1 M, respectively. Moreover, Figure 5.3.3 and table 5.3.2. provides the pH values obtained when the dissociation factor achieved was α = 0.5, which should approximately correspond to the apparent pKa value of chitosan (Equation 5.3.2).

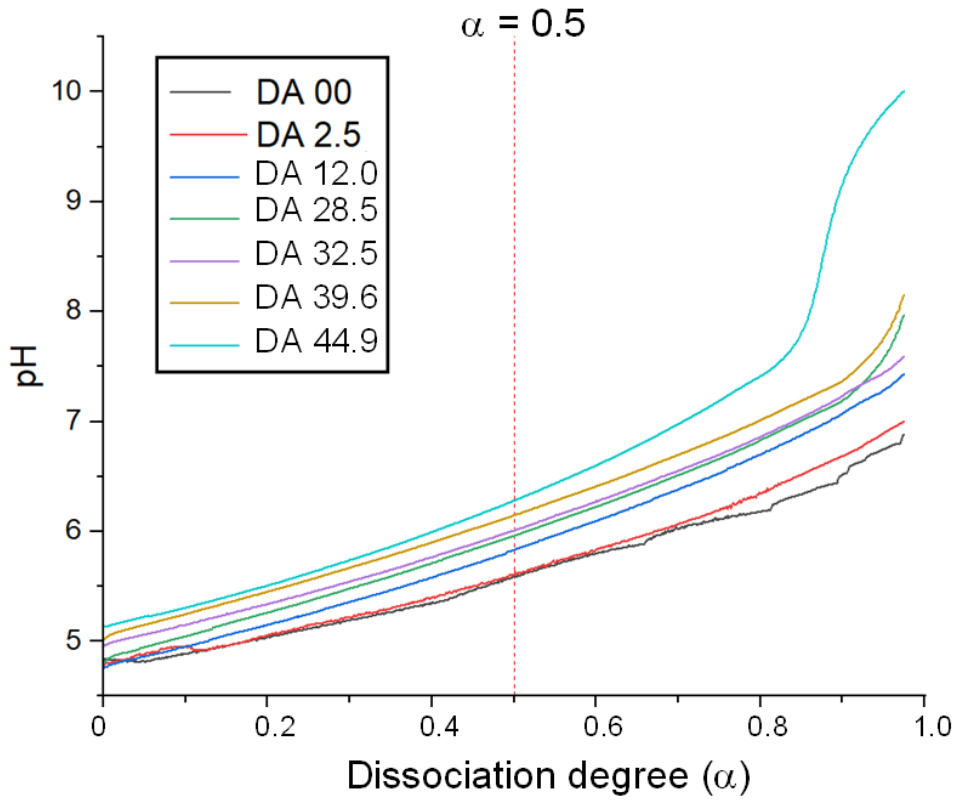

Figure 5.3.4. Titration curves (pH vs. alpha α) of the obtained chitosans of different DAs.

Table 5.3.2. shows the pKa values for the different random copolymer chitosan samples of different degrees of acetylation (DA), which were obtained by reacetylation of fully deacetylated chitosan. The pKa value was determined as the pH obtained at degree of ionization α=0.5 in the curves of potentiometric titration of chitosan solutions (Figure 5.3.4).

Table 5.3.2. pKa values for chitosan random copolymer samples of different degrees of acetylation (DA) obtained by reacetylation of fully deacetylated chitosan.

Chitosan samples	**DA (%)**	**pKa** *(pH at α=0.5, Fig. 5.3.4)*
DA 00	0	5.58
CHI	2.5	5.61
R 0.1	12.0	5.83
R 0.2	28.5	5.96
R 0.3	32.5	6.01
R 0.4	39.6	6.15
R 0.5	44.86	6.28

The pKa value increases from roughly 5.5 to 6.3 when the DA increases from 0 to approximately 45%, respectively. These results suggest that the increase of chitosan DA values enhances the polymer's hydrophobicity, which is connected to the cationicity of the polymer chain provided by the amine functionalities. This suggests that chitosans with increasing DAs become more soluble, as the cationicity of the protonated amine functionalities increases. A more open arrangement of the polymer chains is obtained because the acetyl groups will constitute a steric hindrance against the self-assembly of the chains, which phenomenon consequently exposes out the cationic protonated amine groups to allow their solvation. Thus, with those chitosans of increased DAs viscous bioinks of “unmodified” chitosan containing cells could be produced for cell-laden 3D bioprinting strategies.

Figure 5.3.4 shows the solubilty appearance of the chitosans of different DAs in aqueous media at different pH values: 4.5; 5.0; 5.3; 5.8; 6.1; 6.5; 7.0, which reveals that for chitosan random copolymers of relatively high DAs like 40 and 45% the pH of solubility could be extended to pH values around 7, allowing for survival of cells in chitosan ink solutions. Even for the random chitosan copolymer of DA 32.5% the solubility was extended till pH 6.1, which also should allow for cell survival. UV spectroscopy was used to comparatively estimate the possible solubilizaton of chitosan at different pHs. The obtained absorbances of the chitosan systems in the different pHs are displayed in Figure 5.3.5. Especially for the chitosans of highest DAs of 40 and 45%, the obtained absorbance values around zero should better correspond to a solubilized system, for which the pH of chitosan solubilization extended till higher pHs around 7, revealing the solubility of those high DA statistical chitosans in pH convenient for the cells.

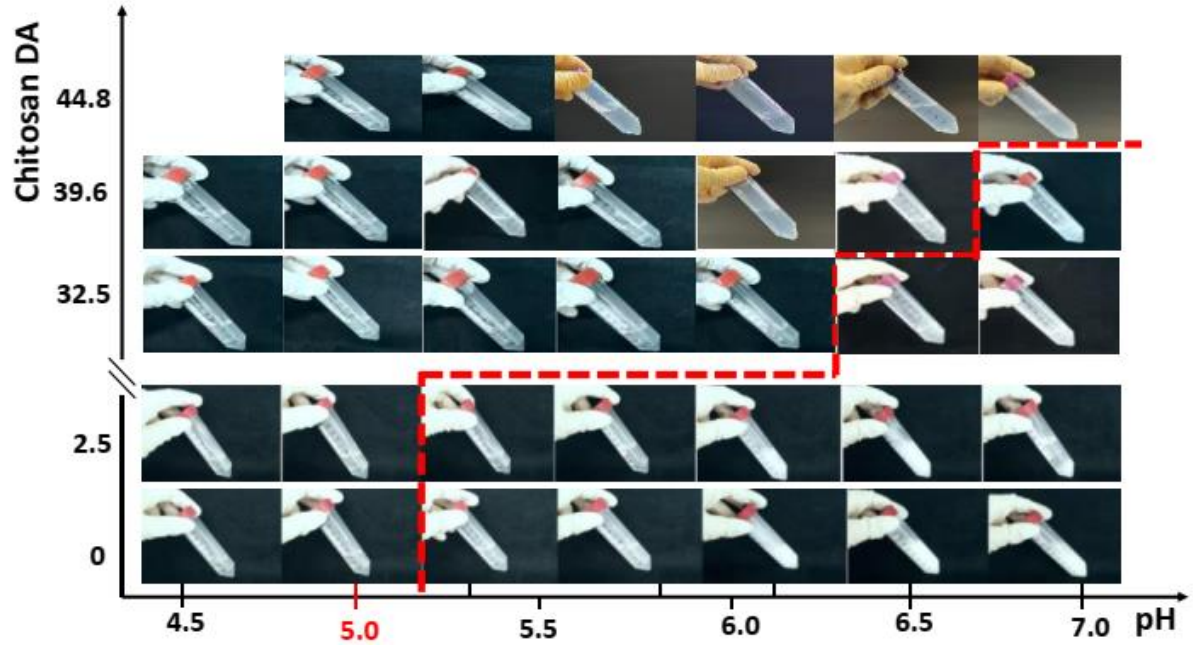

Figure 5.3.5. Appearance of chitosan systems of different DA values in varied medium pHs, after full deacetylation (DA = 0) of starting chitosan (DA = 2.5%), and further reacetylation of that fully deacetylated chitosan of DA=0. Amonium acetate/acetic acid NH_4Ac/HAc aqueous buffer of different pHs (pH 4.5; 5.0; 5.3; 5.8; 6.1; 6.5; 7.0) were prepared as medium to solubilize the chitosans. Red dashed-line highlights the obtained limit of pH of apparent solubilization.

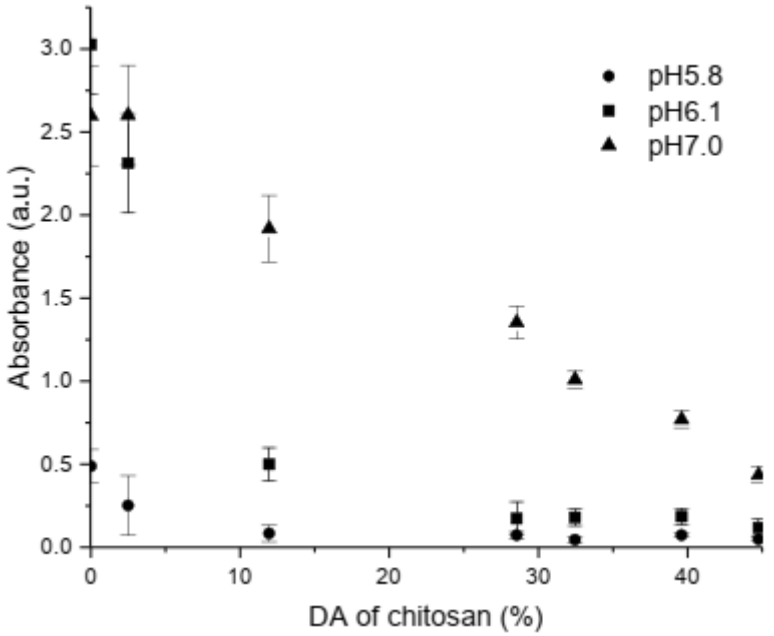

Figure 5.3.6. Absorbance value obtained at λ=600 nm for mixtures of chitosan of different DAs with the aqueous buffer (NH_4Ac/HAc) at given pH.

5.3.4. Rheological Evaluation and Printability of Different Chitosan Bioink Conditions

The DA also has effect on the printability as well as on the physical and mechanical properties of the printed hydrogel scaffold. By evaluating the viscosity of chitosan inks, we identify hydrogel conditions that kept both the material's printability and the viability of cells in scaffolds. Rheological graphs (flow diagrams) of chitosan inks with varying DAs and pHs for chitosan inks of 2 % (w/v) are shown in Figure 5.3.7. At high shear rates, we notice the material' shear thinning property in all conditions. In the flow diagrams showing viscosity vs. shear rate, it was observed that specially the viscosity value at the given shear rate 0.1 s-1 (normally used as reference viscosity for printing) of the different chitosan inks are within the limit of the ink viscosity that can be used in microextrusion, which is up to 6 x 10^7 mPa/s. Figure 5.3.7 shows that we obtained chitosan ink conditions with various Newtonian viscosities ranging from 15 to 200 Pa.s.

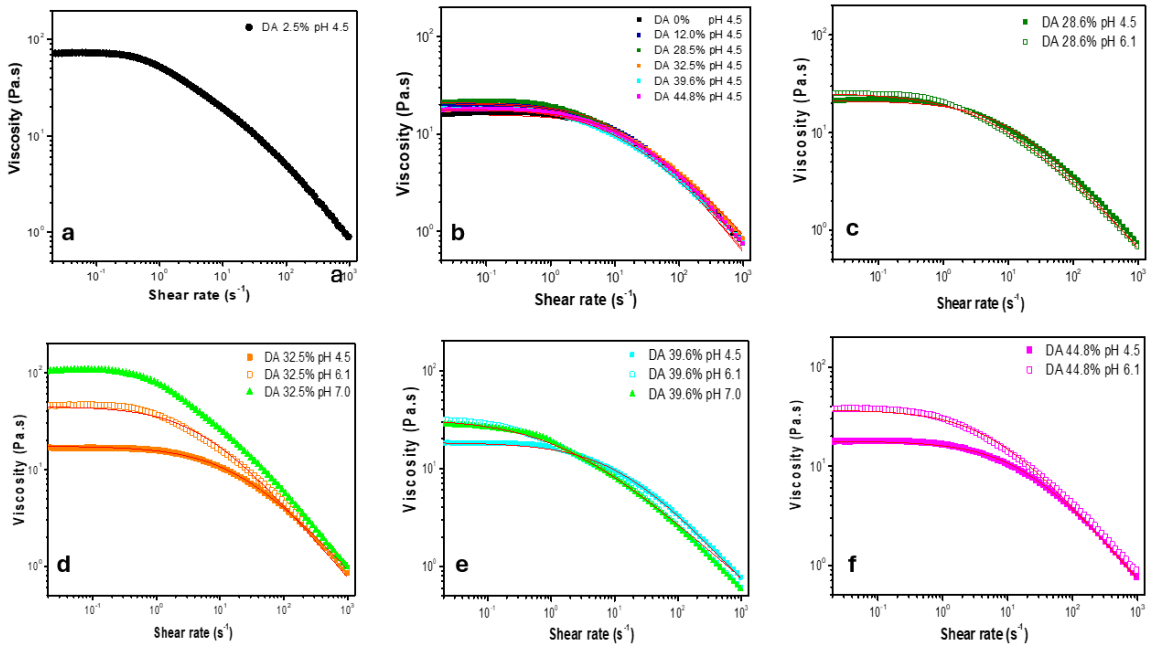

Figure 5.3.7. Flow diagrams (viscosity vs. shear rate) of chitosan solutions with varying degrees of acetylation (DA) solubilized in aqueous buffers (NH_4Ac/HAc) at different pHs. The continuous red line shows the fitting of the rheological data with the Cross model (Equation 5.3.3). (a) Starting chitosan with DA 2.5% at pH 4.5, (b) Fully deacetylated chitosan (DA = 0) and all reacetylated chitosans (DA: 12.0% - 44.8% at pH 4.5, (c, d, e, f) Comparison of reacetylated chitosans (DA: 28.6% - 44.8%) at relevant solubilizing pHs for good compatibility with cells (pH: 6.1 or 7.0) and reference pH 4.5.

The flow diagrams (η vs. shear rate (dγ/dt)) of the chitosan solutions (Fig. 5.3.6) could be modelled with the three-parameter Cross law:

$$\eta = \frac{\eta_{0,CHI}}{1 + (\dot{\gamma}\tau_{CHI})^{1-n_{CHI}}} \qquad \text{(Eq. 5.3.3)}$$

The steady-shear rheological behavior of chitosan solutions with varying degrees of acetylation (DA) and pH was quantitatively analyzed using the Cross model, which describes the shear-dependent viscosity (η) as a function of zero-shear viscosity (η_0), relaxation time (τ), and the flow behavior index (n, where $p = 1 - n$). The parameters extracted from nonlinear regression are summarized in Table 5.3.3, and representative flow curves with corresponding model fits are shown in Figure 5.3.7. All chitosan samples displayed characteristic non-Newtonian, shear-thinning behavior, consistent with the disruption of transient molecular networks and chain alignment under flow. The excellent correlation between experimental data and the Cross model ($R^2 > 0.998$) confirms its suitability for describing the viscoelastic flow response of chitosan systems across the studied conditions.

Table 5.3.3. Flow parameters determined from the rheological analysis by using the Cross model for random copolymer chitosans of different DAs solubilized at different pHs, including pH close to 7 for good biocompatibility in cell-laden bioprinting.

Chitosan DA	$\eta_{0,CHI}$ (Pa.s)	τ_{CHI} (s)	p_{CHI}
	In buffer pH 4.5:		
2.5	69,17 ± 1,98	0,23 ± 0,05	0,91 ± 0,128
0.0	15,84915 ± 0,28182	0,04684 ± 0,00392	0,83735 ± 0,04807
12.0	20,55078 ± 0,07611	0,07561 ± 0,00114	0,73396 ± 0,0055
28.5	21.12 ± 0.72	0.08 ± 0.01	0.78 ± 0.05
32.5	17.40 ± 0.05	0.05 ± 0.01	0.72 ± 0.01
39.6	18.36 ± 0.20	0.09 ± 0.01	0.71 ± 0.01
44.8	17.82 ± 0.24	0.06 ± 0.01	0.77 ± 0.02
	In buffer pH 6.1:		
28.5	25.51 ± 0.38	0.19 ± 0.01	0.68 ± 0.03
32.5	44.77 ± 1.60	0.19 ± 0.03	0.77 ± 0.06
39.6	32.33 ± 3.28	0.68 ± 0.35	0.57 ± 0.10
44.8	36.80 ± 1.15	0.17 ± 0.02	0.76 ± 0.05
	In buffer pH 7.0:		
32.5	98,80 ± 2,86	0,22 ± 0,07	1,03 ± 0,22
39.6	28,44 ± 0,49	0,48 ± 0,04	0,59 ± 0,01

From the rheological analysis and Cross model fit (Figure 5.3.7, Table 5.3.2), the analysis revealed that at the reference pH 4.5 (which is the commonly reported pH of solubilization of chitosan in weakly acidic aqueous media), for the obtained homopolymer (fully deacetylated chitosan, DA = 0) and random chitosan copolymers (reacetylated chitosans, DA: 12.0% – 44.8%), the zero-shear viscosities values (η_0) were moderate and similar, ranging from around

16 to 21 Pa.s, accompanied by short relaxation times (τ: 0.05 – 0.09 s) and consistent shear-thinning indices (p ≈ 0.71 – 0.78). These results indicate that under acidic conditions (pH 4.5), where the amino groups of chitosan are extensively protonated to form the charged group – NH_3^+, it results in highly solvated, positively charged polymer chains. The strong electrostatic repulsion among chains prevents aggregation and promotes expanded conformations, leading to moderate viscosities and rapid stress relaxation. The weak dependence of viscosity on DA at this weakly acidic pH 4.5 suggests that protonation overrides the influence of acetylation, maintaining chain solubility and mobility even as DA increases.

In contrast, substantial changes were observed as the pH increased to 6.1. The zero-shear viscosities increased significantly, reaching 44.77 Pa.s for DA 32.5%, with relaxation times rising to 0.68 s for DA 39.6%. The shear-thinning index became more variable (p = 0.57 – 0.77), indicating that the flow behavior was increasingly sensitive to chemical structure differences due to acetylation. These effects arise from reduced protonation of amino groups at that almost neutral pH, which diminishes electrostatic repulsion and facilitates intermolecular association through hydrogen bonding and hydrophobic interactions among acetylated segments.

As the charge density decreases by increasing DA, polymer chains approach each other more closely, forming transient network structures that resist deformation and relax more slowly. The longer relaxation times observed for higher-DA samples at this pH suggest enhanced molecular association due to the increased presence of hydrophobic acetamide groups. This trend seems to be significant till a threshold DA around 33%, then, the further increase of DA should enhance the rigidity of the chains and expressed apparent charge density, making the balance of these effects to be so important, yielding an optimum for viscosity and solubilization for a chitosan of DA 39.6% at any pH, even neutral pH 7.0.

To summarize, at low DA (0–12%) in random copolymer chitosan contains a high density of protonatable amino groups, which contributes to strong electrostatic repulsion and extensive hydrogen bonding, producing highly entangled and viscous solutions. As the DA increases (≥ 28–45%), substitution of amino groups with acetyl groups into acetamide (–$NHCOCH_3$) reduces both the number of available protonation sites and the capacity for hydrogen bonding, while introducing hydrophobicity and more rigidity to the chains. This shift in molecular architecture weakens interchain cohesion and lowers chain entanglement density, leading to decreased viscosity. The combined effect of DA and pH thus dictates the balance between solubilization and intermolecular association, determining the flow behavior of chitosan solutions. As illustrated in Figure 5.3.7, low DA chitosan at acidic pH exhibits strong shear-thinning and moderate viscosity dominated by charge repulsion and hydrogen-bonded interactions and water solvation, whereas higher DA and elevated pH promote hydrophobic associations and network formation, resulting in higher zero-shear viscosities and slower

relaxation dynamics. These results highlight the dynamic interplay between molecular charge, hydrogen bonding, and hydrophobic forces in governing chitosan solubilty and rheological response. Such tunable flow behavior is critical for extrudability and bioprinting to develop chitosan-based 3D biomaterials with spatio-resolution of cells, which requires controlled viscosity of bioinks and mechanical stability for the production of stable 3D hydrogels through bioprinting. Overall, the Cross-model analysis provided an application-oriented theoretical basis for correlating molecular structure and environmental conditions with the viscoelastic response of chitosan, offering valuable insight for the rational design of cell-laden chitosan-based bioprinted functional biomaterials, including cell-laden chitosan-based hydrogel scaffolds.

5.3.5. Development of Cell-Laden Chitosan Hydrogels by Extrusion Based Bioprinting by Using Re-Acetylated Chitosans. Biocompatibility Studies

In most works producing chitosan hydrogels, the chitosan inks are usually crosslinked through neutralization with a concentrated base, which also would compromise cell survival. To avoid the use of concentrated base, in this work we used tripolyphosphate (TPP) as biocompatible strategy to coagulate the cell-laden chitosan inks into hydrogels in the 3D bioprinting process (Fig. 5.3.8).

The bioprinting of cell-laden chitosan hydrogel scaffolds by using bioinks of chitosans of DA 39.6% dissolved in buffers of pH 6.1 or pH 7.0, at polymer concentrations of 1.5% and 3.0% (w/w), by using conic extrusion needles of different inner diameters: 840 µm; 610 µm and 580 µm, was successfully achieved (Figure 5.3.8.). The gelation bath consisted of TPP 3 or 5 % w/v dissolved in PBS pH 7.4, which allowed the crosslinking of chitosan into cell-laden hydrogels. Figures 5.3.8. and 5.3.9. show examples of results corresponding to bioprinted cell/hydrogel scaffolds for varied conditions.

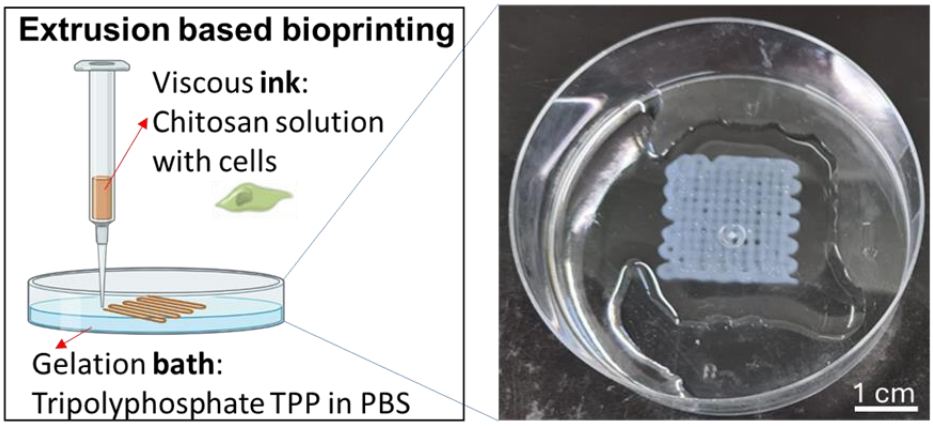

Figure 5.3.8: 3D bioprinting of cell/chitosan bioinks of chitosan of DA 39.6% by extrusion-based bioprinting into a coagulation bath of TPP 5 % in PBS pH7.4, using an extrusion needle of inner diameter 840 µm.

The microscopic observation of the cell-laden scaffolds after incubation for cell culture studies showed that lower TPP concentration in coagulation bath yielded softer hydrogels. The cells show higher survivability when exposure time in TPP gelation bath is kept short like 1-3 min as well as at lower TPP concentration (Figure 5.3.9). Cell viability increases from 55 to 70% when TPP concentration was lower (3% w/v) and relatively short crossliniking time was used.

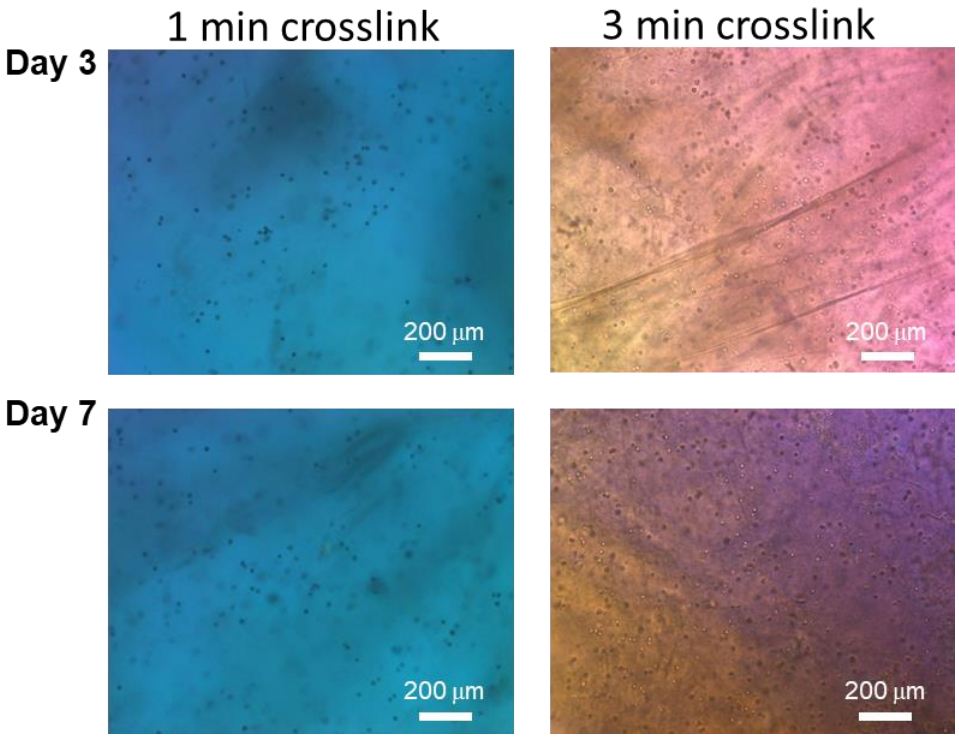

Figure 5.3.9. Microscopic view on 3D bioprinted cell/chitosan bioinks of chitosan of DA 39.6%, initially dissolved at 1.5 % (w/v) in pH 7.0, obtained by extrusion-based bioprinting into a coagulation bath of either TPP 5% (*Left*) or 3% (w/v) (*Right*) in PBS. Extrusion needle inner diameter 580 µm. Cell line NIH-3T3 fibroblasts.

A successful crosslinking of the printed cell-laden chitosan scaffolds was already achieved using 3% (w/v) sodium tripolyphosphate (TPP). At higher c(TPP), a pronounced pH shift in the surrounding culture medium was observed, evidenced by a noticeable color change, as shown in Figure 5.3.9. This alteration in medium pH adversely affected cell viability within the scaffolds. To mitigate this issue, even milder crosslinking conditions were also adopted like employing low TPP concentration of 0.5% (w/v) and relatively short crosslinking time of 3 min.

3D Bioprinting of Cell-Laden Chitosan-Based Hydrogels by Formation of Polyelectrolyte Complex Formation in Core-Shell Bioprinting Strategies

As the crosslinking of cell-laden chitosan inks with TPP would produce a chitosan-tripolyphosphate hydrogel, which if still being biocompatible, could compromise the outstanding biological activity of “pure” chitosan [1, 3, 15], in an alternative method for 3D

bioprinting of cell-laden chitosan inks into cell/chitosan hydrogels, the cell-laden chitosan bioink was gelled by using a shell fluid containing a negatively-charged polyelectrolyte like alginate to induce polyelectrolyte complex formation and thereby gelation of the cell/chitosan bioink when in contact the positively-charge polyelectrolyte chitosan, contained in the core of a printhead constituted of a core-shell coaxial nozzle (Fig. 5.3.10).

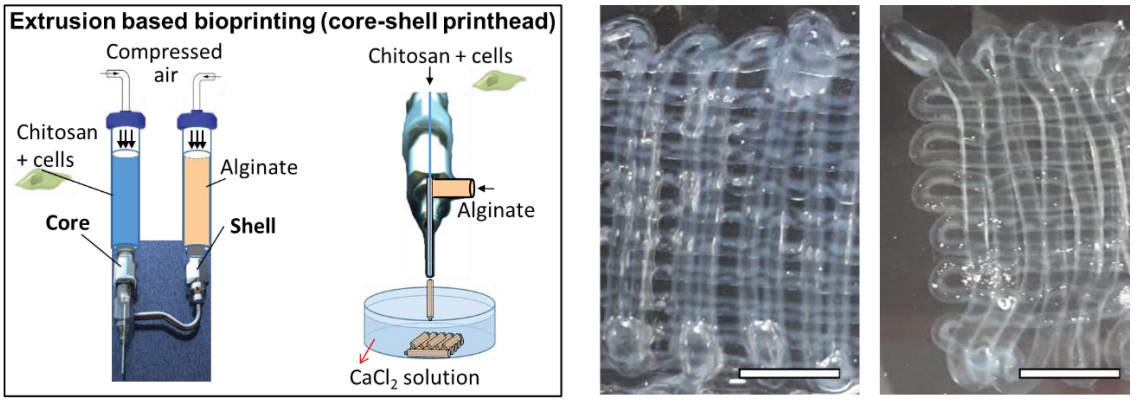

Figure 5.3.10. Scheme of 3D bioprinting of cell/chitosan bioinks of chitosan of DA 39.6% in pH 7.0 by core-shell extrusion-based bioprinting into gelation bath of $CaCl_2$ 0.2 M, using the chitosan ink (image left; chitosan 3% (w/w), image right: 1.5 % (w/w)) in the core, and alginate 4% (w/w) ink in the shell, and observations at different days of culture of cell-laden bioprinted hydrogels. Scale bar 2.5 mm.

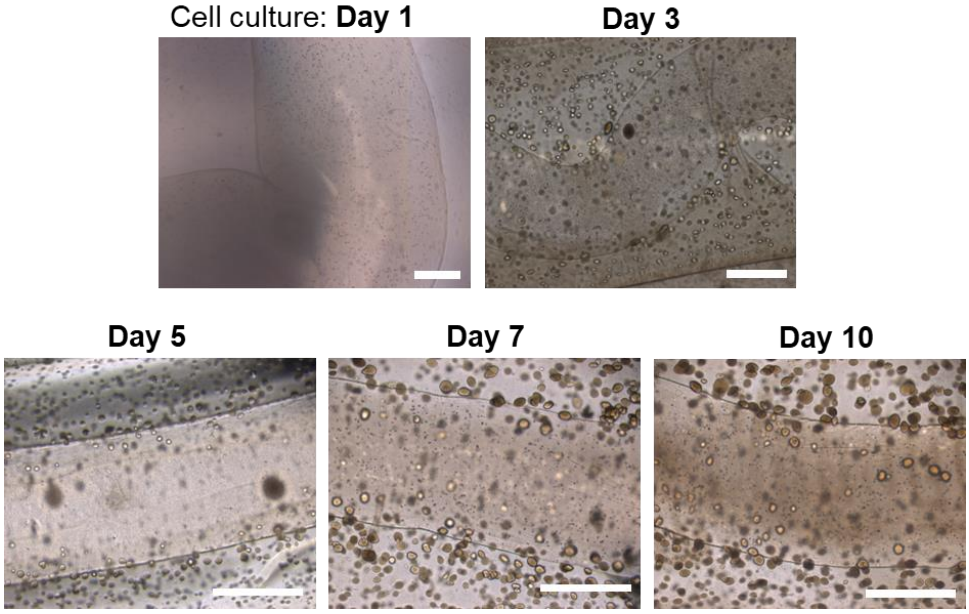

Figure 5.3.11. Microscopic observation of 3D bioprinted cell/chitosan bioinks of chitosan of DA 39.6% in pH 7.0 by core-shell extrusion-based bioprinting, with chitosan ink 2 % w/v in the core, and alginate 4 % ink in the shell, at different days of culture of cell-laden bioprinted hydrogels. Cell line NIH 3T3 fibroblasts. Scale bar 200 µm.

The coaxial bioprinting of fibroblast-laden bioinks demonstrated favorable cell viability and dynamic cellular responses over the 10-day observation period. Figure 5.3.10 reveals a steady increase in fibroblast number, indicating active proliferation within the printed constructs. This trend suggests that the encapsulated microenvironment provided by the chitosan bioink of DA

around 40% was appropriate for cellular growth, supporting both nutrient diffusion and metabolic activity. In addition to proliferation, qualitative observations showed that fibroblasts began to migrate outward from the core region into the surrounding shell material as culture time progressed. Such migration reflects the intrinsic motility of fibroblasts and highlights the permissive nature of the shell matrix in enabling cell infiltration. The progressive colonization of the shell is particularly significant, as it suggests that the coaxial bioprinting approach successfully creates a compartmentalized yet interconnected environment that facilitates cellular expansion beyond the initial deposition zone. In a step forward, to avoid diffusion of the cells contained in the chitosan compartment into the shell alginate compartment used for polyelectrolyte complexation, an alginate/gelatin ink was instead flowing in the shell during coaxial bio-printing. The alginate-based hydrogel shell was denser, cells diffusion was reduced and cells likely stay distributed in the inner chitosan hydrogel (Fig. 5.3.12).

Figure 5.3.12 shows progressive cellular proliferation and spreading within the printed constructs during the 13-day culture period. Bright-field images in Figure 5.3.12 reveals a steady increase in fibroblast number throughout the observation window, accompanied by clear evidence of cell spreading and network formation inside the core region of the coaxial structure. Similarly to what we observed in Figure 5.3.11, these findings suggest that the bioink composition of re-acetylated chitosan of DA around 40% provided a favorable microenvironment for fibroblast attachment and proliferation. Viability assays using calcein-AM and ethidium homodimer in Figure 5.3.13 bottom further confirmed the suitability of the system, demonstrating predominantly live, metabolically active cells with minimal cell death across most time points. Only at days 7 and 13, it was observed a slight reduction in viability, which is likely attributable to spatial constraints within the core as proliferating fibroblasts approached confluence, limiting further expansion and nutrient accessibility (Fig. 5.3.13). The overall results highlight that the coaxial bioprinting strategy effectively supports fibroblast growth, viability, and organization within the bioink matrix, while also underscoring the importance of spatial design and matrix remodeling in sustaining long-term cultures. These findings support the potential of coaxial bioconstructs as dynamic, cell-permissive systems for engineering cell-laden tissue models.

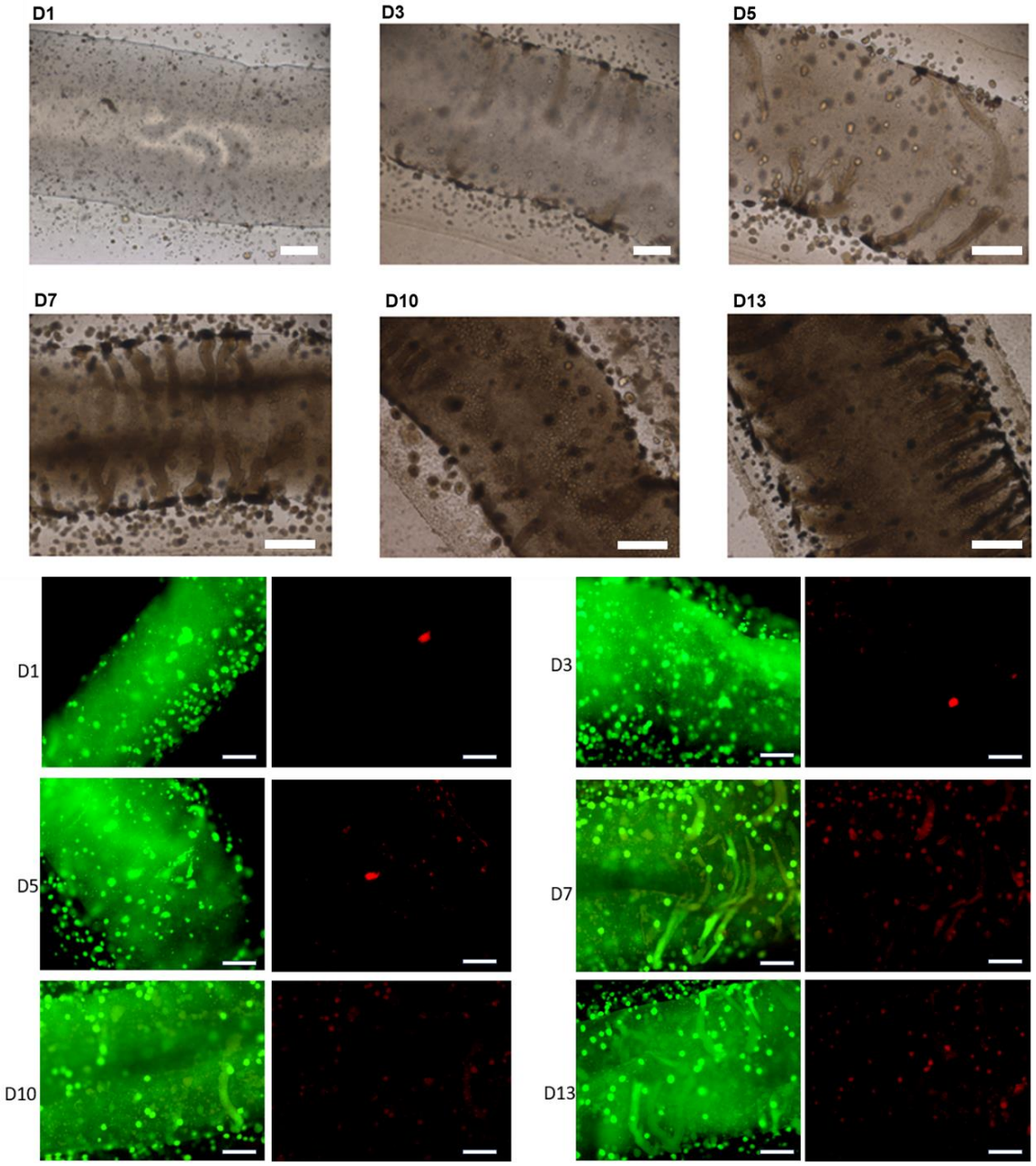

Figure 5.3.12. Bright field and fluorescence microscope view on 3D bioprinted cell/chitosan-based hydrogels obtained by core-shell extrusion-based bioprinting, using chitosan DA 39.6% dissolved in pH7.0 at a concentration of 2 % (w/v) as ink in the core, and alginate 3 % (w/v)/ gelatin 4 % (w/v) as ink in the shell. Cell culture at different days (D). Cell line NIH-3T3 fibroblasts. Scale bar 100 µm.

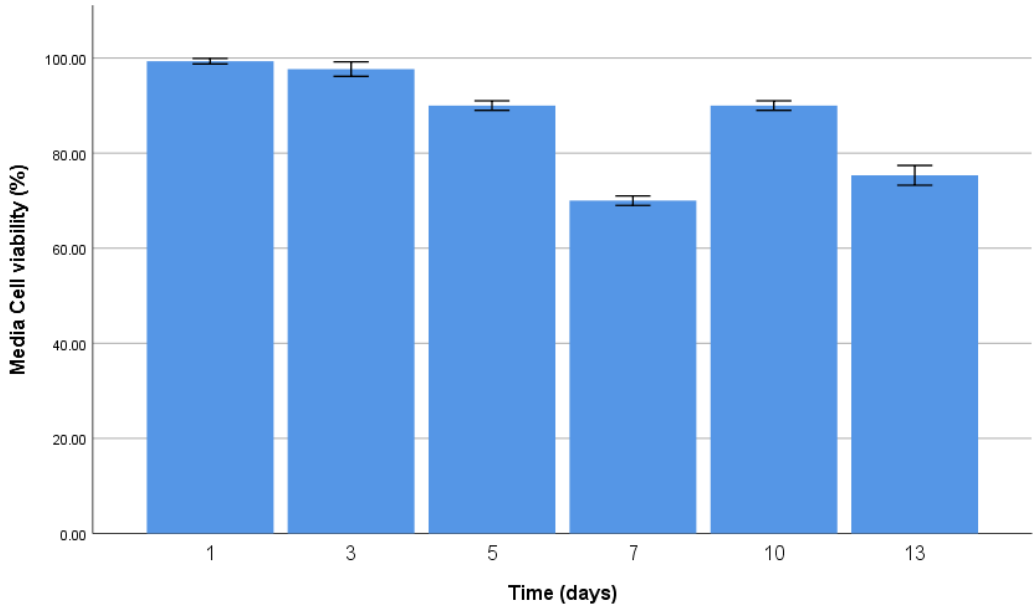

Figure 5.3.13. Cell viability evaluation of core-shell extrusion-based bioprinting, using ink of chitosan DA 40% ink in core, and alginate/gelatin ink in shell, and cell culture at different days.

3D Bioprinting of Cell-Laden Fiber/Hydrogels like Cellulose Nanofiber-Filled Chitosan System

Additionally, in a further proof-of-concept cellulose nanofibers (0.4% wt) of the type nanofibrillated cellulose (CNF) were incorporated into the cell-laden chitosan bioinks to produce cell-laden fiber reinforcen 3D bioprinted hydrogel constructs with enhanced structural integrity and possible anisotropy, which should serve as potential directional cues for the embedded cells (Fig. 5.3.14). Due to their high aspect ratio and abundant hydroxyl groups, CNFs can form hydrogen-bond networks and have electrostatic interactions with chitosan chains, without compromising printability or initial cell viability. Figure 5.3.14 shows the results of 3D bioprinting cell-laden chitosan/CNF hydrogels by using a conic extrusion needle of 580 μm and the chitosan of optimal DA 39.6%. It shows that immediately after extrusion and ionic crosslinking with TPP, the printed constructs displayed good shape fidelity, with printed lines maintaining their geometry and spacing. The reinforcement is likely mediated by hydrogen bonding and mechanical interlocking between the nanofibers and chitosan matrix, resulting in enhanced stability. These results are promising and set the pathway for systematic studies to optimize the crosslinking method to induce gelation to ensure sustained scaffold stability.

Fluorescent imaging of the constructs revealed that cell density within the printed scaffolds was lower than in control samples, suggesting that encapsulation in the CNF-reinforced matrix may temporarily restrict cell distribution or spreading (Fig 5.3.14). However, these observations must be interpreted with caution. Imaging captured only the focal plane of the 3D constructs, potentially underestimating the total number of viable cells within the hydrogel. Attempts to acquire full 3D fluorescence images were challenging due to high background interference,

likely arising from light diffraction caused by the nanofibers and the heterogeneous structure of this hybrid hydrogel system. Consequently, the apparent reduction in cell density may partly reflect imaging limitations rather than true cell loss.

These results indicate that while CNFs improve initial print fidelity and mechanical stability, their presence can complicate fluorescent cell imaging and may influence cell distribution within the scaffold. The combination of ionic crosslinking and CNF reinforcement is sufficient for short-term construct integrity, but further optimization, potentially through secondary covalent crosslinking, increased CNF content, or nanofiber alignment strategies, is required to maintain long-term structural stability while supporting uniform cell encapsulation.

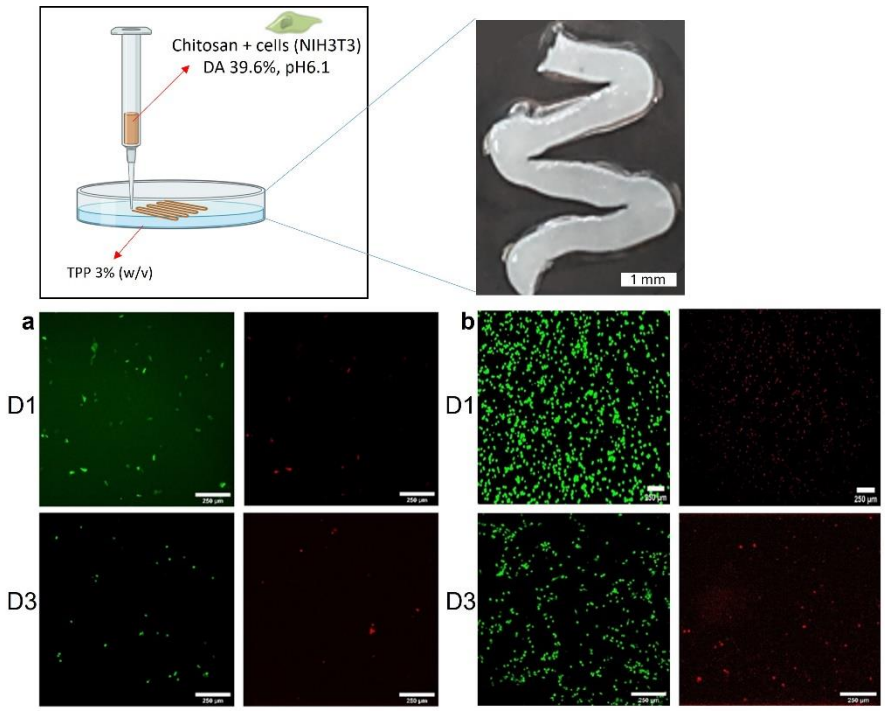

Figure 5.3.14. Scheme of extrusion 3D bioprinting of cell-laden chitosan/CNF (chitosan DA; 39.6%, bioink; chitosan at 2% / cellulose nanofibers 0.4%). (a) Live/Dead NIH-3T3 cell viability assay after incubation of the bioprinted constructs at Day 1 and Day 3, scale bar: 250μm (green: Live, red: Dead). (b) Control (Live/Dead NIH-3T3 cell viability assay after culture on Petri dish, 2D cell culture).

6. Summary and Outlook

In this thesis, the extrudability, spinnability and printability of chitosan-based chitosan gels systems was investigated, with emphasis in using cellulose nanofibers as filler to achieve biomaterials of enhanced mechanical performance and anisotropic behavior.

The fabrication of cellulose nanofiber-filled chitosan hydrogel constructs via three-dimensional (3D) extrusion-based printing technology as well as the quantification of the developed anisotropy during extrusion was systematically investigated. The comprehensive analysis demonstrated that this fabrication strategy facilitates the formation of intricate, customizable, biocompatible architectures possessing tunable mechanical properties and controlled preferential orientation. These features allowed producing constructs particularly suitable for advanced 3D cell culture and tissue engineering applications. The conducted research and resultant findings underscore the considerable potential of this approach for the development of novel, bioinspired fiber-filled 3D hydrogel bioconstructs with prospective applications in regenerative medicine. The principal outcomes of this study are as follows:

- This study demonstrated that tailoring the molecular weight of chitosan and incorporating cellulose nanofibers (CNFs) play a decisive role in optimizing the structural and mechanical performance of chitosan-based composite fibers processed by gel spinning. Chitosan-based fibers with increased stiffness and tensile strength were developed by incorporating small amounts of nanofibrillated cellulose (CNF) into a viscous chitosan (CHI) collodion solution containing both high and low molecular weight chitosans in a gel spinning process. This approach resulted in anisotropic, nanofiber-reinforced biocomposite fibers with superior mechanical properties. Low molecular weight chitosan (LMW) allowed contributing to lower viscosity, higher chain mobility and solubility, while it should help to enhance biological activity due to know improved bioavailability of shorter polymer chains. In contrast, high molecular weight chitosan (HMW) contributes to increase viscosity in collodions, lower the solubility by approaching neutral pH for gelation, and those larger polymer chains are better for structural applications like the processing of fibers, films, hydrogels. Then, the inclusion of CNFs in the CHI matrix plays a crucial role in shaping the morphological characteristics, thermal and mechanical properties of the spun fibers. The CNFs significantly enhanced the stiffness, tensile strength, strain at break, and toughness of the CHI-based fibers, owing to the remarkable mechanical properties, high aspect ratio of the nanofibers, and strong compatibility of the cellulose nanofiber reinforcement with chitosan. This led to robust interfacial interaction between the components, mainly involving physical interactions. Additionally, it was found that the mechanical and structural properties of these fibers are heavily influenced by the proportion of chitosan short chains (LMW) in the spinning solution. As the chitosan short-

chain content increases, the viscosity of the collodion decreases, potentially facilitating the spinning process of collodions with higher polymer concentrations. Results from X-ray diffraction analysis show that the addition of LMW chitosan of intermediate Mw around 4.4 × 10^4 g/mol produced the highest increase of the crystallinity index (CrI) and orientation in the fibers, yielding the best mechanical performance and higher anisotropy. The incorporation of low molecular weight chitosan oligomers, in combination with high molecular weight chitosan and cellulose nanofibers, allows the processing of fibers with tunable mechanical properties. While high molecular weight chitosan provides strength and stiffness through enhanced chain entanglement, the LMW chitosan improves ductility and extrudability of the collodions, leading to a synergistic enhancement in fiber performance. These findings underscore the critical role of chitosan polymer molecular weight tailoring in optimizing chitosan-based nanocomposite fibers for advanced biomedical and textile applications.

- In this thesis we were able to develop and characterize in situ, during processing, the anisotropy in extrusion-based 3D printing hydrogel biomaterials. Printed hydrogel filaments of crystalline polysaccharide nanofiber-filled chitosan inks were processed by microextrusion at the X-ray synchrotron beamline. Different types of cellulose nanofibers were considered as filler of the inks in the study: cellulose whisker nanocrystals (CNC), and nanofibrillated cellulose (CNF). The orientation of the extruded filaments could be quantified in real time during processing, by recording *in situ* the synchrothron X-ray scattering at small (SAXS) and wide angles (WAXS). The extrusion of crystalline cellulose nanofiber/chitosan viscous inks induced a preferential orientation, parallel to the axis of the extrusion needle, in the printed biomaterial. At the exit of the printing nozzle, the SAXS analysis revealed the orientation of elongated self-assembly chitosan aggregates containing the cellulose nanofibers, with this effect being enhanced at approaching the nozzle wall (higher x/R) where a higher shear stress of the ink occurs during extrusion. Besides, higher orientation was achieved when using shorter and slender nanocrystals of cellulose (CNC) than when using a hairy network of longer cellulose nanofibrils (CNF) as nanofiber filler in the chitosan-based inks. At the lowest length scale like that of cellulose crystalline lattice, the WAXS analysis of the printed CHI/cellulose nanofiber materials mainly showed isotropic behavior with practically no orientation of the cellulose crystallites constituting the nanofibers. These findings are interesting to mimic and model the development of anisotropy in 3D bioprinted hydrogel constructs obtained by microextrusion for applications in tissue engineering.
- This work demonstrates the successful development of cell-laden bioinks composed of unmodified chitosan to make major profit of the biological properties of this biopolymer.

The 3D bioprinting of viable, structurally stable, and biologically active hydrogel constructs was successfully achieved. By overcoming the challenges of acidic solubilization and non-physiological gelation, these bioinks leverage the unique nature and high molecular weight of chitosan to create long-term stable scaffolds suitable for tissue engineering. The incorporation of cellulose nanofibers offers a promising approach, enhancing the rheological properties of the bioink to improve extrusion fidelity while providing anisotropic structural cues that would guide cell adhesion, orientation, and adaptation within the printed constructs. Future work should focus on optimizing the cellulose nanofiber content, bioink rheology, and extrusion parameters to maximize cell viability, structural precision, and functional tissue organization. This approach holds significant potential for creating advanced, long-term stability, bioinspired 3D scaffolds for regenerative medicine applications.

This thesis demonstrates significant advancements in the design and fabrication of chitosan-based biomaterials for biomedical and tissue engineering applications. Tailoring the molecular weight of chitosan and incorporating cellulose nanofibers (CNFs) enabled the production of anisotropic, nanofiber-reinforced composite fibers with tunable mechanical properties, including enhanced stiffness, tensile strength, ductility, and toughness. Low molecular weight chitosan improved solubility, chain mobility, and biological activity, while high molecular weight chitosan provided structural integrity and processability, resulting in a synergistic enhancement of fiber performance. Furthermore, extrusion-based 3D printing of nanofiber-filled chitosan inks allowed in situ control and quantification of hydrogel filament anisotropy using synchrotron SAXS/WAXS simultaneously, revealing preferential alignment of chitosan aggregates and cellulose nanofibers along the extrusion direction. Shorter cellulose nanocrystals promoted higher orientation compared to longer nanofibrils, demonstrating the potential to tailor filament architecture and mimic tissue anisotropy. Finally, the successful development of cell-laden bioinks composed of unmodified chitosan represents a major step forward, overcoming solubilization and gelation challenges while maintaining cell viability. Incorporation of cellulose nanofibers improves extrusion fidelity and should provide anisotropic cues for cell adhesion and orientation, addressing current limitations in 3D bioprinting.

Future perspectives include optimizing CNF content, bioink rheology, and extrusion parameters to maximize print fidelity, cell viability, and structural precision, as well as exploring gradient or patterned CNF alignment to guide tissue organization. These strategies will advance unmodified chitosan-based bioinks toward robust, long-lasting, and biologically instructive 3D scaffolds for regenerative medicine and complex tissue engineering applications.

References

1. Casadidio, C., Peregrina, D. V., Gigliobianco, M. R., Deng, S., Censi, R. et al. (2019). Chitin and chitosans: Characteristics, eco-friendly processes, and applications in cosmetic science. Marine Drugs, 17(6), 369. DOI:10.3390/md17060369.
2. Alinejad Y, Adoungotchodo A, Grant MP, et al. (2019). Injectable Chitosan Hydrogels with Enhanced Mechanical Properties for Nucleus Pulposus Regeneration. *Tissue Engineering Part A*.;25(5–6). DOI:10.1089/ten.TEA.2018.0170.
3. Yan, N., Chen, X. (2015). Sustainability: Don't waste seafood waste. Nature, 524(7564), 155–157. DOI:10.1038/ 524155a.
4. Park, J. J., Luo, X., Yi, H., Valentine, T. M., Payne, G. F., Bentley, W. E., Ghodssi, R., & Rubloff, G. W. (2006). Chitosan-mediated in situ biomolecule assembly in completely packaged microfluidic devices. Lab on a Chip, 6(10), 1315. DOI:10.1039/b603101c.
5. Revathi, M., Saravanan, R., Shanmugam, A. (2012). Production and characterization of chitinase from Vibrio species, a head waste of shrimp metapenaeusdobsonii (Miers, 1878) and chitin of sepiellainermis orbigny, 1848. Advances in Bioscience and Biotechnology, 3(4), 392–397. DOI:10.4236/abb.2012.34056.
6. Boudouaia, N., Bengharez, Z., Jellali, S. (2019). Preparation and characterization of chitosan extracted from shrimp shells waste and chitosan film: Application for eriochrome black T removal from aqueous solutions. Applied Water Science, 9(4), 1–12. DOI:10.1007/s13201-019-0967-z.
7. Hahn, T., Roth, A., Ji, R., Schmitt, E., Zibek, S. (2020). Chitosan production with larval exoskeletons derived from the insect protein production. Journal of Biotechnology, 310, 62–67. DOI:10.1016/j.jbiotec.2019.12.015.
8. Bhuiyan, M. R., Shaid, A., Bashar, M. M., Haque, P., Hannan, M. A. (2013). A novel approach of dyeing jute fiber with reactive dye after treating with chitosan. Open Journal of Organic Polymer Mater, 3(4), 87–91. DOI:10.4236/ojopm.2013.34014.
9. Ferraro, V., Cruz, I. B., Jorge, R. F., Malcata, F. X., Pintado, M. E. et al. (2010). Valorisation of natural extracts from marine source focused on marine by-products: A review. Food Research International, 43(9), 2221– 2233. DOI:10.1016/j.foodres.2010.07.034.
10. Abo Elsoud, M. M., El Kady, E. M. (2019). Current trends in fungal biosynthesis of chitin and chitosan. Bulletin of the National Research Centre, 43(1), 59. DOI:10.1186/s42269-019-0105-y.
11. Chien, R., Yen, M., Mau, J. (2016). Antimicrobial and antitumor activities of chitosan from shiitakestipes, compared to commercial chitosan from crab shells. Carbohydrates Polymers, 138(1), 259–264. DOI:10.1016/j.carbpol.2015.11.061.
12. Kaur, S., Dhillon, G. S. (2014). The versatile biopolymer chitosan: Potential sources evaluation of extraction methods and applications. Critical Reviews in Microbiology, 40(2), 155–175. DOI:10.3109/1040841X.2013.770385.
13. Merzendorfer, H., Zimoch, L. (2003). Chitin metabolism in insects: Structure, function and regulation of chitin synthases and chitinases. Journal of Experimental Biology, 206(24), 4393–4412. DOI:10.1242/jeb.00709.
14. Schmitz, C., Auza, L. G., Koberidze, D., Rasche, S., Fischer, R. et al. (2019). Conversion of chitin to defined chitosan oligomers: Current status and future prospects. Marine Drugs, 17(8), 452. DOI:10.3390/md17080452.
15. João, C. F. C., Silva, J. C., Borges, J. P. (2015). Chitin-based nanocomposites: Biomedical applications. In: Eco-friendly polymer nanocomposites, pp. 439–457. New Delhi: Springer.
16. Kaya, M., Lelesius, E., Nagrockaite, R., Sargin, I., Arslan, G. et al. (2015). Differentiations of chitin content and surface morphologies of chitins extracted from male and female grasshopper species. PLoS One, 10(1), e0115531. DOI:10.1371/journal.pone.0115531.

17. Jang, M. K., Kong, B. G., Jeong, Y. I., Lee, C. H., Nah, J. W. (2004). Physicochemical characterization of α-chitin, β-chitin, and γ-chitin separated from natural resources. Journal of Polymer Science Part A–Polymer Chemistry, 42(14), 3423–3432. DOI:10.1002/(ISSN)1099-0518.
18. Muzzarelli, R. A. (2011). Chitin nanostructure in living organisms. In: Gupta, N. (Eds), In: Chitin: Formation and diagenesis, pp. 1–34. Netherland: Dordrecht.
19. Zainol Abidin, N. A., Kormin, F., ZainolAbidin, N. A., Mohamed Anuar, N. A. F., Abu Bakar, M. F. (2020). The potential of insects as alternative sources of chitin: An overview on the chemical method of extraction from various sources. International Journal of Molecular Sciences, 21(14), 4978. DOI:10.3390/ijms21144978.
20. Pilai, K. S., Paul, W., Sharma, C. P. (2009). Chitin and chitosan polymers: Chemistry, solublity and fiber formation. Progress in Polymer Science, 34, 641–678. DOI:10.1016/j.progpolymsci.2009.04.001.
21. Dong D, Lu H, Lai X, Zeng X, Li H. Cellulose nanofiber-reinforced chitosan conductive hydrogel tailored by double-network strategy for stretchable strain sensor. International Journal of Biological Macromolecules. 2025;333(Pt 1):148851. DOI:10.1016/j.ijbiomac.2025.148851
22. Shojaeiarani J, Bajwa DS, Chanda S. Cellulose nanocrystal based composites: A review. Composites Part C Open Access. 2021;5:100164. DOI:10.1016/j.jcomc.2021.100164
23. Arockiasamy FS, Manoharan B, Santhi VM, et al. Navigating the nano-world future: Harnessing cellulose nanocrystals from green sources for sustainable innovation. Heliyon. 2024;11(1):e41188. DOI:10.1016/j.heliyon.2024.e41188
24. De Mulder ELW, Buma P, Hannink G. Anisotropic porous biodegradable scaffolds for musculoskeletal tissue engineering. Materials. 2009;2(4):1674-1696. DOI:10.3390/ma2041674
25. Mostert D, Van Der Putten C, Sahlgren CM, Kurniawan NA, Bouten CVC. Bioengineering structural anisotropy in living tissues. Nature Reviews Bioengineering. 2025;3(9):727-741. DOI:10.1038/s44222-025-00338-x
26. Zhang L, Fu L, Zhang X, Chen L, Cai Q, Yang X. Hierarchical and heterogeneous hydrogel system as a promising strategy for diversified interfacial tissue regeneration. Biomaterials Science. 2020;9(5):1547-1573. DOI:10.1039/d0bm01595d
27. Wanjare M, Hou L, Nakayama KH, et al. Anisotropic microfibrous scaffolds enhance the organization and function of cardiomyocytes derived from induced pluripotent stem cells. Biomaterials Science. 2017;5(8):1567-1578. DOI:10.1039/c7bm00323d
28. Pardo A, Gomez-Florit M, Davidson MD, et al. Hierarchical design of Tissue-Mimetic fibrillar hydrogel scaffolds. Advanced Healthcare Materials. 2024;13(16). DOI:10.1002/adhm.202303167
29. Hao L, Mao H. Magnetically anisotropic hydrogels for tissue engineering. Biomaterials Science. 2023;11(19):6384-6402. DOI:10.1039/d3bm00744h
30. Ma W, Yang Z, Lu M, Ma H, Wu C, Lu H. Hierarchically structured biomaterials for tissue regeneration. Microstructures. 2024;4(2):2024014. DOI:10.20517/microstructures.2023.61
31. Liu G, Gan J, Chen A, Liu Q, Zhao X. Synthesis and characterization of an amphiphilic chitosan bearing octyl and methoxy polyethylene. Natural Science. 2010;02(07):707-712. DOI:10.4236/ns.2010.27087
32. Hao L, Mao H. Magnetically anisotropic hydrogels for tissue engineering. Biomaterials Science. 2023;11(19):6384-6402. DOI:10.1039/d3bm00744h
33. Cong M, Wu X, Zhu L, et al. Anisotropic microtopography surface of chitosan scaffold regulating skin precursor-derived Schwann cells towards repair phenotype promotes neural regeneration. Regenerative Biomaterials. 2024;11:rbae005. DOI:10.1093/rb/rbae005
34. Burgert I, Fratzl P. Plants control the properties and actuation of their organs

through the orientation of cellulose fibrils in their cell walls. Integrative and Comparative Biology. 2009;49(1):69-79. DOI:10.1093/icb/icp026

35. Spauwen L, Moliner AP, Van Veenendaal P, Custers R, Malda J, De Ruijter M. Engineering anisotropic mechanical properties in Large-Scale fabricated cartilage constructs using microfiber reinforcement. Advanced Healthcare Materials. 2025;14(19):e2501014. DOI:10.1002/adhm.202501014
36. Elbaum R, Abraham Y. Insights into the microstructures of hygroscopic movement in plant seed dispersal. Plant Science. 2014;223:124-133. DOI:10.1016/j.plantsci.2014.03.014
37. Jana S, Levengood SKL, Zhang M. Anisotropic materials for Skeletal-Muscle-Tissue Engineering. Advanced Materials. 2016;28(48):10588-10612. DOI:10.1002/adma.201600240
38. Safavi HR, Amiri A, Baniassadi M, Zolfagharian A, Baghani M. An anisotropic constitutive model for fiber reinforced salt-sensitive hydrogels. Mechanics of Advanced Materials and Structures. 2022;30(23):4814-4827. DOI:10.1080/15376494.2022.2106523
39. Rešetič A. Shape programming of liquid crystal elastomers. Communications Chemistry. 2024;7(1):56. DOI:10.1038/s42004-024-01141-2
40. Peng X, Xu J, Cheng Y, Zhang L, Yang J, Li Y. An analytical model for Cure-Induced deformation of composite laminates. Polymers. 2022;14(14):2903. DOI:10.3390/polym14142903
41. Abdel-Rahman, R. M., Hrdina, R., Abdel-Mohsen, A. M., Fouda, M. M. G., Soliman, A. Y. et al. (2015). Chitin and chitosan from Brazilian Atlantic Coast: Isolation, characterization and antibacterial activity. International Journal of Biological Macromolecules, 80, 107–120. DOI:10.1016/j.ijbiomac.2015.06.027
42. Boucard N, David L, Rochas C, Montembault A, Viton C, Domard A. (2007) *Polyelectrolyte Microstructure in Chitosan Aqueous and Alcohol Solutions.* Biomacromolecules.;8(4):1209–1217. DOI: 10.1021/bm060911m.
43. Yang, J. K., Shih, I. L., Tzeng, Y. M., Wang, S. L. (2000). Production and purification of protease from a Bacillus subtilis that can deproteinize crustacean wastes. Enzyme and Microbial Technology, 26(5–6), 406–413. DOI:10.1016/S0141-0229(99)00164-7.
44. Abdou, E. S., Nagy, K. S., Elsabee, M. Z. (2008). Extraction and characterization of chitin and chitosan from local sources. Bioresource Technology, 99(5), 1359–1367. DOI:10.1016/j.biortech.2007.01.051.
45. Di Nardo, T. (2018). Deacetylation by mechanochemistry and aging as a pathway to high molecular weight chitosan from chitin (Masters Thesis). Montreal, Canada: McGill University Canada.
46. Nemtsev, S.V.; Gamzazade, A.I.; Rogozhin, S.V.; Bykova, V.M.; Bykov, V.P. (2002). Applied Biochemistry and Microbiology, 38, 521–526, DOI:10.1023/A:1020766325395. Batista, I.; Roberts, G.A.F. (1990). Makromol. Chem., 191, 429–434, DOI:10.1002/macp.1990.021910217.
47. Tolaimate, A.; Desbrières, J.; Rhazi, M.; Alagui, A.; Vincendon, M.; Vottero, P. (2000). On the Influence of Deacetylation Process on the Physicochemical Characteristics of Chitosan from Squid Chitin. Polymer, 41, 2463–2469, DOI:10.1016/S0032-3861(99)00400-0.
48. Lamarque, G.; Cretenet, M.; Viton, C.; Domard, A. (2005). New Route of Deacetylation of α- and β-Chitins by Means of Freeze-Pump Out-Thaw Cycles. Biomacromolecules, 6, 1380–1388, DOI:10.1021/bm049322b.
49. Arnold, N. D., Brück, W. M., Garbe, D., & Brück, T. B. (2020). Enzymatic Modification of Native Chitin and Conversion to Specialty Chemical Products. Marine Drugs, 18(2), 93. DOI:10.3390/md18020093.
50. Kasaai, M.R. (2009). Various Methods for Determination of the Degree of N-Acetylation of Chitin and Chitosan: A Review. J. Agric. Food Chem., 57, 1667–1676, DOI10.1021/jf803001m.

51. Hirai, A.; Odani, H.; Nakajima, A. (1991). Determination of Degree of Deacetylation of Chitosan by 1H NMR Spectroscopy. Polymer Bulletin, 26, 87–94, DOI:10.1007/BF00299352.
52. Zhang H, Neau SH. (2001). In vitro degradation of chitosan by a commercial enzyme preparation: Effect of molecular weight and degree of deacetylation. Biomaterials;22(12):1653–1658. DOI: 10.1016/S0142-9612(00)00359-9.
53. Wang, W.; Bo, S.; Li, S.; Qin, W. (1991). Determination of the Mark-Houwink Equation for Chitosans with Different Degrees of Deacetylation. International Journal of Biological Macromolecules, 13, 281–285, DOI:10.1016/0141-8130(91)90027-R.
54. Terbojevich, M.; Cosani, A.; Conio, G.; Marsano, E.; Bianchi, E. (1991). Chitosan: Chain Rigidity and Mesophase Formation. Carbohydrate Research, 209, 251–260, DOI:10.1016/0008-6215(91)80161-F.
55. Brugnerotto, J.; Desbrières, J.; Roberts, G.; Rinaudo, M. (2001). Characterization of Chitosan by Steric Exclusion Chromatography. Polymer, 42, 09921–09927, DOI:10.1016/S0032- 3861(01)00557-2.
56. Beri, R.G.; Walker, J.; Reese, E.T.; Rollings, J.E. (1993). Characterization of Chitosans via Coupled Size-Exclusion Chromatography and Multiple-Angle Laser Light-Scattering Technique. Carbohydrate Research, 238, 11–26, DOI:10.1016/0008-6215(93)87002-A.
57. Lee, S., Hao, L. T., Park, J., Oh, D. X., & Hwang, D. S. (2022). Nanochitin and Nanochitosan: Chitin Nanostructure Engineering with Multiscale Properties for Biomedical and Environmental Applications. Advanced Materials, 35(4). DOI:10.1002/adma.202203325.
58. Hamdan, Y. A., Amerany, F. E., Desbrières, J., Aghrinane, A., Oudadesse, H., & Rhazi, M. (2022). The evolution of the global COVID-19 epidemic in Morocco and understanding the different therapeutic approaches of chitosan in the control of the pandemic. Polymer Bulletin, 80(10), 10633–10659. DOI:10.1007/s00289-022-04579-3.
59. Wang, S. L., Kaoc, T. Y., Wang, Y. H., Yen, Y. H., Chern, T. Y. et al. (2006). Solvent stable metalloprotease produced by Bacillus sp. TKU004 and its application in deproteinization of squid pen for bchitin preparation. Enzyme and Microbial Technology, 39(4), 724–727. DOI:10.1016/j.enzmictec.2005.12.007.
60. Yang, J. K., Shih, I. L., Tzeng, Y. M., Wang, S. L. (2000). Production and purification of protease from a Bacillus subtilis that can deproteinize crustacean wastes. Enzyme and Microbial Technology, 26(5–6), 406–413. DOI:10.1016/S0141-0229(99)00164-7
61. Di Nardo, T. (2018). Deacetylation by mechanochemistry and aging as a pathway to high molecular weight chitosan from chitin (Masters Thesis).
62. Montreal, Canada: McGill University Canada. Nemtsev, S.V.; Gamzazade, A.I.; Rogozhin, S.V.; Bykova, V.M.; Bykov, V.P. (2002). Applied Biochemistry and Microbiology, 38, 521–526, DOI:10.1023/A:1020766325395.
63. Batista, I.; Roberts, G.A.F. (1990). Makromol. Chem., 191, 429–434, DOI:10.1002/macp.1990.021910217.
64. Tolaimate, A.; Desbrières, J.; Rhazi, M.; Alagui, A.; Vincendon, M.; Vottero, P. (2000). On the Influence of Deacetylation Process on the Physicochemical Characteristics of Chitosan from Squid Chitin. Polymer, 41, 2463–2469, DOI:10.1016/S0032-3861(99)00400-0.
65. Lee, S., Hao, L. T., Park, J., Oh, D. X., & Hwang, D. S. (2022). Nanochitin and Nanochitosan: Chitin Nanostructure Engineering with Multiscale Properties for Biomedical and Environmental Applications. Advanced Materials, 35(4). DOI:10.1002/adma.202203325.
66. Arnold, N. D., Brück, W. M., Garbe, D., & Brück, T. B. (2020). Enzymatic Modification of Native Chitin and Conversion to Specialty Chemical Products. Marine Drugs, 18(2), 93. DOI:10.3390/md18020093.
67. Kasaai, M.R. (2009). Various Methods for Determination of the Degree of N-

Acetylation of Chitin and Chitosan: A Review. J. Agric. Food Chem., 57, 1667–1676, DOI10.1021/jf803001m.

68. Elizalde-Cárdenas, A., Ribas-Aparicio, R. M., Rodríguez-Martínez, A., Leyva-Gómez, G., Ríos-Castañeda, C., & González-Torres, M. (2024). Advances in chitosan and chitosan derivatives for biomedical applications in tissue engineering: An updated review. International Journal of Biological Macromolecules, 262, 129999. DOI:10.1016/j.ijbiomac.2024.129999.
69. Vårum, K.M.; Myhr, M.M.; Hjerde, R.J.N.; Smidsrød, O. (1997). In Vitro Degradation Rates of Partially N-Acetylated Chitosans in Human Serum. Carbohydrate Research, 299, 99–101, DOI:10.1016/S0008-6215(96)00332-1.
70. Wang, W.; Bo, S.; Li, S.; Qin, W. (1991). Determination of the Mark-Houwink Equation for Chitosans with Different Degrees of Deacetylation. International Journal of Biological Macromolecules, 13, 281–285, DOI:10.1016/0141-8130(91)90027-R.
71. Terbojevich, M.; Cosani, A.; Conio, G.; Marsano, E.; Bianchi, E. (1991). Chitosan: Chain Rigidity and Mesophase Formation. Carbohydrate Research, 209, 251–260, DOI:10.1016/0008-6215(91)80161-F.
72. Rinaudo M, Milas M, Le Dung P. Characterization of chitosan (1993). Influence of ionic strength and degree of acetylation on chain expansion. *Int J Biol Macromol*.;15(5):281-285. DOI:10.1016/0141-8130(93)90027-j
73. Beri, R.G.; Walker, J.; Reese, E.T.; Rollings, J.E. (1993). Characterization of Chitosans via Coupled Size-Exclusion Chromatography and Multiple-Angle Laser Light-Scattering Technique. Carbohydrate Research, 238, 11–26, DOI:10.1016/0008-6215(93)87002-A.
74. Schatz, C.; Viton, C.; Delair, T.; Pichot, C.; Domard, A. (2003). Typical Physicochemical Behaviors of Chitosan in Aqueous Solution. Biomacromolecules, 4, 641–648, DOI:10.1021/bm025724c.
75. Sorlier, P.; Denuzière, A.; Viton, C.; Domard, A. (2001). Relation between the Degree of Acetylation and the Electrostatic Properties of Chitin and Chitosan. Biomacromolecules, 2, 765–772, DOI:10.1021/bm015531+.
76. Schatz C, Pichot C, Delair T, Viton C, Domard A. (2003). Static Light Scattering Studies on Chitosan Solutions: From Macromolecular Chains to Colloidal Dispersions. Langmuir.;19(23):9896–9903. DOI: 10.1021/la034410n.
77. Lamarque, G.; Lucas, J.-M.; Viton, C.; Domard, A. (2005). Physicochemical Behavior of Homogeneous Series of Acetylated Chitosans in Aqueous Solution: Role of Various Structural Parameters. Biomacromolecules, 6, 131–142, DOI:10.1021/bm0496357.
78. Caltabiano, A.M.; Foley, J.P.; Striegel, A.M. (2018). Aqueous Size-Exclusion Chromatography of Polyelectrolytes on Reversed-Phase and Hydrophilic Interaction Chromatography Columns. Journal of Chromatography A, 1532, 161–174, DOI:10.1016/j.chroma.2017.12.007.
79. Kamdem Tamo, A.; Doench, I.; Morales Helguera, A.; Hoenders, D.; Walther, A.; Madrazo, A.O. (2020). Biodegradation of Crystalline Cellulose Nanofibers by Means of Enzyme Immobilized-Alginate Beads and Microparticles. Polymers, 12, DOI:10.3390/polym12071522.
80. Astefanei, A.; Dapic, I.; Camenzuli, M. (2017). Different Stationary Phase Selectivities and Morphologies for Intact Protein Separations. Chromatographia, 80, 665–687, DOI:10.1007/s10337-016-3168-z.
81. Aiba, S.-I. (1989) Studies on chitosan: 2. Solution stability and reactivity of partially N-acetylated chitosan derivatives in aqueous media. Int J of Biol Macromol, 11, 249-252.
82. Kurita, K., Sannan, T. and Iwakura, Y. (1977) Studies on chitin: 4. Evidence for formation of block and random copolymers of N-acetyl-D-glucosamine and D-glucosamine by hetero and homogeneous hydrolysis. Makromol Chem, 178, 3197-3202.
83. Hirano, S., Tsuchida, H. and Nagao, N. (1989) N-acetylation in chitosan and

the rate of its enzymatic hydrolysis. Biomaterials, 10, 574-576.
84. Ottoy, M.H., Varum, K.M. and Smidsrod, O. (1996) Compositional Heterogeneity of heterogeneously deacetylated chitosans. Carbohyd Polym, 29, 17-24.
85. Sashiwa, H., Saimoto, H., Shigemasa, Y., Ogawa, R. and Tokura, S. (1991) Distribution of the acetamide group in partially deacetylated chitins. Carb. Polym., 16, 291-296.
86. Sashiwa, H., Saimoto, H., Shigemasa, Y. and Tokura, S. (1993) N-acetyl group distribution in partially deacetylated chitins prepared under homogeneous conditions. Carbohydr. Res., 242, 167-172.
87. Chaussard, G. (2002) Elaboration et étude de matériaux innovants pour la reconstruction cellulaire. Thèse de Doctorat. Université Claude Bernard Lyon 1, Lyon.
88. Lamarque, G., Viton, C. and Domard, A. (2004) Comparative Study of the First Heterogeneous Deacetylation of Chitins in a Multistep Process. Biomacromolecules, 5, 992-1001.
89. Mima S, Miya M, Iwamoto R, Yoshikawa S. (1983). Highly Deacetylated Chitosan and Its Properties. Journal of Applied Polymer Science;28(6):1909–1917. DOI: 10.1002/app.1983.070280607.
90. Domard, A. (1997) Chitosan interactions. In Domard, A., Roberts, G.A.F. and Varum, K.M. (eds.), Advances in Chitin Science. (II). Jacque André, Lyon, pp. 410-420.
91. Flory, P.J. (1967) Principles of polymer chemistry. Cornell University press, Ithaca, New York.
92. Katchalsky, A. (1954) J. Polym. Sci. Part A, 12, 159.
93. Domard, A. (1987) pH and C.D. measurements on a Fully Deacetylated Chitosan: Application to Cu(II)-polymer interactions. Int J of Biol Macromol, 9, 98-104.
94. Sorlier, P. (2002) Etude physico-chimique de solutions de chitosane et relation avec ses propriétés antigéniques. Thèse de Doctorat. Université Claude Bernard Lyon 1, Lyon.
95. Anthonsen, M.W. and Smidsrod, O. (1995) Hydrogen ion titration of chitosans with varying degrees of N-acetylation by monitoring induced 1H-NMR chemical shifts. Carbohydrate Polymers, 26, 303-305.
96. Strand, S.P., Tommeraas, K., Varum, K.M. and Ostgaard, K. (2001) Electrophoretic light scattering studies of chitosans with different degrees of N-acetylation. Biomacromolecules, 2, 1310-1314.
97. Rinaudo, M., Pavlov, G. and Desbriéres, J. (1999) Influence of acetic acid concentration on the solubilization of chitosan. Polymer, 40, 7029-7032.
98. Varum, K.M., Ottoy, M.H. and Smidsrod, O. (1994) Water-solubility of partially N-acetylated chitosans as a function of pH: effect of chemical composition and depolymerisation. Carbohydrate Polymers, 25, 65-70.
99. Rinaudo, M., Pavlov, G. and Desbrières, J. (1999) Solubilization of Chitosan in Strong Acid Medium. International Journal of Polymer Analysis and Characterization, 5, 267 – 276.
100. Elizalde-Cárdenas, A., Ribas-Aparicio, R. M., Rodríguez-Martínez, A., Leyva-Gómez, G., Ríos-Castañeda, C., & González-Torres, M. (2024). Advances in chitosan and chitosan derivatives for biomedical applications in tissue engineering: An updated review. International Journal of Biological Macromolecules, 262, 129999. DOI:10.1016/j.ijbiomac.2024.129999.
101. Xiao, H., Chen, X., Liu, X., Wen, G., & Yu, Y. (2023). Recent advances in decellularized biomaterials for wound healing. Materials Today Bio, 19, 100589. DOI:10.1016/j.mtbio.2023.100589.
102. Wang, L., Xu, Z., Zhang, H., & Yao, C. (2023). A review on chitosan-based biomaterial as carrier in tissue engineering and medical applications. European Polymer Journal, 191, 112059. DOI:10.1016/j.eurpolymj.2023.112059.
103. Hofmann, E., Schwarz, A., Fink, J., Kamolz, L., & Kotzbeck, P. (2023). Modelling

the complexity of human skin in vitro. Biomedicines, 11(3), 794. DOI:10.3390/biomedicines11030794.
104. Chua, A. W. C., Khoo, Y. C., Tan, B. K., Tan, K. C., Foo, C. L., & Chong, S. J. (2016). Skin tissue engineering advances in severe burns: review and therapeutic applications. Burns & Trauma, 4. DOI:10.1186/s41038-016-0027-y.
105. Madni, A., Kousar, R., Naeem, N., & Wahid, F. (2021). Recent advancements in applications of chitosan-based biomaterials for skin tissue engineering. Journal of Bioresources and Bioproducts, 6(1), 11–25. DOI:10.1016/j.jobab.2021.01.002.
106. Yu, R., Zhang, H., & Guo, B. (2021). Conductive biomaterials as bioactive wound dressing for wound healing and skin tissue engineering. Nano-Micro Letters, 14(1). DOI:10.1007/s40820-021-00751-y.
107. Vivcharenko, V., Benko, A., Palka, K., Wojcik, M., & Przekora, A. (2020). Elastic and biodegradable chitosan/agarose film revealing slightly acidic pH for potential applications in regenerative medicine as artificial skin graft. International Journal of Biological Macromolecules, 164, 172–183. DOI:10.1016/j.ijbiomac.2020.07.099.
108. Alam, M. R., Alimuzzaman, S., Shahid, M. A., Fahmida-E-Karim, N., & Hoque, M. E. (2023). Collagen/Nigella sativa/chitosan inscribed electrospun hybrid bio-nanocomposites for skin tissue engineering. Journal of Biomaterials Science Polymer Edition, 34(11), 1517–1538. DOI:10.1080/09205063.2023.2170139.
109. Chen, S., Gao, J., Luo, X., Sun, Y., Jin, W., & He, R. (2023). Therapy of reprogrammable immune activating supramolecular-based chitosan membranes for skin regeneration. Materials & Design, 227, 111713. DOI:10.1016/j.matdes.2023.111713.
110. Hassani, M. S., Salehi, M., Ehterami, A., Mahami, S., Bitaraf, F. S., & Rahmati, M. (2023). Evaluation of collagen type I and III, TGF-β1, and VEGF gene expression in rat skin wound healing treated by alginate/chitosan hydrogel containing crocetin. Biochemical Engineering Journal, 195, 108895. DOI:10.1016/j.bej.2023.108895.
111. Ghatar, J. M., Ehterami, A., Nazarnezhad, S., Hassani, M. S., Kolarijani, N. R., Mahami, S., & Salehi, M. (2023). A novel hydrogel containing 4-methylcatechol for skin regeneration: in vitro and in vivo study. Biomedical Engineering Letters, 13(3), 429–439. DOI:10.1007/s13534-023-00273-z.
112. Yasin, A., Ren, Y., Li, J., Sheng, Y., Cao, C., & Zhang, K. (2022). Advances in hyaluronic acid for biomedical applications. Frontiers in Bioengineering and Biotechnology, 10. DOI:10.3389/fbioe.2022.910290.
113. Drozdova, M., Vodyakova, M., Tolstova, T., Chernogortseva, M., Sazhnev, N., Demina, T., Aksenova, N., Timashev, P., Kildeeva, N., & Markvicheva, E. (2023). Composite hydrogels based on Cross-Linked chitosan and low molecular weight hyaluronic acid for tissue engineering. Polymers, 15(10), 2371. DOI:10.3390/polym15102371.
114. Zhang, M., Peng, X., Huang, Y., Li, K., Zhang, J., Xiao, P., & Zhou, Y. (2023). Naturally derived maleic Chitosan/Thiolated sodium hyaluronate hydrogels as potential 3D printing tissue engineering materials. Macromolecular Materials and Engineering, 308(10). DOI:10.1002/mame.202300085.
115. Yuan, J., Hou, Q., Chen, D., Zhong, L., Dai, X., Zhu, Z., Li, M., & Fu, X. (2019). Chitosan/LiCl composite scaffolds promote skin regeneration in full-thickness loss. Science China Life Sciences, 63(4), 552–562. DOI:10.1007/s11427-018-9389-6.
116. Zhu H., Lin Z., He R., Pan J., Liu X., He X., Zhang J. (2023). Antibacterial and hemostatic properties of chitosan collagen sponge. Chinese Journal of Tissue Engineering Research, 27 (16), 2525.
117. Jiang, M., Li, S., Ming, P., Guo, Y., Yuan, L., Jiang, X., Liu, Y., Chen, J., Xia, D., He, Y., & Tao, G. (2023). Rational design of porous structure-based sodium alginate/chitosan sponges loaded with green synthesized hybrid antibacterial agents for infected wound healing. International Journal of Biological Macromolecules, 237, 123944. DOI:10.1016/j.ijbiomac.2023.123944.
118. Black, C. R. M., Goriainov, V., Gibbs, D., Kanczler, J., Tare, R. S., & Oreffo, R.

O. C. (2015). Bone tissue engineering. Current Molecular Biology Reports, 1(3), 132–140. DOI:10.1007/s40610-015-0022-2.

119. Sadeghinia, A., Davaran, S., Salehi, R., & Jamalpoor, Z. (2018). Nano-hydroxy apatite/chitosan/gelatin scaffolds enriched by a combination of platelet-rich plasma and fibrin glue enhance proliferation and differentiation of seeded human dental pulp stem cells. Biomedicine & Pharmacotherapy, 109, 1924–1931. DOI:10.1016/j.biopha.2018.11.072.
120. Koons, G. L., Diba, M., & Mikos, A. G. (2020). Materials design for bone-tissue engineering. Nature Reviews Materials, 5(8), 584–603. DOI:10.1038/s41578-020-0204-2.
121. Tajvar, S., Hadjizadeh, A., & Samandari, S. S. (2023). Scaffold degradation in bone tissue engineering: An overview. International Biodeterioration & Biodegradation, 180, 105599. DOI:10.1016/j.ibiod.2023.105599.
122. Fourie, J., Taute, F., Du Preez, L., & De Beer, D. (2020). Chitosan Composite Biomaterials for Bone Tissue Engineering—A review. Regenerative Engineering and Translational Medicine, 8(1), 1–21. DOI:10.1007/s40883-020-00187-7.
123. Shaabani, A., & Sedghi, R. (2021). Preparation of chitosan biguanidine/PANI-containing self-healing semi-conductive waterborne scaffolds for bone tissue engineering. Carbohydrate Polymers, 264, 118045. DOI:10.1016/j.carbpol.2021.118045
124. Sani, I. S., Rezaei, M., Khoshfetrat, A. B., & Razzaghi, D. (2021). Preparation and characterization of polycaprolactone/chitosan-g-polycaprolactone/hydroxyapatite electrospun nanocomposite scaffolds for bone tissue engineering. International Journal of Biological Macromolecules, 182, 1638–1649. DOI:10.1016/j.ijbiomac.2021.05.163.
125. Lu, H., Huang, G., Chang, W., Lu, T., Huang, T., Ho, M., & Mi, F. (2022). Modification of chitosan nanofibers with CuS and fucoidan for antibacterial and bone tissue engineering applications. Carbohydrate Polymers, 281, 119035. DOI:10.1016/j.carbpol.2021.119035.
126. Chang, H. K., Yang, D. H., Ha, M. Y., Kim, H. J., Kim, C. H., Kim, S. H., Choi, J. W., & Chun, H. J. (2022). 3D printing of cell-laden visible light curable glycol chitosan bioink for bone tissue engineering. Carbohydrate Polymers, 287, 119328. DOI:10.1016/j.carbpol.2022.119328.
127. Singh, A. K., & Pramanik, K. (2023). Fabrication and investigation of physicochemical and biological properties of 3Dprinted sodium alginate-chitosan blend polyelectrolyte complex scaffold for bone tissue engineering application. Journal of Applied Polymer Science, 140(12). DOI:10.1002/app.53642.
128. Yousefiasl, S., Sharifi, E., Salahinejad, E., Makvandi, P., & Irani, S. (2022). Bioactive 3D-printed chitosan-based scaffolds for personalized craniofacial bone tissue engineering. Engineered Regeneration, 4(1), 1–11. DOI:10.1016/j.engreg.2022.09.005.
129. Jazayeri, H. E., Fahimipour, F., Tahriri, M., Almeida, L., & Tayebi, L. (2017). Oral nerve tissue repair and regeneration. In Elsevier eBooks (pp. 319–336). DOI:10.1016/b978-0-08-100961-1.00019-0.
130. Hsu, R., Chen, P., Fang, J., Chen, Y., Chang, C., Lu, Y., & Hu, S. (2019). Adaptable microporous hydrogels of propagating NGF-Gradient by injectable building blocks for accelerated axonal outgrowth. Advanced Science, 6(16). DOI:10.1002/advs.201900520.
131. Luo, J., Shi, X., Li, L., Tan, Z., Feng, F., Li, J., Pang, M., Wang, X., & He, L. (2021). An injectable and self-healing hydrogel with controlled release of curcumin to repair spinal cord injury. Bioactive Materials, 6(12), 4816–4829. DOI:10.1016/j.bioactmat.2021.05.022.
132. Kharaziha M, Shin SR, Nikkhah M, et al. Tough and flexible CNT–polymeric hybrid scaffolds for engineering cardiac constructs. Biomaterials. 2014;35(26):7346-7354. DOI:10.1016/j.biomaterials.2014.05.014.

133. Bhuiyan, M. H., Clarkson, A. N., & Ali, M. A. (2023). Optimization of thermoresponsive chitosan/β-glycerophosphate hydrogels for injectable neural tissue engineering application. Colloids and Surfaces B Biointerfaces, 224, 113193. DOI:10.1016/j.colsurfb.2023.113193.
134. Squair, J. W., Gautier, M., Sofroniew, M. V., Courtine, G., & Anderson, M. A. (2021). Engineering spinal cord repair. Current Opinion in Biotechnology, 72, 48–53. DOI:10.1016/j.copbio.2021.10.006.
135. Ma, Q., Liao, J., & Cai, X. (2018). Different Sources of Stem Cells and their Application in Cartilage Tissue Engineering. Current Stem Cell Research & Therapy, 13(7), 568–575. DOI:10.2174/1574888x13666180122151909.
136. Xiang, W., Cao, H., Tao, H., Jin, L., Luo, Y., Tao, F., & Jiang, T. (2023). Applications of chitosan-based biomaterials: From preparation to spinal cord injury neuroprosthetic treatment. International Journal of Biological Macromolecules, 230, 123447. DOI:10.1016/j.ijbiomac.2023.123447.
137. Chang, P., Chao, H., Chern, E., & Hsu, S. (2020). Chitosan 3D cell culture system promotes naïve-like features of human induced pluripotent stem cells: A novel tool to sustain pluripotency and facilitate differentiation. Biomaterials, 268, 120575. DOI:10.1016/j.biomaterials.2020.120575.
138. Ham, T. R., Pukale, D. D., Hamrangsekachaee, M., & Leipzig, N. D. (2020). Subcutaneous priming of protein-functionalized chitosan scaffolds improves function following spinal cord injury. Materials Science and Engineering C, 110, 110656. DOI:10.1016/j.msec.2020.110656.
139. Lee, H. J., Lim, I. J., Lee, M. C., & Kim, S. U. (2010). Human neural stem cells genetically modified to overexpress brain-derived neurotrophic factor promote functional recovery and neuroprotection in a mouse stroke model. Journal of Neuroscience Research, 88(15), 3282–3294. DOI:10.1002/jnr.22474.
140. Liu, X., Hao, M., Chen, Z., Zhang, T., Huang, J., Dai, J., & Zhang, Z. (2021). 3D bioprinted neural tissue constructs for spinal cord injury repair. Biomaterials, 272, 120771. DOI:10.1016/j.biomaterials.2021.120771.
141. Cheng, K., Sun, Y., & Hsu, S. (2023). Development of double network polyurethane–chitosan composite bioinks for soft neural tissue engineering. Journal of Materials Chemistry B, 11(16), 3592–3606. DOI: 10.1039/d3tb00120b.
142. Bentley FE, Passieux R, David L, Osorio-Madrazo A. Pure Chitosan Biomedical Textile Fibers from Mixtures of Low- and High-Molecular Weight Bidisperse Polymer Solutions: Processing and Understanding of Microstructure–Mechanical Properties' Relationship. International Journal of Molecular Sciences. 2022;23(9):4767. DOI:10.3390/ijms23094767
143. Marquez-Bravo S, Doench I, Molina P, et al. Functional Bionanocomposite Fibers of Chitosan Filled with Cellulose Nanofibers Obtained by Gel Spinning. Polymers. 2021;13(10):1563. DOI:10.3390/polym13101563
144. Liu B, Wang S, Guo H, et al. High-Strength and Rapidly Degradable Nanocomposite Yarns from Recycled Waste Poly(glycolic acid) (PGA). Polymers. 2025;17(1):100. DOI:10.3390/polym17010100
145. Munton CG, Phillips CI, Martin B, Bartholomew RS, Capperauld I. Vicryl (Polyglactin 910): a new synthetic absorbable suture in ophthalmic surgery. A preliminary study. British Journal of Ophthalmology. 1974;58(11):941-947. DOI:10.1136/bjo.58.11.941
146. Edwards SJ, Crawford F, Van Velthoven MH, et al. The use of fibrin sealant during non-emergency surgery: a systematic review of evidence of benefits and harms. Health Technology Assessment. 2016;20(94):1-224. DOI:10.3310/hta20940
147. Desorme M, Montembault A, Tamet T, Maleysson P, Bouet T, David L. Spinning of hydroalcoholic chitosan solutions: Mechanical behavior and multiscale microstructure of resulting fibers. Journal of Applied Polymer Science. 2018;136(9). DOI:10.1002/app.47130
148. Passieux R, Sudre G, Montembault A, et al. Cytocompatibility / antibacterial

activity trade-off for knittable Wet-Spun chitosan monofilaments functionalized by the in situ incorporation of CU2+ and ZN2+. ACS Biomaterials Science & Engineering. 2022;8(4):1735-1748. DOI:10.1021/acsbiomaterials.2c00079
149. Balea L, Dusserre G, Bernhart G. Mechanical behaviour of plain-knit reinforced injected composites: Effect of inlay yarns and fibre type. Composites Part B Engineering. 2013;56:20-29. DOI:10.1016/j.compositesb.2013.07.028
150. Tamo AK, Tran TA, Doench I, et al. 3D Printing of Cellulase-Laden Cellulose Nanofiber/Chitosan Hydrogel Composites: Towards Tissue Engineering Functional Biomaterials with Enzyme-Mediated Biodegradation. Materials. 2022;15(17):6039. DOI:10.3390/ma15176039
151. Tamo AK, Doench I, Walter L, et al. Development of bioinspired functional Chitosan/Cellulose nanofiber 3D hydrogel constructs by 3D printing for application in the engineering of mechanically demanding tissues. Polymers. 2021;13(10):1663. DOI:10.3390/polym13101663
152. Doench I, Tran TA, David L, et al. Cellulose Nanofiber-Reinforced Chitosan Hydrogel composites for intervertebral disc tissue repair. Biomimetics. 2019;4(1):19. DOI:10.3390/biomimetics4010019
153. Doench I, Torres-Ramos M, Montembault A, et al. Injectable and Gellable Chitosan Formulations Filled with Cellulose Nanofibers for Intervertebral Disc Tissue Engineering. Polymers. 2018;10(11):1202. DOI:10.3390/polym10111202
154. Montembault A, Tahiri K, Korwin-Zmijowska C, Chevalier X, Corvol M t., Domard A. A material decoy of biological media based on chitosan physical hydrogels: application to cartilage tissue engineering. Biochimie. 2006;88(5):551-564. DOI:10.1016/j.biochi.2006.03.002
155. Boucard N, Viton C, Agay D, et al. The use of physical hydrogels of chitosan for skin regeneration following third-degree burns. Biomaterials. 2007;28(24):3478-3488. DOI:10.1016/j.biomaterials.2007.04.021
156. Ladet SG, Tahiri K, Montembault AS, Domard AJ, Corvol M t. M. Multi-membrane chitosan hydrogels as chondrocytic cell bioreactors. Biomaterials. 2011;32(23):5354-5364. DOI:10.1016/j.biomaterials.2011.04.012
157. Ng WL, Yeong WY, Naing MW. Polyelectrolyte gelatin-chitosan hydrogel optimized for 3D bioprinting in skin tissue engineering. International Journal of Bioprinting. 2016;2(1):53. DOI:10.18063/ijb.2016.01.009
158. Surendran G, Sherje AP. Cellulose nanofibers and composites: An insight into basics and biomedical applications. Journal of Drug Delivery Science and Technology. 2022;75:103601. DOI:10.1016/j.jddst.2022.103601
159. Colvin JR, Sowden LC, Leppard GG. The structure of cellulose-producing bacteria, Acetobacter xylinum and Acetobacter acetigenus. Canadian Journal of Microbiology. 1977;23(6):790-797. DOI:10.1139/m77-116
160. Nishiyama Y, Sugiyama J, Chanzy H, Langan P. Crystal Structure and Hydrogen Bonding System in Cellulose Iα from Synchrotron X-ray and Neutron Fiber Diffraction. Journal of the American Chemical Society. 2003;125(47):14300-14306. DOI:10.1021/ja037055w
161. Elazzouzi-Hafraoui S, Nishiyama Y, Putaux JL, Heux L, Dubreuil F, Rochas C. The shape and size distribution of crystalline nanoparticles prepared by acid hydrolysis of native cellulose. Biomacromolecules. 2007;9(1):57-65. DOI:10.1021/bm700769p
162. Vestena M, Gross IP, Muller CMO, Pires ATN. Isolation of whiskers from natural sources and their dispersed in a non-aqueous medium. Polímeros. 2016;26(4):327-335. DOI:10.1590/0104-1428.2367
163. Redlinger-Pohn JD, Petkovšek M, Gordeyeva K, et al. Cavitation fibrillation of cellulose fiber. Biomacromolecules. 2022;23(3):847-862. DOI:10.1021/acs.biomac.1c01309
164. Pan M, Zhou X, Chen M. Cellulose Nanowhiskers Isolation and Properties from Acid Hydrolysis Combined with High Pressure Homogenization. BioResources.

2013;8(1). DOI:10.15376/biores.8.1.933-943.
165. Chen, Z., Zhao, D., Liu, B., Niu, C., Lu, S., Li, Y., 2018. 3D bioprinting of chitosan-based hydrogel scaffolds with controlled structure for cartilage tissue engineering. Materials Science & Engineering C, 83, 195–201.
166. Dutta, P.K., Dutta, J., Tripathi, V.S., 2004. Chitin and chitosan: Chemistry, properties and applications. Journal of Scientific and Industrial Research, 63(1), 20–31.
167. Jayakumar, R., Prabaharan, M., Nair, S.V., Tamura, H., 2011. Novel chitin and chitosan nanofibers in biomedical applications. Biotechnology Advances, 29(3), 322–337. DOI: 10.1016/j.biotechadv.2009.11.001
168. Bai, X., Gao, M., Syed, S., Zhuang, J., Xu, X., Zhang, X.Q., 2015. Bioactive hydrogels for bone regeneration. Bioactive Materials, 1(1), 82–89. DOI: 10.1016/j.bioactmat.2018.05.006
169. Huang, Z.M., et al., 2017. Electrospinning of aligned nanofibers for tissue engineering. Advanced Functional Materials, 27(45), 1700012. Hoque, M.E., Nuge, T., Yeow, T.K., et al., 2015. Chitosan-based nanocomposite scaffolds for tissue engineering applications. Materials & Manufacturing Processes, 30(4), 351–356.
170. Lee, S., et al., 2021. Magnetic-field assisted fabrication of anisotropic scaffolds for tissue engineering. ACS Applied Materials & Interfaces, 13, 23456–23468.
171. Li, X., et al., 2019. Shear-induced fiber alignment in bioprinted hydrogels. Biofabrication, 11, 025012.
172. Li, Y., et al., 2020. Design of anisotropic bioinspired scaffolds for tissue regeneration. Materials Today Bio, 5, 100035.
173. Miller, A.L., et al., 2019. Freeze-casting for hierarchical pore alignment in biomaterials. Biomaterials, 197, 22–36.
174. Shao, C., et al., 2017. Quantitative characterization of fiber orientation in scaffolds using SAXS and XRD. Journal of Materials Chemistry B, 5, 10102–10112.
175. Sisson, K., et al., 2012. Image-based analysis of fiber alignment in tissue scaffolds. Journal of Biomedical Materials Research Part A, 100, 3035–3044.
176. Xie, J., et al., 2009. Aligned electrospun fibers for tissue engineering. Biomaterials, 30, 3547–3557. Lenas, P.; Moos, M.; Luyten, F.P. (2009) Developmental Engineering: A New Paradigm for the Design and Manufacturing of Cell-Based Products. Part I: From Three-Dimensional Cell Growth to Biomimetics of In vivo Development. Tissue Eng. Part. B Rev., 15, 381–394.
177. Tiruvannamalai-Annamalai, R., Armant, D. R., & Matthew, H. W. T. (2014). A glycosaminoglycan based, modular tissue scaffold system for rapid assembly of perfusable, high cell density, engineered tissues. PLoS ONE, 9(1), e84287. DOI:10.1371/journal.pone.0084287.
178. Caddeo, S., Boffito, M., & Sartori, S. (2017). Tissue engineering approaches in the design of healthy and pathological in vitro tissue models. Frontiers in Bioengineering and Biotechnology, 5. DOI:10.3389/fbioe.2017.00040.
179. Marga, F., Neagu, A., Kosztin, I., & Forgacs, G. (2007). Developmental biology and tissue engineering. Birth Defects Research, 81(4), 320–328. DOI:10.1002/bdrc.20109.
180. Takezawa, T. (2003). A strategy for the development of tissue engineering scaffolds that regulate cell behavior. Biomaterials, 24(13), 2267–2275. DOI:10.1016/s0142-9612(03)00038-3.
181. Grounds, M. D. (2017). Obstacles and challenges for tissue engineering and regenerative medicine: Australian nuances. Clinical and Experimental Pharmacology and Physiology, 45(4), 390–400. DOI:10.1111/1440-1681.12899.
182. Williams, D. F. (2019). Challenges with the development of biomaterials for sustainable tissue engineering. Frontiers in Bioengineering and Biotechnology, 7. DOI:10.3389/fbioe.2019.00127.
183. Lenas, P., Ikonomou, L. (2018). Developmental engineering: design of clinically efficacious bioartificial tissues through developmental and systems biology. Sci. China

Life Sci. 61, 978–981. DOI:10.1007/s11427-017-9255-3.
184. Ziółkowska, K., Kwapiszewski, R., & Brzózka, Z. (2011). Microfluidic devices as tools for mimicking the in vivo environment. New Journal of Chemistry, 35(5), 979. DOI:10.1039/c0nj00709a.
185. Vacanti, C. A. (2006). The history of tissue engineering. Journal of Cellular and Molecular Medicine, 10(3), 569–576. DOI:10.1111/j.1582-4934.2006.tb00421.
186. Lenas, P. (2018). Developmental biology in bioartificial tissue Design: manufacturing and regulatory considerations. Regenerative Medicine, 13(1), 7–11. DOI:10.2217/rme-2017-0126.
187. Lu, T., Li, Y., & Chen, T. (2013). Techniques for fabrication and construction of three-dimensional scaffolds for tissue engineering. International Journal of Nanomedicine, 337. DOI:10.2147/ijn.s38635.
188. Ma, X., Qu, X., Zhu, W., Li, Y. S., Yuan, S., Zhang, H., Liu, J., Wang, P., Lai, C. S., Zanella, F., Feng, G. S., Sheikh, F., Chien, S., & Chen, S. (2016). Deterministically patterned biomimetic human iPSC-derived hepatic model via rapid 3D bioprinting. Proceedings of the National Academy of Sciences of the United States of America, 113(8), 2206–2211. DOI:10.1073/pnas.1524510113.
189. Kang, H. W., Lee, S. J., Ko, I. K., Kengla, C., Yoo, J. J., & Atala, A. (2016). A 3D bioprinting system to produce human-scale tissue constructs with structural integrity. Nature biotechnology, 34(3), 312–319. DOI:10.1038/nbt.3413.
190. Cui, X., & Boland, T. (2009). Human microvasculature fabrication using thermal inkjet printing technology. Biomaterials, 30(31), 6221–6227. DOI:10.1016/j.biomaterials.2009.07.056.
191. Zhang, Z., Xiong, R., Mei, R., Huang, Y., & Chrisey, D. B. (2015). Time-Resolved Imaging Study of Jetting Dynamics during Laser Printing of Viscoelastic Alginate Solutions. Langmuir: the ACS journal of surfaces and colloids, 31(23), 6447–6456. DOI:10.1021/acs.langmuir.5b00919.
192. Lorber, B., Hsiao, W. K., Hutchings, I. M., & Martin, K. R. (2014). Adult rat retinal ganglion cells and glia can be printed by piezoelectric inkjet printing. Biofabrication, 6(1), 015001. DOI:10.1088/1758-5082/6/1/015001.
193. Donderwinkel, I., Van Hest, J. C. M., & Cameron, N. R. (2017). Bio-inks for 3D bioprinting: recent advances and future prospects. Polymer Chemistry, 8(31), 4451–4471. DOI:10.1039/c7py00826k.
194. Murphy, S., Atala, A. 3D bioprinting of tissues and organs. NatBiotechnol 32, 773–785 (2014). DOI:10.1038/nbt.2958. Setti, L., Piana, C., Bonazzi, S., Ballarin, B., Frascaro, D., Fraleoni-Morgera, A., & Giuliani, S. (2004). Thermal Inkjet Technology for the Microdeposition of Biological Molecules as a Viable Route for the Realization of Biosensors. Analytical Letters, 37(8), 1559-1570. DOI:10.1081/al-120037587.
195. Chahal, D., Ahmadi, A., & Cheung, K. C. (2012). Improving piezoelectric cell printing accuracy and reliability through neutral buoyancy of suspensions. Biotechnology and bioengineering, 109(11), 2932–2940. DOI:10.1002/bit.24562.
196. Peng, W., Unutmaz, D., & Ozbolat, I. T. (2016). Bioprinting towards Physiologically Relevant Tissue Models for Pharmaceutics. Trends in biotechnology, 34(9), 722–732. DOI:10.1016/j.tibtech.2016.05.013.
197. Kolesky, D. B., Truby, R. L., Gladman, A. S., Busbee, T. A., Homan, K. A., & Lewis, J. A. (2014). 3D bioprinting of vascularized, heterogeneous cell-laden tissue constructs. Advanced materials (Deerfield Beach, Fla.), 26(19), 3124–3130. DOI:10.1002/adma.201305506.
198. Derakhshanfar, S., Mbeleck, R., Xu, K., Zhang, X., Zhong, W., & Xing, M. (2018). 3D bioprinting for biomedical devices and tissue engineering: A review of recent trends and advances. Bioactive materials, 3(2), 144–156. DOI:10.1016/j.bioactmat.2017.11.008.
199. Nair, K., Gandhi, M., Khalil, S., Yan, K. C., Marcolongo, M., Barbee, K., & Sun, W. (2009). Characterization of cell viability during bioprinting processes. Biotechnology journal, 4(8), 1168–1177. DOI:10.1002/biot.200900004.

200. Tabriz, A. G., Hermida, M. A., Leslie, N. R., & Shu, W. (2015). Three-dimensional bioprinting of complex cell laden alginate hydrogel structures. Biofabrication, 7(4), 045012. DOI:10.1088/1758-5090/7/4/045012.
201. Hölzl, K., Lin, S., Tytgat, L., Van Vlierberghe, S., Gu, L., & Ovsianikov, A. (2016). Bioink properties before, during and after 3D bioprinting. Biofabrication, 8(3), 032002. DOI:10.1088/1758-5090/8/3/032002.
202. He, Y., Yang, F., Zhao, H., Gao, Q., Xia, B., & Fu, J. (2016). Research on the printability of hydrogels in 3D bioprinting. Scientific reports, 6, 29977. DOI:10.1038/srep29977.
203. Mironov, V., Visconti, R. P., Kasyanov, V., Forgacs, G., Drake, C. J., & Markwald, R. R. (2009). Organ printing: tissue spheroids as building blocks. Biomaterials, 30(12), 2164–2174. DOI:10.1016/j.biomaterials.2008.12.084.
204. Akkineni, A. R., Ahlfeld, T., Lode, A., & Gelinsky, M. (2016). A versatile method for combining different biopolymers in a core/shell fashion by 3D plotting to achieve mechanically robust constructs. Biofabrication, 8(4), 045001. DOI:10.1088/1758-5090/8/4/045001.
205. Jia, W., Gungor-Ozkerim, P. S., Zhang, Y. S., Yue, K., Zhu, K., Liu, W., Pi, Q., Byambaa, B., Dokmeci, M. R., Shin, S. R., & Khademhosseini, A. (2016). Direct 3D bioprinting of perfusable vascular constructs using a blend bioink. Biomaterials, 106, 58–68. DOI:10.1016/j.biomaterials.2016.07.038.
206. Ahn, S., Lee, H., Lee, JS. et al. A novel cell-printing method and its application to hepatogenic differentiation of human adipose stem cell-embedded mesh structures. Sci Rep 5, 13427 (2015). DOI:10.1038/srep13427.
207. Yeo, M., Lee, J. S., Chun, W., & Kim, G. H. (2016). An Innovative Collagen-Based Cell-Printing Method for Obtaining Human Adipose Stem Cell-Laden Structures Consisting of Core-Sheath Structures for Tissue Engineering. Biomacromolecules, 17(4), 1365–1375. DOI:10.1021/acs.biomac.5b01764.
208. Costantini, M., Colosi, C., Święszkowski, W., & Barbetta, A. (2018). Co-axial wet-spinning in 3D bioprinting: state of the art and future perspective of microfluidic integration. Biofabrication, 11(1), 012001. DOI:10.1088/1758-5090/aae605.
209. Mombini S, Mohammadnejad J, Bakhshandeh B, et al. Chitosan-PVA-CNT nanofibers as electrically conductive scaffolds for cardiovascular tissue engineering. Int J Biol Macromol. 2019;140:278-287. DOI:10.1016/j.ijbiomac.2019.08.046.
210. Gerasimenko AY, Kurilova UE, Savelyev MS, Murashko DT, Glukhova OE. Laser fabrication of composite layers from biopolymers with branched 3D networks of single-walled carbon nanotubes for cardiovascular implants. Compos Struct. 2021;260:113517. DOI:10.1016/j.compstruct.2020.113517.
211. Tondnevis F, Keshvari H, Mohandesi JA. Fabrication, characterization, and in vitro evaluation of electrospun polyurethane–gelatin–carbon nanotube scaffolds for cardiovascular tissue engineering applications. J Biomed Mater Res B Appl Biomater. 2020;108(5):2276-2293. DOI:10.1002/jbm.b.34564.
212. Kharaziha M, Shin SR, Nikkhah M, et al. Tough and flexible CNT–polymeric hybrid scaffolds for engineering cardiac constructs. Biomaterials. 2014;35(26):7346-7354. DOI:10.1016/j.biomaterials.2014.05.014.
213. Tamo AK, Doench I, Roshanbinfar K, et al. Electrically conductive biopolymer-based hydrogels and fibrous materials fabricated using 3D printing and electrospinning for cardiac tissue engineering. Bioactive Materials. 2025;51:650-719. DOI:10.1016/j.bioactmat.2025.05.014
214. Lee, D., Lee, H., Kim, Y., Yoo, S.Y., Chung, W., & Kim, G. (2016). Phage as versatile nanoink for printing 3-D cell-laden scaffolds. Acta biomaterialia, 29, 112-124.
215. Pati, F., Jang, J., Ha, D. H., Won Kim, S., Rhie, J. W., Shim, J. H., Kim, D. H., & Cho, D. W. (2014). Printing three-dimensional tissue analogues with decellularized extracellular matrix bioink. Nature communications, 5, 3935. DOI:10.1038/ncomms4935.
216. Lee, K. Y., & Mooney, D. J. (2012). Alginate: properties and biomedical

applications. Progress in polymer science, 37(1), 106–126. DOI:10.1016/j.progpolymsci.2011.06.003.
217. Pati, F., Ha, D. H., Jang, J., Han, H. H., Rhie, J. W., & Cho, D. W. (2015). Biomimetic 3D tissue printing for soft tissue regeneration. Biomaterials, 62, 164–175. DOI:10.1016/j.biomaterials.2015.05.043.
218. Pati, F., Ha, D. H., Jang, J., Han, H. H., Rhie, J. W., & Cho, D. W. (2015). Biomimetic 3D tissue printing for soft tissue regeneration. Biomaterials, 62, 164–175. DOI:10.1016/j.biomaterials.2015.05.043.
219. Zhao, Y., Li, Y., Mao, S., Sun, W., & Yao, R. (2015). The influence of printing parameters on cell survival rate and printability in microextrusion-based 3D cell printing technology. Biofabrication, 7(4), 045002. DOI:10.1088/1758-5090/7/4/045002.
220. Kim, Y. B., Lee, H., Yang, G. H., Choi, C. H., Lee, D., Hwang, H., Jung, W. K., Yoon, H., & Kim, G. H. (2016). Mechanically reinforced cell-laden scaffolds formed using alginate-based bioink printed onto the surface of a PCL/alginate mesh structure for regeneration of hard tissue. Journal of colloid and interface science, 461, 359–368. DOI:10.1016/j.jcis.2015.09.044.
221. Luo, Y., Luo, G., Gelinsky, M., Huang, P., & Ruan, C. (2017). 3D bioprinting scaffold using alginate/polyvinyl alcohol bioinks. Materials Letters, 189, 295-298.
222. Zhao, Y., Li, Y., Mao, S., Sun, W., & Yao, R. (2015). The influence of printing parameters on cell survival rate and printability in microextrusion-based 3D cell printing technology. Biofabrication, 7(4), 045002. DOI:10.1088/1758-5090/7/4/045002.
223. Jia, J., Richards, D. J., Pollard, S., Tan, Y., Rodriguez, J., Visconti, R. P., Trusk, T. C., Yost, M. J., Yao, H., Markwald, R. R., & Mei, Y. (2014). Engineering alginate as bioink for bioprinting. Acta biomaterialia, 10(10), 4323–4331. DOI:10.1016/j.actbio.2014.06.034.
224. Lee, H. J., Kim, Y. B., Ahn, S. H., Lee, J. S., Jang, C. H., Yoon, H., Chun, W., & Kim, G. H. (2015). A New Approach for Fabricating Collagen/ECM-Based Bioinks Using Preosteoblasts and Human Adipose Stem Cells. Advanced healthcare materials, 4(9), 1359–1368. DOI:10.1002/adhm.201500193
225. Ang, T., Sultana, F., Hutmacher, D., Wong, Y., Fuh, J., Mo, X., Loh, H., Burdet, E., & Teoh, S. (2002). Fabrication of 3D chitosan–hydroxyapatite scaffolds using a robotic dispensing system. Materials Science and Engineering C, 20(1–2), 35–42. DOI:10.1016/s0928-4931(02)00010-3.
226. Geng, L., Feng, W., Hutmacher, D. W., Wong, Y. S., Loh, H. T., & Fuh, J. Y. (2005). Direct writing of chitosan scaffolds using a robotic system. Rapid Prototyping Journal, 11(2), 90–97. DOI:10.1108/13552540510589458.
227. Wu, Q., Therriault, D., & Heuzey, M. (2018). Processing and properties of chitosan inks for 3D printing of hydrogel microstructures. ACS Biomaterials Science & Engineering, 4(7), 2643–2652. DOI:10.1021/acsbiomaterials.8b00415.
228. Pääkkö M, Ankerfors M, Kosonen H, et al. Enzymatic hydrolysis combined with mechanical shearing and high-pressure homogenization for nanoscale cellulose fibrils and strong gels. Biomacromolecules. 2007;8(6):1934-1941. DOI:10.1021/bm061215p
229. Araujo-Rufino C, Fernandes-Vieira J, Martín-Ramos P, et al. Synthesis of chitosan oligomers composite systems and study of their activity against *Bipolaris oryzae*. Journal of Materials Science and Engineering with Advanced Technology. 2016;13(1):29-52. DOI:10.18642/jmseat_7100121578
230. Passieux R, Sudre G, Montembault A, et al. Cytocompatibility / antibacterial activity trade-off for knittable Wet-Spun chitosan monofilaments functionalized by the in situ incorporation of CU2+ and ZN2+. ACS Biomaterials Science & Engineering. 2022;8(4):1735-1748. DOI:10.1021/acsbiomaterials.2c00079
231. Peniche H, Razonado IA, Alcouffe P, et al. (2024). Wet-Spun Chitosan-Sodium Caseinate Fibers for Biomedicine: From Spinning Process to Physical Properties. *Int J Mol Sci*. 2024;25(3):1768. DOI:10.3390/ijms25031768

232. Notin L, Viton C, Lucas J, Domard A. Pseudo-dry-spinning of chitosan. Acta Biomaterialia. 2006;2(3):297-311. DOI:10.1016/j.actbio.2005.12.005 Yudin VE, Dobrovolskaya IP, Neelov IM, et al. Wet spinning of fibers made of chitosan and chitin nanofibrils. Carbohydrate Polymers. 2014;108:176-182. DOI:10.1016/j.carbpol.2014.02.090
233. Chattopadhyay DP, Inamdar MS. Aqueous behaviour of Chitosan. International Journal of Polymer Science. 2010;2010:1-7. DOI:10.1155/2010/939536 Martínez A, Chornet E, Rodrigue D. STEADY-SHEAR RHEOLOGY OF CONCENTRATED CHITOSAN SOLUTIONS. Journal of Texture Studies. 2004;35(1):53-74. DOI:10.1111/j.1745-4603.2004.tb00822.x
234. Tanaka F, Iwata T. Estimation of the elastic modulus of cellulose crystal by molecular mechanics simulation. Cellulose. 2006;13(5):509-517. DOI:10.1007/s10570-006-9068-x Cai Y, Geng L, Chen S, Shi S, Hsiao BS, Peng X. Hierarchical assembly of nanocellulose into filaments by flow-assisted alignment and interfacial complexation: Conquering the conflicts between strength and toughness. ACS Appl Mater Interfaces. 2020;12(29):32090–32098. DOI:10.1021/acsami.0c07908
235. Másson, M. The quantitative molecular weight-antimicrobial activity relationship for chitosan polymers, oligomers, and derivatives. Carbohydr. Polym. 2024, 337, 122159. DOI: 10.1016/j.carbpol.2024.122159.
236. Lall A, Kamdem Tamo A, Doench I, David L, Nunes de Oliveira P, Gorzelanny C, Osorio-Madrazo A. Nanoparticles and colloidal hydrogels of chitosan–caseinate polyelectrolyte complexes for drug-controlled release applications. Int J Mol Sci. 2020;21(16):5602. DOI:10.3390/ijms21165602
237. Marín-Silva DA, Rivero S, Pinotti A. Chitosan-based nanocomposite matrices: Development and characterization. Int J Biol Macromol. 2019;123:189–200. DOI:10.1016/j.ijbiomac.2018.10.176
238. Tran T.A., Doench I., Kamdem Tamo A., Jahangir, S., Marquez-Bravo, S, Molina, P., Helmstaedter, M., Morales-Helguera, A., Gorzelanny, C., Osorio-Madrazo A. “Biopolymer fibers of high strength and enhanced orientation by the synergy of high/low molecular weight chitosans in hybrid biomaterials processed by gel spinning”. *Journal of Functional Biomaterials* (2025),16(11):405. DOI:10.3390/jfb16110405
239. Wang X, Tang R, Zhang Y, Yu Z, Qi C. Preparation of a novel chitosan-based biopolymer dye and application in wood dyeing. Polymers (Basel). 2016;8(11):338. DOI:10.3390/polym8110338.